SYNTHESIS AND CHARACTERIZATION OF LATE TRANSITION METAL OLIGOTHIOPHENE COMPLEXES FOR LIGHT HARVESTING APPLICATIONS

by

Stephanie Amber Moore

B.Sc. (Hons.), St. Francis Xavier University, 2006

A THESIS SUBMITTED IN PARTIAL FULFILLMENT OF
THE REQUIREMENTS FOR THE DEGREE OF

DOCTOR OF PHILOSOPHY

in

The Faculty of Graduate Studies
(CHEMISTRY)

THE UNIVERSITY OF BRITISH COLUMBIA

(Vancouver)

June 2012

ABSTRACT

The synthesis and characterization of late transition metal complexes combined with the β-substituted 3′-(diphenylphosphino)-2,2′:5′,2″-terthiophene (PT_3) to yield metal-oligothiophene hybrid complexes are reported. These new complexes (shown on the following page) were studied with absorption, emission, and transient absorption spectroscopies, electrochemistry and X-ray crystallography.

Ru(II) and Os(II) bis(diimine) complexes (**52**-**53** and **54**-**55**, respectively) containing PT_3 in two different coordination modes (*PS* and *PC* bound) are reported. The binding mode is shown to affect the structural, photophysical and electronic properties of the complexes. Transient absorption spectra and lifetimes were obtained for all the complexes, and support a PT_3 ligand-based lowest excited state in the case of the *PS* bound complexes, and a charge separated lowest excited state in the *PC* bound complexes. The DFT calculations and experimental results agree well.

Cyclometalated iridium (III) complexes (**58**-**63**) were synthesized using microwave irradiation. In addition to the *PS* and *PC* coordination modes observed in the group 8 complexes, a third, monodentate, coordination mode was observed (*P*). The lowest energy absorption band and emission band shift based on the PT_3 coordination mode. The nature of the excited state lifetimes did not change with coordination mode; all were assigned as a PT_3 ligand-based excited state, however, the excited state lifetimes are influenced by the coordination mode.

Heteroleptic Cu(I) complexes (**75**-**76**) were synthesized and yielded three and four coordinate complexes. The electrochemical and photophysical properties of these complexes vary with solvent. Minor changes are observed in the absorption spectra when obtained in different solvents, but interesting differences are observed in the electrochemical reversibility, excited state lifetimes, and profiles of the emission and transient absorption spectra.

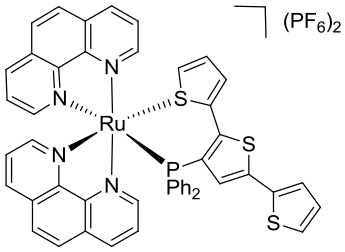

[Ru(phen)$_2$PT$_3$-*PS*](PF$_6$)$_2$
52

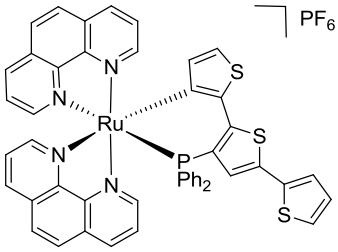

[Ru(phen)$_2$PT$_3$-*PC*](PF$_6$)
53

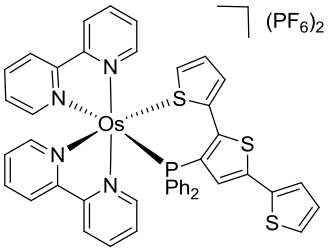

[Os(bpy)$_2$PT$_3$-*PS*](PF$_6$)$_2$
54

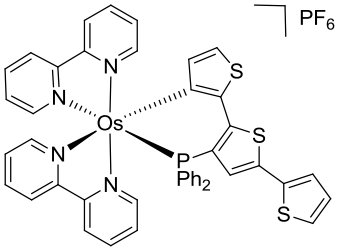

[Os(bpy)$_2$PT$_3$-*PC*](PF$_6$)
55

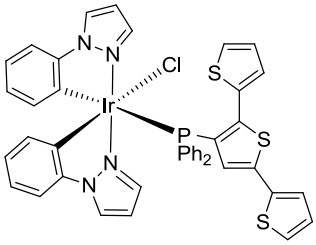

Ir(ppz)$_2$PT$_3$Cl-*P*
58

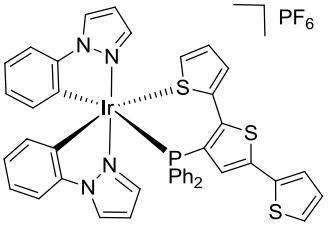

[Ir(ppz)$_2$PT$_3$-*PS*](PF$_6$)
59

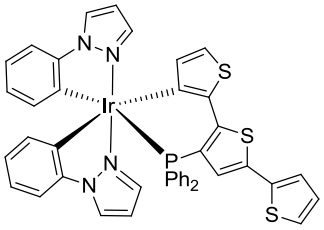

Ir(ppz)$_2$PT$_3$-*PC*
60

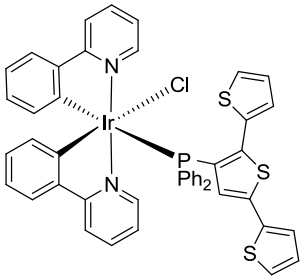

Ir(ppy)$_2$PT$_3$Cl-*P*
61

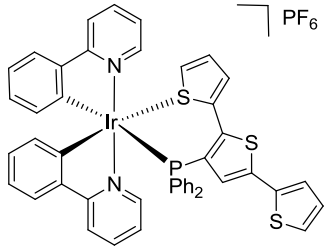

[Ir(ppy)$_2$PT$_3$-*PS*](PF$_6$)
62

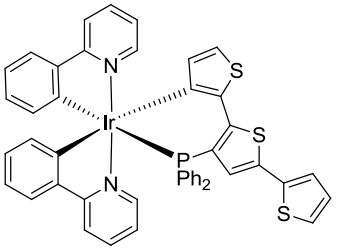

Ir(ppy)$_2$PT$_3$-*PC*
63

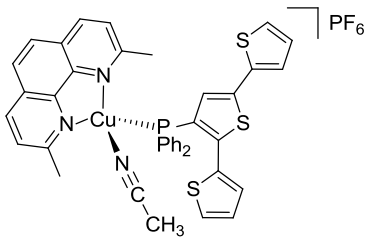

[Cu(dmp)(MeCN)PT$_3$-*P*](PF$_6$)
75

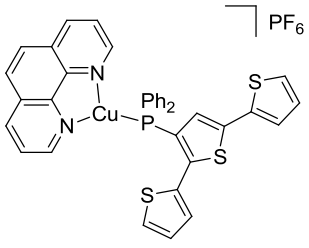

[Cu(phen)PT$_3$-*P*](PF$_6$)
76

PREFACE

Material in Chapter 2 has been previously published as a full paper: Moore, S.A., Nagle, J.K., Wolf, M.O., Patrick, B.O. *Inorg. Chem.*, **2011**, *50*, 5113-5122. I am the primary author under the supervision of Professor Michael O. Wolf. Dr. Brian O. Patrick determined the X-ray crystal structures of **52**, **54** and **55**. Dr. Jeffrey Nagle of Bowdoin College in Brunswick, Maine carried out the DFT calculations on **48**, **49**, **54** and **55,** and analyzed the results.

Material in Chapter 3 will be published in the future with authors Moore, S.A., Wolf, M.O., Patrick, B.O. I am the primary author under the supervision of Professor Michael O. Wolf. Dr. Brian O. Patrick determined the X-ray crystal structures of **58**, **59**, **60** and **61**.

Material in Chapter 4 will be published in the future with authors Moore, S.A., Wolf, M.O., Patrick, B.O. I am the primary author under the supervision of Professor Michael O. Wolf. Dr. Brian O. Patrick determined the X-ray crystal structures of **75** and **76**.

TABLE OF CONTENTS

LIST OF TABLES

LIST OF FIGURES

LIST OF CHARTS

LIST OF SCHEMES

LIST OF SYMBOLS AND ABBREVIATIONS

Abbreviation	Description
A	amperes
Å	Ångstrom
ADF	Amsterdam density functional
ADF-DFT	Amsterdam density functional - density functional theory
AIM	atoms in molecule
Anal.	Analysis
AO	atomic orbital
A_2T_3	3,3″-*bis*(acetylene)-2,2′-5′,2″-terthiophene
a.u.	arbitrary units
bdpp	1,2- *bis*(diphenylphosphino)benzene
bpy	2,2'-bipyridine
br.	broad
Calcd	calculated
CB	conduction band
cm	centimeter
C^N	cyclometalating ligand
CS	charge-separated
CT	charge transfer
CV	cyclic voltammogram/ voltammetry
δ	chemical shift (ppm)
°	degrees
°C	degrees Celsius
Δ	heat
Δ	difference
ΔE	energy difference between redox couples (mV)
D	dye
d	doublet
DCM	dichloromethane
dd	doublet of doublets

ddd	doublet of doublets of doublets
DFT	density functional theory
DMF	dimethylformamide
dmp	2,9-dimethyl-1,10-phenanthroline
dppe	1,2- *bis*(diphenylphosphino)ethane
dppf	1,1′- *bis*(diphenylphosphino)ferrocene
dppm	*bis*(diphenylphosphinomethane)
dppp	1,3- *bis*(diphenylphosphino)propane
DSSC	dye-sensitized solar cell
ε	molar absorptivity ($M^{-1}cm^{-1}$)
η^x	hapticity
e^-	electron
$E_{1/2}$	half wave redox potential (V)
EA	elemental analysis
EDOT	3,4-ethylenedioxythiophene
E_g	band gap
E_p	peak potential, irreversible wave (V)
EPR	electron paramagnetic resonance
esd	estimated standard deviation
ESI	electrospray ionization
Et_2O	diethylether
EtOH	ethanol
eq.	equivalents
eV	electron volts
F	X-ray scattering factor
Fc	ferrocene
g	gram
GGA	generalized gradient approximation
GHz	gigahertz
G-J	Gophinatan-Jug
HH	Head-to-Head
HOMO	highest occupied molecular orbital

hr	hour
HRMS	electron high-resolution mass spectrometry
HT	Head-to-Tail
Hz	Hertz
I	intensity of the X-ray reflection
IPCE	incident photon to current efficiency
IR	infrared
ITO	indium doped tin oxide
J	magnetic coupling constant
K	Kelvin
k_{nr}	non-radiative decay constant
k_r	radiative decay constant
λ_{em}	emission wavelength
λ_{ex}	excitation wavelength (nm)
λ_{max}	wavelength at band maximum (nm)
L	ligand
LC	ligand centered
LDA	lithium diisopropylamide
LEC	light-emitting electrochemical cell
LL′CT	ligand to ligand charge transfer
LMCT	ligand to metal charge transfer
LUMO	lowest unoccupied molecular orbital
μ	X-ray linear absorption coefficient
μ	micro
μA	microamperes
μs	microseconds
M	molarity (mol/L), molecule (MS), metal
m	multiplet (NMR), milli
MALDI-TOF	matrix-assisted laser desorption ionization time of flight
MC	metal centered
MDC-q	multipole-derived quadrupole
MeOH	methanol

MeCN	acetonitrile
mg	milligram
MHz	Megahertz
min	minute
mL	millilter
MLCT	metal to ligand charge transfer
MLL′CT	mixed metal-ligand to ligand charge transfer
mm	millimeter
mmol	millimole
MO	molecular orbital
mol	mole
MS	mass spectra
mV	millivolts
m/z	mass-to-charge ratio
n	number of units (ligands, oligomer, polymer), nano
Nd:YAG	neodymium-doped yttrium aluminium garnet
NHC	N-heterocyclic carbene
NIR	near infrared
nm	nanometer
N-M(1)	Nalejawski-Mrozek method1
N-M(2)	Nalejawski-Mrozek method2
N-M(3)	Nalejawski-Mrozek method3
NMR	nuclear magnetic resonance
N^N	diimine ligand
NPA	natural population analysis
ns	nanosecond
ω	angle the X-ray source makes with the crystal
OLED	organic light emitting diode
ORTEP	Oak Ridge Thermal Ellipsoid Plot
Os*PC*	osmium complex with *PC* coordination of PT_3
Os*PS*	osmium complex with *PS* coordination of PT_3
Φ_{em}	emission quantum yield

ϕ	X-ray rotation axis
P	phosphine coordination
PAT	polyalkylthiophene
PEDOT	poly(3,4-ethylenedioxythiophene)
PC	phosphine, thienyl carbon coordination
Ph	phenyl (C_6H_5)
phen	1,10-phenanthroline
POP	*bis*(2-(diphenylphosphanyl)phenyl)ether
P^P	diphosphine ligand
ppm	parts per million
ppy	2-phenylpyridine
ppz	1-phenylpyrazole
PS	phosphine, thienyl sulphur coordination
PT	polythiophene
PT_3	3´-(diphenylphosphino)-2,2′:5′,2″-terthiophene
P_2T_3	3,3″-*bis*(diphenylphosphino)-2,2′:5′,2″-terthiophene
py	pyridine
q	quartet
ρ	density (g cm^{-1})
R	linear regression goodness of fit
Ref.	reference
Ru*PC*	ruthenium complex with *PC* coordination of PT_3
Ru*PS*	ruthenium complex with *PS* coordination of PT_3
$\sum$	the sum of
σ	standard deviation of the X-ray intensity
s	singlet (NMR), second
SCE	standard calomel electrode
SEM	scanning electron microscopy
sh	shoulder
SOMO	singly occupied molecular orbital
τ	lifetime
θ	angle

θ	angle of diffraction
t	triplet
T_3	terthiophene
TA	transient absorption
$TBAPF_6$	tetrabutylammonium hexafluorophosphate
terpy	2,2';6',2''-terpyridine
TGA	thermogravimetric analysis
THF	tetrahydrofuran
tht	tetrahydrothiophene
TOF	time of flight
TT	Tail-to-Tail
UBC	University of British Columbia
UV	ultraviolet
V	volt, volume
VB	valence band
VDD	Voronoi deformation density
vis	visible
XY	bidentate ligand
ζ_c	one electron spin-orbit coupling constant
Z	number of molecules in a crystallographic unit cell
ZORA	zeroth-order relativestic approximation

ACKNOWLEDGEMENTS

Throughout this process there have been many people who have helped me achieve my goals. First and foremost, I would like to thank my supervisor, Dr. Mike Wolf, for his support, guidance, and helpful advice. Many thanks to my fellow Wolf group members, both past and present. I enjoyed the atmosphere, friendship, and support. It was a pleasure to work with each of you and to benefit from your knowledge, whether it was in the lab, at a pub or out in the wilderness. I am especially grateful to Tim Kelly for teaching me the ropes, and Glen Bremner for all his help with the potentiostat.

Thanks to my friends outside of the Wolf group as well. You have made this journey much easier. Although I don't have room to mention everyone by name, I hope you know who you are! Yasmin, you are a wonderful and generous friend, and I admire your positive outlook despite some tough situations. CT, you are a fabulous friend. Your smile and support has been greatly appreciated. Thanks for everything.

I wish to thank all the shops, services, technicians and staff for keeping everything running smoothly. Special thanks are extended to the staff at the UBC Mass Spectrometry Centre, for collecting elemental analysis and mass spectrometry data on my complexes, Dr. Brian Patrick, for solving my crystal structures, and Saeid Kamal, for his vast knowledge and assistance with the TA instrument. Something that was once only considered future work is now a big part of my thesis. My thanks also go to Dr. Jeff Nagle (Bowdoin College) for calculations on the group 8 complexes, and Dr. Dai Davies (University of Leicester) for his helpful chats and suggestions related to the iridium work. Thanks to the Orvig group for the use of their microwave reactor. I am also thankful for funding from NSERC, UBC and the Walter C. Sumner Foundation.

Of course no acknowledgments would be complete without giving thanks to my family. My parents have always expressed how proud they are of me and how much they love me. I too am proud of them and love them very much. I am grateful for them both and for the 'smart genes' they passed on to me. I am also extremely grateful for my brother, Greg. In addition to knowing how to drive me crazy, he can always make me smile. Thanks for all your support, and for dragging me out of the house on more than one occasion.

To Mom and Dad

CHAPTER 1

INTRODUCTION

Section 1.1 – Overview

The development and use of sustainable energy sources in a society that is overly reliant on petroleum based fuels is essential. Alternative energy sources, such as solar, wind and hydrogen are all being actively investigated for replacements to fossil fuels.[1, 2] The sun gives us our most abundant energy source, and there is a need to acquire new methods to capture, transfer, store and use solar energy effectively. Photovoltaic cells based on inorganic semiconductors (silicon) have long been commercially available, but have a high production cost (compared to electrical energy generated using coal or oil).[3] Semiconducting organic π-conjugated materials, such as polythiophene, are attractive for application in solar cells, sensors, optical devices and electrical conductors.[4] They have good thermal stability, and can be functionalized to alter their optical and electronic properties, as well as lead to increased solubility.[4] Conjugated polymer or oligomer materials may be easily spray or spin coated, reducing production costs significantly.

When metal complexes are coordinated to conjugated polymers, interactions occur which modify the physical, chemical and electronic properties of both species.[5] Metals can be incorporated into oligothiophene or polythiophene chains by direct insertion into the chain,[6] direct bonding to the backbone through a thiophene,[7] bypyridyl[8] or other group, or as pendant groups attached directly through a ligand.[9] Numerous analogues and derivatives can be made, resulting in a wide variety of materials. For example, oligo- and polythiophenes have been incorporated into organic light-emitting diodes (OLEDs), photovoltaics, transistors and other devices.[10]

This thesis focuses on the synthesis and characterization of metal-terthiophene complexes. The photophysical properties are investigated, along with the electrochemical properties of the complexes, to determine if there is promise for use of these, or similar, complexes as solar energy harvesters, such as dyes in dye-sensitized solar cells (DSSCs).

In this Chapter, π – conjugated materials, with emphasis on oligo- and polythiophenes, are discussed, followed by a section on metal organic hybrid materials. The effects of the incorporation of metal centers into conjugated materials are examined. Examples of some late transition metal oligo – and polythiophenes hybrids are given. Finally, a brief discussion on DSSCs and useful dye properties is included.

Section 1.2– π – Conjugated Materials

π – Conjugated materials have alternating single and double bonds resulting in a backbone of sp^2 hybridized carbon centers and/or heteroatoms with an extended π conjugated system. Common examples of conjugated polymers are shown in Chart 1-1. Heeger, MacDiarmid and Shirakawa discovered high conductivity in oxidized iodine-doped polyacetylene in 1977.[11] Their discovery showing doped polyacetylene has up to 12 orders of magnitude greater conductivity than undoped polyacetylene launched research in the area of conducting polymers.[12-15] The Nobel prize in Chemistry was awarded to these researchers in 2000[16] for "the discovery and development of conducting polymers."

Chart 1-1

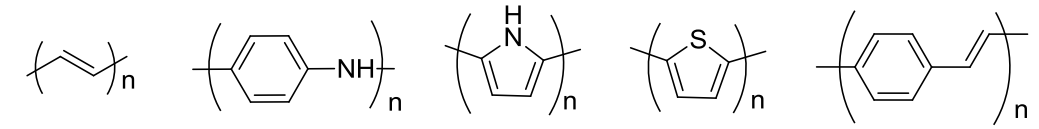

polyacetylene polyaniline polypyrrole polythiophene polyphenylene vinylene

Polyacetylene, and shorter oligomers, are composed of repeating ethylene units. The highest occupied molecular orbital (HOMO) and lowest unoccupied molecular orbital (LUMO) of polyacetylene oligomers are π and π* orbitals, respectively. With each additive ethylene unit in the chain, there is an increase in the number of π and π* MOs. This increase in conjugation causes a decrease in the HOMO-LUMO gap. In a polymer of infinite length, the π-orbitals overlap and form a valence band (VB), while the overlapping π*-orbitals form a conduction band (CB), similar to the bands found in

conventional (inorganic) semiconductors. The energy difference between the two bands is known as the band gap, or E_g. (Figure 1-1) If this value is small, as is the case for most conjugated polymers, the polymer behaves as an organic semiconductor. Conductivity of conjugated polymers varies greatly between different types of polymers, and is affected by a number of different factors. More background information on π – conjugated systems can be found in the *Handbook of Conducting Polymers*.[17]

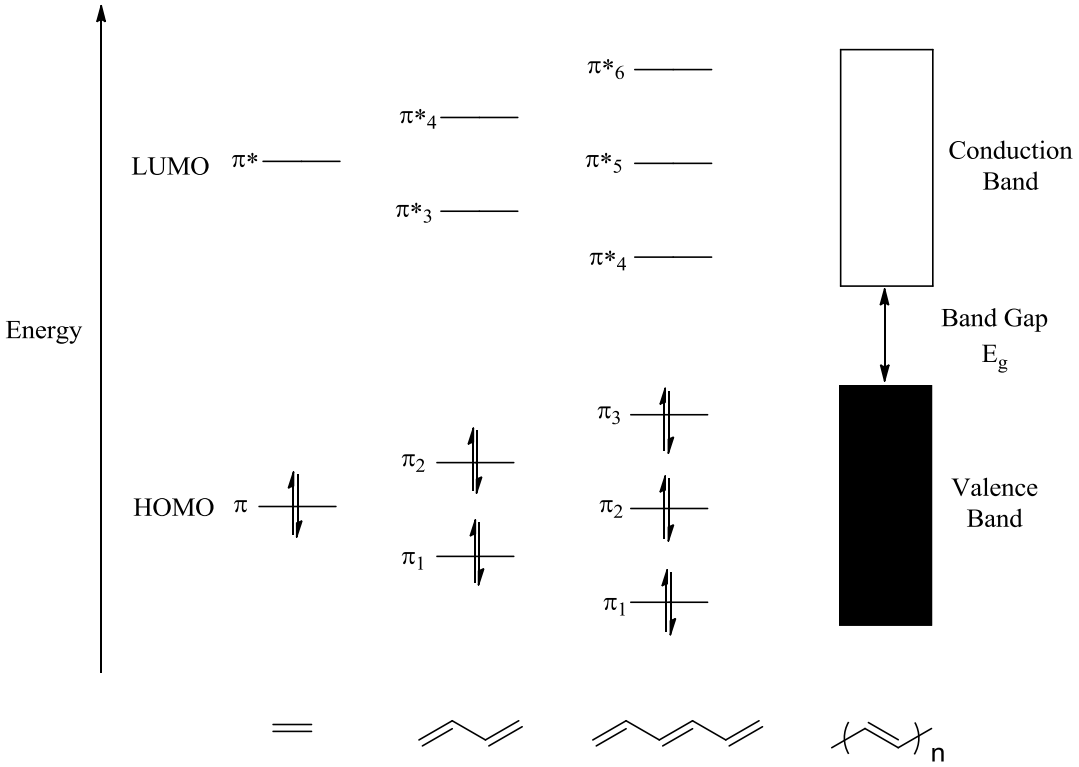

Figure 1-1 Energy level diagram for conjugated oligomers from ethylene to polyacetylene.

Section 1.3– Oligo- and Polythiophenes

Polythiophenes (PTs) are one of the most extensively studied classes of conducting polymers as they have interesting optical and electronic properties.[4] Thiophenes are relatively stable and can be functionalized fairly easily, allowing for increased solubility and processability. PTs can be polymerized through the α or β positions of the thiophene ring (Chart 1-2). In terms of conductivity, it is most ideal to

have α,α linkages because other types of linkages (α,β or β,β) can lead to defects in the chain, such as twisting, which reduces the effective conjugation length. Therefore, although further functionalization can be carried out at either the α or β positions, it is more common for substituents to be incorporated at the β position(s).

Chart 1-2

The discovery of polyalkylthiophenes (PATs),[18,19] such as poly(3-hexylthiophene), has resulted in materials with greatly increased solubility and allows for drop casting and spin coating of these materials. The introduction of a new functional group in the β position also leads to the possibility of more regioisomers being produced (Chart 1-3). Regioregular Head-to-Tail (HT) PATs have improved properties over non-regioregular analogues.[20] As PATs have a β position functionalized, Head to Head (HH) coupling produces steric hindrance which can cause the thiophene rings to twist out of the plane,[21] reducing the π-orbital overlap, and thus, conjugation of the chain.

Chart 1-3

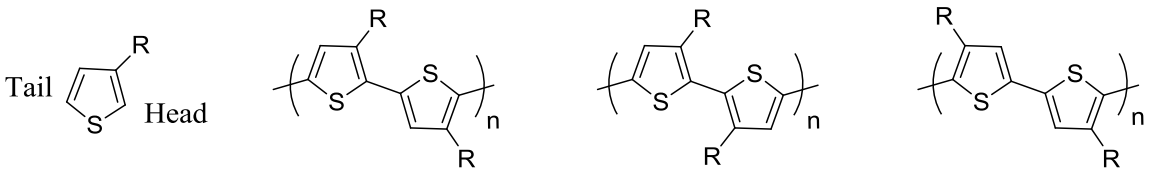

There are numerous methods reported for the synthesis of polythiophenes. For a complete review, the *Handbook of Oligo-and Polythiophenes*[4] is recommended. The main methods for synthesis include metal catalyzed cross coupling reactions, chemical oxidation or electrochemical polymerization. There are advantages and disadvantages to each method.

During electrochemical polymerization, a potential is applied across a solution containing a thiophene monomer. Oxidation of the monomer results in a radical cation, which can then couple with a second radical cation to form a dication dimer. Loss of two protons gives bithiophene, which can then react with another radical cation to form terthiophene. This process continues until a polymer is formed. As the chain gets longer, the oxidation potential decreases, driving formation of polymer. While electrochemical polymerization is convenient, since the polymer does not need to be isolated and purified (it is deposited directly on a substrate), it can produce polymers with undesirable $\alpha - \beta$ linkages and varying degrees of regioregularity. Additionally, the oxidation potential of the thiophene monomers is typically higher than the oxidation potential of the resulting polymer. Therefore, the polymer can be irreversibly oxidized and decompose at a rate comparable to the polymerization of the corresponding monomer. This phenomenon is referred to as the "polythiophene paradox".[22] Polymerization via chemical oxidation is similar, except the source of oxidant is different. In this case, $FeCl_3$ is typically used as the oxidant. Chemical polymerization results in defects in the chain, and it has been reported that adding the oxidant very slowly may help to achieve better control of regioregularity.[23] The oxidative polymerization of thiophenes can be performed at room temperature under less demanding conditions than required for the chemical cross-couplings described later in this chapter.

Scheme 1-1

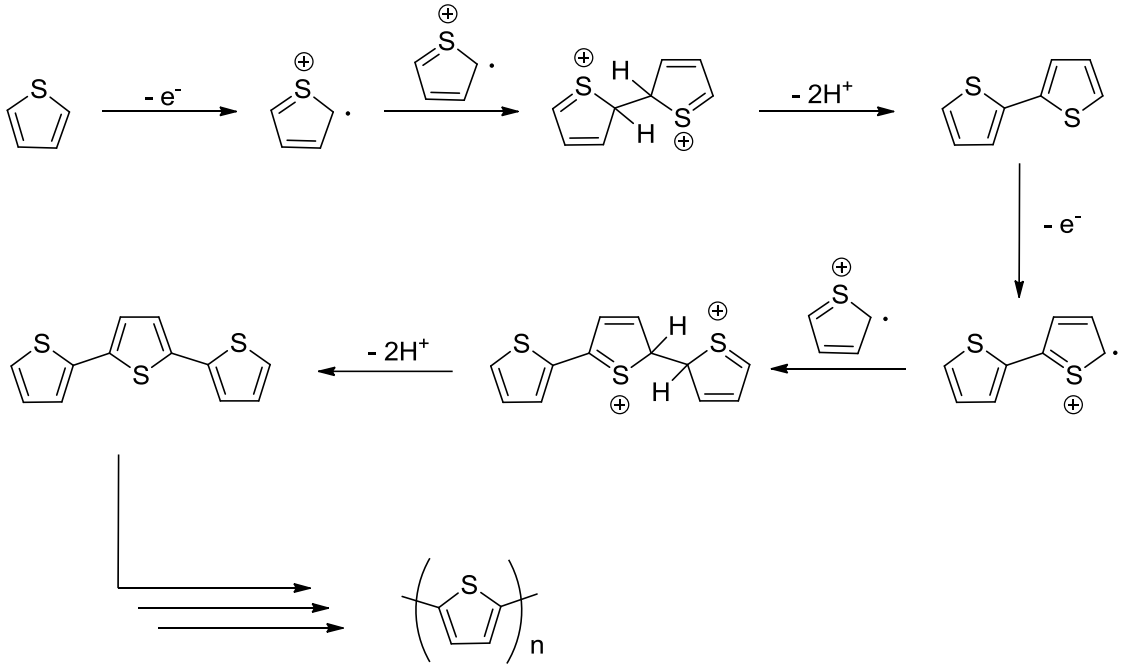

Chemical synthesis allows for the use of a more diverse selection of monomers, and, with the appropriate catalysts, the ability to synthesize highly regioregular substituted PTs. Yamamoto *et al.* reported one of the first procedures for PT,[24] based on the Kumada coupling[25] of Grignard reagents (Scheme 1-2). Lin and Dudek[26] published a similar route in the same year. The synthesis generally produces low molecular weight polymers caused by poor solubility of the unsubstituted thiophene. McCullough *et al.* developed the first synthesis of regioregular PATs[27] (Scheme 1-2). Selective bromination forms 2-bromo-3-alkylthiophene, followed by a lithiation step, transmetallation and then Kumada cross-coupling with a nickel catalyst. This method produces nearly 100% HT–HT couplings.[28] Rieke *et al.* observed selection of catalyst is important. When 2,5-dibromo-3-alkylthiophene is treated with highly reactive “Rieke zinc," addition of $Pd(PPh_3)_4$ produces a regiorandom polymer.[29] Using $Ni(dppe)Cl_2$ instead yields regioregular PAT.[29] Both McCullough and Rieke’s methods produce fairly high molecular weight regioregular polymers, but also require low temperatures, and the careful exclusion of water and oxygen.

Scheme 1-2

Yamamoto Method

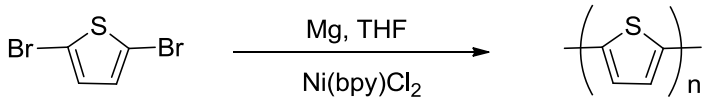

McCullough Method

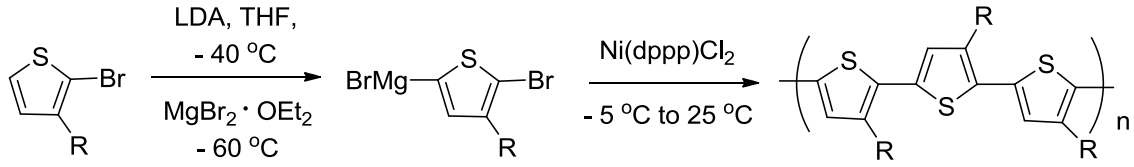

Oligo- and polythiophenes have the capability to bind to metals. They can do so through the lone pair of the S atom, or via the ring in an η^2, η^4, or η^5 fashion. The metal can possibly back-bond into the π^* orbital as well.

Section 1.4– Metal Organic Hybrid Materials

Section 1.4.1 – General

The incorporation of transition metals into conjugated materials can alter the chemical and electronic properties of the organic polymer. The metal groups can be incorporated in various ways, but can generally be classified as Type I, Type II or Type III (Figure 1-2).[30, 31] In Type I hybrid materials, the metal is attached to the backbone, typically through a saturated linker, such as an alkyl chain. The metal and conjugated polymer are separated enough that there is no electronic communication between the components. The properties of the metal complex are similar to the untethered analogues. In Type II materials, the metal and polymer backbone are electronically coupled. This occurs when the metal is closely or directly tethered to the backbone of the polymer. This causes the properties of the material to be influenced by each component. In Type III materials, the metal center is directly inserted into the polymer backbone. Here, the

polymer is very strongly coupled to the metal, leading to electronic interactions between the two components and perturbation of both the polymer and metal system can occur.

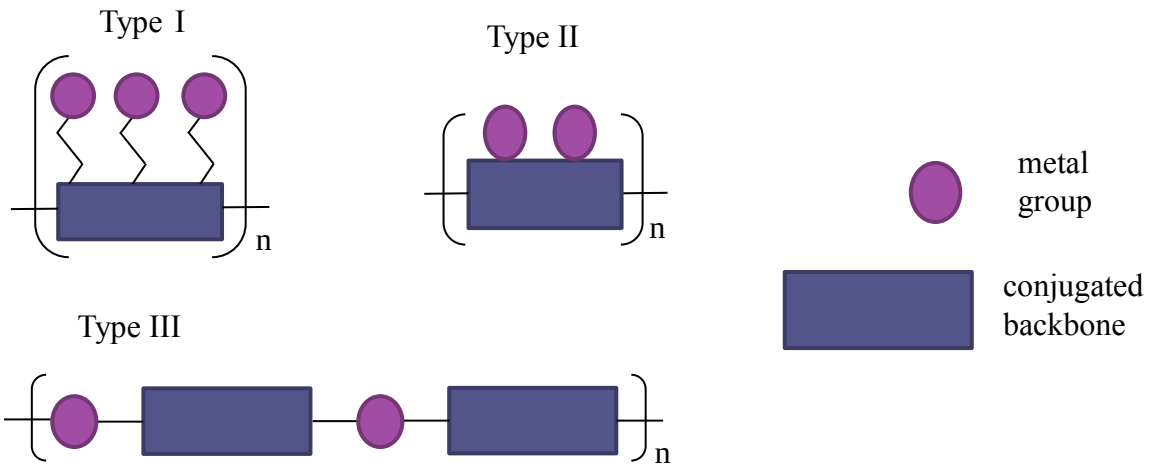

Figure 1-2 Schematic of different types of metal-containing polymer systems.

The use of monomer or oligomer units when probing interactions between metal and polymer components are advantageous. Shorter chained systems are easier to synthesize and isolate, and their properties are usually characteristic of their extended structures. There are several examples of oligo- and polythiophene complexes that fall into each hybrid classification, along with various metal groups that have been appended to or inserted into the polymer chain. As this thesis focuses on late transition metal complexes, selected examples of oligo- and polythiophene with metals from groups 8-12 of the periodic table will be discussed. For the interested reader, there are several reviews of metal containing polymers and oligomers of thiophene,[30,31, 32] as well as book chapters[33, 34] that cover the field thoroughly.

Section 1.4.2 – Group 8 Metal Oligo- and Polythiophene Hybrids

Ferrocene is stable, easy to functionalize and has a reversible $Fe^{II/III}$ redox couple. For these reasons, ferrocene has been incorporated into a number of conjugated oligomers and polymers. Chart 1-4 shows examples where ferrocene has been

incorporated into a polythiophene backbone, or attached to the backbone by a linker group.

Higgins and co-workers polymerized oligothiophenes where ferrocene was directly inserted into the backbone (**1**). When only one thiophene unit was attached to the ferrocene, electropolymerization was not observed.[35] When bithiophene or terthiophene was used, the peak current for ferrocene oxidation shifted to a more positive potential and diminished with repeated scans, while the ferrocenium couple moved to a more negative potential and eventually disappeared. A new redox wave appeared at 0.89-0.92 V while this occurred, and was assigned as the reversible oxidation of quaterthiophene or sexithiophene, respectively.

Curtis used polythiophene with a pendant ferrocene moiety to make regiorandom polymers (**2**). Fluorescence quenching of the polymer shows charge transfer between the pendant ferrocene groups and main chain of the polymer.[36] Organic p/n photocells were created which demonstrated improved photoconductivities over the polymer without the ferrocene unit. This may be from efficient hole-hopping between the ferrocenes, provided the number of ferrocene groups is above the critical concentration.

Swager used azaferrocene with polythiophene dervivatives (**3**, **4**, and **5**) to investigate the nature of metal – polymer interactions.[37] The π-bound metal is inserted into a fully conjugated chain. The PEDOT analogue (**4**) shows larger separation between oxidation and reduction peaks than the others polymers. Desired properties could be improved upon with redox matching.

Chart 1-4 Ref.[35-37]

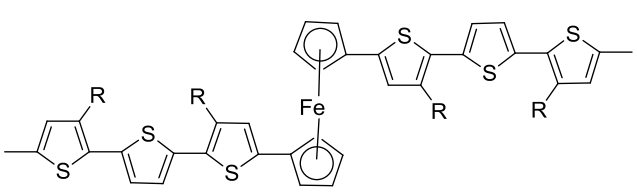

1

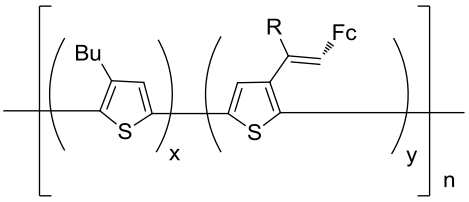

R = H, CN; Fc = ferrocene

2

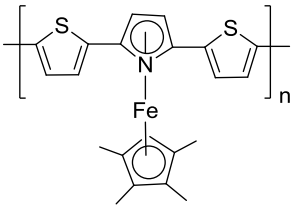

3

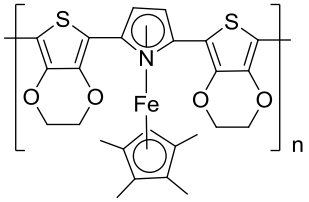

4

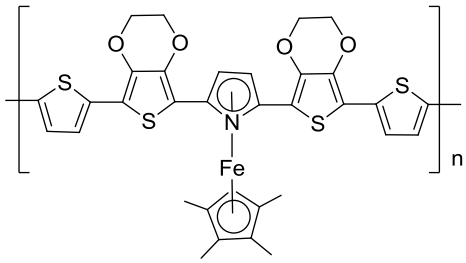

5

Mirkin's group has synthesized Ru(II) complexes from redox switchable hemilabile ligands (**6** and **7**, Chart 1-5).[7, 38] The complexes show that tunable ligands can be used to electrochemically vary the metal center properties.[7] The ligand allowed for a direct probe of the oxidation state of the metal center. Changes in the CO stretching band were observed upon oxidation of the monomer, as well as with polymerization.

Guillerez and coworkers have created d^6 transition metal polypyridine complexes interspersed within a poly(3-octylthiophene) π conjugated network (**8**, Chart 1-5).[39, 40] These soluble polymers exhibited long-lived MLCT luminescence, although the emission was quite weak. In order for the materials to display efficient MLCT emission, it was determined the $^3\pi - \pi^*$ state of conjugated system must be kept above the MLCT energy state. These systems may be useful for applications that require photoconductivity.

Ogawa and Araki describe complexes which show an intense broad band in the visible region (**9**, Chart 1-5).[41] Electrochemistry of the complex shows four reversible reduction waves. In dimethylformamide (DMF), film formation was not observed. However, when using acetonitrile (CH_3CN), electropolymerization occurs. In the film, two reversible reductions were observed at -1.12 and -1.34 V when scanned out to -1.6 V.

Irreversible and reversible oxidations were observed at 1.08 and 1.38 V, respectively. The films could be deposited onto several different substrates.

Chart 1-5 Ref.[7, 39, 41]

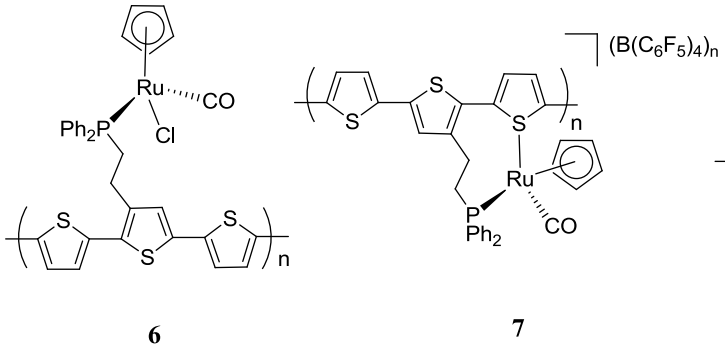

6 **7** **8**

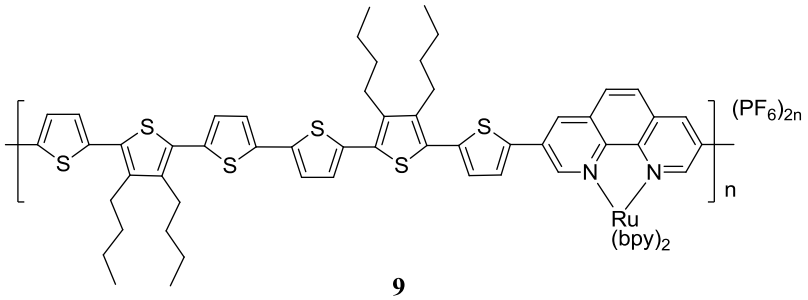

9

Swager showed electrochemical behavior of complexes is dependent on the amount and position of bithienyl substituents (**10** and **11**, Chart 1-6).[8, 42] The bithienyl moieties cause reduction at more positive potential than the parent ($Ru(bpy)_3^{2+}$) species. Changing the position of the thienyl groups from the 5, 5′ to the 4, 4′ positions decreases conductivity from 1×10^{-3} to 3×10^{-4} S cm^{-1}.[42] The Ru centers are in direct communication via a conjugated bridge, and it was noted self-exchange between Ru centers is more favourable than through space.

Wu and coworkers replaced one of the anchoring 2,2′-bipyridyl-4,4′-dicarboxylate ligands of N3[43] (**12**, Chart 1-6) with a highly conjugated ancillary ligand to give **13**. (Chart 1-6).[44] There are three absorption bands observed: 533 nm (MLCT transition), 400 nm ($\pi - \pi^*$ transition of the alkyl bithiophene substituted bipyridine and MLCT transitions), and 312 nm ($\pi - \pi^*$ transition of the dicarboxylatebipyridine).[44] Complex **13**

demonstrated a broad IPCE curve, covering almost the entire visible spectrum, from 350-700 nm. Additionally, the alkyl groups can prevent complexes from water induced desorption of dye molecules from TiO_2 surfaces, when used in DSSCs. Recent work in our group indicates the introduction of an amide linker between the diimine and oligothiophene group may be beneficial for use in photoactive devices due to long lifetimes.[45]

Chart 1-6 Ref.[42-44]

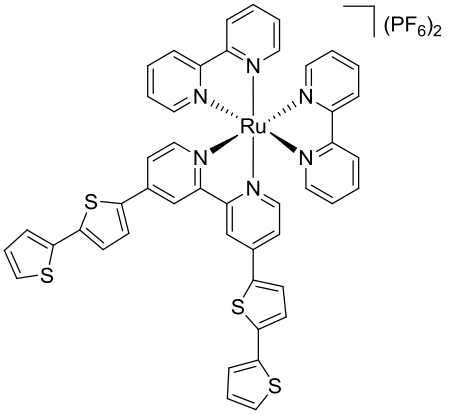

10

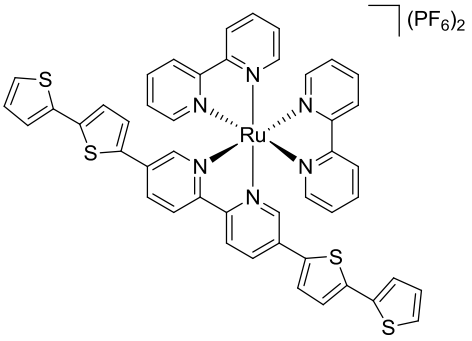

11

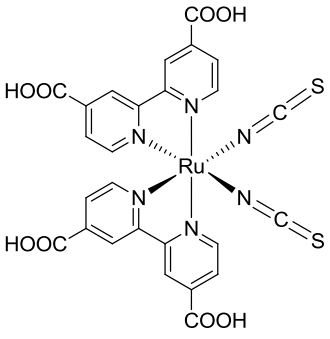

12

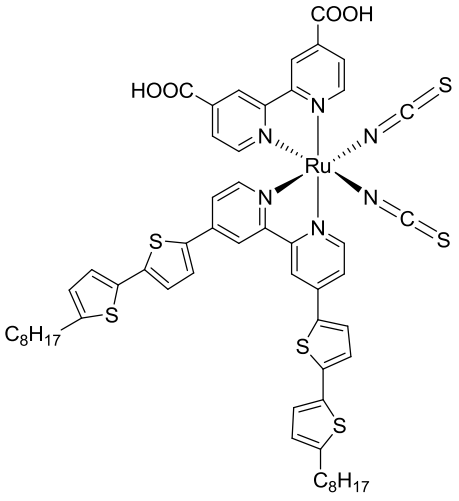

13

Constable and co-workers electropolymerized Ru(II) and Os(II) terpyridine complexes with thiophene (**14**, Chart 1-7).[46] Upon electropolymerization, a red shift in the MLCT transition, due to increased conjugation, was observed. The terthienyl radical cation was the least stable, and rigorous exclusion of H_2O and nucleophiles was required to achieve polymerization. The bithiophene complexes easily electropolymerized to give quaterthienyl bridged polymers, with conductivity of 1.6 (±0.3) × 10^{-3} S cm^{-1} regardless of the specific metal center (Ru or Os) used. The polymer displayed distinct metal and thienyl-bridged based redox waves.[46] Charge transport rates were enhanced by matching the redox potential of the metal center and bridge states using different conjugated bridges.

Chart 1-7 Ref.[46, 47]

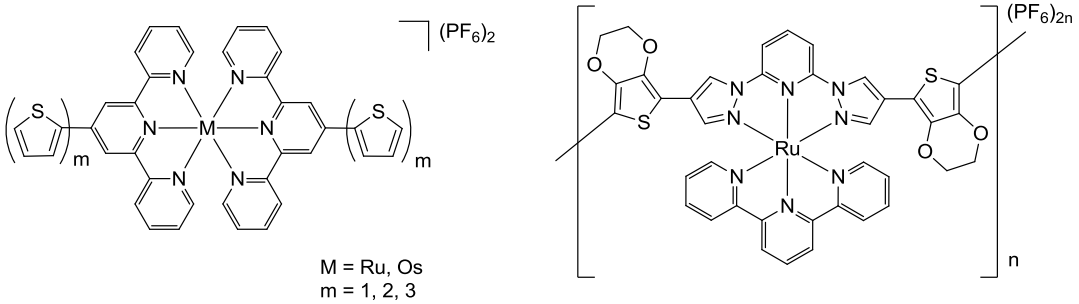

14 **15**

Holliday's group synthesized a tridentate system incorporating poly(3,4-ethylenedioxythiophene) (PEDOT) (**15**, Chart 1-7).[47] The monomer shows π-π* transitions and an MLCT transition, whereas the polymer exhibits a broad absorption of overlapping bands between 300 and 700 nm, suggesting potential for application in photovoltaic devices. With oxidation, a new band around 900 nm was observed. Most likely this band is caused by a localized EDOT based radical cation or polaron. The electropolymerized polymer shows two oxidation waves, similar to the monomer, attributed to the $Ru^{II/III}$ and $PEDOT^{0/I}$ oxidations.

Section 1.4.3– Group 9 Metal Oligo- and Polythiophene Hybrids

Endo and coworkers demonstrated reaction of organocobalt polymers with S_8 to give substituted thiophenes (**16**, Chart 1-8).[48] Cyclic voltammetry showed two oxidation peaks at high potentials, possibly because of the sterically hindered thiophene, and irregularities in the chain. The UV-vis spectra showed the main chain is partially conjugated, and thermogravimetric analyses (TGA) revealed the material displayed fairly high thermal stabilities.

Chart 1-8 Ref.[9, 48-52]

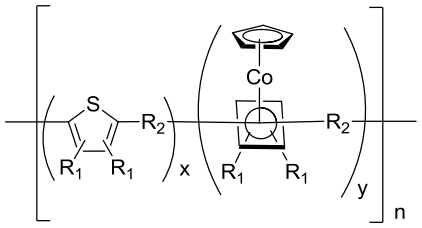

16

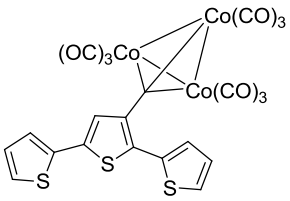

17

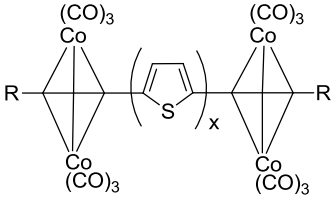

18

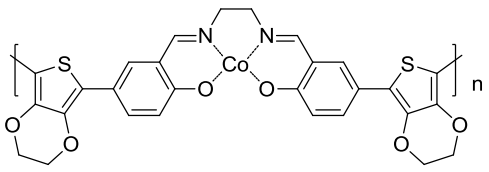

19

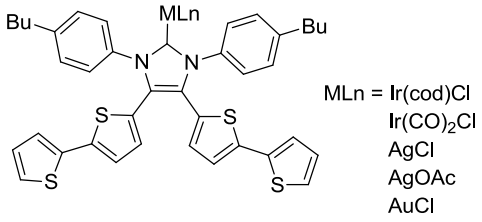

20

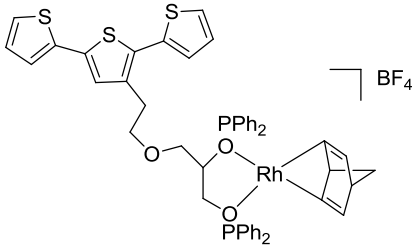

21

Shin produced the first example of a conducting polymer appended by an organometallic cluster unit (**17**, Chart 1-8).[49] When electropolymerized, a large anodic

shift with large peak separation was observed, possibly due to high resistivity from the strongly electron withdrawing $Co(CO)_3$ groups. The UV-vis spectrum of the polymer exhibited a red shift in the $\pi - \pi^*$ transition of the thiophene compared to the monomer. Shin also investigated other Co clusters with thiophene.[50] Complex **18** shows two highly irreversible oxidations due to the oligothiophene, and one reductive process from the metal cluster between 0 and -1.6 V. As only one irreversible reduction process was observed, it was suggested the redox centers of the clusters do not interact with each other. If there was mixing between the metal orbitals and π orbitals of the spacer, two redox waves would be observed in the CV due to the electronic communication between the metal centers. In the UV-vis spectrum, the high energy bands are assigned to $\pi - \pi^*$ transitions of thiophene, while medium to low energy bands are assigned as MLCT transitions.

Swager and co-workers synthesized a cobalt salen-containing polymer with EDOT (**19**, Chart 1-8).[51] It was observed that there was chemical degradation in acidic media via hydrolysis of the imine functionality. In pH 7 buffer, a featureless trace was observed in the absence of O_2. However, in the presence of oxygen, a large enhancement of the reduction wave was observed. This wave is assigned as a four electron reduction of O_2 to H_2O, and no H_2O_2 is formed. It was found the reduction current was related to the rate of O_2 arriving at electrode surface.

Cowley used N-heterocyclic carbenes (NHCs) to bind metals to a polymer chain (**20**, Chart 1-8).[52] The polymers were formed by electrochemical oxidation. These were robust complexes with a high degree of electrochromic reversibility. The UV-vis spectrum is red shifted compared to monomer, and showed a feature at 700 nm attributed to polaron induced $\pi - \pi^*$ transition. In **20** when the metal group (M) is $Ir(CO)_2Cl$, a band attributed to a bipolaron was observed also. It is believe the CO ligands help to stabilize the formation of polarons and bipolarons.

Mirkin electrochemically polymerized **21** (Chart 1-8) and saw terthiophene based redox processes.[9] Oxidation of Rh(I) does not significantly interfere with the terthiophene polymerization, but it does for the corresponding monothiophene monomer.

Hydrogenation of the polymer results in the removal of C_7H_8 to give a crosslinked polymer with dimerized Rh centers.

Section 1.4.4– Group 10 Metal Oligo- and Polythiophene Hybrids

Pickup has investigated polymerizable Ni-dithiolene complexes where Ni atoms form links in the polymer chain or peripheral to the polymer chain (**22** and **23**, Chart 1-9).[53] No reduction was observed for **23**, but one is observed in **22**, likely because the electron donating strength of the phosphine ligand shifts the reduction. The oxidation potential was similar for both complexes. The monomer of complex **22** has intense absorptions at low energy transitions (visible/NIR) over delocalized orbitals of the NiS_4C_4 core. The monomer of complex **23** does not exhibit the low energy transitions. The electrochemistry studies show insight into the structurally different polymers and their conductivities.

Skabara cross-linked polythiophene with nickel bis(dithiolene) units fused to main chain (**24**, Chart 1-9).[54] Performing cyclic voltammetery resulted in the observation of three waves, which is different from what was observed for the bisdithienyl-dithiolene complexes of the Pickup group. One wave at -0.13 V is described as the oxidation of metal dithiolene, the one at 0.46 V is the second oxidation of the dithiolene, and the reduction at -1.16 V is thiophene based. The UV-vis spectra of the polymer is bathochromically shifted compared to the monomer, indicating increased conjugation. The polymer has a very broad absorption range, from 300 to 1000 nm, and therefore could be a useful light-harvesting component.

Chart 1-9 Ref.[53, 54]

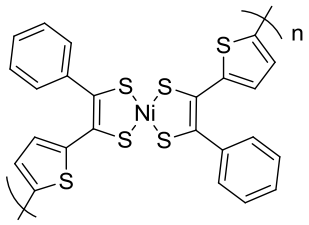

22

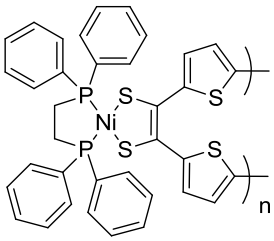

23

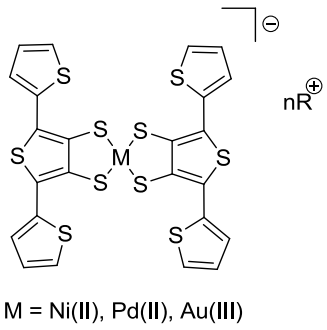

24

Kim found that metals, such as Pd, could be attached to a polymer backbone via the pyridine N and β carbon of thiophene ring (**25**, Chart 1-10).[55] Alternatively, it was observed the binding could be forced to only occur through β carbon, if Pd had strongly coordinating ligands (**26**). This results in rod shaped dinuclear complexes. Thus, Kim and coworkers demonstrate a hemilability of pyridyl thiophene ligands.

Similar hemilability was previously observed with Pd complexes where a thienyl ring bound through the S was displaced.[56] Our group showed metal centers could act as crosslinkers between conjugated chains. One thiophene ring was bound η^1 through the sulfur, while the other is bound through the β carbon (**27**, Chart 1-10).[56] Cyclic voltammetry showed complexes could be polymerized if methyl groups do not block the α positions of the polymer. The complexes had absorption bands red shifted from the parent complex and terthiophene ligands, while polymerization caused a red shift and broadening of the bands, indicative of formation of longer oligomers. Small changes in the UV-vis spectra occur when the complex is reacted with isocyanide ligands, suggesting non-optimal electronic interactions between the metal and polymer backbone.

Chart 1-10 Ref.[55-57]

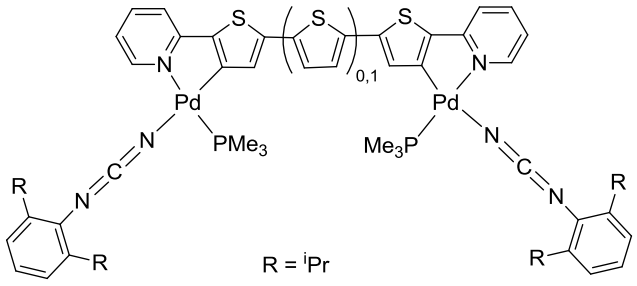

25

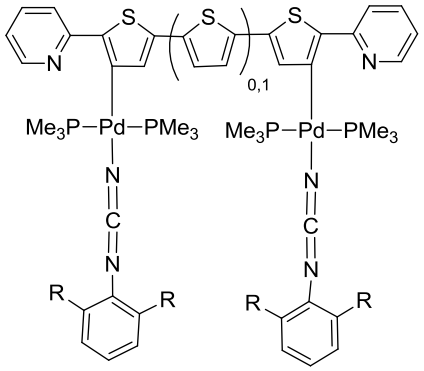

26

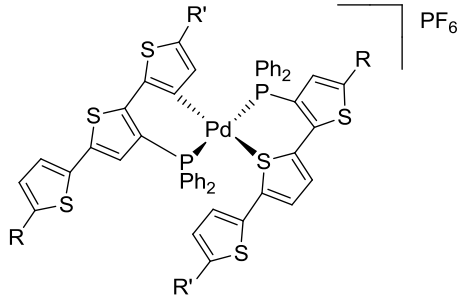

27

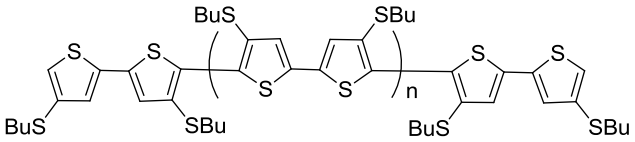

28

Seeber found that addition of Pd(II) to polymer or oligomer of **28** (Chart 1-10) caused a decrease of absorbance, due to conformational changes of the backbone when Pd is bound.[57] However, a new band with a broad tail in the UV-vis spectrum was observed at 400 nm. The presence of the metal increases the oxidation potential of the ligand (due to the electron withdrawing nature). There was no evidence of polymer formation when starting with the bithenyl Pd complex. This is believed to be caused by dissociation to form free ligand, which then polymerizes.

Bäuerle and co-workers demonstrated Pt-oligothiophene rings containing up to 35 thiophene units (**29**, Chart 1-11).[58] The rings, where Pt^{II} centers act as templates before undergoing reductive elimination, are easily oxidized and aggregate. The method of formation allows for odd number of repeat units. It is believed some of the complexes exhibit a monomeric-dimeric equilibrium, probably due to $\pi - \pi^*$ interactions.[58,59] Earlier

work showed the Pt could directly bind to oligothiophenes, and oxidants, such as silver triflate, removed the Pt. Homocoupling occurred to produce sexithiophene at room temperature, with comparable yields to other homocoupling methods to produce oligothiophene. Their results showed a red-shift in the UV-vis absorption band with increasing conjugation, and evidence of a Pt(II) to Pt(IV) oxidation. Potentiostatic electrolysis also yielded sexithiophene.[59]

Holliday used a pincer NCN ligand to incorporate Pt to an oliothiophene (**30**, Chart 1-11).[60] With Pt incorporation, the $\pi - \pi^*$ transition of bithiophene red shifts and a new LMCT band is observed. With polymerization, the $\pi - \pi^*$ transition shifts out to about 400 nm. Doping was monitored, and changes in the LMCT transition could directly examine changes in electron density at the metal center.

Wong and coworkers varied the number of thiophene rings in the backbone with Pt directly inserted (**31**, Chart 1-11).[61, 62] It was observed that increasing the number of thiophene rings decreased the band gap. Also, as the number of thiophene units increased, the overall effect on the band gap decreased, therefore the investigators thought there would be little benefit in incorporating more than a terthienyl unit. The introduction of a Pt group also lowers the energy of the transitions, suggesting that π conjugation extends through the metal center.

Chart 1-11 Ref.[58, 60, 61]

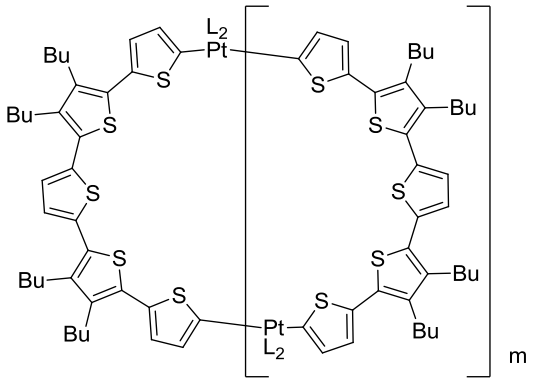

29

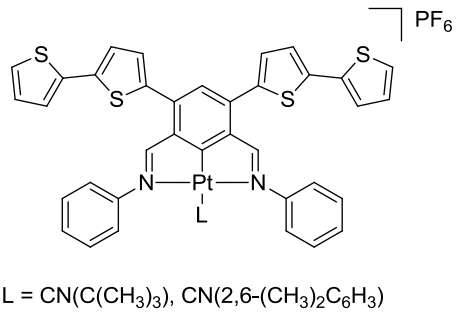

30

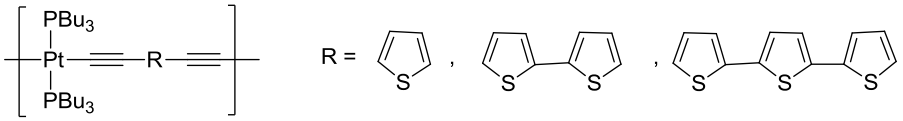

31

Section 1.4.5– Group 11 Metal Oligo- and Polythiophene Hybrids

Sauvage and co-workers made a conjugated polyrotaxane with a linear conjugated backbone[63] (**32**) for better π orbital overlap, compared to the u-shaped backbones[64, 65] (**33**) they previously used (Chart 1-12). In the methylated species (**32**, R=CH_3), a reversible wave at 0.52 V was assigned as Cu redox wave, while the non-methylated analogue (**32**, R=H), showed an irreversible couple at 0.28 V.[63] When polymerized, the waves assigned as thiophene-based shift to higher potentials, which suggests enhanced electron delocalization in the linear backbone. Complex **32** could be reversibly metallated and demetallated, either using Li^+ as a template or without a template. In previous investigations with the u-shaped backbone, Li^+ had to be present or the complex would collapse on itself.[64, 65] Additionally, **32** could remetalate with a different metal.[63] In those cases, a different value for the metal redox wave was observed but the polymer showed very similar values. This suggests there is weak electronic interaction between the metal

complex and thiophene backbone. Interestingly, there is a more pronounced interaction in the u-shaped complexes.[63, 65]

Similar to motifs employed by Sauvage and co-workers, Bäuerle made several different sized catenanes with thienyl groups appended to the phenanthroline units (**34**, Chart 1-12).[66] In this case, the system is fully conjugated. Bäuerle and co-workers employed a similar template approach to one they used previously, where *cis*-[Pt(dppp)Cl_2] is incorporated into the ring structure, and then is eliminated along with C-C bond formation to produce a macrocycle. It was observed that smaller catenanes cannot be demetalated, but the larger ones can.

Chart 1-12 Ref.[63, 65-67]

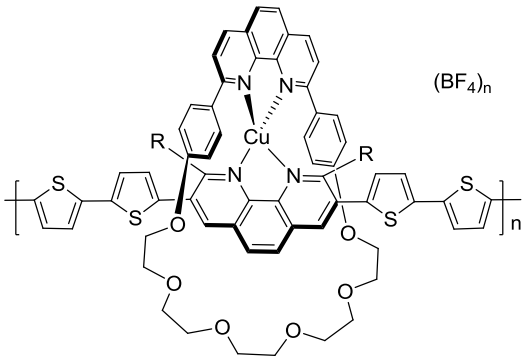

32

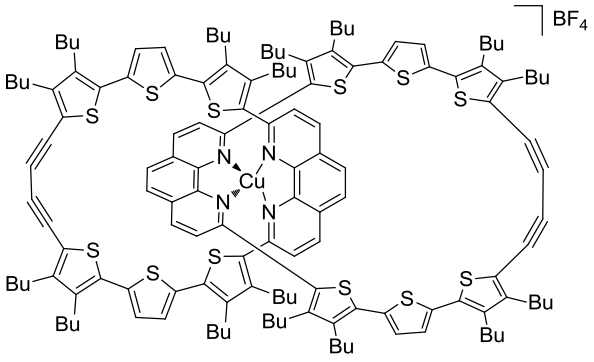

34

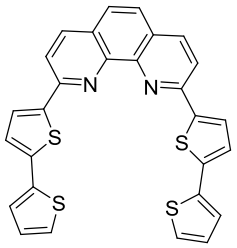

33

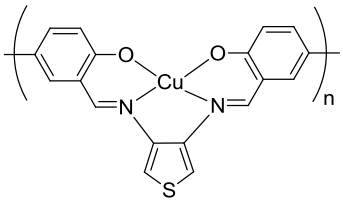

35

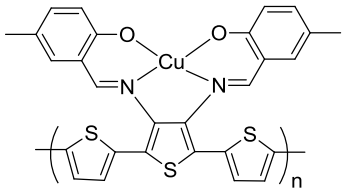

36

Reynolds has made species with multiple polymerization sites; polymerization could occur through the phenylene or thiophene groups, or mixture of the two sites (**35** and **36**, Chart 1-12).[67] The polymerization of the thiophene resulted in the presence of a

low potential feature and a broad sloping onset. The phenylene systems showed a very sharp onset. Reynolds also synthesized Ni complexes in order to demonstrate that the type of metal dictates the electrochromic properties of these systems.[67]

Swager made complex **19** (Chart 1-8) using Cu as well.[68] The polymer had two overlapping redox waves, and a well-defined wave at higher potentials in MeCN. The appearance of the CV was found to be dependent on the solvent. Only two waves were displayed in the CV when the films were grown in CH_2Cl_2 (versus three in MeCN). Perturbations of the interchain distance greatly alter the polymer conductivity profile, and increasing the steric bulk of the diamine bridge results in a drop in conductivity. The UV-vis spectrum shows a sharp band at 430 nm, suggesting conjugation in the system is limited.

Binding metal groups via chelating phosphines to thiophene showed significant effects on the electronic properties of the conjugated system. Our group has investigated several gold-phosphino-oligothiophene species (**37**, **38**, **39**, Chart 1-13).[69-71] Complex **37** shows a blue shift in the $\pi - \pi^*$ transition band and an increase in oxidation potential compared to the ligands.[70] Increasing the number of thienyl units decreases the oxidation potential and red shifts the absorption bands. When the complex has two Au atoms attached (**37**, R = PPh_2-AuCl), the complex crystallizes as a dimer that displays gold-gold interactions.[70] Dual emission is observed, attributed to monomer and dimer emission. The solution absorbance spectra of **38** show a bathochromic shift with increased conjugation length, but a hypsochromic shift relative to the unbound thienyl ligands.[69] Increasing the conjugation led to a decrease in the oxidation potentials of **38.** Gold-acetylene-terthiophene complexes have also been investigated in our group. When the linear A_2T_3 ligand is reacted with gold, a digold complex is formed (**39**, Chart 1-13).[71] The coordination of the metal results in a small red shift of the absorption bands. The dppm complex exhibits Au-Au interactions. The complexes are emissive at room temperature, except for the dppm complex. All complexes could be electropolymerized. The PPh_3 complex shows an irreversible oxidation wave which shifts to higher potential with repeated scanning. This suggests a poorly conducting film is being formed, or the conjugation is decreased compared to the monomer. The dppm complex shows two oxidation waves, and still exhibits Au-Au interactions when polymerized.

Chart 1-13 Ref.[69-73]

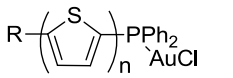

n 1, 2, 3

R = H, PPh_2-AuCl

37

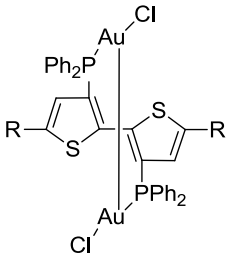

38

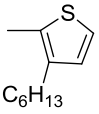

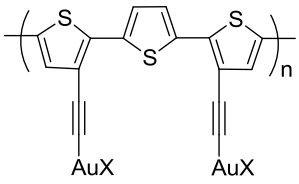

X = PPh_3, CN^-, dppm

39

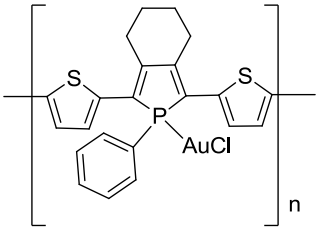

40

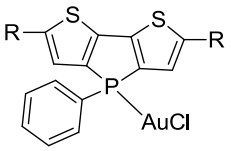

R = $SiMe_3$, $SiMe_2{}^tBu$

41

Phospholes substituted for a thiophene unit in oligo- and polythiophene systems cause a red shift in the UV-vis absorption spectrum and lower the HOMO-LUMO gap.[73] These factors indicate systems like these may be useful in applications where band gap optimization is important. Complex **40** (Chart 1-13) and similar species are not air or moisture sensitive.[72] **40** could be demetalated with PPh_3 and remetalated with (tht)AuCl. The investigators found that gold was intimately connected to the extended π conjugated system of the polythiophene. Reau demonstrated post-functionalization could be performed on polymeric material of this type. The gold complexes showed promising optoelectronic properties and some complexes have been incorporated into OLEDs.[73]

Fused cyclic thienyl phospholes force rings to adopt coplanar geometry, maximizing π orbital overlap.[73] Studies have included incorporation of various metals, but the system seemed relatively insensitive to the type of metal, except with gold. For complex **41** (Chart 1-13), two absorption bands were observed. Depending on the R group, either broad bands (R = $SiMe_3$) or narrow bands (R = $SiMe_2{}^tBu$) were observed, likely due to reduced intermolecular interactions from steric bulk. No gold-gold

interactions were observed. The emission in both solution and solid-state suggest little or no aggregation is occurring. It is believed these complexes are well suited for functional materials and devices.

Section 1.4.6 – Group 12 Metal Oligo- and Polythiophene Hybrids

Li and coworkers synthesized and electropolymerized thiophene and EDOT substituted porphyrins and their zinc complexes (**42**, Chart 1-14).[74] They used linear units allowing the metal centers to be in direct communication with the backbone. However, due to minimal π overlap between aryl rings and porphyrin, the polymer showed two isolated redox systems. The EDOT substituted porphyrin complex, **42**, polymerized well on a number of different electrodes. When films formed, there was peak broadening and a red-shift, likely due to aggregation and stacking of porphyrins in solution. Overall, the spectra looked very similar to the spectra of the monomer, but with broader features. The metal containing species demonstrated a higher electrochemical stability than similar previously reported complexes. After 1000 scans, there was only a 5% decrease in the intensity of the peak currents were observed. This may be due to improved thermal and electrochemical stability, and higher conductivity of PEDOT compared to other polymers.

Chart 1-14 Ref.[74-77]

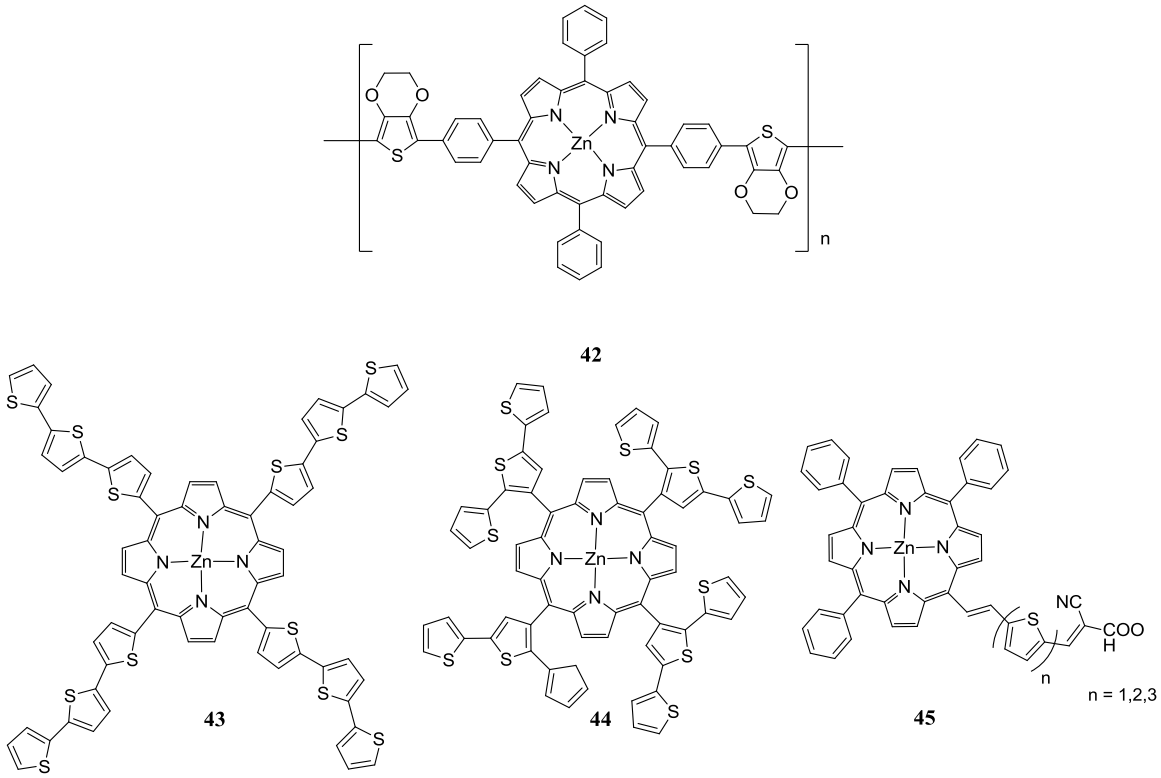

Shimidzu showed Zn porphyrins with terthiophene units were able to be polymerized (**43**, Chart 1-14).[75, 78] A decrease in the IR band for α-CH out of plane vibrations was noted, suggesting α-α coupling, and a quasi-two dimensional species. SEM confirmed this, although some disorder was observed. The thickness of the single scan suggested the porphyrin rings are in a planar orientation. With polymerization, absorption of the film is considerably broadened, suggesting strong π-π interaction. The authors suggest this and related materials offer the opportunity for 3-D materials, which may be used in organic electronic devices.[75]

Officer and co-workers made similar compounds, but some had the terthiophenes attached via the β positions of the thiophene[76] (**44**, Chart 1-14) rather than the α positions. They attempted to make porphyrin/thiophene hybrids where porphyrins are attached via a conjugated linker, directly in the chain, or act as a crosslinker between two chains. There was difficulty making the pure compounds, as atropisomers were possibly formed. Metallation with zinc was successful (**44**) but required the use of excess zinc acetate at

high temperatures to obtain the desired product.[75, 78] Slower metallation of specific atropisomers, along with sterically hindered terthiophenes was used to explain the difficulty of complexation.

Officer also synthesized **45** (Chart 1-14), via Wittig reactions and poryphrin condensation reactions, under the belief they would be useful for DSSCs.[77] The longer thiophene chains exhibited more donor-acceptor character, red shifted the absorption bands, and decreased the band gap. However, the longer chains also had a lower solar cell efficiency. Further work is needed to rationalize the DSSC efficiency and the electronic properties for complexes of this type.

Section 1.5 – Dye Sensitized Solar Cells

Dye sensitized solar cells have received much attention over the past few decades as they are promising alternatives to conventional silicon based photovoltaic devices due to their low production cost, good conversion efficiencies, and ability to tune their absorption range. In the dye-sensitized solar cell (DSSC) pioneered by Grätzel,[79] electron injection into a wide bandgap semiconductor from dyes is central to absorption of solar light and charge separation. Typically in DSSCs, the sensitizer, or dye, is excited by absorbing a photon. The dye injects an electron into the conduction band of the TiO_2, which travels through the TiO_2 layer to the anode (often ITO or SnO coated glass). For dye regeneration, an electron is donated from the electrolyte, usually the iodide/triiodide redox couple. The iodide is regenerated by the reduction of triiodide at the cathode with the circuit being complete when connected to an external load (Figure 1-3).

The most efficient DSSCs to date have ~10 – 13% efficiency, and are obtained using Ru-based dyes, such as Black dye[80] and N719[81] (Chart 1-15, **46** and **47**, respectively), with an I^-/I_3^- donor. Other "champion dyes" (dyes with more than 10 % efficiency) have been produced, and are typically a modification of these known dyes. Replacement of one of the anchoring 4,4′-dicarboxylic acid-2,2′-bipyridine (dcbpy) ligands with a highly conjugated ancillary ligand has led to an increase in the absorption coefficient, and therefore, photocurrent of the sensitizers.[44, 82, 83] For example, replacing a

dcbpy ligand with a bipyridine substituted with alkyl bithiophene units led to a very high molar absorption coefficient, in addition to a high current density and conversion efficiency. The thiophene moieties allow for relatively easy functionalization, which can aid with solubility, polarity, and band-gap tuning.[44] Substituting the alkyl chain for thioalkyl moieties on the bithiophene substituted bipyridines have also improved efficiencies.[82]

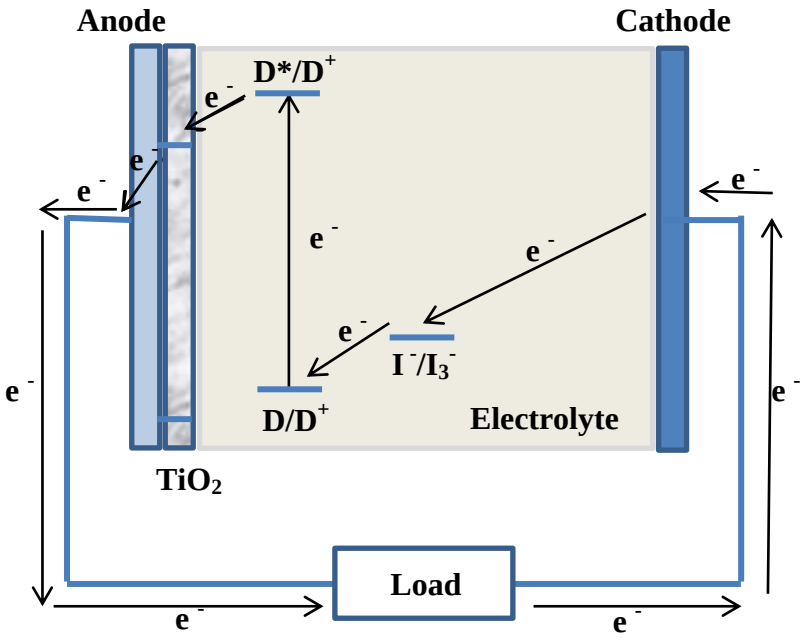

Figure 1-3 Schematic of a DSSC showing the flow of electrons, adapted from Ref.[84]

Chart 1-15 Ref.[80, 81]

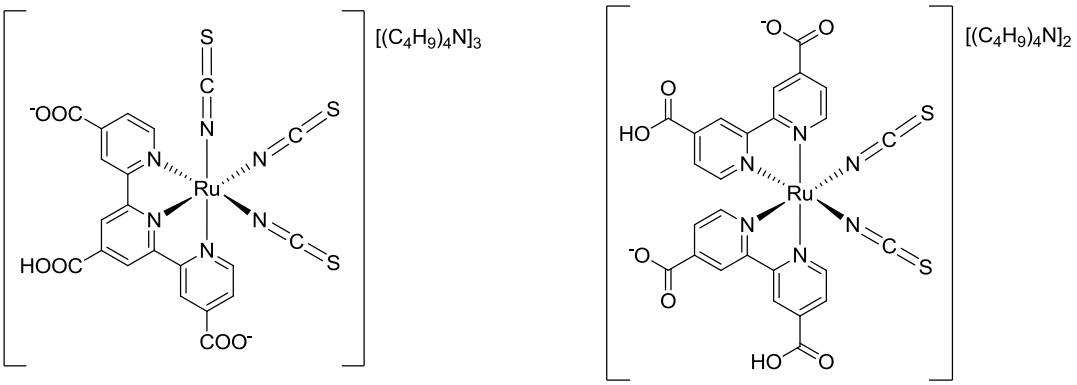

Black Dye
46

N719
47

It is believed that the NCS^- groups can cause problems and lead to degradation over time. Recently, a *bis*-tridentate dye (without any NCS^- groups) was reported which avoids isomerization issues and is believed to improve upon the long term stability of dyes.[85] Also, it has been noted that modification by replacing NCS^- groups with cyclometalating groups allows for retention of the light-harvesting properties of these complexes.[86-88]

Another method which has recently yielded high efficiency DSSCs uses a porphyrin complex with a cobalt (II/III) based redox electrolye.[89] While this redox couple often demonstrates faster charge recombination than iodide/triiodide, the introduction of long alkoxy groups can slow the charge recombination process. Grätzel and coworkers established that using a substituted zinc-porphyrin, which itself consists of a donor-π bridge-acceptor structure and absorbs across the visible spectrum, gives high conversion efficiencies using various electrolytes.

Research focusing on the various components of a solar cell is still quite important, as each component influences the overall efficiency. The structures of the dyes themselves are central to a highly efficient device. In addition to requiring a broad absorption range and high photostability, the electronic ground and excited states are an important aspect to investigate as well. Several reviews have been published focusing on the synthesis and design of photosensitizers for this type of device.[90-92]

Section 1.6 – Goals and Scope

The primary goal of this thesis is the synthesis and characterization of transition-metal complexes appended to a phosphino(terthiophene) for use in light-harvesting applications. A terthiophene ligand with a diphenylphosphine linker was employed to study Type I and Type II materials. The diphenylphosphine group, situated at the β position of an oligothiophene chain is used to anchor the metal group, creating a Type I metal-terthiophene hybrid material. When the terthiophene moiety is in close proximity to the metal center, the S or C of a thiophene ring adjacent to the diphenylphosphine group may also coordinate to the metal center, creating Type II materials. Both classes of materials are investigated in this thesis.

When considering complexes and materials for use as energy harvesters, such as dyes in DSSCs, certain criteria must be kept in mind. Ideal dyes will absorb all light below 920 nm, contain ligands that are functionalized or can be functionalized (with carboxylate, for example) for attachment to TiO_2, or another semiconductor, and should be stable to photoinduced ligand loss.[84] A relativity long-lived charge-separated excited state, with an energy well matched to the lower limit of the conduction band of the oxide material (to minimize loss during electron transfer) are desirable, as are appropriate redox potentials to allow for regeneration.

Ruthenium polypyridyl complexes have been widely studied and produced the most promising complexes to date. Therefore, group 8 polypyridyl phosphino-(terthiophene) complexes were explored. Chapter 2 investigates the ground and excited state behavior of Ru(II) and Os(II) diimine complexes containing 3′-diphenylphosphino-terthiophene (PT_3) in different coordination modes. The effect the coordination mode has on the complexes stability, absorption, transient absorption, emission and electrochemical properties are evaluated.

Cyclometallated iridium (III) complexes have also shown promise in this field.[93] Cyclometalated iridium (III) complexes may be isoelectronic to Ru(II) diimine complexes, and exhibit similar spectroscopic properties. Enhanced absorption across the UV-vis spectrum may be observed due to enhanced spin-orbit coupling of the Ir. In Chapter 3, cyclometalated Ir(III) complexes with phenylpyrazole or phenylpyridine

ligands and a PT_3 ligand are explored. In this case, three different coordination modes of the PT_3 ligand are observed, yielding Type I and Type II complexes. The photophysical and electrochemical properties are investigated, and comparisons to the Os(II) complexes are made.

Cu(I) complexes with substituted 1,10-phenantroline (phen) ligands possess similar photophysical properties as $[Ru(bpy)_3]^{2+}$ salts. Incorporation of ligands containing phosphines or with chelating phosphines have produced complexes with long lifetimes, attributed to charge transfer states.[94] Coupled with the distinct cost advantage of Cu over Ru, it is beneficial to consider these types of complexes as dyes. Chapter 4 discusses diimine Cu(I) complexes with phosphino-terthiophene ligands. Their synthesis and their photophysical and electrochemical properties are evaluated.

CHAPTER 2

GROUP 8 DIPHENYLPHOSPHINO(TERTHIOPHENE) COMPLEXES*

Section 2.1– Introduction

Group 8 polypyridyl complexes, particularly Ru(II) complexes, have been widely studied as photosensitizing dyes for solar energy harvesting because of their chemical stability, absorbance and emission properties, and their ability to participate in electron and energy transfer processes.[95, 96] Conjugated oligomers and polymers are another class of materials that are being investigated for application as light absorbers in organic solar cells.[97, 98] The efficiency of cells based on these materials is typically limited by exciton recombination on the conjugated chains.[99] Another approach involves coupling a light absorbing metal dye to a conjugated backbone, with the goal of exciting an electron from the conjugated group to a peripheral ligand on the metal complex generating a charge-separated excited state. This approach offers the possibility of hole transport over longer distances via the π-conjugated backbone. However, energy transfer to competing, low-lying states can present complications.[100, 101]

Previous studies in our group have shown that the ground and excited state behavior of the Ru(II) *bis*(bipyridyl) complexes[102, 103] **48** and **49**, where an oligothiophene is tethered to the metal through a diphenylphosphine ligand (Chart 2-1) either via *PS* or *PC* coordination, differ significantly from each other. Visible light excitation of an analogue of $[Ru(bpy)_2PT_3\text{-}PC](PF_6)$, in which the conjugation in the phosphino(oligothiophene) ligand is extended to five thiophene rings (**51**), resulted in a transient species assigned as a charge-separated excited state.[104] As mentioned above, others have recently explored the utility of cyclometallated complexes as dyes in DSSCs,[86-88, 93] raising the possiblity that cyclometallated complexes such as these may find application in these types of cells.

*Part of this chapter has been published. Reproduced with permission from Moore, S.A., Nagle, J.K., Wolf, M.O., Patrick, B.O. (2011) Coordination Mode Dependent Excited State Behavior in Group 8 Phosphino(terthiophene) Complexes. *Inorg. Chem.*, **50**, 5113-5122.

Chart 2-1 Ref.[102-104]

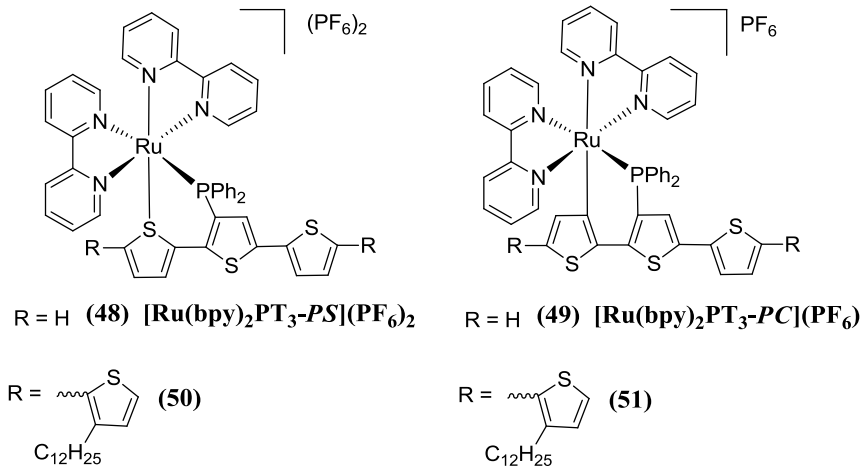

The possible presence of low-lying metal-centered (MC) excited states[101] or low-lying ligand-based triplet states[100] which can be populated from the metal-to-ligand charge transfer (MLCT) state may lead to alternate routes for deactivation of the excited state in these Ru complexes. Os(II) has a larger ligand field splitting energy (by about ~30%) than Ru(II) which results in an increased energy gap between MLCT and MC states,[101] thus Os(II) analogs of the Ru(II) complexes may have longer charge-separated lifetimes. On the other hand, some Os(II) polypyridyl complexes have been shown to have shorter excited state lifetimes than the analogous Ru(II) complexes due to enhanced spin-orbit coupling,[105] and in cases where ligands with a triplet state close in energy to the ^{3}MLCT state are present, energy transfer between the two states may occur.[106] Os(II) polypyridyl complexes also typically have lower energy MLCT states, leading to broader absorption of light over more of the visible spectrum. This is an advantage for solar energy harvesting where low energy photons must also be captured for maximum efficiency. Additionally, the bipyridyl ligands on the Ru complexes were replaced with phenanthroline (phen) ligands. With their extended ring system, the phen complexes are known to result in increased emission lifetimes with respect to the analogous bpy complexes,[107] and may exhibit other beneficial characteristics over the bpy analogues.

In this chapter, four new complexes with a conjugated terthiophene based ligand are described: $[Ru(phen)_2PT_3$-*PS*$](PF_6)_2$, $[Ru(phen)_2PT_3$-*PC*$](PF_6)$, $[Os(bpy)_2PT_3$-*PS*$](PF_6)_2$, and $[Os(bpy)_2PT_3$-*PC*$](PF_6)$. Their electrochemical, photophysical and excited

state electronic properties are compared to the $[Ru(bpy)_2PT_3\text{-}PS](PF_6)_2$ and $[Ru(bpy)_2PT_3\text{-}PC](PF_6)$ analogues and their usefulness as dyes are discussed.

Chart 2-2

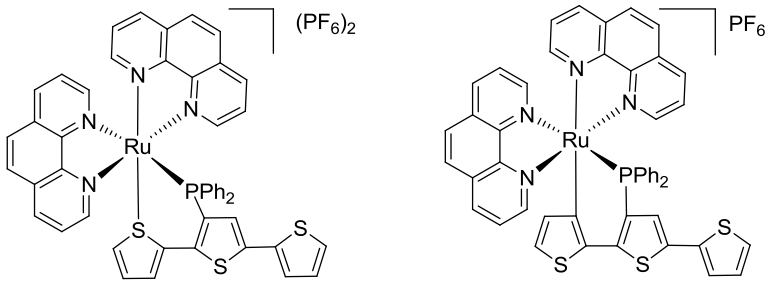

$[Ru(phen)_2PT_3\text{-}PS](PF_6)_2$
52

$[Ru(phen)_2PT_3\text{-}PC](PF_6)$
53

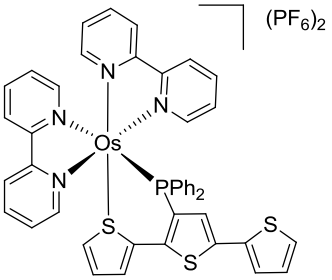

$[Os(bpy)_2PT_3\text{-}PS](PF_6)_2$
54

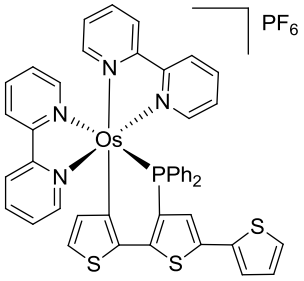

$[Os(bpy)_2PT_3\text{-}PC](PF_6)$
55

Section 2.2 – Experimental

Section 2.2.1 – General

All reactions were performed under N_2 (99.0%). The compounds *cis*-$Os(bpy)_2Cl_2$,[108] and 3′-(diphenylphosphino)-2,2′:5′,2″-terthiophene (PT_3)[109] were synthesized according to literature procedures. The compound *cis*-$Ru(phen)_2Cl_2$ was synthesized according to literature procedure for *cis*-$Ru(bpy)_2Cl_2$,[110] but bipyridine (bpy) was replaced with phenanthroline (phen). All other reagents were purchased from Aldrich, Alfa Aesar and Strem and used as received. ^1H and $^{31}P\{^1H\}$ NMR spectra were collected on either a Bruker AV-300 or AV-400 spectrometer. ^1H NMR spectra were referenced to residual solvent, and $^{31}P\{^1H\}$ NMR spectra referenced to external 85% H_3PO_4. ESI mass spectra were recorded on Bruker Esquire-LC ion trap mass

spectrometer equipped with an electrospray ion source. The solvent for the ESI-MS experiments was either methanol or dichloromethane/methanol and the concentration of the compound was ~10 μM. High resolution mass spectra were recorded on a Waters Micromass LCT time-of-flight mass spectrometer equipped with an electrospray ion source. CHN elemental analyses were performed using an EA1108 elemental analyzer, using calibration factors. The calibration factor was determined by analyzing a suitable certified organic standard (OAS) of a known elemental composition. All mass spectrometry and microanalysis results were obtained by the staff at the UBC Mass Spectrometry Centre. Cyclic voltammetry experiments were carried out on an Autolab PG STAT 12 potentiostat or Pinechem potentiostat using a Pt working electrode, Pt mesh counter electrode and a silver wire reference electrode with 0.1 M $[(n\text{-}Bu)_4N]PF_6$ supporting electrolyte which was re-crystallized 3 times from ethanol and dried under vacuum at 100 °C for 3 days. Decamethylferrocene (-0.125 V vs SCE in acetonitrile)[111] was used as an internal reference to correct the measured potentials with respect to the saturated calomel electrode (SCE). UV-vis spectra were obtained on a Cary 5000 spectrometer in HPLC grade solvent. Emission spectra were obtained on a PTI Quantamaster spectrometer. Transient absorption measurements and fluorescence lifetimes were carried out on a Princeton Instruments Spectra Pro 2300i Imaging Triple Grating Monochrometer/Spectrograph with a Hamamatsu Dynamic Range Streak Camera (excitation source: EKSPLA Nd:YAG laser, 35 ps pulse duration, λ = 355 nm). Solutions of the complexes in CH_3CN having an optical density of 1 at 355 nm were prepared. The UV-vis spectra were obtained before and after each TA experiment to ensure the bulk of the sample did not change, due to degradation or another process.

Section 2.2.2 – Procedures

$[Ru(phen)_2PT_3\text{-}PS](PF_6)_2$, (52).

This compound was prepared based on the literature procedure for the preparation of the analogous bipyridine complex,[102] but using $Ru(phen)_2Cl_2{\cdot}2H_2O$ in place of $Ru(bpy)_2Cl_2{\cdot}2H_2O$. $AgBF_4$ (0.068 g) was added to a nitrogen-sparged acetone solution (15 mL) of $Ru(phen)_2Cl_2{\cdot}2H_2O$ (0.100 g), stirred for 12 hours and filtered. 3′-(diphenylphosphino)-2,2′:5′,2″-terthiophene (0.092 g) was added to the filtrate and the

mixture was heated at reflux for 24 hours. The resulting solution was reduced in volume, added dropwise to a solution of ammonium hexafluorophosphate (0.284 g) in H_2O (17 mL) and stirred at room temperature for 30 minutes. The precipitate was filtered and washed with copious amounts of water and diethyl ether to yield 64 mg (62%) of a yellow or orange-yellow solid. ^{1}H NMR (300 MHz, $CO(CD_3)_2$): δ 6.52-6.66 (m, 3H), 6.67-6.73 (m, 1H), 7.06 (d, *J* = 3.0 Hz, 3H), 7.12 (dd, *J* = 5.0, 3.9 Hz, 1H), 7.30 (d, *J* = 3.0, 2H), 7.35-7.45 (m, 3H), 7.46-7.63 (m, 5H), 7.64-7.73 (m, 1H), 7.86 (dd, *J* = 8.1, 5.4 Hz, 1H), 7.92-8.01 (m, 1H), 8.05 (dd, *J* = 8.1, 5.4 Hz, 1H) 8.23-8.41 (m, 5H), 8.68 (d, *J* = 7.8 Hz, 1H), 8.74-8.84 (m, 1H), 8.89 (dd, *J* = 7.9, 2.9 Hz, 2H), 9.36 (d, *J* = 5.0 Hz, 1H), 9.48 (d, *J* = 5.3 Hz, 1H). ^{31}P{^{1}H} NMR (121 MHz, $CO(CD_3)_2$): δ 28.3 (s), -143.6 (septet, J_{PF} = 708 Hz, PF_6). m/z $[M\text{-}PF_6]^+$ 1039. HRMS (ESI) Calcd for $C_{48}H_{33}F_6N_4PS_3Ru$ (m/z $[M\text{-}PF_6]^+$): 1036.0306; Found: 1036.0327. Anal. $C_{48}H_{33}F_{12}N_4S_3P_3Ru$ requires C, 48.69; H, 2.81; N, 4.73. Found C, 48.45; H, 2.91; N, 4.64 %.

[Ru(phen)$_2$PT$_3$-*PC*](PF$_6$), (53).

This compound was prepared based on the literature procedure for the preparation of the analogous bipyridine complex,[102] with slight modification. Complex **52** (45 mg) was added to a solution of NaOH (0.20 g) dissolved in degassed methanol (5 mL) and heated to reflux under nitrogen, with stirring, for 18 hours. The solution was cooled to room temperature, and the MeOH was removed *in vacuo*. The precipitate was redissolved in 2 mL MeOH. The resulting dark solution was added dropwise to a solution of ammonium hexafluorophosphate (0.284 g) in H_2O (17 mL) and stirred at room temperature for 30 minutes. The precipitate was filtered and washed with copious amounts of water and diethyl ether to yield 26 mg (66%) of a reddish-brown solid. ^{1}H NMR (300 MHz, $CO(CD_3)_2$): δ 6.52-6.66 (m, 3H), 6.67-6.73 (m, 1H), 7.06 (d, *J* = 3.0 Hz, 3H), 7.12 (dd, *J* = 5.0, 3.9 Hz, 1H), 7.30 (d, *J* = 3.0, 2H), 7.35-7.45 (m, 3H), 7.46-7.63 (m, 5H), 7.64-7.73 (m, 1H), 7.86 (dd, *J* = 8.1, 5.4 Hz, 1H), 7.92-8.01 (m, 1H), 8.05 (dd, *J* = 8.1, 5.4 Hz, 1H) 8.23-8.41 (m, 5H), 8.68 (d, *J* = 7.8 Hz, 1H), 8.74-8.84 (m, 1H), 8.89 (dd, *J* = 7.9, 2.9 Hz, 2H), 9.36 (d, *J* = 5.0 Hz, 1H), 9.48 (d, *J* = 5.3 Hz, 1H). ^{31}P{^{1}H} NMR (121 MHz, $CO(CD_3)_2$): δ 46.1 (s), -143.6 (septet, J_{PF} = 708 Hz, PF_6). m/z $[M\text{-}PF_6]^+$ 893. HRMS (ESI) Calcd for $C_{48}H_{32}N_4S_3Ru$ (m/z $[M\text{-}PF_6]^+$): 887.0603; Found: 887.0593.

Anal. $C_{48}H_{32}F_6N_4S_3P_2Ru$ requires C, 55.54; H, 3.11; N, 5.40. Found C, 55.19; H, 3.29; N, 5.05%.

[Os(bpy)$_2$PT$_3$-*PS*](PF$_6$)$_2$, (54).

PT_3 (0.164 g) was added to a degassed 2:1 EtOH-H_2O mixture containing $Os(bpy)_2Cl_2$ (0.200 g). The reaction mixture was heated to reflux under nitrogen with stirring for 48 hours. The EtOH was removed *in vacuo*, and the remaining solution was added to aqueous ammonium hexafluorophosphate (1.136 g in 70 mL H_2O) and stirred at room temperature for 30 minutes. The precipitate was filtered, washed with copious amounts of water and diethyl ether, and then dissolved in DCM and purified over neutral alumina. Once the brown band was eluted with DCM, acetone was used to elute the reddish-orange product band. The volume was reduced in vacuo, and the remaining solution was added to aqueous ammonium hexafluorophosphate (0.568 g in 30 mL H_2O) and stirred at room temperature for 30 minutes. The precipitate was filtered and washed with copious amounts of water and diethyl ether to yield 0.1810 g (42%) of red solid. ^{1}H NMR (300 MHz, $CO(CD_3)_2$): δ 9.16 (d, *J* = 5.9 Hz, 1H), 8.96 (d, *J* = 5.7 Hz, 1H), 8.71 (d, *J* = 8.2 Hz, 1H), 8.67-8.60 (m, 3H), 8.23-8.02 (m, 5H), 7.70 (d, *J* = 5.7 Hz, 1H), 7.64-7.47 (m, 7H), 7.43-7.29(m, 6H), 7.23-7.16 (m, 3H), 7.11-7.05(m, 2H), 6.97 (d, *J* = 3.3 Hz, 1H), 6.87-6.81(m, 2H). $^{31}P\{^1H\}$ NMR (121 MHz, $CO(CD_3)_2$): δ -14.2 (s), -143.6 (septet, J_{PF} = 708 Hz, PF_6). m/z $[M\text{-}PF_6]^+$ 1080. HRMS (ESI) Calcd for $C_{44}H_{33}N_4F_6OsP_2S_3$ (m/z $[M\text{-}PF_6]^+$): 1081.0845; Found: 1081.0862. Anal. $C_{44}H_{33}N_4S_3OsP_3F_{12}$ requires C, 43.14; H, 2.72; N, 4.57. Found C, 42.88; H, 2.99; N, 4.40%.

[Os(bpy)$_2$PT$_3$-*PC*](PF$_6$), (55).

Complex **54** (50 mg) was added to a solution of NaOH (0.20 g) dissolved in degassed methanol (5 mL) and heated to reflux under nitrogen, with stirring, for 36 hours. The solution was cooled to room temperature, and the MeOH was removed *in vacuo*. The precipitate was redissolved in 2 mL MeOH. The resulting dark solution was added dropwise to a solution of ammonium hexafluorophosphate (0.284 g) in H_2O (17 mL) and stirred at room temperature for 30 minutes. The precipitate was filtered and washed with copious amounts of water and diethyl ether to yield 27 mg (61%) of a dark

brown solid. ^{1}H NMR (300 MHz, $CO(CD_3)_2$): δ 8.94 (d, J = 5.8 Hz, 1H), 8.57 (d, J = 8.2 Hz, 1H), 8.51-8.37 (m, 4H), 7.97(t, J = 7.8 Hz, 1H), 7.88-7.62 (m, 6H), 7.58-7.53(m, 1H), 7.43-7.35 (m, 6H), 7.18-7.02 (m, 4H), 6.95-6.81 (m, 4H), 6.65 (d, J = 2.7 Hz, 1H), 6.43 (t, J = 8.7 Hz, 2H), 6.20 (d, J = 4.9 Hz, 1H) $^{31}P\{^{1}H\}$ NMR (121 MHz, $CO(CD_3)_2$): δ -2.4 (s), -143.6 (septet, J_{PF} = 708 Hz, PF_6) m/z $[M\text{-}PF_6]^+$ 935. HRMS (ESI) Calcd for $C_{44}H_{32}N_4OsPS_3$ (m/z $[M\text{-}PF_6]^+$): 935.1142; Found: 935.1155. Anal. $C_{44}H_{32}F_6N_4OsP_2S_3 \cdot 2H_2O$ requires C, 47.38 ; H, 3.26; N, 5.03. Found C, 47.59; H, 3.11; N, 4.89%.

Section 2.2.3 – X-Ray Crystallography

Suitable crystals of $[Ru(phen)_2PT_3\text{-}PS](PF_6)_2$, (**52**), $[Os(bpy)_2PT_3\text{-}PS](PF_6)_2$, (**54**), and $[Os(bpy)_2PT_3\text{-}PC](PF_6)$, (**55**), were grown from solution. The X-ray data were collected and solved by Dr. B.O. Patrick. In all cases, the crystals were mounted on a glass fiber and a Bruker X8 APEX II diffractometer with graphite monochromated Mo-Kα radiation was used for all measurements. Data were collected and integrated using the Bruker SAINT[112-114]software package. Data were corrected for absorption effects using the multi-scan technique (SADABS).[115-117] The data were corrected for Lorentz and polarization effects. The structures were solved by direct methods.[118] Solid-state diagrams were visualized using Mercury.[119]

$[Ru(phen)_2PT_3\text{-}PS](PF_6)_2$, (52).

Data were collected in a series of ϕ and ω scans in 0.50° oscillations using 20.0 second exposures. The crystal to detector distance was 36.00 mm. The data were collected to a maximum 2θ value of 55.9°. Of the 51075 reflections that were collected, 12063 were unique (R_{int} = 0.040); equivalent reflections were merged. Data were corrected for absorption effects using multi-scan the technique (SADABS),[117] with minimum and maximum transmission coefficients of 0.825 and 0.970, respectively. The material crystallizes with one molecule of acetone in the asymmetric unit. One thiophene ring (S3 → C12) is disordered by a two-fold rotation about the C8 – C9 bond. The two ring fragments were modeled in both orientations using restraints to maintain reasonable

ring geometries. Additionally, the fluorines of one PF_6^- anion were disordered, again in two orientations. All non-hydrogen atoms were refined anisotropically. All hydrogen atoms were placed in calculated positions but were not refined. The final cycle of full-matrix least-squares refinement[120] on F^2 was based on 12063 reflections and 734 variable parameters and converged (largest parameter shift was 0.00 times its esd).

$[Os(bpy)_2PT_3$-*PS*$](PF_6)_2$, (54).

Data were collected in a series of ϕ and ω scans in 0.50° oscillations using 10.0 second exposures. The crystal to detector distance was 36.00 mm. The data were collected to a maximum 2θ value of 56.2°. Of the 82845 reflections that were collected, 12304 were unique (R_{int} = 0.039); equivalent reflections were merged. Data were corrected for absorption effects using multi-scan the technique (SADABS),[115] with minimum and maximum transmission coefficients of 0.613 and 0.861, respectively. The terminal thiophene ring of the material is disordered as was modeled in two orientations with roughly equal populations. Mild restraints were used to maintain reasonable geometries for the two fragments. Additionally, the material crystallizes with two molecules of CH_2Cl_2 solvent in the asymmetric unit. All non-hydrogen atoms were refined anisotropically. All hydrogen atoms were placed in calculated positions but were not refined. The final cycle of full-matrix least-squares refinement[120] on F^2 was based on 12304 reflections and 695 variable parameters and converged (largest parameter shift was 0.00 times its esd).

$[Os(bpy)_2PT_3$-*PC*$](PF_6)$, (55).

Data were collected in a series of ϕ and ω scans in 0.50° oscillations using 5.0 second exposures. The crystal to detector distance was 40.00 mm. The data were collected to a maximum 2θ value of 56.0°. Of the 56287 reflections that were collected, 9648 were unique (R_{int} = 0.050); equivalent reflections were merged. Data were corrected for absorption effects using multi-scan the technique (SADABS),[116] with minimum and maximum transmission coefficients of 0.499 and 0.900, respectively. The terminal thiophene ring is disordered in two orientations. Mild restraints were employed to

maintain similar bond lengths and angles in the minor disordered fragment. All non-hydrogen atoms were refined anisotropically. All C-H hydrogen atoms were placed in calculated positions but were not refined. The final cycle of full-matrix least-squares refinement[120] on F^2 was based on 9648 reflections and 573 variable parameters and converged (largest parameter shift was 0.00 times its esd).

Section 2.2.4 – DFT Calculations

All calculations were performed by Dr. J. K. Nagle (Bowdoin College) using the 2009.01 version of the Amsterdam Density Functional (ADF) program.[121-135] Experimental X-ray crystallographic cation geometries (C_1 point group) were used for all four complexes. All calculations included scalar and spin-orbit relativistic effects through the zeroth-order relativistic approximation (ZORA),[136-138] except for bond orders and natural population analysis (NPA) atomic charges[139] which included only scalar relativistic effects. The generalized gradient approximation (GGA) of density functional theory (DFT) at the BP86 level was used in all cases.[131-133] and all-electron (i. e., no frozen core approximation was applied) TZ2P basis sets from the ADF basis sets ZORA library were used for all atoms. Atomic charges on all atoms were calculated within ADF using the Voronoi (VDD),[140] Hirshfeld,[141-144] Bader atoms in molecule (AIM),[145, 146] NPA, Mulliken, and multipole-derived quadrupole (MDC-q) methods. Bond orders were calculated within ADF using the Mayer, Gophinatan-Jug, and three Nalejawski-Mrozek methods N-M (1), N-M (2), and N-M (3) provided with the ADF program.[147]

Section 2.3– Results and Discussion

Section 2.3.1 – Synthesis

The $[Ru(phen)_2PT_3\text{-}PS](PF_6)_2$ and $[Ru(phen)_2PT_3\text{-}PC](PF_6)$ complexes were prepared analogously to the previously synthesized Ru(II) bipyridine complexes.[102] Dechlorination of $Ru(phen)_2Cl_2$ with silver tetrafluoroborate followed by addition of PT_3 and precipitation with a hexafluorophosphate salt gave $[Ru(phen)_2PT_3\text{-}PS](PF_6)_2$. The reddish-brown $[Ru(phen)_2PT_3\text{-}PC](PF_6)$ complex (**53**) was obtained by reaction of **52** with base.

Scheme 2-1

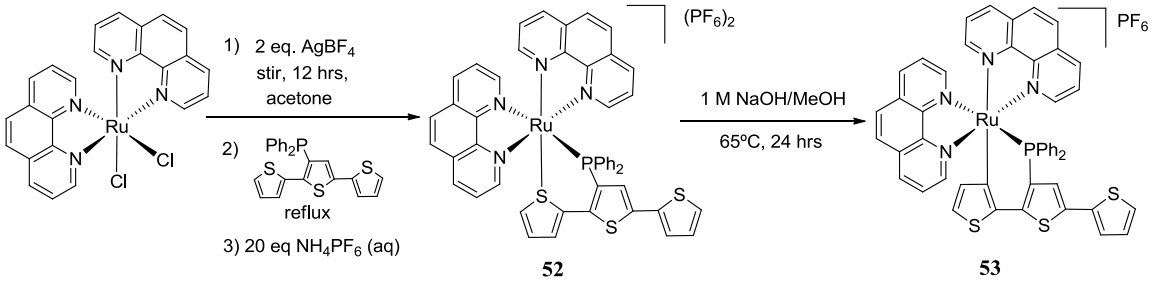

Preparation of the corresponding Os(II) complexes were initially attempted using the same route, but the poor solubility of the $(NH_4)_2OsCl_6$ starting material prevented successful isolation of $[Os(bpy)_2PT_3\text{-}PS](PF_6)_2$. Variation of the volume of solvent used, the time at reflux, and deletion of the filtering step did not help, and in all cases isolation of the desired Os analog of **48** was unsuccessful. Meyer and co-workers have previously reported that the use of Ag salts for dechlorination of Os complexes does not work well, and recommended heating the metal precursor and ligand together in high boiling solvents such as glycerol or ethylene glycol.[148] When attempted here, this method yielded only a small amount of the desired product along with multiple other products, including the monochloro species according to mass spectroscopic analysis. Longer heating at reflux (up to 5 days) did not improve the yield. Further modifications to the conditions established that using a solvent mixture of ethanol and water, in a two-to-one ratio, with extended (36-48 hours) heating at reflux, gave the desired $[Os(bpy)_2PT_3\text{-}PS](PF_6)_2$ (**54**) in 42% yield (Scheme 2-2). The product was purified by column chromatography on neutral alumina. A similar procedure to that used to obtain $[Ru(bpy)_2PT_3\text{-}PC](PF_6)$ was employed to obtain the brown cyclometallated species $[Os(bpy)_2PT_3\text{-}P,C](PF_6)$, **55**, in 61% yield.

Scheme 2-2

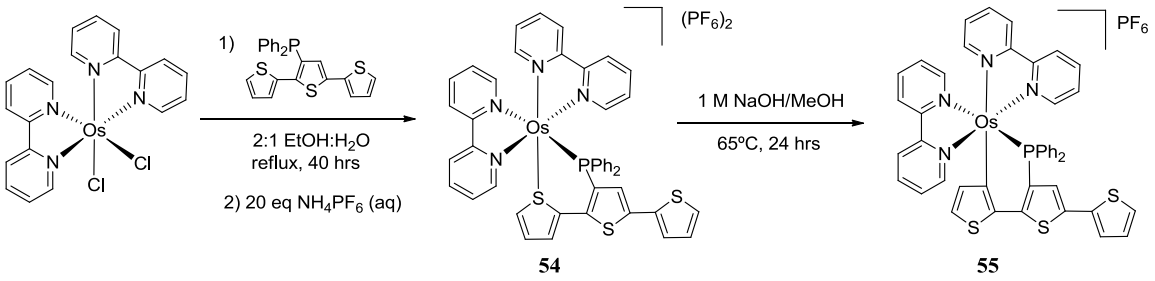

Section 2.3.2– Solid-State Molecular Structures

Crystals suitable for X-ray diffraction of three of the complexes were grown from appropriate solvents. The structures demonstrate the effects of the metal – diimine group and binding mode of the terthiophene ligand on the torsion angles and tilt angle of the metal bound thiophene ring. In all the solid-state structures, the metal center is in a slightly distorted octahedral environment.

Single crystals of $[Ru(phen)_2PT_3\text{-}PS](PF_6)_2$ were grown from a CH_2Cl_2 – acetone – hexanes solution, and the solid-state structure is shown in Figure 2-1. Disorder was present in the thiophene ring containing S3. The Ru – N bond lengths are similar to those in $[Ru(phen)_3](PF_6)_2$.[149] There is very little difference between the bond lengths and angles between the previously synthesized bpy complex[102] and the phen complex here. The torsion angles between the S1 and S2 rings as well as S2 to S3 rings are slightly more co-planar in the $[Ru(phen)_2PT_3\text{-}PS](PF_6)_2$ complex than the analogous $Ru(bpy)_2$ complex. The thiophene ring coordinated to the metal through the sulfur is tilted out of the equatorial plane because of its sp^3 hybridization. The tilt angle of the thiophene away from the Ru – S bond is 58.9 ° in the $[Ru(phen)_2PT_3\text{-}PS](PF_6)_2$ complex, whereas this ring is tilted 58.3 ° in $[Ru(bpy)_2PT_3\text{-}PS](PF_6)_2$. This tilting reorients the lone pair of electrons on the sulfur, allowing for a reduction in the unfavorable π antibonding interactions.[150, 151]

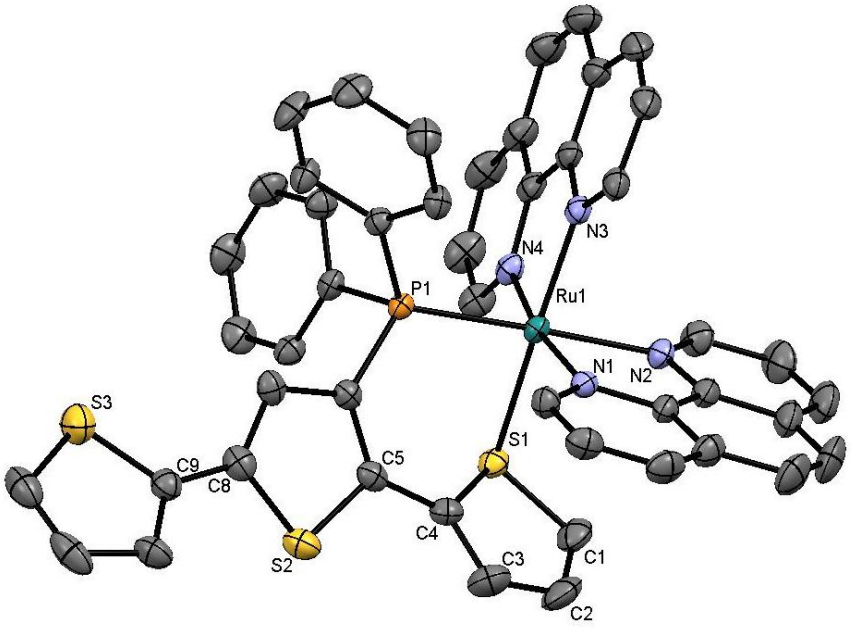

Figure 2-1 Solid-state structure of $[Ru(phen)_2PT_3\text{-}PS](PF_6)_2$, (**52**). Hydrogen atoms, counterions, and solvent in lattice removed for clarity. Thermal ellipsoids are drawn at 50% probability.

Table 2-1 Selected bond lengths and angles for $[Ru(phen)_2PT_3\text{-}PS](PF_6)_2$, (**52**).

Bond Lengths (Å)			
Ru1 – S1	2.3579(7)	S1 – C1	1.742(3)
Ru1 – P1	2.3181(7)	C1 – C2	1.339(5)
Ru1 – N1	2.097(2)	C2 – C3	1.428(5)
Ru1 – N2	2.118(2)	C3 – C4	1.352(4)
Ru1 – N3	2.063(2)	C4 – S1	1.753(3)
Ru1 – N4	2.086(2)	C4 – C5	1.450(4)
Torsion Angles (°)			
S1 – C4 – C5 – S2	148.48(16)	S2 – C8 – C9 – S3	148.4(2)

Single crystals of $[Os(bpy)_2PT_3\text{-}PS](PF_6)_2$ were grown from a CH_2Cl_2 – hexanes solution (Figure 2-2). The metal – nitrogen bonds are slightly longer in $[Os(bpy)_2PT_3\text{-}PS](PF_6)_2$ than in $[Os(bpy)_3](PF_6)_2$.[152] The bonding arrangement in this new structure is identical to the Ru analogue, and some differences in bond lengths and angles are observed between the two structures (Table 2-2). The $S_1 - C_{36} - C_{37} - S_2$ torsion angle of 154.9(3)° in $[Os(bpy)_2PT_3\text{-}PS](PF_6)_2$ is somewhat larger than in $[Ru(bpy)_2PT_3\text{-}PS](PF_6)_2$. The larger torsion angle indicates increased co-planarity, resulting in increased π-orbital overlap between adjacent thienyl rings. In the Os complex, the bound thiophene ring is tilted away from the the Os – S bond at an angle of 59.7°, slightly larger than the tilt angle in $[Ru(bpy)_2PT_3\text{-}PS](PF_6)_2$ (58.3°). The thiophene tilts away from the metal-sulfur bonds in these compounds in order to reduce unfavorable π*-antibonding interactions between the thiophene and metal.[150] The Os center may result in a greater degree of antibonding interaction, and consequently a larger tilt angle.

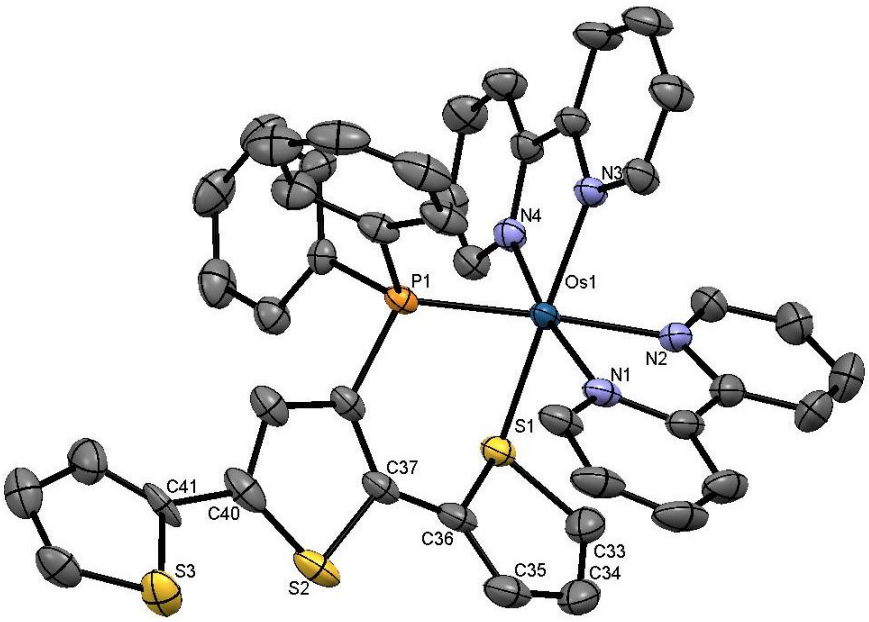

Figure 2-2 Solid-state structure of $[Os(bpy)_2PT_3\text{-}PS](PF_6)_2$, (**54**). Hydrogen atoms, counterions, and solvent in lattice removed for clarity. Thermal ellipsoids are drawn at 50% probability.

Table 2-2 Selected bond lengths and angles for $[Os(bpy)_2PT_3\text{-}PS](PF_6)_2$, (**54**).

Bond Lengths (Å)			
Os1 – S1	2.3543(11)	S1 – C33	1.742(5)
Os1 – P1	2.3101(11)	C33 – C34	1.353(8)
Os1 – N1	2.105(4)	C34 – C35	1.421(8)
Os1 – N2	2.100(4)	C35 – C36	1.351(7)
Os1 – N3	2.072(4)	C36 – S1	1.751(5)
Os1 – N4	2.075(3)	C36 – C37	1.444(7)
Torsion Angles (°)			
S1 – C36 – C37 – S2	154.9(3)	S2 – C40 – C41 – S3	33(3)

Single crystals of $[Os(bpy)_2PT_3\text{-}PC](PF_6)$ were grown from a CH_2Cl_2 – hexanes solution, and the solid-state structure is shown in Figure 2-3. In the $[Os(bpy)_2PT_3\text{-}PC](PF_6)$ complex, the Os – P bond was found to be 2.2892(9) Å, which is comparable to the metal carbon bond length in the Ru analogue, as are the other bond lengths. The $S_1 – C_{36} – C_{37} – S_2$ torsion angle indicates the two locked thiophene rings in $[Os(bpy)_2PT_3\text{-}PC](PF_6)$ are more coplanar than in $[Ru(bpy)_2PT_3\text{-}PC](PF_6)$. The thiophene ring is almost coplanar with the vector of the Os – C bond (tilted 5.9°), a smaller tilt angle relative to the Ru analogue (7.3°). Here, the bound carbon is sp^2 hybridized, and the tilt angle suggests antibonding interactions may also play a role in these complexes.

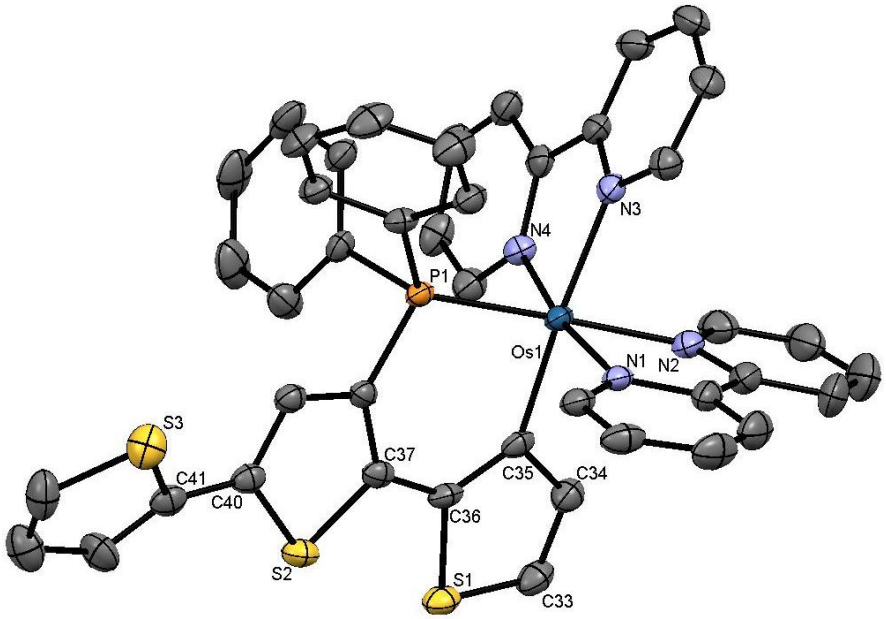

Figure 2-3 Solid-state structure of [Os(bpy)$_2$PT$_3$-*PC*](PF$_6$), (**55**). Hydrogen atoms and counterions removed for clarity. Thermal ellipsoids drawn at 50% probability.

Table 2-3 Selected bond lengths and angles for [Os(bpy)$_2$PT$_3$-*PC*](PF$_6$) , (**55**).

Bond Lengths (Å)			
Os1 – C35	2.095(3)	C35 – C36	1.396(5)
Os1 – P1	2.2892(9)	C36 – C37	1.445(5)
Os1 – N1	2.060(3)	C36 – S1	1.753(3)
Os1 – N2	2.105(3)	S1 – C33	1.698(4)
Os1 – N3	2.124(3)	C33 – C34	1.362(5)
Os1 – N4	2.077(3)	C34 – C35	1.435(5)
Torsion Angles (°)			
S1 – C36 – C37 – S2	5.0(4)	S2 – C40 – C41 – S3	153.0(2)

Section 2.3.3– DFT Calculations

Orbital plots for complexes [Ru(bpy)$_2$PT$_3$-*PS*](PF$_6$)$_2$, [Ru(bpy)$_2$PT$_3$-*PC*](PF$_6$), [Os(bpy)$_2$PT$_3$-*PS*](PF$_6$)$_2$, and [Os(bpy)$_2$PT$_3$-*PC*](PF$_6$) together with their energies, electron populations, and calculated metal contributions are shown in Figure 2-4 to

Figure 2-7. Spin-orbit effects were included in the calculations so that all orbitals are listed as $a_{1/2}$ pairs. The results reveal many similarities in bonding between the corresponding Ru and Os complexes. In comparing the corresponding *PS* bound and *PC* bound complexes, it is found that for the $[Ru(bpy)_2PT_3$-*PS*$](PF_6)_2$ and $[Os(bpy)_2PT_3$-*PS*$](PF_6)_2$ complexes both the HOMO and HOMO-1 have no metal contributions while the $[Ru(bpy)_2PT_3$-*PC*$](PF_6)$ and $[Os(bpy)_2PT_3$-*PC*$](PF_6)$ complexes have minor metal character for the HOMO (3% Ru for $[Ru(bpy)_2PT_3$-*PC*$](PF_6)$ and 10% Os for $[Os(bpy)_2PT_3$-*PC*$](PF_6)_2$) and nearly equal metal and PT_3 contributions for the HOMO-1 (56% Ru for $[Ru(bpy)_2PT_3$-*PC*$](PF_6)$ and 43% Os for $[Os(bpy)_2PT_3$-*PC*$](PF_6)$).

DFT calculations on all four complexes indicate that the total metal bond order calculated by five different methods (Mayer, Gophinatan-Jug, and three Nalejawski-Mrozek definitions) is greater by about 0.6 for $[Os(bpy)_2PT_3$-*PS*$](PF_6)_2$ vs. $[Ru(bpy)_2PT_3$-*PS*$](PF_6)_2$ and $[Os(bpy)_2PT_3$-*PC*$](PF_6)$ vs. $[Ru(bpy)_2PT_3$-*PC*$](PF_6)$, indicating stronger overall M – L bonding in the Os complexes compared to the corresponding Ru complexes. The increase in the total metal bond orders of 0.3 for both the *PC* bound complexes over their respective *PS* bound complexes indicates stronger overall M – L bonding in the *PC* coordination mode where the PT_3 ligand is formally deprotonated, compared to the *PS* mode where the ligand is formally uncharged. This is not surprising given the lower positive charge in $[Ru(bpy)_2PT_3$-*PC*$](PF_6)$ and $[Os(bpy)_2PT_3$-*PC*$](PF_6)$, which arises due to a negative formal charge on the coordinated C atom in the deprotonated PT_3 ligand. The significantly larger M – C bond orders for $[Ru(bpy)_2PT_3$-*PC*$](PF_6)$ and $[Os(bpy)_2PT_3$-*PC*$](PF_6)$ compared to $[Ru(bpy)_2PT_3$-*PS*$](PF_6)_2$ and $[Os(bpy)_2PT_3$-*PS*$](PF_6)_2$ are consistent with this conclusion. There is little difference in the calculated M – P and M – N (N *trans* to P) bond orders between the Ru complexes and between the Os complexes. The values of the total metal bond orders are provided in Table 2-4 and range from 4.2 ± 0.4 for $[Ru(bpy)_2PT_3$-*PS*$](PF_6)_2$ to 5.0 ± 0.5 for $[Os(bpy)_2PT_3$-*PC*$](PF_6)$ depending on the method used to calculate them.

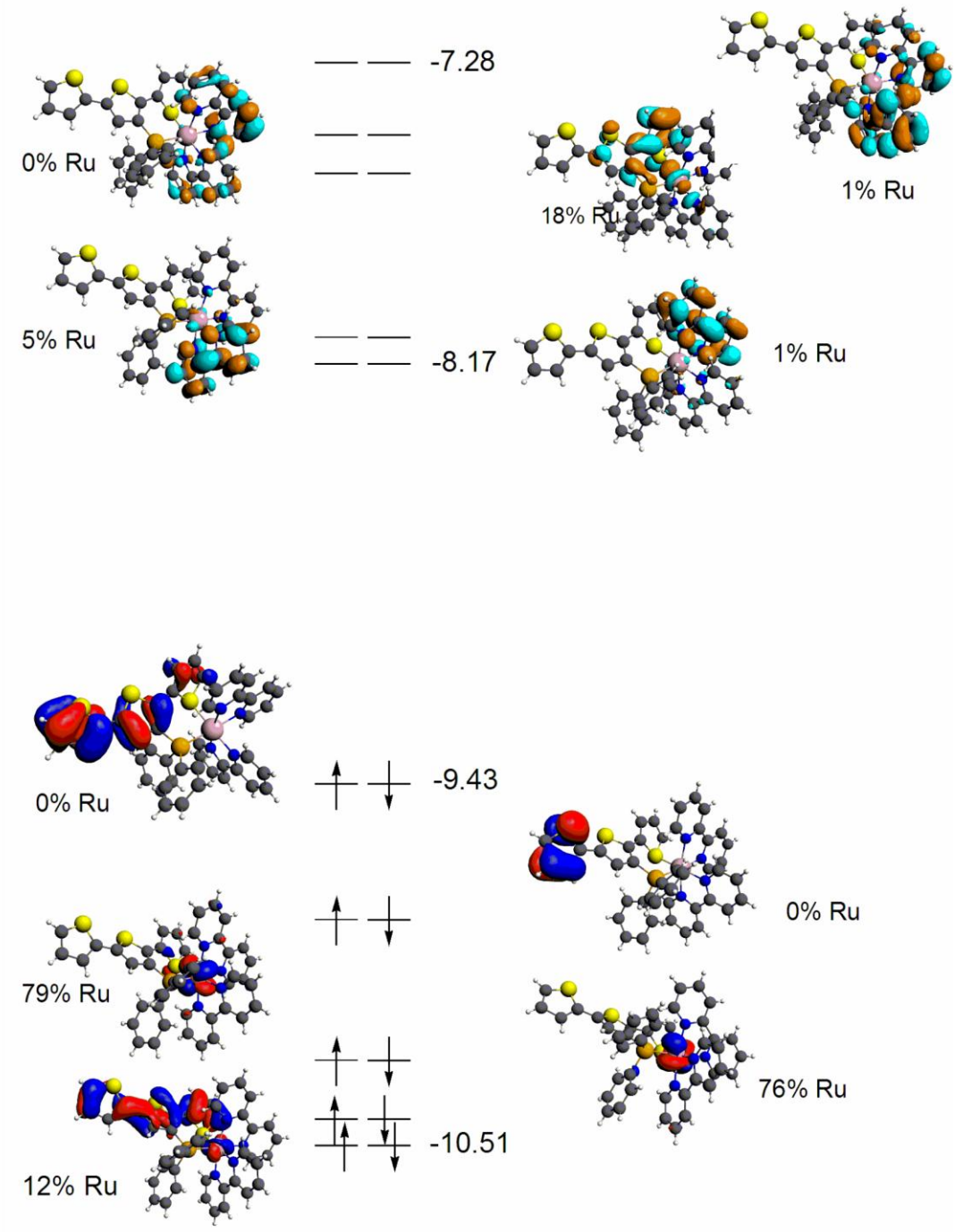

Figure 2-4 ADF-calculated plots of some frontier molecular orbitals (one of each spin-orbit pair shown, all $a_{1/2}$ in C_1 symmetry) for [Ru(bpy)$_2$PT$_3$-*PS*](PF$_6$)$_2$, (**48**), together with calculated energies (eV) for selected orbitals, electron occupations, and Mulliken metal atomic orbital percentages. The lowest energy orbital (453 $a_{1/2}$ for both complexes) plot is lower left in each case, alternating from one side to another with increasing energy so that the HOMO plot is on the left side and the LUMO plot is on the right side.

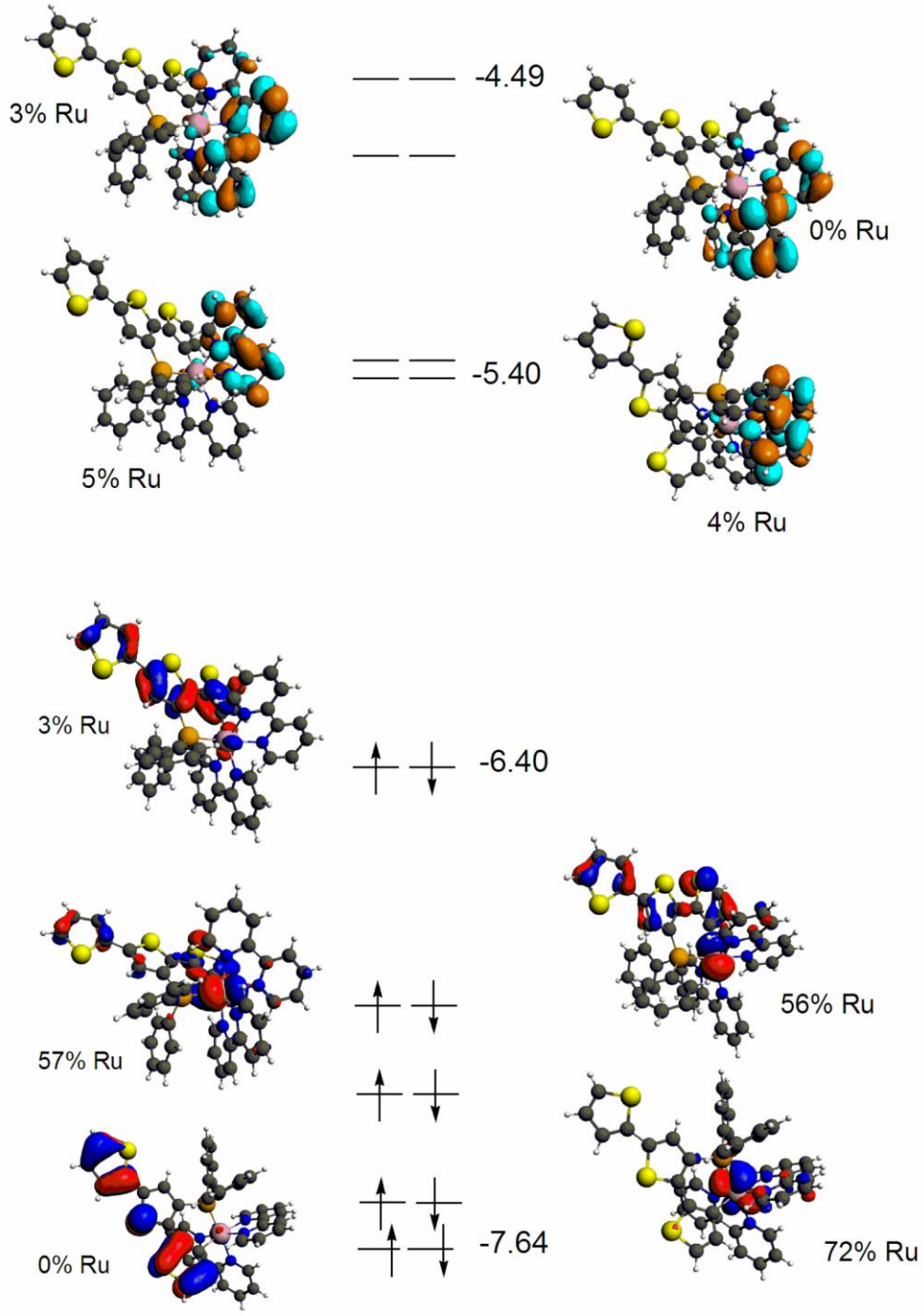

Figure 2-5 ADF-calculated plots of some frontier molecular orbitals (one of each spin-orbit pair shown, all $a_{1/2}$ in C_1 symmetry) for [Ru(bpy)$_2$PT$_3$-*PC*](PF$_6$), (**49**), together with calculated energies (eV) for selected orbitals, electron occupations, and Mulliken metal atomic orbital percentages. The lowest energy orbital (453 $a_{1/2}$ for both complexes) plot is lower left in each case, alternating from one side to another with increasing energy so that the HOMO plot is on the left side and the LUMO plot is on the right side.

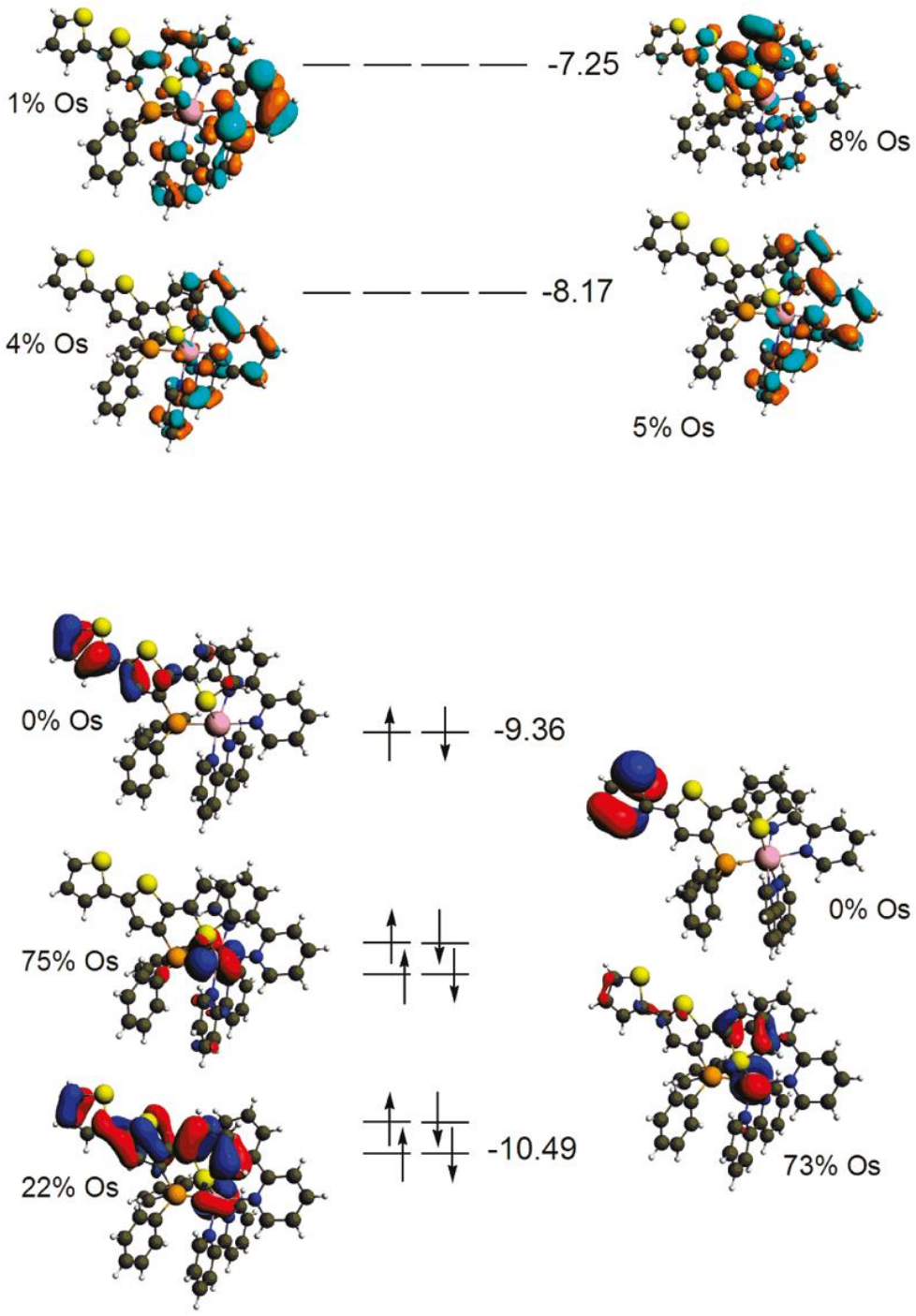

Figure 2-6 ADF-calculated plots of some frontier molecular orbitals (one of each spin-orbit pair shown, all $a_{1/2}$ in C_1 symmetry) for $[Os(bpy)_2PT_3\text{-}PS](PF_6)_2$, (**54**), together with calculated energies (eV) for selected orbitals, electron occupations, and Mulliken metal atomic orbital percentages. The lowest energy orbital (453 $a_{1/2}$ for both complexes) plot is lower left in each case, alternating from one side to another with increasing energy so that the HOMO plot is on the left side and the LUMO plot is on the right side.

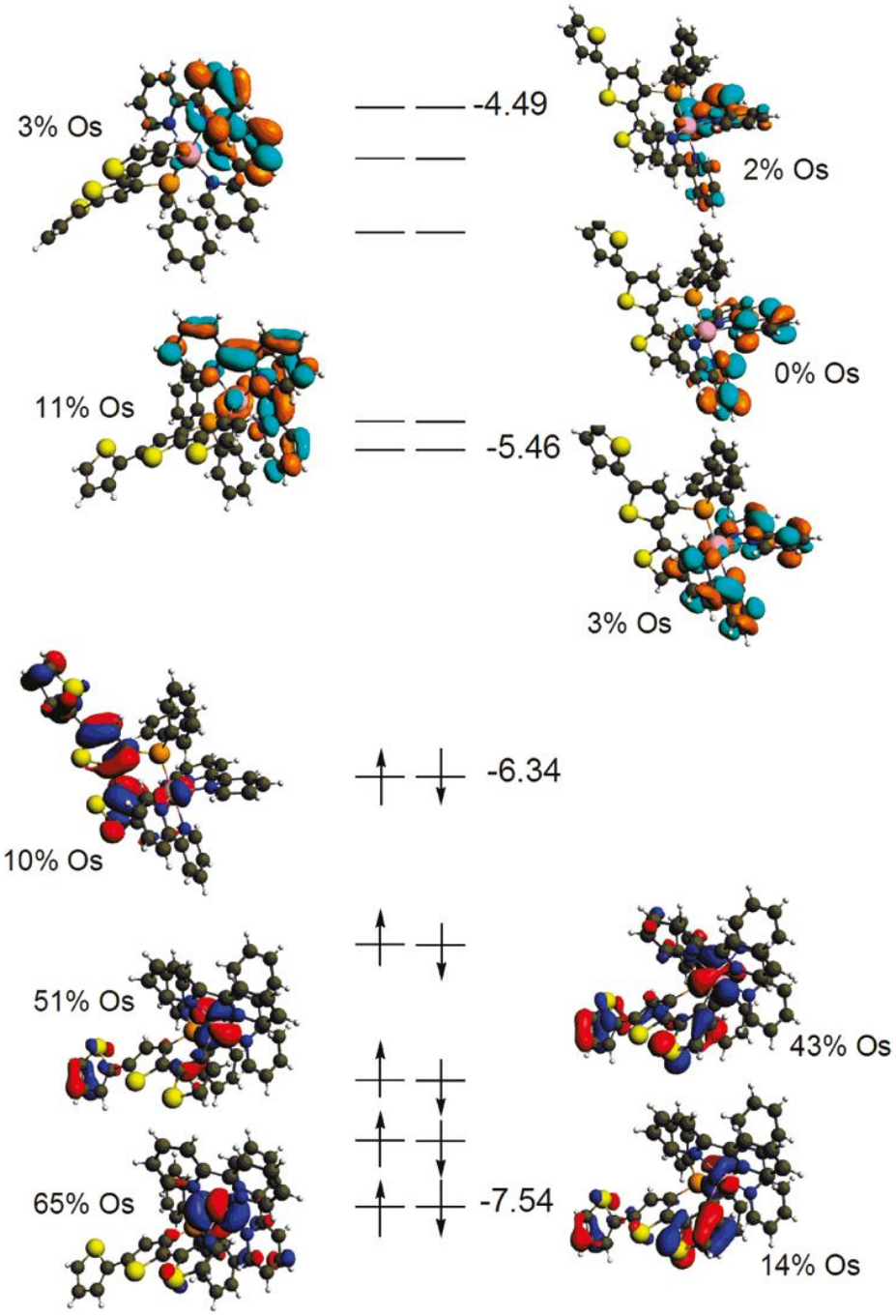

Figure 2-7 ADF-calculated plots of some frontier molecular orbitals (one of each spin-orbit pair shown, all $a_{1/2}$ in C_1 symmetry) for [Os(bpy)$_2$PT$_3$-*PC*](PF$_6$), (**55**), together with calculated energies (eV) for selected orbitals, electron occupations, and Mulliken metal atomic orbital percentages. The lowest energy orbital (453 $a_{1/2}$ for both complexes) plot is lower left in each case, alternating from one side to another with increasing energy so that the HOMO plot is on the left side and the LUMO plot is on the right side.

Table 2-4 Total metal bond orders from ADF scalar relativistic calculations (G-J: Gophinatan-Jug; N-M: Nalejawski-Mrozek).

Compound	Mayer	G-J	N-M (1)	N-M (2)	N-M (3)
$[Ru(bpy)_2PT_3$-*PS*$](PF_6)_2$	4.18	3.82	4.62	3.93	4.41
$[Ru(bpy)_2PT_3$-*PC*$](PF_6)$	4.10	4.09	4.77	4.37	4.57
$[Os(bpy)_2PT_3$-*PS*$](PF_6)_2$	4.86	4.20	5.27	4.37	5.01
$[Os(bpy)_2PT_3$-*PC*$](PF_6)$	4.97	4.51	5.44	4.95	5.17

The Hirshfeld, VDD, Mulliken, and MDC-q methods of calculating atomic charges on the metals all result in higher positive charges by 0.1-0.2 for $[Ru(bpy)_2PT_3$-*PS*$](PF_6)_2$ vs. $[Os(bpy)_2PT_3$-*PS*$](PF_6)_2$ and $[Ru(bpy)_2PT_3$-*PC*$](PF_6)$ vs. $[Os(bpy)_2PT_3$-*PS*$](PF_6)$, while the opposite is found with the AIM and NPA methods (Table 2-5). The higher metal atomic charges for the Ru complexes compared to the corresponding Os complexes calculated by all but the AIM and NPA methods are consistent with a slightly higher electronegativity for Os compared to Ru,[153] and in fact the electronegativity equalized charges[154] calculated for the Ru complexes are higher by 0.1 than those for the corresponding Os complexes. All six ADF methods of calculating atomic charges on the metals show an increase in positive charge for the *PC* vs. the *PS* complexes. The unexpectedly larger charges for the complexes with the *PC* coordination mode suggest greater M – bpy π back-bonding and/or less bpy – M σ donation compared to those with the *PS* mode. The more negative charges on the N atom *trans* to the coordinated C atom in $[Ru(bpy)_2PT_3$-*PC*$](PF_6)$ and $[Os(bpy)_2PT_3$-*PC*$](PF_6)$ compared to those for the N atom *trans* to the coordinated S atom in $[Ru(bpy)_2PT_3$-*PS*$](PF_6)_2$ and $[Os(bpy)_2PT_3$-*PS*$](PF_6)_2$ are consistent with this conclusion. The longer M – N bond distances for the N atom *trans* to C in the $[Ru(bpy)_2PT_3$-*PC*$](PF_6)$ and $[Os(bpy)_2PT_3$-*PS*$](PF_6)$ complexes (2.15 and 2.12 Å, respectively) compared to the M – N bond distances for the N atom *trans* to S in $[Ru(bpy)_2PT_3$-*PS*$](PF_6)_2$ and $[Os(bpy)_2PT_3$-*PS*$](PF_6)_2$ (2.07 Å for both complexes) suggests less N – M σ donation in the *PC* bound complexes compared to the *PS* bound complexes.

Table 2-5 Metal atom atomic charges *Q*/*e* from ADF relativistic calculations according to six different methods: Hirshfeld, Voronoi deformation density (VDD), Bader atoms in molecule (AIM), Weinhold natural population analysis (NPA), Mulliken, and multipole-derived quadrupole (MDC-q). Spin-orbit effects were included in all but the NPA charges.

Compound	Hirshfeld	VDD	AIM	NPA	Mulliken	MDC-q
$[Ru(bpy)_2PT_3$-*PS*$](PF_6)_2$	0.17	0.11	0.81	0.23	0.43	0.87
$[Ru(bpy)_2PT_3$-*PC*$](PF_6)$	0.18	0.15	0.88	0.29	0.73	0.88
$[Os(bpy)_2PT_3$-*PS*$](PF_6)_2$	0.06	-0.03	0.93	0.30	0.37	0.69
$[Os(bpy)_2PT_3$-*PC*$](PF_6)$	0.09	0.01	1.03	0.44	0.62	0.71

Section 2.3.4– Cyclic Voltammetry

The cyclic voltammogram of $[Os(bpy)_2PT_3$-*PS*$](PF_6)_2$ (Figure 2-8(a)) shows a quasi-reversible oxidation peak at 1.23 V vs SCE, ~ 0.25 V lower than the first oxidation peak of $[Ru(bpy)_2PT_3$-*PS*$](PF_6)_2$. ADF-calculated Mulliken AO contributions indicate that both the HOMO and HOMO-1 orbitals of $[Ru(bpy)_2PT_3$-*PS*$](PF_6)_2$ and $[Os(bpy)_2PT_3$-*PS*$](PF_6)_2$ are completely localized on the PT_3 ligand. The first reduction peak of $[Os(bpy)_2PT_3$-*PS*$](PF_6)_2$ occurs at -1.36 V vs SCE and is irreversible. This reduction is presumably localized on the bpy ligands, consistent with ADF calculations that reveal neither the LUMO nor LUMO+1 have more than a 5% Os AO contribution. The cyclic voltammogram of $[Os(bpy)_2PT_3$-*PC*$](PF_6)$ (Figure 2-8(b)) shows two reversible waves, at 0.28 and 0.95 V vs. SCE. Some small features are observed in the voltammogram and are attributed to products resulting from scanning over the full potential range. For $[Os(bpy)_2PT_3$-*PC*$](PF_6)$, the ADF-calculated HOMO is about 90% PT_3 localized while the HOMO-1 (0.48 eV lower in energy) is nearly equally distributed between the Os and PT_3 units, suggesting the oxidation wave at 0.28 V to be PT_3-localized and the 0.95 V oxidation wave to be due to removal of an electron from a mixed Os-PT_3 orbital. These assignments differ from those previously reported for the Ru analogs.[103] These earlier assignments were based only on the observation of small shifts in potential with methyl substitution on the PT_3. The oxidation potential of 0.95 V for $[Os(bpy)_2PT_3$-*PC*$](PF_6)$ is 0.16 V lower than the corresponding value for $[Ru(bpy)_2PT_3$-*PC*$](PF_6)$ and is consistent with the smaller calculated atomic charge for the metal in the

Os complex relative to the Ru complex. In addition, [Os(bpy)$_2$PT$_3$-*PC*](PF$_6$) has reduction waves at -1.45 and -1.75 V vs SCE, both presumably corresponding to bpy-based processes as indicated by the ADF-calculated AO parentages for the LUMO and LUMO+1. These values are 0.08 V and 0.03 V less negative, respectively, than the corresponding values for [Ru(bpy)$_2$PT$_3$-*PC*](PF$_6$) and are consistent with the 0.06 V lower calculated LUMO energy for [Os(bpy)$_2$PT$_3$-*PC*](PF$_6$) versus [Ru(bpy)$_2$PT$_3$-*PC*](PF$_6$).

The cyclic voltammogram of [Ru(phen)$_2$PT$_3$-*PS*](PF$_6$)$_2$ (Figure 2-9) shows a quasi-reversible oxidation peak at 1.39 V vs SCE. The first reduction peak of [Ru(phen)$_2$PT$_3$-*PS*](PF$_6$)$_2$ occurs at -1.19 V vs SCE and is irreversible. This reduction is presumably localized on the phen ligands, as the first reduction for [Ru(bpy)$_2$PT$_3$-*PS*](PF$_6$)$_2$ is assigned as a bpy based reduction. The less negative reduction here than for the bpy analogue (-1.28 V)[103] may be due to the phenanthroline being a slightly better π acceptor than bipyridine. In the [Ru(phen)$_2$PT$_3$-*PC*](PF$_6$) complex, two reversible oxidation waves are observed at 0.51 V and 1.04 V vs SCE. These oxidation waves occur at a potential slightly less positive than the [Ru(bpy)$_2$PT$_3$-*PC*](PF$_6$) analogue (0.57 V and 1.11 V vs SCE).[103] Using the information obtained from the calculations, the oxidation and reduction waves in [Os(bpy)$_2$PT$_3$-*PC*](PF$_6$) were assigned (see above). Based on these assignments, the oxidation at 0.51 V in [Ru(phen)$_2$PT$_3$-*PC*](PF$_6$) was determined to be PT$_3$-localized while the wave at 1.04 V was assigned as an oxidation of a mixed metal-PT$_3$ state. Three reduction waves were observed in the [Ru(phen)$_2$PT$_3$-*PC*](PF$_6$) complex. These waves, occurring at -1.33 V, -1.66 V and -1.87 V vs. SCE, are assigned as phenanthroline based. These values are slightly more negative than the redox potentials observed for [Ru(phen)$_3$](PF$_6$)$_2$.[155]

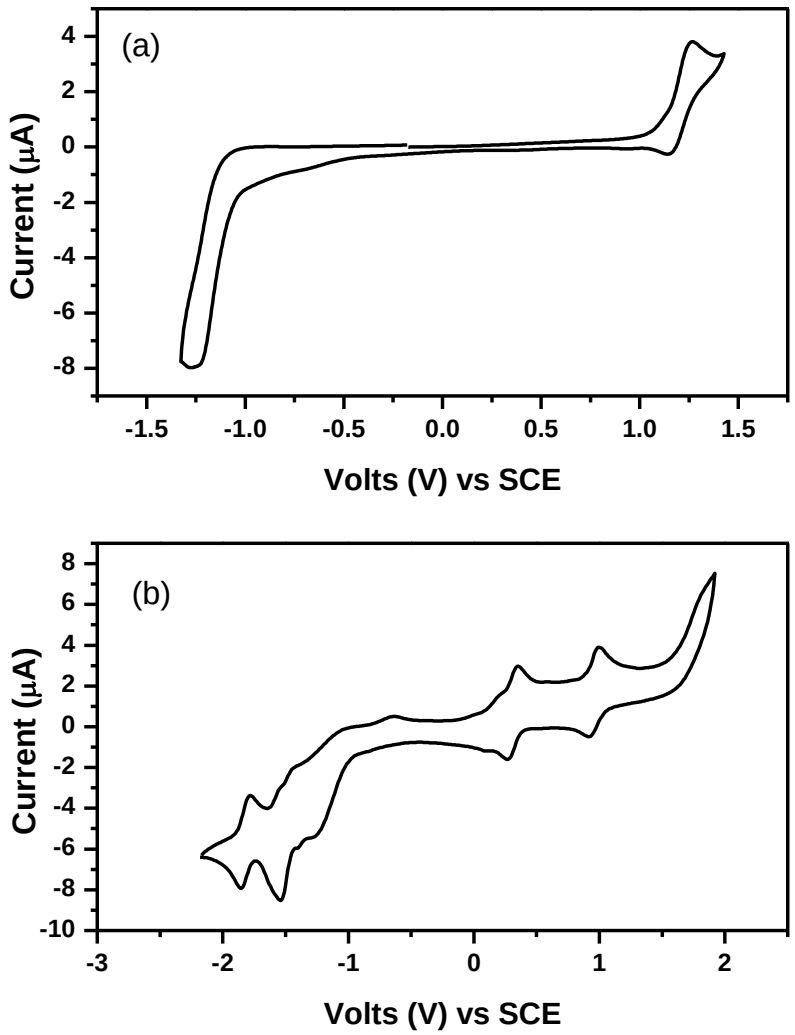

Figure 2-8 Cyclic voltammograms of (a) $[Os(bpy)_2PT_3\text{-}PS](PF_6)_2$, (**54**), and (b) $[Os(bpy)_2PT_3\text{-}PC](PF_6)$, (**55**), in CH_3CN, 0.1 M $TBAPF_6$, 100mV/s scan rate, Pt disc working electrode, Pt mesh counter electrode and silver wire reference electrode.

The substantial decrease in the $Os^{2+/3+}$ oxidation potential between $[Os(bpy)_2PT_3\text{-}PS](PF_6)_2$ and $[Os(bpy)_2PT_3\text{-}PC](PF_6)$ is consistent with the lower energy of the mixed metal-ligand to ligand charge transfer transition (MLL'CT) transition (see below). A similar reduction in the $Ru^{2+/3+}$ oxidation potential was also observed between the *PS* and *PC* bound Ru bipyridine [103] and phenanthroline complexes, and can be accounted for at least in part by the reduction in overall charge from +2 for $[Ru(bpy)_2PT_3\text{-}PS](PF_6)_2$ and $[Os(bpy)_2PT_3\text{-}PS](PF_6)_2$ to +1 for $[Ru(bpy)_2PT_3\text{-}PC](PF_6)$ and $[Os(bpy)_2PT_3\text{-}PC](PF_6)$.

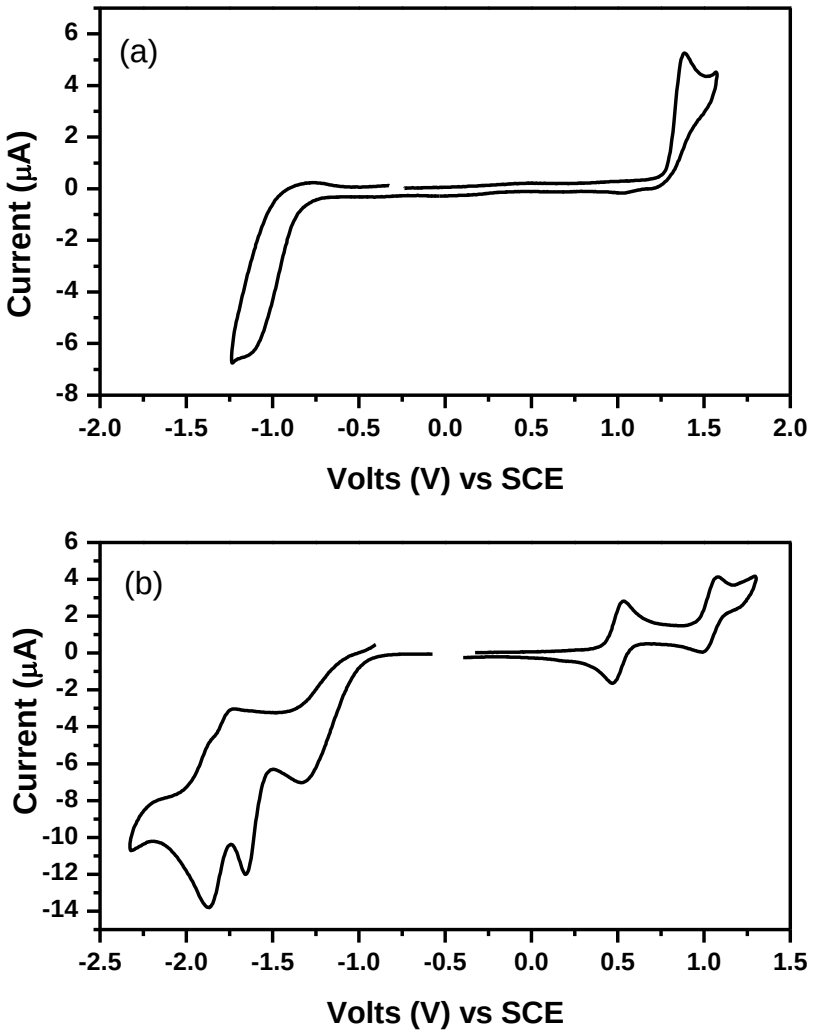

Figure 2-9 Cyclic voltammograms of (a) $[Ru(phen)_2PT_3\text{-}PS](PF_6)_2$, (**52**), and (b) $[Ru(phen)_2PT_3\text{-}PC](PF_6)$, (**53**), in CH_3CN, 0.1 M $TBAPF_6$, 50mV/s scan rate, Pt disc working electrode, Pt mesh counter electrode and silver wire reference electrode.

Section 2.3.5– Electronic Absorption Spectra

The UV-vis absorption spectra of $[Ru(phen)_2PT_3\text{-}PS](PF_6)_2$, $[Ru(phen)_2PT_3\text{-}PC](PF_6)$, $[Os(bpy)_2PT_3\text{-}PS](PF_6)_2$ and $[Os(bpy)_2PT_3\text{-}PC](PF_6)$ in CH_3CN are shown in Figure 2-10, along with the spectra of the Ru(II) bipyridine analogues for comparison. The absorption spectrum of complex $[Ru(phen)_2PT_3\text{-}PS](PF_6)_2$ contains two major bands, a band at 261 nm assigned to the $\pi \rightarrow \pi^*$ transition of the phenanthroline group, and a lower energy band with λ_{max} = 382 nm. The low energy band is slightly blue shifted from the corresponding band in the spectrum of $[Ru(bpy)_2PT_3\text{-}PS](PF_6)$, similar to observations of the spectra of tris(bipyridine) metal complexes, where the ^{1}MLCT band

in $[Ru(bpy)_3]^{2+}$ has λ_{max} = 451 nm[156] and λ_{max} = 446 nm[155] in $[Ru(phen)_3]^{2+}$. Changing the diimine ligands from bpy to phen caused the $\pi \rightarrow \pi^*$ transition of the diimine ligands in the *PS* coordinated complexes to blue shift. A similar shift is observed when comparing the diimine $\pi \rightarrow \pi^*$ transition of $[Ru(bpy)_3]^{2+}$ (286 nm) to $[Ru(phen)_3]^{2+}$ (262 nm).[157] In $[Ru(bpy)_2PT_3\text{-}PS](PF_6)_2$, the shoulder at 320 nm was assigned to the terthienyl $\pi \rightarrow \pi^*$ transition. This band is observed at 295 nm in $[Ru(phen)_2PT_3\text{-}PS](PF_6)_2$.

The absorption spectrum of $[Os(bpy)_2PT_3\text{-}PS](PF_6)_2$ contains two major bands, a band at 286 nm assigned to the $\pi \rightarrow \pi^*$ transition of the bipyridine group, and a lower energy band with λ_{max} = 394 nm. The low energy band is shifted only very slightly from the corresponding band in the spectrum of $[Ru(bpy)_2PT_3\text{-}PS](PF_6)_2$, similar to observations of the spectra of tris(bipyridine) metal complexes, where the ^{1}MLCT band in $[Ru(bpy)_3]^{2+}$ has λ_{max} = 451 nm[156] and λ_{max} = 450 nm in $[Os(bpy)_3]^{2+}$ with the ^{3}MLCT band observed between 520-700 nm.[158] This lower energy band in $[Ru(bpy)_2PT_3\text{-}PS](PF_6)_2$ was assigned to a charge transfer transition involving a mixed metal/terthiophene HOMO and bipyridyl based LUMO (a ^{1}MLL'CT transition).[103, 104] ADF calculations for the *PS* bound complexes indicate that the HOMO and HOMO-1 have no metal atomic orbital contributions, whereas the HOMO-2, -3, and -4 orbitals all contain substantial metal contributions and all lie within about 1 eV of the HOMO in energy. Therefore, for these complexes, the broad, overlapping absorption bands above 350 nm are likely to contain orbital contributions from both PT_3-localized and M-PT_3 delocalized orbitals and are best considered as ^{1}MLL'CT bands. Similarly, the broad band between 450-575 nm in the spectrum of $[Os(bpy)_2PT_3\text{-}PS](PF_6)_2$ is assigned as a ^{3}MLL'CT transition based on the ADF calculations, increased in intensity relative to the Ru analogue due to the larger spin-orbit coupling in Os. In $[Ru(bpy)_2PT_3\text{-}PS](PF_6)_2$, the shoulder at 320 nm was assigned to the terthienyl $\pi \rightarrow \pi^*$ transition. This blue-shifts in $[Os(bpy)_2PT_3\text{-}PS](PF_6)_2$, and is almost completely hidden under the bpy transition, and a small shoulder can be seen at ~300 nm.

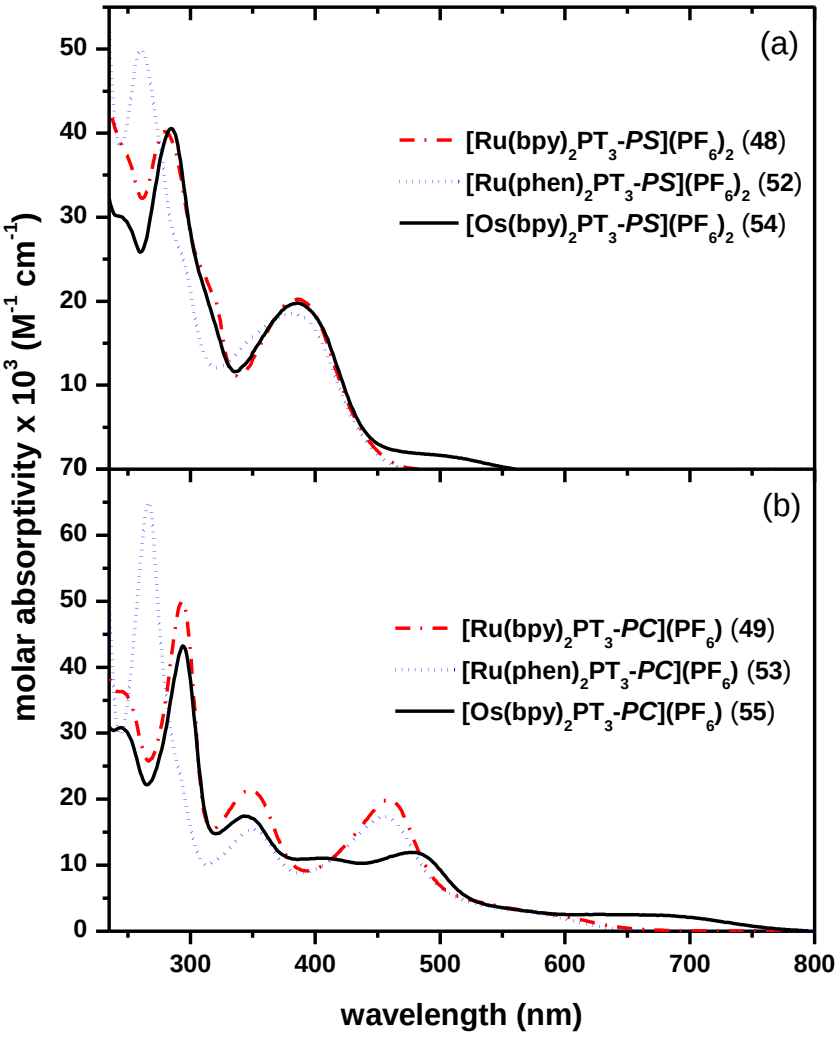

Figure 2-10 UV-vis absorption spectra of (a) $[Ru(bpy)_2PT_3$-*PS*$](PF_6)_2$, (**48**), $[Ru(phen)_2PT_3$-*PS*$](PF_6)_2$, (**52**), $[Os(bpy)_2PT_3$-*PS*$](PF_6)_2$, (**54**) and (b) $[Ru(bpy)_2PT_3$-*PC*$](PF_6)$, (**49**), $[Ru(phen)_2PT_3$-*PC*$](PF_6)$, (**53**), and $[Os(bpy)_2PT_3$-*PC*$](PF_6)$, (**55**), in CH_3CN.

The absorption spectra of the *PC* complexes contain more peaks than their corresponding *PS* complexes. The $\pi \rightarrow \pi^*$ transition of the phenanthroline group in $[Ru(bpy)_2PT_3$-*PC*$](PF_6)$ (268 nm) is blue shifted from that in $[Ru(bpy)_2PT_3$-*PC*$](PF_6)$ (294 nm). Otherwise, the spectra are very similar. The high energy peaks ($\lambda < 375$ nm, assigned to bpy and terthienyl based π–π^* transitions do not shift much between $[Ru(bpy)_2PT_3$-*PS*$](PF_6)$ and $[Os(bpy)_2PT_3$-*PS*$](PF_6)$. A band at 400 nm is observed in the spectrum of the $[Os(bpy)_2PT_3$-*PS*$](PF_6)$ which is not present in the spectrum of $[Ru(bpy)_2PT_3$-*PC*$](PF_6)$ or $[Ru(phen)_2PT_3$-*PC*$](PF_6)$, it is not clear what the origin of this

new peak is. The charge transfer transition in $[Os(bpy)_2PT_3\text{-}PC](PF_6)$ is red-shifted relative to the corresponding band in the Ru complexes (Table 2-6). The ^{3}MLL'CT transition, that ADF calculations suggest corresponds to a HOMO and/or HOMO-1 to LUMO transition, red shifts to 650 nm, with the addition of a new shoulder at 560 nm. This red shift is consistent with the lower calculated atomic charge on the metal in $[Os(bpy)_2PT_3\text{-}PC](PF_6)$ relative to that in $[Os(bpy)_2PT_3\text{-}PS](PF_6)_2$. There is a significant red-shift of the terthienyl band between the *PS* and *PC* complexes due to either the increased planarity of the thiophene rings in the *PC* bound complexes or the change in the charge of the PT_3 ligand accompanying the orthometallation to form the *PC* derivatives.

Table 2-6 Absorption spectroscopy data for $[Ru(phen)_2PT_3\text{-}PS](PF_6)_2$, (**52**), $[Ru(phen)_2PT_3\text{-}PC](PF_6)$, (**53**), $[Os(bpy)_2PT_3\text{-}PS](PF_6)_2$, (**54**), and $[Os(bpy)_2PT_3\text{-}PC](PF_6)$, (**55**).

Compound	Abs λ_{max} (nm) [ε ($M^{-1}cm^{-1}$)][a]
$[Ru(phen)_2PT_3\text{-}PS](PF_6)_2$	260 (50.0×10^3), 293 (sh) (25.6×10^3), 383 (18.5×10^3)
$[Ru(phen)_2PT_3\text{-}PC](PF_6)$	267 (65.0×10^3), 350 (15.4×10^3), 455 (17.3×10^3), 568 (sh) (2.96×10^3)
$[Os(bpy)_2PT_3\text{-}PS](PF_6)_2$	285 (40.6×10^3), 313 (sh) (20.6×10^3), 386 (17.8×10^3), 492 (sh) (1.75×10^3)
$[Os(bpy)_2PT_3\text{-}PC](PF_6)$	285 (40.6×10^3), 313 (sh) (20.6×10^3), 386 (17.8×10^3), 492 (sh) (1.75×10^3)

[a] Measurements carried out in CH_3CN solution.

Photostability studies of PT_3 and the bipyridine complexes in CH_3CN were carried out by extended irradiation with 366 nm light, using UV-vis spectroscopy as a tool to probe stability. Irradiation of PT_3 resulted in a decrease in the main absorption bands, and the growth of a low energy shoulder at ~450 nm (Figure 2-11 (a)). Previous studies have shown that irradiation of 2,2′:5′2″-terthiophene (T_3) with UV light results in polymerization to give longer oligomers.[159] The low energy absorption band observed upon irradiation of PT_3 is consistent with oligomerization of the terthiophene, resulting in a red shift in the absorption band. Irradiation of complexes $[Ru(bpy)_2PT_3\text{-}PC](PF_6)$,

[Os(bpy)$_2$PT$_3$-*PS*](PF$_6$)$_2$, and [Os(bpy)$_2$PT$_3$-*PC*](PF$_6$) under the same conditions resulted in only very small changes to the UV-vis spectra (Figure 2-11 (c)-(e)), indicating that these complexes are all photostable under the irradiation conditions.

On the contrary, irradiation of [Ru(bpy)$_2$PT$_3$-*PS*](PF$_6$)$_2$ results in substantial changes in the UV-vis spectrum (Figure 2-11 (b)), demonstrating that this complex is not photostable under these conditions in solution. Although a small low energy shoulder also appears in this experiment, the higher energy region shows different changes than observed when PT$_3$ is irradiated, suggesting that different products are formed in the case of the [Ru(bpy)$_2$PT$_3$-*PS*](PF$_6$)$_2$ complex. Mass spectrometric analysis of a solution of photoirradiated [Ru(bpy)$_2$PT$_3$-*PS*](PF$_6$)$_2$ suggests that a bipyridyl group is being lost during the irradiation process. This has been observed before in other photoactive metal bipyridyl complexes.[160] It is believed that excited state ligand dissociation proceeds via population of a low-lying ligand state.[161] The photostability of the complexes did not change when irradiated under nitrogen or oxygen. Decomposition reactions of other metal bipyridyl complexes have been observed when MC states are accessible.[162] The increased photostability of the *PC* bound species may be due to the reactive MC state lying higher in energy due to the coordination of the formally anionic ligand. The higher photostability of the [Os(bpy)$_2$PT$_3$-*PS*](PF$_6$)$_2$ complex may also be due to a higher barrier to the MC state, since the lowest energy CT excited state in this complex is lower in energy than in complex [Ru(bpy)$_2$PT$_3$-*PS*](PF$_6$)$_2$.

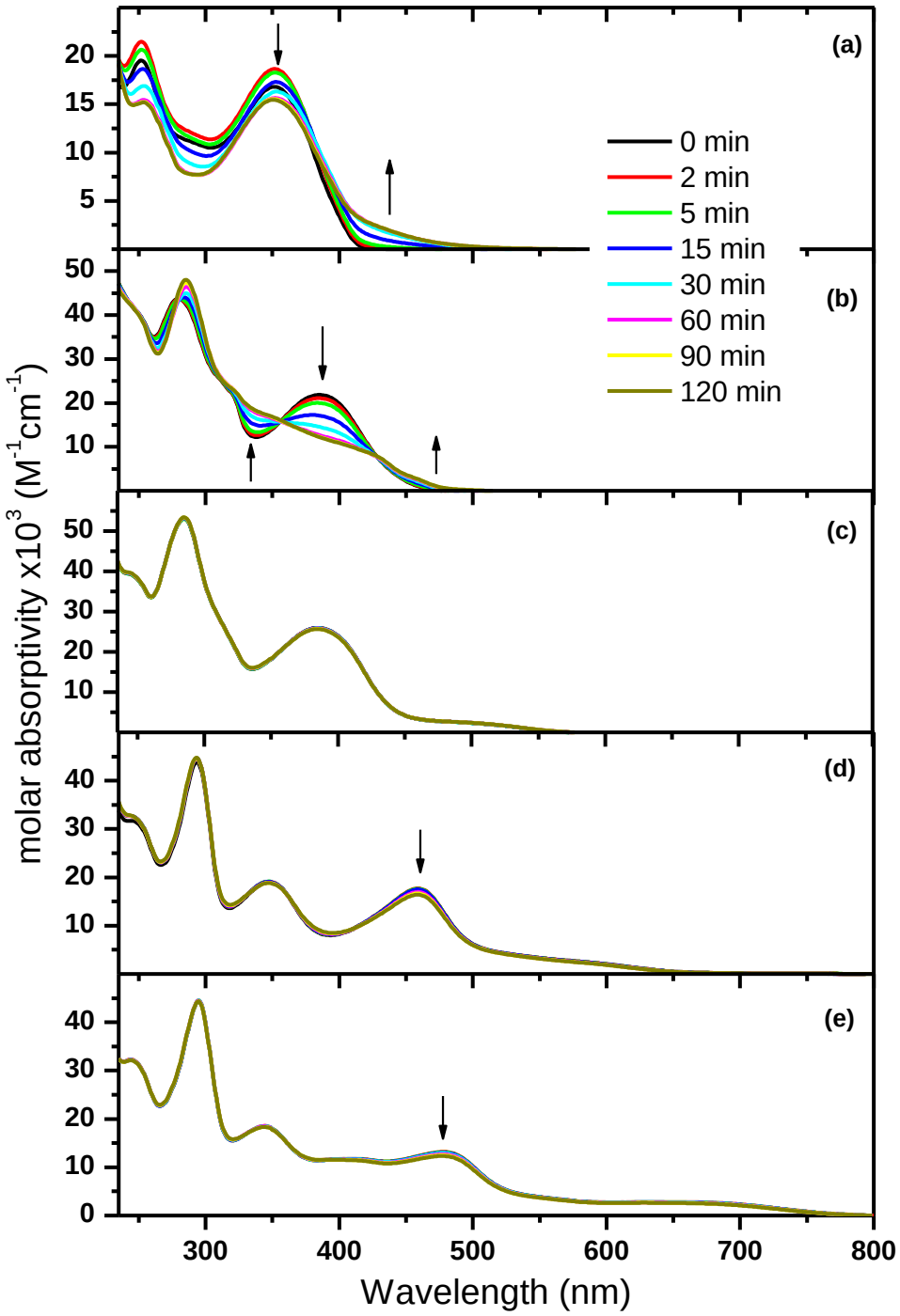

Figure 2-11 UV-vis spectra of (a) PT_3, (b) $[Ru(bpy)_2PT_3$-*PS*$](PF_6)_2$, (**48**), (c) $[Os(bpy)_2PT_3$-*PS*$](PF_6)_2$, (**54**), (d) $[Ru(bpy)_2PT_3$-*PC*$](PF_6)$, (**49**), and (e) $[Os(bpy)_2PT_3$-*PC*$](PF_6)$, (**55**), in CH_3CN after 0, 2, 5, 15, 30, 60, 90, and 120 minutes of irradiation at 366 nm.

Section 2.3.6– Emission Spectra

PT_3 has a short-lived emission centered at 435 nm (Table 1), attributed to radiative decay of the singlet $\pi-\pi*$ state. The $[Ru(bpy)_2PT_3$-*PS*$](PF_6)_2$ and $[Ru(bpy)_2PT_3$-*PC*$](PF_6)$ complexes were previously reported to be either non-emissive or very weakly emissive upon excitation with visible light.[103] However, when excited at 355 nm, $[Ru(bpy)_2PT_3$-*PS*$](PF_6)_2$ exhibited short-lived emission at 430 nm.[163] $[Ru(phen)_2PT_3$-*PS*$](PF_6)_2$ exhibited a weak short-lived emission at 450 nm when excited at 355 nm (Figure 2-12). The Os-bipyridine analogue showed dual emission, with bands at 447 and 640 nm (Figure 2-13). Dual emission from metal complexes is unusual, but has been previously observed in some cases.[164-168] In all the *PS* bound complexes, the lifetime of the species giving rise to the higher energy band is not sensitive to the presence of oxygen. The lifetime of the species giving rise to the lower energy band in $[Os(bpy)_2PT_3$-*PS*$](PF_6)_2$ is significantly shorter in oxygen sparged solution. Based on these observations, the higher energy band in the complexes is assigned to emission from a terthiophene-localized singlet state. In $[Os(bpy)_2PT_3$-*PS*$](PF_6)_2$, enhanced intersystem crossing due to the heavier Os center also populates either a ^{3}MLL'CT or ^{3}LL'CT state which emits at lower energy, and has a longer lifetime. The Ru *PC* bound complexes also emit when excited at 355 nm. In addition, upon excitation into the lowest energy absorption band of these complexes, $[Ru(bpy)_2PT_3$-*PC*$](PF_6)$ and $[Ru(phen)_2PT_3$-*PC*$](PF_6)$ emit at 730 nm and 790 nm, respectively (spectra of $[Ru(phen)_2PT_3$-*PC*$](PF_6)$ shown in Figure 2-12). The $[Os(bpy)_2PT_3$-*PC*$](PF_6)$ also shows two emission bands (Figure 2-13). In the presence of O_2 the lower energy band becomes very weak in these complexes, and in $[Os(bpy)_2PT_3$-*PC*$](PF_6)$ the lifetime is shorter in the presence of oxygen, supporting the assignment of this band to a triplet emission.

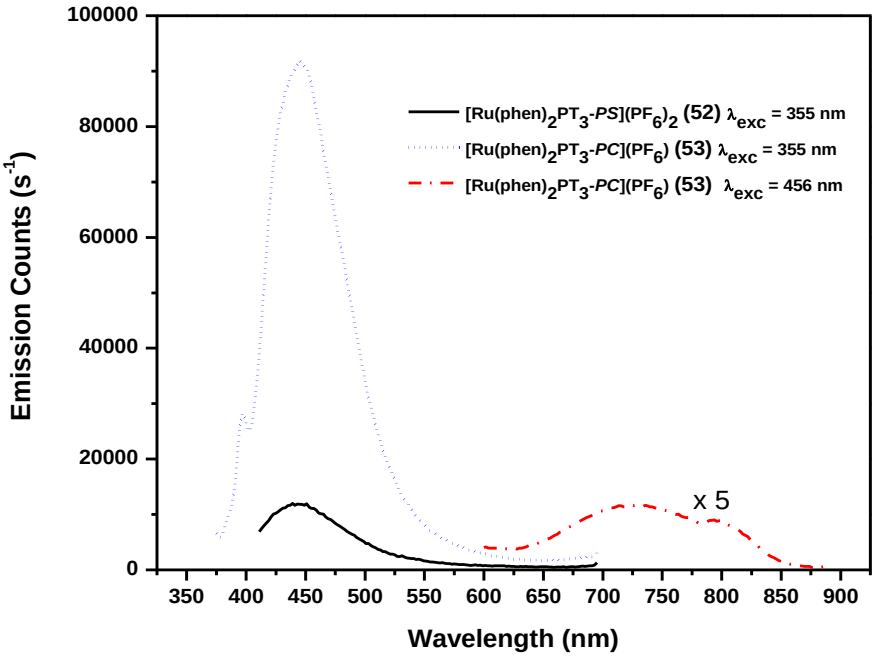

Figure 2-12 Emission spectra of [Ru(phen)$_2$PT$_3$-*PS*](PF$_6$)$_2$, (**52**), and [Ru(phen)$_2$PT$_3$-*PC*](PF$_6$) , (**53**), in nitrogen-sparged CH$_3$CN. The emission of [Ru(phen)$_2$PT$_3$-*PC*](PF$_6$) excited at 456 nm has been expanded by a factor of 5.

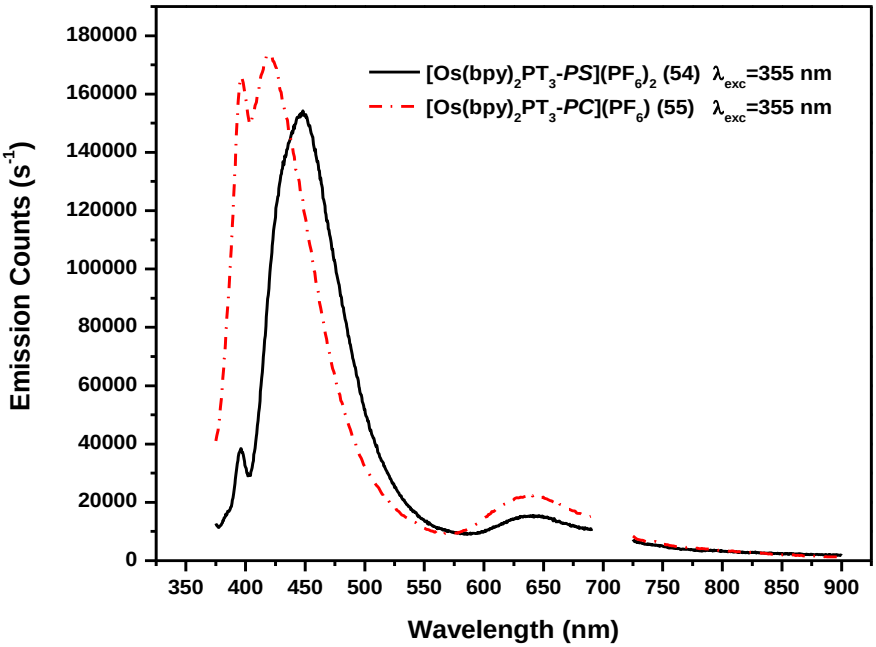

Figure 2-13 Emission spectra of [Os(bpy)$_2$PT$_3$-*PS*](PF$_6$)$_2$, (**54**), and [Os(bpy)$_2$PT$_3$-*PC*](PF$_6$), (**55**) in nitrogen-sparged CH$_3$CN.

Despite careful efforts to purify the complexes, the possibility of the higher energy emission band arising from free ligand cannot be entirely ruled out. However, emission of PT_3 occurs with λ_{max} = 435 nm, and the higher energy emission band observed in all the complexes is shifted from this maximum. Quantum yields were obtained for the lower energy emission band of the bipyridine complexes, and are comparable to those reported for related Os and Ru complexes.[169, 169, 170] Values were calculated for the radiative (k_r) and non-radiative (k_{nr}) decay constants and show the non-radiative decay dominates.

Table 2-7 Photophysical data for PT_3 and complexes $[Ru(bpy)_2PT_3$-*PS*$](PF_6)_2$, (**48**), $[Ru(bpy)_2PT_3$-*PC*$](PF_6)$, (**49**), $[Ru(phen)_2PT_3$-*PS*$](PF_6)_2$, (**52**), $[Ru(phen)_2PT_3$-*PC*$](PF_6)$, (**53**), $[Os(bpy)_2PT_3$-*PS*$](PF_6)_2$, (**54**), and $[Os(bpy)_2PT_3$-*PC*$](PF_6)$ (**55**).

Compound	λ_{em}[a] ±2nm	τ_{em}[a,b] ±5%		τ_{TA}[a,b] ±5%		Φ_{em}[a,c] ±10%	$k_r \times 10^{-4}$ (s^{-1})[d] ±10%	$k_{nr} \times 10^{-4}$ (s^{-1})[e] ±10%	$E_{1/2\ ox}$ ±0.01V vs SCE	$E_{1/2\ red}$ ±0.01V vs SCE
		N_2 Sparged	O_2 sparged	N_2 sparged	O_2 sparged					
PT_3	435 nm	< 0.05 ns	< 0.05 ns	9 μs	-	-	-	-	1.30[f,g]	
48	430 nm	0.2 ns	0.1 ns	100 ns	35 ns	-	-	-	1.48[f]	-1.28[d]
49	423 nm	2 ns	1.5 ns	20 ns	10 ns	-	-	-	0.57	-1.53
	730 nm	8 ns	7 ns			0.0001	1.9	58.6	1.11	-1.78
52	439 nm	-	-	100 ns	-	-	-	-	1.39[f]	-1.19[d]
53	445 nm	-	-	60 ns	-	-	-	-	0.51	-1.33
	790 nm	-	-			-	-	-	1.04	-1.66
										-1.87
54	447 nm	< 0.05 ns	< 0.05 ns	800 ns	70 ns	-	-	-	1.23	-1.36
	640 nm	170 ns	30 ns			0.003	1.1	399		
55	419 nm	1.8 ns	1.5 ns	2 ns	2 ns	-	-	-	0.28	-1.45
	640 nm	25 ns	10 ns			0.0002	1.5	1249	0.95	-1.75

[a]λ_{ex} = 355 nm, CH_3CN, [b]τ = time for intensity to decay to 1/e of the initial intensity [c]Φ_{em} = # photons emitted/# photons absorbed, [d]calculated using $k_r = \Phi_{em}\tau_{em}^{-1}$, [e]calculated using $k_{nr} = \tau_{em}^{-1} - k_r$ using N_2 sparged emission lifetimes, [f]irreversible wave, E_p reported, [g]reference[56]

Section 2.3.7– Transient Absorption Spectra

Transient absorption (TA) spectroscopy uses an excitation pulse to promote a fraction of molecules into the excited state and measures the difference in absorption between the ground state and excited state. The bands in a TA spectrum indicate an excited state absorption, while bleaches are due to stronger ground state absorptions than that of the excited state. The TA spectrum of PT_3 is shown in Figure 2-14 (a). This spectrum shows a transient species absorbing between 400-600 nm, with a lifetime of about 9-10 μs under N_2 (Table 2-7, Appendix Figure A-1), that is quenched under O_2. Excitation of unsubstituted terthiophene, T_3, (Figure 2-14 (b)) also results in a species with a similar, but sharper, absorbance from 400-600 nm with a 2.8 μs lifetime (Appendix Figure A-2). Under oxygen, the TA spectrum of T_3 is also quenched. These data are consistent with the TA of both T_3 and PT_3 being due to a triplet-triplet excitation localized on the π system.

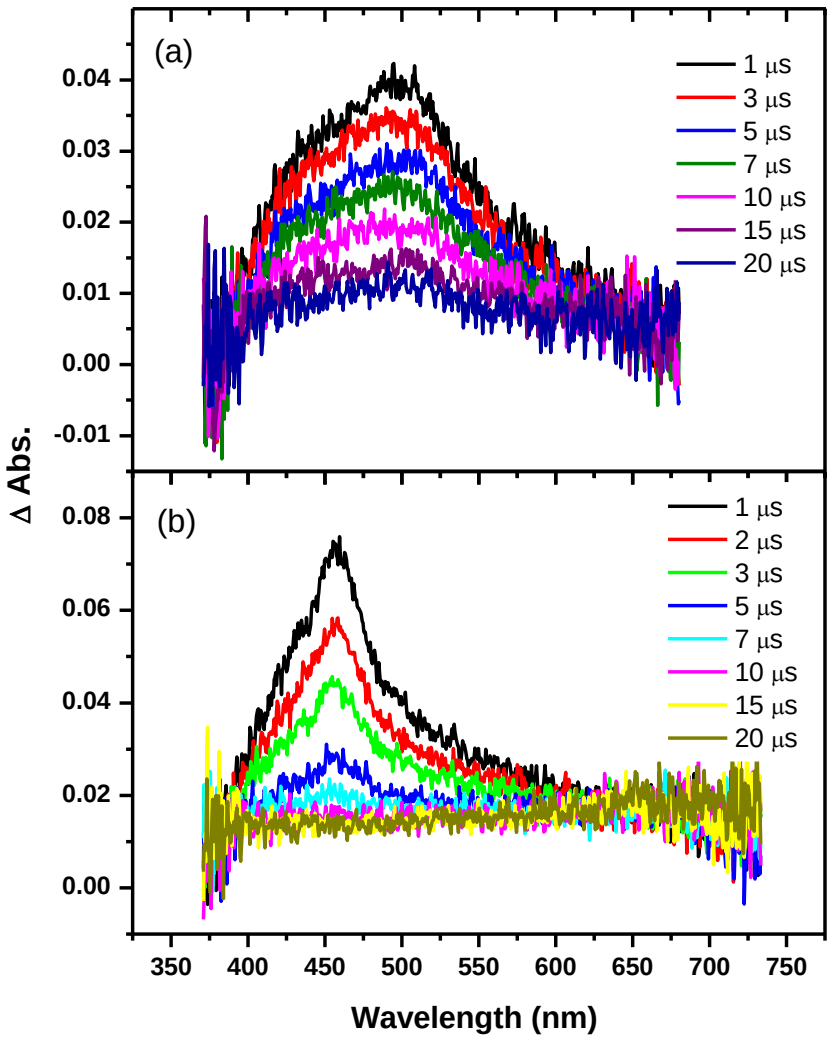

Figure 2-14 Time-resolved transient absorption spectra of (a) PT_3 and (b) T_3 in CH_3CN. λ_{ex} = 355 nm.

Excitation of $[Ru(bpy)_2PT_3$-*PS*$](PF_6)_2$ resulted in a broad TA spectrum with two overlapping bands between 400-700 nm (Figure 2-15 (a)). The species decays with a lifetime of 100 ns in nitrogen-sparged acetonitrile (Appendix Figure A-3), which is significantly reduced with oxygen sparging (Table 1). A similar broad TA spectrum is observed for $[Ru(phen)_2PT_3$-*PS*$](PF_6)_2$ (Figure 2-15 (b)), but the relative ratio of the overlapping bands is different. Both bands decay with a lifetime of approximately 100 ns, and the presence of oxygen decreased this value (Appendix Figure A-4). The $[Os(bpy)_2PT_3$-*PS*$](PF_6)_2$ complex also shows an intense, broad TA with two bands between 450-625 nm (Figure 2-15(c)). In addition, there is a bleach centered at 400 nm.

Both the absorptions and bleach decay with a lifetime of 800 ns (Appendix Figure A-5), which decreases in the presence of oxygen. The TA spectra of these *PS* bound complexes resemble the TA spectrum of PT_3, although slightly red-shifted. In addition, no absorption due to a bipyridyl or phenanthroline anion is seen at ~375 nm,[171] suggesting that the excited state observed in the TA spectra does not have metal-to-diimine or thiophene-to-diimine charge transfer character. Even at short times following excitation, the TA spectra do not show features associated with an MLL'CT state. The dependence of the lifetime and intensity of these bands on the presence of oxygen supports the conclusion that these are due to a triplet state, and the similarity of the TA spectra to that of PT_3 suggests that a PT_3 ligand-centered triplet state (^{3}LC) is being observed.

The lack of observable emission in $[Ru(bpy)_2PT_3$-*PS*$](PF_6)_2$ suggests that in this complex triplet energy transfer to the ^{3}LC state is very efficient. In the Os complex, $[Os(bpy)_2PT_3$-*PS*$](PF_6)_2$, weak emission attributed to decay of the ^{3}MLL'CT or ^{3}LL'CT is observed, and the ^{3}LC state is still relatively efficiently populated and is the major species observed in the TA spectrum. The longer TA lifetime in $[Os(bpy)_2PT_3$-*PS*$](PF_6)_2$ indicates that the ^{3}LC state must lie substantially lower in energy than the ^{3}MLL'CT and ^{3}LL'CT states, and these states are not in thermal equilibrium as has been observed previously in pyrene functionalized Ru diimine complexes.[172, 173] In these cases the pyrene ^{3}LC state and Ru ^{3}MLCT states have the same lifetimes due to the equilibrium between them. The longer TA lifetime for $[Os(bpy)_2PT_3$-*PS*$](PF_6)_2$ relative to $[Ru(bpy)_2PT_3$-*PS*$](PF_6)_2$ and $[Ru(phen)_2PT_3$-*PS*$](PF_6)_2$ is attributed to the higher energy barrier to the MC state (see above), consequently this deactivation pathway is less prevalent in the Os complex than in the Ru complexes.

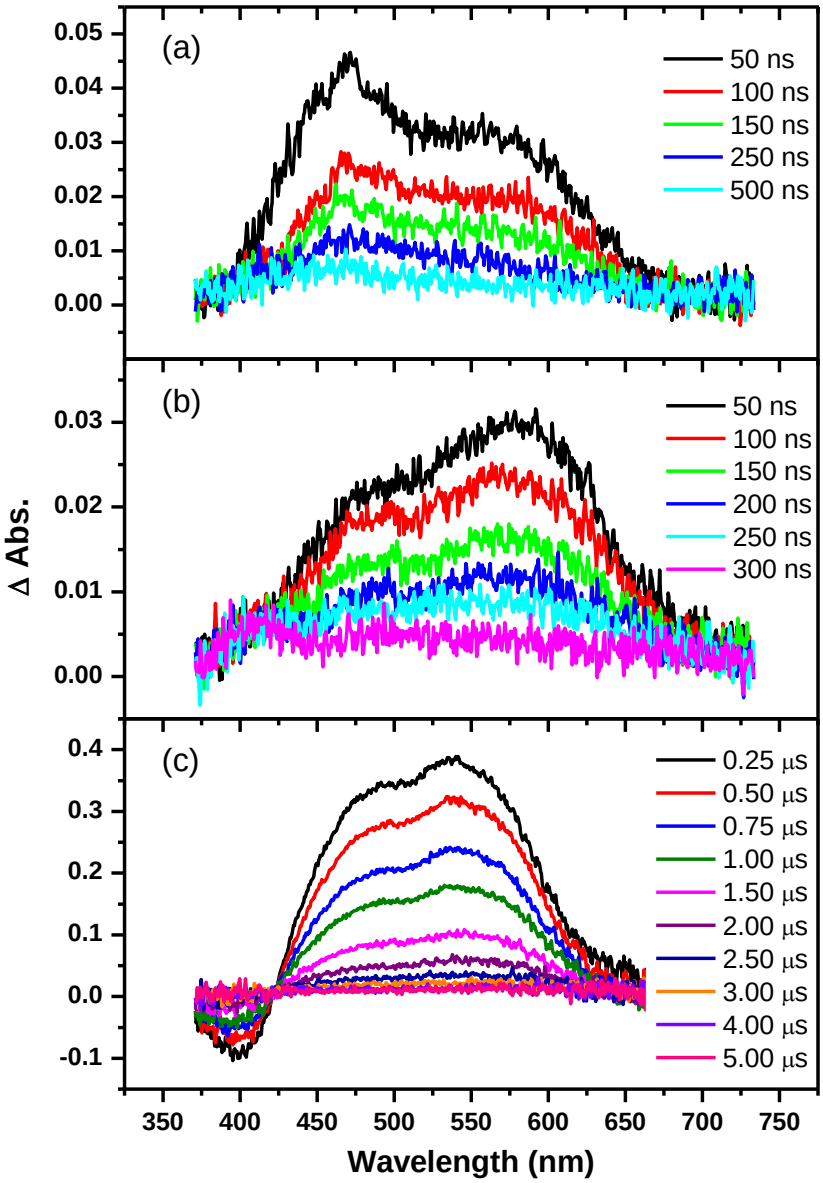

Figure 2-15 Time-resolved transient absorption spectra of (a) $[Ru(bpy)_2PT_3\text{-}PS](PF_6)_2$, (**48**), (b) $[Ru(phen)2PT_3\text{-}PS](PF_6)_2$, (**52**), and (c) $[Os(bpy)_2PT_3\text{-}PS](PF_6)_2$, (**54**), in CH_3CN. λ_{ex} = 355 nm.

Interestingly, the TA spectra of the *PC* bound complexes (Figure 2-16) are very different from the corresponding *PS*-coordinated complexes. Each of the *PC* bound complexes shows an absorption at ~375 nm, and a bleach at ~450-475 nm. The TA spectra of $[Ru(bpy)_2PT_3\text{-}PC](PF_6)$ and $[Ru(phen)_2PT_3\text{-}PC](PF_6)$ also contain broad, tailing absorptions above 500 nm, while $[Os(bpy)_2PT_3\text{-}PC](PF_6)$ shows a weak, broad bleach in this region. The TA of $[Ru(bpy)_2PT_3\text{-}PC](PF_6)$ decays monoexponentially with

a lifetime of 20 ns under nitrogen (Appendix Figure A-6), which decreases under O_2. The [Ru(phen)$_2$PT$_3$-*PC*](PF$_6$) complex decays monoexponentially with a lifetime of about 60 ns under nitrogen (Appendix Figure A-7).

The absorption at ~375 nm in the TA spectrum of these complexes is assigned as a transition of the bpy$^-$ or phen$^-$ anion based on comparison to related compounds.[171] The presence of this band indicates the observed excited state has charge transfer character. The lower energy absorption bands (>500 nm) in [Ru(bpy)$_2$PT$_3$-*PC*](PF$_6$) and [Ru(phen)$_2$PT$_3$-*PC*](PF$_6$) are assigned to transitions of a cationic species having mixed-metal and ligand (PT$_3$) character. This assignment is based on several comparisons. The TA spectrum of T$_3^+$ shows an absorbance band between 530 and 545 nm,[174, 175] and spectroelectrochemical studies on oxidized [Ru(bpy)$_2$PT$_3$-*PC*](PF$_6$) have shown that this species has bands with absorption maxima at 558 and 632 nm.[176] Both these species have similar absorptions to the band observed in the TA spectrum of [Ru(bpy)$_2$PT$_3$-*PC*](PF$_6$) at ~515 nm, suggesting a similar origin. An EPR study of oxidized [Ru(bpy)$_2$PT$_3$-*PC*](PF$_6$) showed that there is a significant metal contribution to the singly occupied molecular orbital (SOMO) in this oxidized complex.[104] This is consistent with ADF-calculations for [Ru(bpy)$_2$PT$_3$-*PC*](PF$_6$) showing the HOMO-1 to have a 56% Ru contribution, but not with oxidation from the HOMO which has only a 3% Ru contribution.

Taking all this data into account does not allow a conclusive assignment to be made of the cation, but a mixed parentage cation with both metal and PT$_3$ ligand character is most likely, thus the observed excited state is characterized as a mixed metal-ligand to ligand CT (^{3}MLL'CT) state. The broad but very weak absorbance tail around 650 nm in [Ru(bpy)$_2$PT$_3$-*PC*](PF$_6$) and [Ru(phen)$_2$PT$_3$-*PC*](PF$_6$) is characteristic of the presence of an anion,[177, 178] cation[179, 180] or a charge transfer transition.[181] The TA and emission lifetimes are similar for [Ru(bpy)$_2$PT$_3$-*PC*](PF$_6$) suggesting that it is possible that these states are close in energy and in thermal equilibrium.

The excited state spectrum of [Os(bpy)$_2$PT$_3$-*PS*](PF$_6$)$_2$ appears to be similar, with the clear presence of a transition assigned to the bpy anion. Transitions that could be assigned to a cation are not observed. [Os(bpy)$_2$PT$_3$-*PS*](PF$_6$)$_2$ absorbs to 700 nm, so the

bleaching that is observed in the TA spectrum of this complex may hide weaker absorptions from a cationic species if these are present. The lifetime of this species is short, 2 ns under either nitrogen (Appendix Figure A-8), or oxygen. The measured lifetime is shorter than the emission lifetime, and it is possible that the weak TA spectrum introduces error and these states are also close in energy as in $[Ru(bpy)_2PT_3\text{-}PS](PF_6)_2$. Other Ru and Os bipyridyl complexes show similar transient spectra. Excited state $Ru(bpy)_3^{2+}$ is reported to have absorption bands at 360 nm and above 525 nm, with a bleach centered at 440.[182] Excited state $Os(dmb)_3^{2+}$ has an absorption around 350 nm, and a strong bleach from 420-500 nm, with a weaker bleach extending past 650 nm.[183]

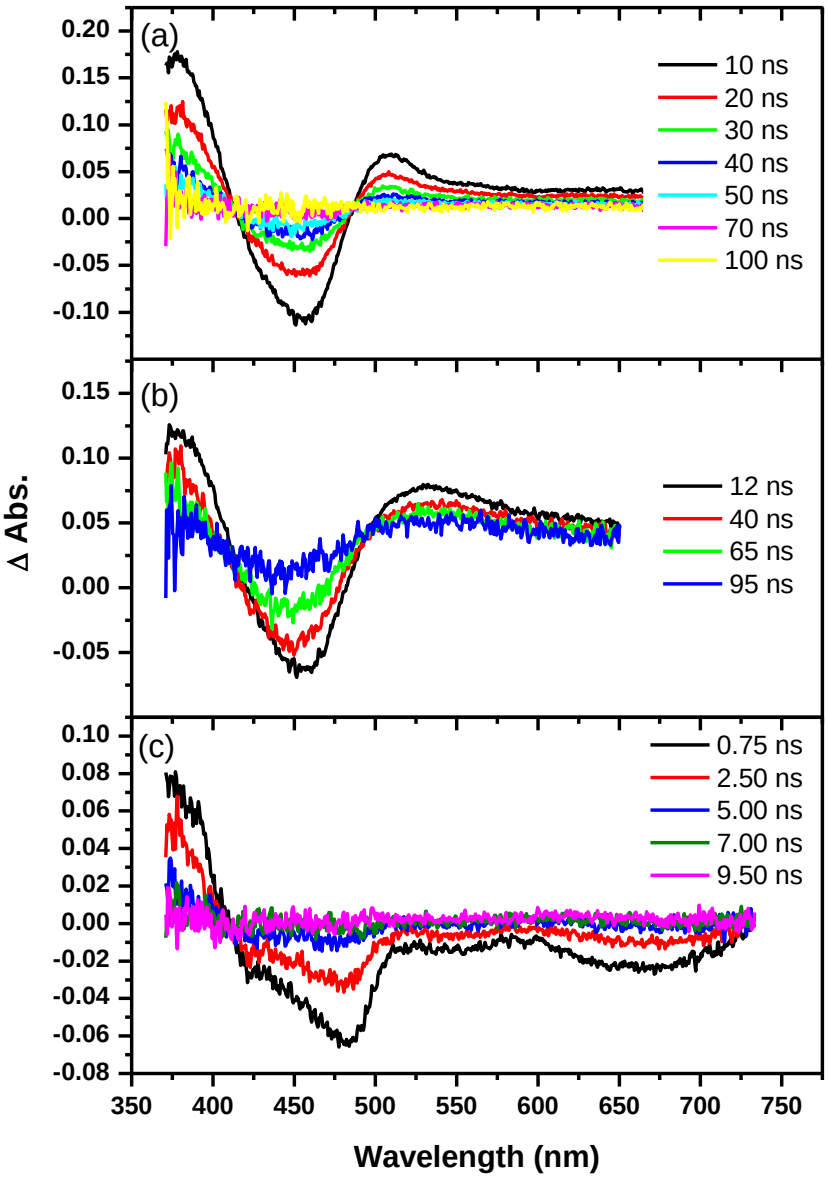

Figure 2-16 Time-resolved transient absorption spectra of (a) [Ru(bpy)$_2$PT$_3$-*PC*](PF$_6$), (**49**), (b) [Ru(phen)2PT$_3$-*PC*](PF$_6$), (**53**), and (c) [Os(bpy)$_2$PT$_3$-*PC*](PF$_6$), (**55**), in CH$_3$CN. λ_{ex} = 355 nm.

The photophysical results for these complexes can be summarized by consideration of the qualitative energy diagram shown in Figure 2-17. For the *PS* bound complexes, excitation at 355 nm results in simultaneous population of both ^{1}MLL'CT and ^{1}LC states. Some emission from the ^{1}LC state is observed for both complexes. Internal conversion followed by intersystem crossing populates the ^{3}MLL'CT or ^{3}LL'CT state, from which some emission is observed for the [Os(bpy)$_2$PT$_3$-*PS*](PF$_6$)$_2$ complex. For the

Ru(II) complexes, the MC state lies close enough in energy to be thermally populated resulting in a photoreaction, and this does not occur in $[Os(bpy)_2PT_3\text{-}PS](PF_6)_2$. In the PS bound complexes, the ^{3}LC state is lower in energy than the ^{3}MLL'CT or ^{3}LL'CT state, resulting in triplet energy transfer and the observation of a transient species attributed to the ^{3}LC state. This coordination mode results in only a small perturbation in the electronic structure of the PT_3 ligand, possibly due to the weakly coordinated thiophene sulfur.

In the *PC* bound complexes, population of both ^{1}MLL'CT and ^{1}LC states occurs, and some emission from the ^{1}LC states is observed. Here, the ^{3}MLL'CT state is also populated, and emission from this state is observed.

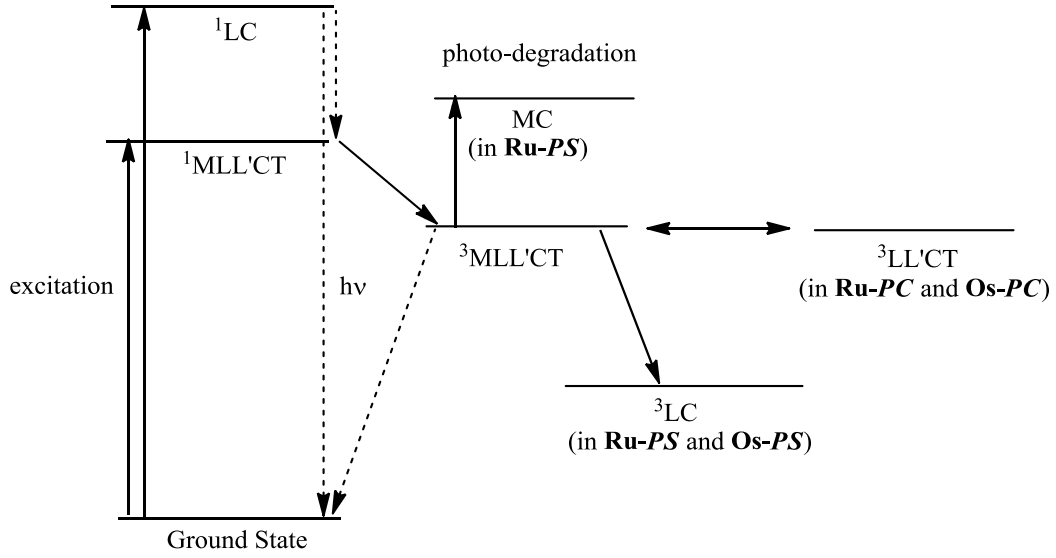

Figure 2-17 Qualitative energy diagram for $[Ru(bpy)_2PT_3\text{-}PS](PF_6)_2$, (**48**), $[Ru(bpy)_2PT_3\text{-}PC](PF_6)$, (**49**), $[Ru(phen)_2PT_3\text{-}PS](PF_6)_2$, (**52**), $[Ru(phen)_2PT_3\text{-}PC](PF_6)$, (**53**), $[Os(bpy)_2PT_3\text{-}PS](PF_6)_2$ (**54**), and $[Os(bpy)_2PT_3\text{-}PC](PF_6)$ (**55**). Abbreviations used indicate metal center and binding mode of the complexes.

Section 2.4– Conclusions

Four new group 8 diimine complexes were synthesized incorporating PT_3 as a ligand: $[Ru(phen)_2PT_3\text{-}PS](PF_6)_2$, $[Ru(phen)_2PT_3\text{-}PC](PF_6)$, $[Os(bpy)_2PT_3\text{-}PS](PF_6)_2$ and $[Os(bpy)_2PT_3\text{-}PC](PF_6)$. The obtained solid-state structures are similar to the previously synthesized $[Ru(bpy)_2PT_3\text{-}PS](PF_6)_2$ and $[Ru(bpy)_2PT_3\text{-}PC](PF_6)$ complexes. DFT

studies indicated that for the $[Ru(bpy)_2PT_3\text{-}PS](PF_6)_2$ and $[Os(bpy)_2PT_3\text{-}PS](PF_6)_2$ complexes both the HOMO and HOMO-1 have no metal contributions, while the $[Ru(bpy)_2PT_3\text{-}PC](PF_6)$ and $[Os(bpy)_2PT_3\text{-}PC](PF_6)$ complexes have minor metal character for the HOMO and nearly equal metal and PT_3 contributions for the HOMO-1. The electrochemistry reveals PT_3 or mixed PT_3 – metal oxidation waves, while the reduction waves are assigned as diimine based. The spectroscopic properties of $[Ru(phen)_2PT_3\text{-}PS](PF_6)_2$ and $[Ru(phen)_2PT_3\text{-}PC](PF_6)$ complexes are akin to the $[Ru(bpy)_2PT_3\text{-}PS](PF_6)_2$ and $[Ru(bpy)_2PT_3\text{-}PC](PF_6)$ analogues. The absorption spectra are dominated by $\pi\rightarrow\pi^*$ transitions for all complexes, and the MLCT band was not shifted a lot between the Ru and Os complexes. The Os analogues had a broader absorption than the Ru complexes due to enhanced spin orbit coupling. Changing the coordination mode of the PT_3 ligand (from *PS* to *PC* coordination) resulted in broader absorption across the UV-vis region. A new band in the absorption spectrum of $[Os(bpy)_2PT_3\text{-}PC](PF_6)$ was observed at ~400 nm. Enhanced photostability of the Os complexes was observed. Weak emission was recorded for all complexes. A shift in the excited state observed by TA spectroscopy from a ^{3}LC triplet localized on the PT_3 group in the *PS* bound complexes to a mixed metal-ligand to ligand CT state in the case of the *PC* bound complexes was also reported. These results have important implications for the design of dyes for DSSCs and other related applications. In the *PC* bound complexes the MLL'CT excited state involves charge transfer from the PT_3 localized HOMO to the bipyridyl localized LUMO. Adsorption of these complexes to nanostructured TiO_2 should allow charge injection from the LUMO and hole transport away from the metal center via the conjugated ligand.

CHAPTER 3

CYCLOMETALATED IRIDIUM (III) PHOSPHINO(TERTHIOPHENE) COMPLEXES

Section 3.1– Introduction

Cyclometalated iridium (III) complexes have received a great deal of interest in the past several years due to their interesting photophysical properties. Luminescent cyclometalated Ir(III) complexes commonly exhibit short phosphorescence lifetimes relative to organic luminophores[184] (microseconds compared to milliseconds) at room temperature and have high quantum yields.[185] They are most notably known for their use as emissive dopants in organic light emitting diodes (OLEDs).[186-190] More recently, complexes of this type have been shown to have useful applications in a number of different fields, including as photocatalysts,[191] oxygen sensors,[192, 193] biological labels,[194,195] in light emitting electrochemical cells (LECs)[196] and in dye sensitized solar cells (DSSCs).[93, 197, 198]

As previously discussed (Introduction), Ru(II) polypyridyl systems have dominated the DSSC field to date. Ir (III) complexes isoelectronic with Ru(II) and Os(II) complexes have good chemical stability, and have potential for application in DSSCs as well. Ir(III) terpyridine complexes have been used as photosensitizers, and exhibit charge-separated states with lifetimes of 100 μs in air equilibrated solution.[197] Their long lifetime in air, coupled with their lower reduction potentials and higher lying excited states (than analogous Ru(II) terpy complexes) are beneficial attributes.

Cyclometalated Ir(III) complexes have also been shown to possess similar spectroscopic and electronic properties to Ru(II) bpy complexes. Due to the wide ligand set available, and enhanced spin orbit coupling of the Ir(III) complexes (the one electron spin-orbit coupling constants, ζ_c, for Ru(II) and Ir(III) are 1051 cm^{-1} and 4430 cm^{-1}, respectively),[199] absorption can span a wide range of the visible/NIR spectrum. Mayo *et al*. have shown that Ir(III) dyes (**56** and **57** Chart 3-1) can sensitize TiO_2 in a DSSC.[93] These complexes have a low energy LLCT state which allows for large spatial separation between holes and electrons. This can facilitate injection into TiO_2 while still possessing reduction potentials sufficient to oxidize I^-.

Chart 3-1 Ref.[93]

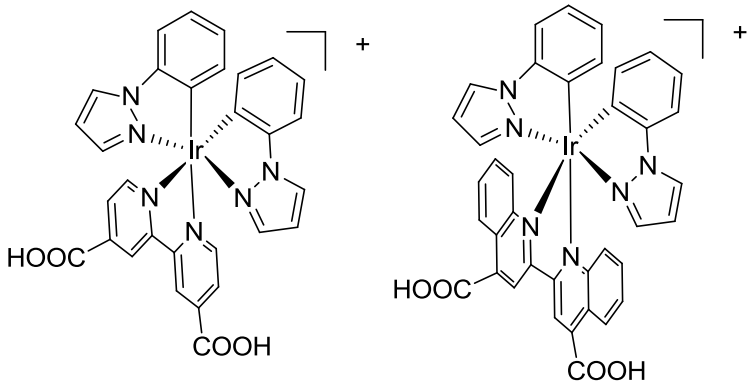

56 **57**

Investigations of Ir (III) complexes have focused on homo- and heteroleptic cyclometalated complexes, with the majority having the general form $[Ir(C\text{^}N)_3]$ or $[Ir(C\text{^}N)_2(XY)]^{n+}(A^-)_n$ (where A^- represents a monoanionic counterion, and n = 0, 1). A wide variety of bidentate XY ligands and cyclometalated (C^N) ligands have been coordinated to Ir(III) metal centers. The XY ligand may be neutral or anionic (Chart 3-2 (a) and (b) respectively), resulting in cationic or neutral complexes, respectively. Likewise, numerous aryl and heteroaryl bidentate C^N ligands have been used in homoleptic and heteroleptic complexes. Examples include phenylpyridine (ppy),[185, 188, 200] phenylpyrazole (ppz),[200,201] thienyl pyridine,[202,203] phenylthiophene,[204] phenylisoquinoline,[205,206] phenyl-imidazole,[207] and derivatives thereof, among others (Chart 3-3).

Chart 3-2

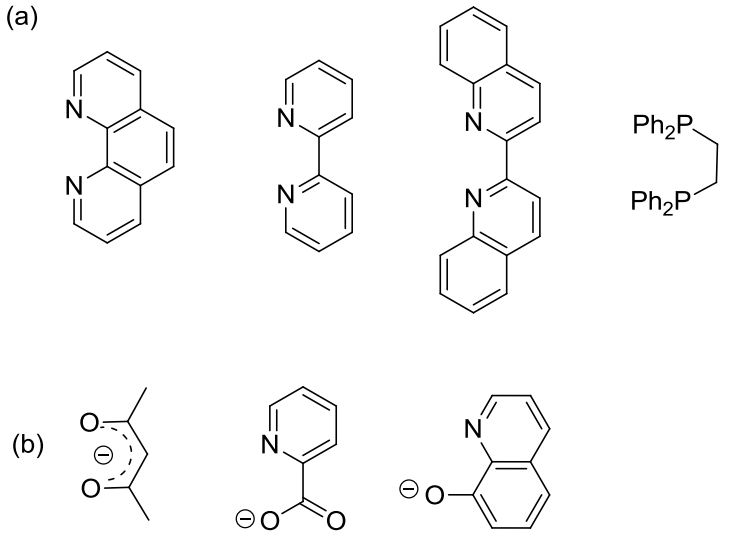

Chart 3-3

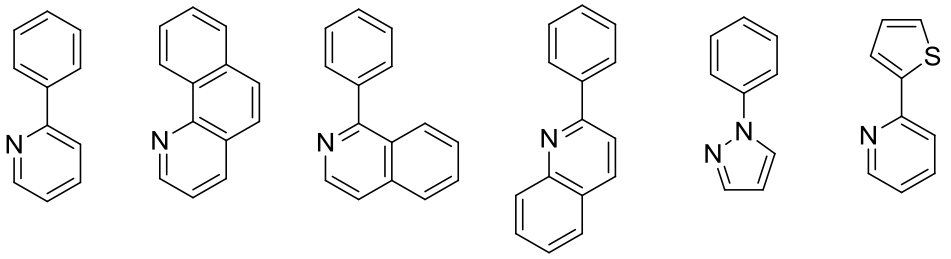

ppy **ppz**

$[Ir(C\hat{}N)_2(XY)]^{n+}$ (n=0,1) species can exist as various stereoisomers, however, the major stereoisomer is typically the one with the two cyclometalating carbon atoms mutually *cis*, and the nitrogen atoms on these ligands mutually *trans* (A, Scheme 3-1).

Scheme 3-1

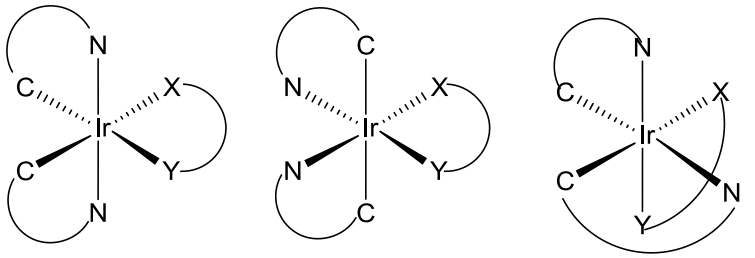

A **B** **C**

The substituents on the C^N ligand affect the emission energy of the complexes, as do the ancillary XY ligands. Further tuning is possible by adding electron donating or electron withdrawing substituents at various positions on the XY and/or C^N ligands. Therefore, a large number of possible complexes can be made by choosing different C^N and XY ligand combinations. This is useful in DSSC applications as it may allow for broader absorption across the visible spectrum, potentially leading to increased efficiency.

In this chapter, six new complexes using PT_3 as a ligand are described: $Ir(ppz)_2PT_3Cl$-*P*, $[Ir(ppz)_2PT_3$-*PS*$](PF_6)$, $Ir(ppz)_2PT_3$-*PC*, $Ir(ppy)_2PT_3Cl$-*P*, $[Ir(ppy)_2PT_3$-*PS*$](PF_6)$, and $Ir(pp)_2PT_3$-*PC* (Chart 3-4). The influence of binding mode of the ancillary PT_3 ligand on torsion angles, emission and excited state are investigated. The properties of these Ir complexes are compared to the Os complexes discussed in Chapter 2.

Chart 3-4

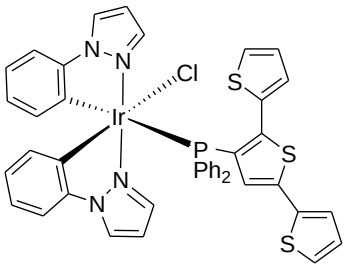

$Ir(ppz)_2PT_3Cl$-*P*
58

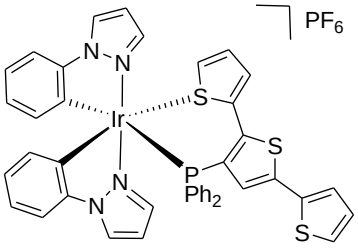

$[Ir(ppz)_2PT_3$-*PS*$](PF_6)$
59

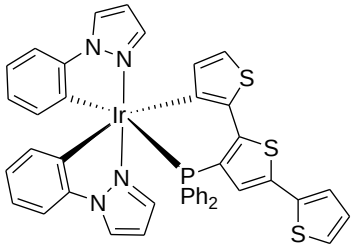

$Ir(ppz)_2PT_3$-*PC*
60

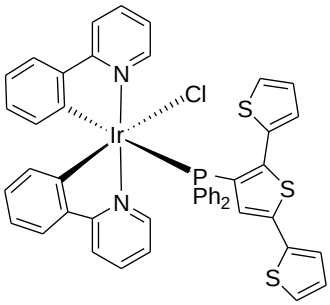

$Ir(ppy)_2PT_3Cl$-*P*
61

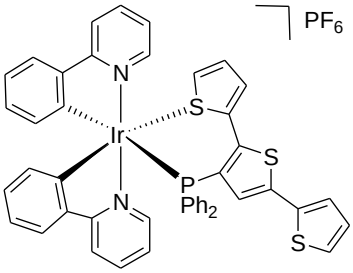

$[Ir(ppy)_2PT_3$-*PS*$](PF_6)$
62

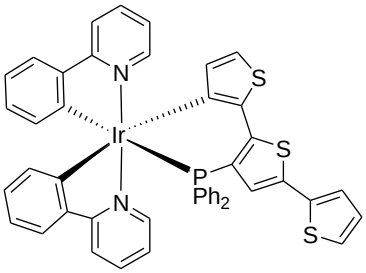

$Ir(ppy)_2PT_3$-*PC*
63

Section 3.2 – Experimental

Section 3.2.1 – General

All reactions were performed under N_2 (99.0%) or Ar (99.997%). The compounds PT_3,[109] $[Ir(ppz)_2Cl]_2$,[208] and $[Ir(ppy)_2Cl]_2$[208, 209] were synthesized according to literature procedures. All other reagents were purchased from Aldrich and Strem and used as received. ^1H and $^{31}P\{^1H\}$ NMR spectra were collected on either a Bruker AV-300 or AV-400 spectrometer. ^1H NMR spectra were referenced to residual solvent, and $^{31}P\{^1H\}$ NMR spectra referenced to external 85% H_3PO_4. ESI mass spectra were recorded on a Bruker Esquire-LC ion trap mass spectrometer equipped with an electrospray ion source. The solvent for the ESI-MS experiments was either methanol or dichloromethane/methanol and the concentration of the compound was ~10 μM. High resolution mass spectra were recorded on a Waters Micromass LCT time-of-flight mass spectrometer equipped with an electrospray ion source. CHN elemental analyses were performed using an EA1108 elemental analyzer, using calibration factors. The calibration factor was determined by analyzing a suitable certified organic standard (OAS) of a known elemental composition. All mass spectrometry and microanalysis results were obtained by the staff at the UBC Mass Spectrometry Centre. Cyclic voltammetry experiments were carried out on an Autolab PG STAT 12 potentiostat or a Pinechem potentiostat using a Pt disk working electrode, Pt mesh counter electrode and a silver wire reference electrode with 0.1 M $[(n\text{-}Bu)_4N]PF_6$ supporting electrolyte which was re-crystallized 3 times from ethanol and dried under vacuum at 100 °C for 3 days. Decamethylferrocene was used as an internal reference to correct the measured potentials with respect to the saturated calomel electrode (SCE). UV-vis spectra were obtained on a Varian Cary 5000 UV-Vis-NIR spectrophotometer in HPLC grade solvent. Emission spectra were obtained on a PTI Quantamaster fluorimeter. Transient absorption measurements and fluorescence lifetimes were carried out on an Princeton Instruments Spectra Pro 2300i Imaging Triple Grating Monochrometer/Spectrograph with a Hamamatsu Dynamic Range Streak Camera (excitation source: EKSPLA Nd:YAG laser, λ = 355 nm). Solutions of the complexes in CH_3CN having an optical density of 1 at 355 nm were prepared. The UV-vis spectra were obtained before and after each TA

experiment to ensure the bulk of the sample did not change, due to sample degradation or another process. Microwave reactions were carried out on a Biotage Initiator 2.5 microwave synthesizer.

Section 3.2.2 – Procedures

$Ir(ppz)_2PT_3Cl$-*P*, (58).

$[Ir(ppz)_2Cl]_2$ (0.045 g) and PT_3 (0.042 g) were added to a 2-5 mL microwave vial. EtOH (4 mL) was added and the mixture was stirred and sparged with N_2 for 5 minutes. The mixture was heated in a 2.2 GHz microwave synthesizer at 100°C for 30 minutes. Upon removal from the microwave, the mixture was centrifuged, and the supernatant was reduced in volume. A mixture of $Ir(ppz)_2PT_3Cl$-*P* and $[Ir(ppz)_2PT_3$-*PS*]Cl was obtained. The $Ir(ppz)_2PT_3Cl$-*P* was slightly soluble in ether. The mixture was washed thoroughly with ether, which was then removed by rotary evaporation, and the residue dissolved in DCM and layered with hexanes to produce yellow crystals of $Ir(ppz)_2PT_3Cl$-*P* (16.4 mg, 20 %). ^{1}H NMR (300 MHz, CD_2Cl_2): δ 5.82 (d, *J* = 7.3 Hz, 1H), 5.91 (t, *J* = 6.1 Hz, 1H), 6.24-6.29 (m, 1H), 6.32-6.39 (m, 2H), 6.48(d, *J* = 7.3 Hz, 1H), 6.56 (br.s., 1H), 6.69-6.83 (m, 2H), 6.91 (d, *J* = 5.5 Hz, 2H), 7.01-7.08 (m, 3H), 7.14 (d, *J* = 4.1 Hz, 2H), 7.20 (d, *J* = 9.1 Hz, 2H), 7.26 (d, *J* =5.9 Hz, 2H), 7.34-7.41 (m, 3H), 7.73 (s, 1H), 7.76-7.83 (m, 3H), 8.12-8.18 (m, 1H). $^{31}P\{^1H\}$ NMR (121 MHz, CD_2Cl_2): δ -15.6 (s). m/z $[M\text{-}Cl]^+$ 911. HRMS (ESI) Calcd for $C_{42}H_{31}N_4PS_3Ir$ (m/z $[M\text{-}Cl]^+$): 909.1055; Found: 909.1061. Anal. $C_{42}H_{31}ClIrN_4PS_3$ requires C, 53.29; H, 3.30; N, 5.92. Found C, 52.02; H, 3.50; N, 5.34%.

$[Ir(ppz)_2PT_3$-*PS*$](PF_6)$, (59).

$[Ir(ppz)_2Cl]_2$ (0.045 g) and PT_3 (0.042 g) were added to a 2-5 mL microwave vial along with $AgBF_4$ (0.018 g). EtOH (4 mL) was added and the mixture was stirred while sparging with N_2 for 5 minutes. The mixture was heated in a 2.2 GHz microwave synthesizer at 100°C for 30 minutes. Upon removal from the microwave, the mixture was centrifuged, and the supernatant was removed. The solid was rinsed and centrifuged again. The supernatant was combined, reduced in volume and added dropwise to an

aqueous ammonium hexafluorophosphate solution (0.284 g in 17 mL H_2O). After stirring for 30 minutes, the solid was collected by filtration and rinsed well with water and diethyl ether to yield 65.5 mg (71 %) of a yellow solid. ^{1}H NMR (300 MHz, CD_2Cl_2): δ 6.10 (ddd, *J* = 7.5, 5.1, 1.3 Hz, 1H), 6.20 (d, *J* = 7.5 Hz, 1H), 6.31 (t, *J* = 2.7 Hz, 1H), 6.38 (dd, *J* = 5.5, 0.9 Hz, 1H), 6.50 (d, *J* = 2.3, 1H), 6.58 (t, *J* = 2.6 Hz, 1H), 6.68-6.75 (m, 2H), 6.78-6.90 (m, 4H), 7.01-7.03 (m, 2H), 7.05-7.10 (m, 3 H), 7.12 (d, *J* = 2.5 Hz, 1H), 7.23 (d, *J* = 2.7 Hz, 1H), 7.26 (dd, *J* = 3.7, 1.1, 1H), 7.30 (d, *J* = 1.1 Hz, 1H), 7.31-7.36 (m, 3H), 7.37-7.45 (m, 3H), 7.49-7.56 (m, 1H), 7.62 (s, 1H), 7.78 (d, *J* = 1.8 Hz, 1H), 8.01 (d, *J* = 3.0 Hz, 1H). ^{31}P{^{1}H} NMR (121 MHz, CD_2Cl_2): δ -29.6 (s), -143.6 (septet, J_{PF} = 708 Hz, PF_6) m/z $[M\text{-}PF_6]^+$ 911. HRMS (ESI) Calcd for $C_{42}H_{31}N_4PS_3Ir$ (m/z $[M\text{-}PF_6]^+$): 909.1055; Found: 909.1049. Anal. $C_{42}H_{31}F_6IrN_4P_2S_3$ requires C, 47.77; H, 2.96; N, 5.31. Found C, 47.52; H, 3.05; N, 4.92%.

Ir(ppz)$_2$PT$_3$-*PC*, (60).

Complex **59** (50 mg) was added to a solution of NaOH (0.20 g) in degassed methanol (5 mL) and heated to reflux under nitrogen, with stirring, for 36 hours. The solution was cooled to room temperature, and the MeOH was removed *in vacuo*. The precipitate was redissolved in 2 mL MeOH, and the resulting solution added dropwise to a solution of ammonium hexafluorophosphate (0.284 g) in H_2O (17 mL) and stirred at room temperature for 30 minutes. The precipitate was filtered and washed with copious amounts of water and diethyl ether to yield 28 mg (65 %) of a yellow solid. ^{1}H NMR (300 MHz, CD_2Cl_2): δ 6.07-6.13 (m,2H), 6.37 (t, *J* = 2.6 Hz, 1H), 6.48 (d, *J* = 2.7 Hz, 1H), 6.49-6.57 (m, 3H), 6.59 (d, *J* = 4.8 Hz, 1H), 6.72-6.88 (m, 5H), 6.90-6.99 (m, 4H), 7.07-7.13 (m, 3H), 7.14-7.21 (m, 2H), 7.24-7.27 (m, 1H), 7.30-7.44 (m, 3H), 7.66-7.74 (m, 2H), 7.84 (d, *J* = 3.2 Hz, 1H), 7.97 (d, *J* = 2.7 Hz, 1H). ^{31}P{^{1}H} NMR (121 MHz, CD_2Cl_2): δ -17.9 (s), m/z $[M+H]^+$ 911. HRMS (ESI) Calcd for $C_{42}H_{31}N_4PS_3Ir$ (m/z $[M+H]^+$): 909.1055; Found: 909.1052. Anal. $C_{42}H_{30}IrN_4PS_3$ requires C, 55.43; H, 3.32; N, 6.16. Found C, 55.45; H, 3.55; N, 5.38%.

$Ir(ppy)_2PT_3Cl$-*P*, (61).

$[Ir(ppy)_2Cl]_2$ (0.045 g) and PT_3 (0.042 g) were added to a 2-5 mL microwave vial. EtOH (4 mL) was added and the mixture was stirred and sparged with N_2 for 5 minutes. The mixture was heated in a 2.2 GHz microwave synthesizer at 100°C for 30 minutes. Upon removal from the microwave, the mixture was centrifuged, and the supernatant was reduced in volume. A mixture of $Ir(ppy)_2PT_3Cl$-*P* and $[Ir(ppy)_2PT_3$-*PS*]Cl was obtained. The $Ir(ppy)_2PT_3Cl$-*P* was slightly soluble in ether. The mixture was washed thoroughly with ether, which was then removed by rotary evaporation, and the residue dissolved in DCM and layered with hexanes to produce yellow crystals of $Ir(ppy)_2PT_3Cl$-*P* (8.1 mg, 10 %). ^{1}H NMR (300 MHz, CD_2Cl_2): δ 5.74-5.82 (m,1H), 5.94 (d, *J* = 7.8 Hz, 1H), 6.18 (d, *J* = 3.0 Hz, 1H), 6.33 (dd, *J* = 5.0, 3.7 Hz, 1H), 6.52-6.58 (m, 1H), 6.68-6.77 (m, 2H), 6.86-6.93 (m, 5H), 7.00-7.10 (m, 7H), 7.17-7.25 (m, 4H), 7.37 (d, *J* = 3.4 Hz, 1H), 7.44-7.56 (m, 2H), 7.59 (d, *J* = 8.2 Hz, 1H), 7.64 (d, *J* = 8.0 Hz, 1H), 7.77-7.85 (m, 1H), 7.93-8.02 (m, 2H), 8.93 (d, *J* = 5.3 Hz, 1H), 9.19 (d, *J* = 5.9 Hz, 1H). $^{31}P\{^1H\}$ NMR (121 MHz, CD_2Cl_2): δ -14.0 (s). m/z $[M\text{-}Cl]^+$ 933. HRMS (ESI) Calcd for $C_{46}H_{33}N_2PS_3Ir$ (m/z $[M\text{-}Cl]^+$): 931.1150; Found: 931.1144. Anal. $C_{46}H_{33}ClIrN_2PS_3 \cdot H_2O$ requires C, 56.00; H, 3.58; N, 2.84. Found C, 55.75; H, 3.54; N, 2.76%

$[Ir(ppy)_2PT_3$-*PS*$](PF_6)$, (62).

$[Ir(ppz)_2Cl]_2$ (0.047 g), PT_3 (0.045 g) and with $AgBF_4$ (0.018 g) were added to a 2-5 mL microwave vial. EtOH (4 mL) was added and the mixture stirred and sparged with N_2 for 5 minutes. The mixture was heated in a 2.2 GHz microwave synthesizer at 100°C for 30 minutes. Upon removal from the microwave, the mixture was centrifuged, and the supernatant was removed. The solid was rinsed and centrifuged again. The supernatant was combined, reduced in volume and added dropwise to an aqueous ammonium hexafluorophosphate solution (0.284 g in 17 mL H_2O). After stirring for 30 minutes, the solid was collected by filtration and rinsed well with water and diethyl ether to yield 62 mg (66 %) of a yellow solid. ^{1}H NMR (400 MHz, CD_2Cl_2): δ 6.05-6.11 (m, 2H), 6.36 (d, *J* = 5.5 Hz, 1H), 6.70 (d, *J* = 7.9 Hz, 1H), 6.67 (d, *J* = 7.9 Hz, 1H), 6.73-6.78 (m, 2H), 6.80-6.92 (m, 3H), 7.01-7.08 (m, 6H), 7.12 (d, *J* = 3.4 Hz, 1H), 7.20-7.27 (m, 4H), 7.32 (td, *J* = 7.9, 5.3 Hz, 3H), 7.45 (t, *J* = 7.2 Hz, 1H), 7.50-7.57 (m, 1H), 7.63

(d, *J* = 7.9 Hz, 1H), 7.69 (d, *J* = 7.9 Hz, 1H), 7.72-7.77 (m, 1H), 7.81 (t, *J* = 7.9 Hz), 7.89 (d, *J* = 7.9 Hz, 1H), 8.06 (d, *J* = 5.8 Hz, 1H), 8.67 (d, *J* = 5.8 Hz, 1H). P{^{1}H} NMR (161 MHz, CD_2Cl_2): δ -23.0 (s), -143.6 (septet, J_{PF} = 708 Hz, PF_6) m/z $[M\text{-}PF_6]^+$ 933. HRMS (ESI) Calcd for $C_{46}H_{33}N_2PS_3Ir$ (m/z $[M\text{-}PF_6]^+$): 931.1150; Found: 931.1140. Anal. $C_{46}H_{33}F_6IrN_2P_2S_3$ requires C, 51.25; H, 3.09; N, 2.60. Found C, 51.54; H, 3.16; N, 2.38 %.

Ir(ppy)$_2$PT$_3$-*PC*, (63).

Complex **62** (50 mg) was added to a solution of NaOH (0.20 g) in degassed methanol (5 mL) and heated to reflux under nitrogen, with stirring, for 36 hours. The solution was cooled to room temperature, and the MeOH was removed *in vacuo*. The precipitate was redissolved in 2 mL MeOH, the resulting solution was added dropwise to a solution of ammonium hexafluorophosphate (0.284 g) in H_2O (17 mL) and stirred at room temperature for 30 minutes. The precipitate was filtered and washed with copious amounts of water and diethyl ether to yield 18 mg (42 %) of yellow solid. ^{1}H NMR (300 MHz, CD_2Cl_2): δ 6.06 (dd, *J* = 7.5, 4.80 Hz, 1H), 6.29-6.35 (m, 1H), 6.42-6.50 (m, 3H), 6.62-6.68 (m, 2H), 6.75-6.84 (m, 7H), 6.85-6.92 (m, 1H), 6.96-7.04 (m, 2H), 7.09 (d, *J* = 3.7 Hz, 1H), 7.15 (d, *J* = 5.0 Hz, 1H), 7.24-7.30 (m, 2H), 7.37-7.43 (m, 2H), 7.50-7.54 (m, 1H), 7.57-7.64 (m, 4H), 7.72 (dd, J = 9.7, 8.3 Hz, 2H), 7.81 (d, J = 8.2 Hz, 1H), 8.73 (d, *J* = 5.9 Hz, 1H). ^{31}P{^{1}H} NMR (121 MHz, CD_2Cl_2): δ -16.1 (s), m/z $[M+H]^+$ 933. HRMS (ESI) Calcd for $C_{46}H_{33}N_2PS_3Ir$ (m/z $[M+H]^+$): 931.1150; Found: 931.1151. Anal. $C_{46}H_{32}IrN_2PS_3 \cdot 2CH_3OH$ requires C, 57.87; H, 4.05; N, 2.81. Found C, 57.73; H, 3.73; N, 3.14%.

Section 3.2.3 – X-Ray Crystallography

Suitable crystals of Ir(ppz)$_2$PT$_3$Cl-*P*, (**58**), [Ir(ppz)$_2$PT$_3$-*PS*](BF$_4$), (**59**), Ir(ppz)$_2$PT$_3$-*PC*, (**60**), and Ir(ppy)$_2$PT$_3$Cl-*P*, (**61**), were grown from solution. The X-ray data were collected and solved by Dr. B.O. Patrick. In all cases, the crystals were mounted on a glass fiber and a Bruker APEX DUO diffractometer with graphite monochromated Mo-Kα radiation was used for all measurements. Data were collected

and integrated using the Bruker SAINT[113] software package. Data were corrected for absorption effects using the multi-scan technique (SADABS).[116] The data were corrected for Lorentz and polarization effects. The structures were solved by direct methods.[118] Solid-state diagrams were visualized using Mercury.[119]

$Ir(ppz)_2PT_3Cl$-*P*, (58).

Data were collected in a series of ϕ and ω scans in 0.5° oscillations using 5.0 second exposures. The crystal to detector distance was 39.96 mm. The data were collected to a maximum 2θ value of 56.3°. Of the 61356 reflections that were collected, 9518 were unique (R_{int} = 0.063); equivalent reflections were merged. Data were corrected for absorption effects using multi-scan the technique (SADABS),[116] with minimum and maximum transmission coefficients of 0.585 and 0.681, respectively. The material crystallizes with one thiophene ring (C9→S3) disordered in two orientations by rotation about the C8 – C9 bond. All non-hydrogen atoms except C9B were refined anisotropically. All hydrogen atoms were placed in calculated positions. The final cycle of full-matrix least squares refinement[120] on F^2 was based on 9518 reflections and 526 variable parameters and converged (largest parameter shift was 0.00 times its esd).

$[Ir(ppz)_2PT_3$-*PS*$](BF_4)$, (59).

Data were collected in a series of ϕ and ω scans in 0.5° oscillations using 3.0 second exposures. The crystal to detector distance was 40.08 mm. The data were collected to a maximum 2θ value of 60.1°. Of the 78800 reflections that were collected, 13494 were unique (R_{int} = 0.058); equivalent reflections (Excluding Friedel pairs) were merged. Data were corrected for absorption effects using multi-scan the technique (SADABS),[116] with minimum and maximum transmission coefficients of 0.725 and 0.935, respectively. The material crystallizes with two molecules of CH_2Cl_2 in the asymmetric unit. One solvent molecule is disordered, and was modeled in three orientations. Restraints were applied to maintain reasonable geometries for all three fragments, and the ISOR and SIMU commands were employed to maintain reasonable anisotropic displacement parameters. All non-hydrogen atoms were refined anisotropically. All hydrogen atoms were placed in calculated positions. The final cycle

of full-matrix least squares refinement[120] on F^2 was based on 13494 reflections and 611 variable parameters and converged (largest parameter shift was 0.00 times its esd).

$Ir(ppz)_2PT_3$-*PC*, (60).

Data were collected in a series of ϕ and ω scans in 0.50° oscillations using 3.0 second exposures. The crystal to detector distance was 37.87 mm. The data were collected to a maximum 2θ value of 60.2°. Of the 62011 reflections that were collected, 10385 were unique (R_{int} = 0.034); equivalent reflections were merged. Data were corrected for absorption effects using multi-scan the technique (SADABS),[116] with minimum and maximum transmission coefficients of 0.330 and 0.447, respectively. All non-hydrogen atoms were refined anisotropically. All hydrogen atoms were placed in calculated positions. The final cycle of full-matrix least squares refinement[120] on F^2 was based on 10385 reflections and 450 variable parameters and converged (largest parameter shift was 0.00 times its esd).

$Ir(ppy)_2PT_3Cl$-*P*, (61).

Data were collected in a series of ϕ and ω scans in 0.5° oscillations using 3.0 second exposures. The crystal to detector distance was 40.11 mm. The data were collected to a maximum 2θ value of 60.2°. Of the 52461 reflections that were collected, 11558 were unique (R_{int} = 0.062); equivalent reflections were merged. Data were corrected for absorption effects using multi-scan the technique (SADABS),[116] with minimum and maximum transmission coefficients of 0.754 and 0.864, respectively. Two of the thiophene rings are disordered and each was modeled in two orientations. The atoms of the major disordered component were refined anisotropically, while the atoms of the minor disordered components were refined isotropically. All hydrogen atoms were placed in calculated positions. The material also crystallizes with one molecule of CH_2Cl_2 in the asymmetric unit. The absolute configuration was determined on the basis of the refined Flack X-parameters.[210, 211] The final cycle of full-matrix least squares refinement[120] on F^2 was based on 11558 reflections and 543 variable parameters and converged (largest parameter shift was 0.00 times its esd).

Section 3.3 – Results and Discussion

Section 3.3.1 – Synthesis

Cyclometalated Ir (III) complexes are typically made by one of three methods (Scheme 3-2). One technique involves reacting $Ir(acac)_3$ with 3 equivalents of ligand in refluxing glycerol.[212] *Tris* cyclometalated complexes can also be prepared from a β-diketonate derivative, of the type [Ir(C^N)(O^O)] by heating the Ir complexes with 2-3 equivalents of C^N ligand in refluxing glycerol.[185,186] A third method, similar to the second, uses chloro-bridged dimers of the type $[Ir(C^N)_2Cl]_2$.[213] Early investigations reported needing 30 molar equivalents of cyclometallating ligand to make homoleptic complexes from the dimer,[214] but 2-6 equivalents are commonly required in more recent literature.[200, 212, 215]

Scheme 3-2

1) $Ir(acac)_3 + 3\ HC^N \xrightarrow{\text{glycerol, } N_2\text{, reflux}} Ir(C^N)_3 + 3\ acacH$

2) $Ir(C^N)_2(O^O) + HC^N \xrightarrow{\text{glycerol, } N_2\text{, reflux}} Ir(C^N)_3 + O^OH$

3) $[Ir(C^N)_2Cl]_2 + 2\ HC^N \xrightarrow{\text{glycerol, } N_2\text{, reflux}} 2\ Ir(C^N)_3 + 2\ KCl + H_2O + CO_2$

Typically, the chloro-bridged dimers and β-diketonate derivatives are easily prepared in high yield from $IrCl_3 \bullet H_2O$. Additionally, with these methods of preparation, homoleptic or heteroleptic complexes can be synthesized. This can be accomplished either through use of a different cyclometalating ligand, or another ancillary bidentate ligand. Synthesis of *tris*-heteroleptic complexes requires an alternative method.[216] Recently the chloro-bridged dimers have been made in even higher yield using microwave irradiation.[208] Microwave reactions can drastically decrease the reaction times, resulting in increased yield and purity of the desired product by reducing side reactions. As there is direct and uniform heating from molecular friction, outside heating sources are not required. Microwave reactions can occur under pressure, and can bring lower boiling solvents above their boiling points at higher pressures, which can result in

increased reaction rates. The chloro-bridged dimers were synthesized as precursors for the desired Ir complexes. These dimers are known and characterization data was consistent with previously published work.[209, 217]

Initial attempts to synthesize [Ir(ppz)$_2$PT$_3$-*PS*](PF$_6$) resulted in a mixture of products. The reaction of the chloro-bridged Ir dimer and PT$_3$ yielded Ir(ppz)$_2$PT$_3$Cl-*P* and [Ir(ppz)$_2$PT$_3$-*PS*]Cl. The formation of a mono-chlorinated species was not surprising here, as it has been reported that breaking the last Ir – Cl bond requires a significant barrier to be overcome.[218] It was previously observed that the chloro-bridged dimers cleave to produce a neutral mono-chloro, mono-solvated complex. Removal of the final chloro group was only achieved when Ag^+ was added.[218] Adding silver tetrafluoroborate to the reaction mixture here, followed by salt metathesis with ammonium hexafluorophosphate, resulted in a single product, [Ir(ppz)$_2$PT$_3$-*PS*](PF$_6$), (**59**), with the thiophene ring bound to the Ir via the sulfur. McGee and Mann previously reported a complex containing a thienyl-pyridine ligand, bound to the Ir in an S^N motif, and upon heating (80-100 °C) the complex isomerized to the cyclometalated C^N species. Carrying out the reaction here at 100 °C yielded the [Ir(ppz)$_2$PT$_3$-*PS*](PF$_6$) complex; cyclometalation did not occur until the *PS* bound complex and NaOH were dissolved in methanol and heated to reflux (Scheme 3-3). Adding trifluoroacetic acid to the cyclometalated (*PC* bound) Ir(ppz)$_2$PT$_3$-*PC* complex immediately resulted in reversion to the original complex (Figure 3-1). Heating to reflux with base resulted in a change in coordination mode to the *PC* complex once again. After carrying out this switching reaction several times, free ligand was also observed. The ligand could be removed by rinsing with ether. The ppy complexes were prepared analogously. Under these conditions, there was no evidence of the pyrazole or pyridine ring undergoing a change in binding mode.

Scheme 3-3

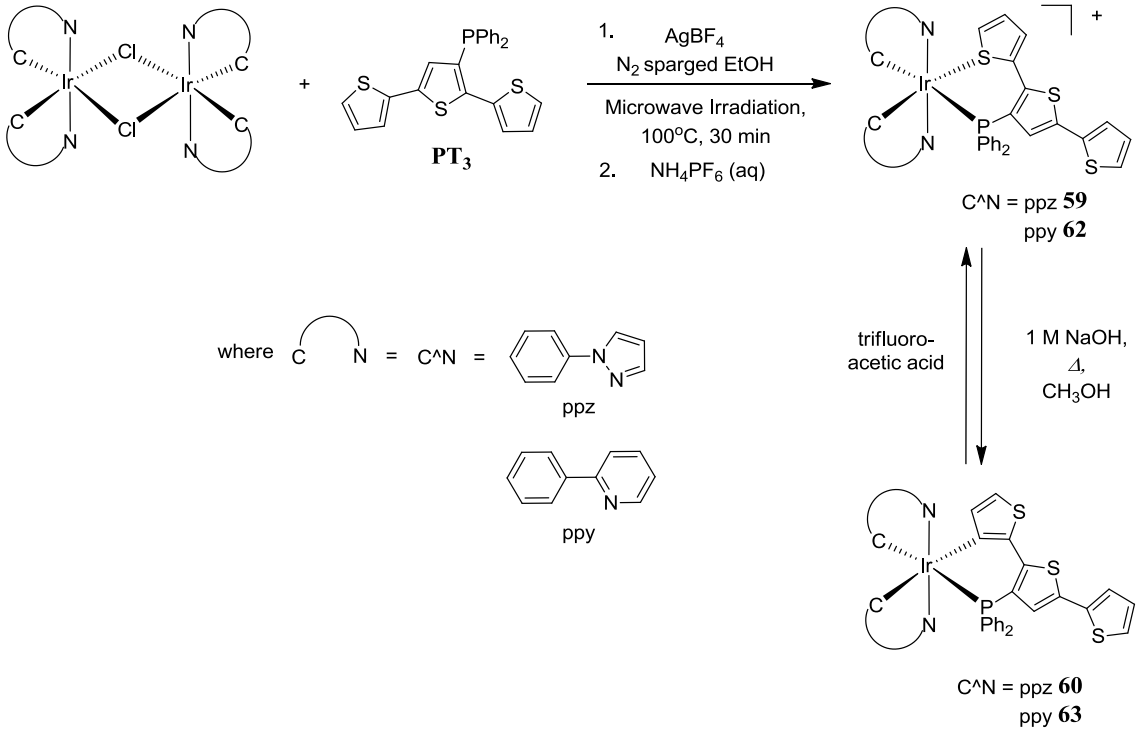

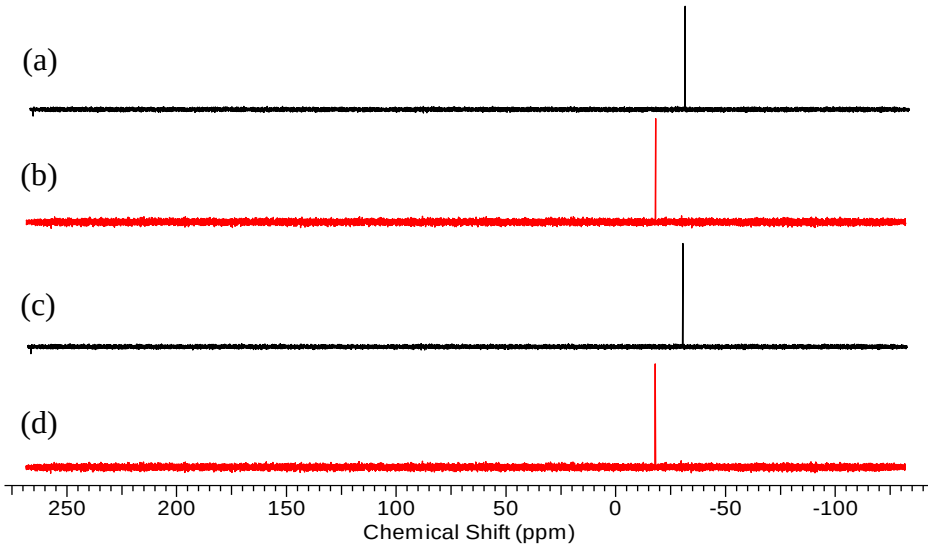

Figure 3-1 $^{31}P\{^{1}H\}$ NMR spectra showing switching between $[Ir(ppz)_2PT_3\text{-}PS](PF_6)$, (**59**), ((a) and (c)) and $Ir(ppz)_2PT_3\text{-}PC$, (**60**), ((b) and (d)). Heating the *PS* bound complex (a) to reflux with base produced the *PC* bound complex (b). Addition of trifluoroacetic acid resulted in the sample switching back to the *PS* bound complex (c). Finally, heating to reflux with base again yielded the *PC* complex (d).

Section 3.3.2 – Solid-State Molecular Structures

Crystals of some of the cyclometalated iridium complexes suitable for X-ray diffraction were grown from appropriate solvents. The structures demonstrate the effects of the binding mode of the terthiophene ligand on the torsion angles of the thiophene rings and the metal – phosphorous distance. In all the solid-state structures, the Ir(III) metal center is in a slightly distorted octahedral environment.

Single crystals of $Ir(ppz)_2PT_3Cl$-*P* were grown from a CH_2Cl_2 – hexanes solution, and the solid-state structure is shown in Figure 3-2. Disorder was present in the thiophene ring containing S3. The ppz ligands are bound with the nitrogen atoms *trans* to one another, while the bound carbon atoms are *cis* with respect to the Ir(III) center, (A, Scheme 3-1) as they are arranged in the dimer. This bonding motif was observed in all three solid-state structures containing the ppz ligand. All Ir – C and Ir – N bond lengths are similar to those in previously reported complexes.[185, 215, 219] In $Ir(ppz)_2PT_3Cl$-*P*, the Ir – Cl bond (2.4716(9) Å, Table 3-1) is longer than some of those reported, but falls within the average range for Ir – Cl bonds *trans* to a carbon. This difference in length is presumably due to the trans effect of a cyclometalating ligand. The Ir – P distance of 2.4075(10) Å is quite typical. The torsion angles between adjacent thiophene rings of 45.3(4)° and 136.2 (14)° (Table 3-1) are less than the calculated value for terthiophene (147.6°).[220] This indicates less π-orbital overlap of the adjacent thiophene rings due to their decreased co-planarity. Weak π-stacking is observed between N1 ppz ring and the C19 phenyl ring (distance between centroids = 3.552 Å).

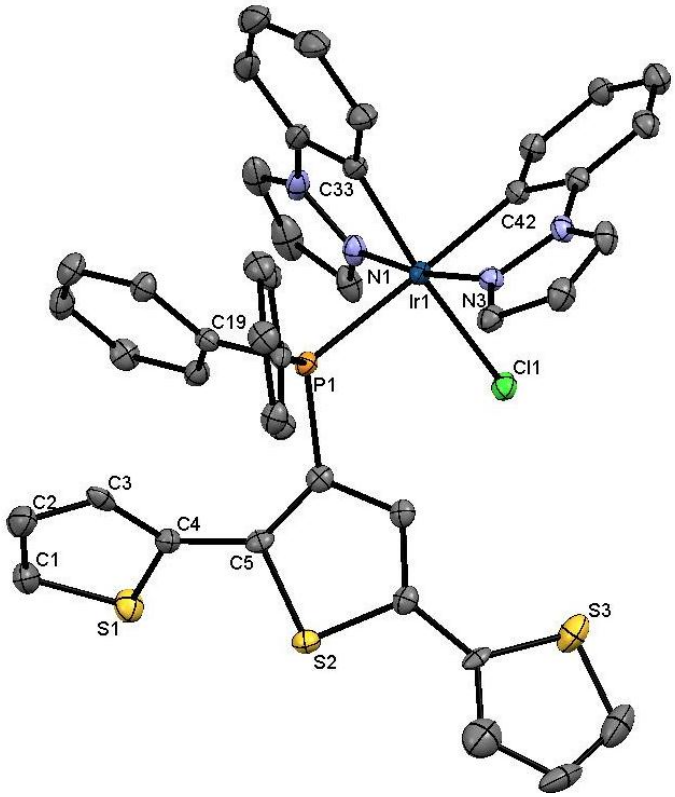

Figure 3-2 Solid-state structure of Ir(ppz)$_2$PT$_3$Cl-*P*, (**58**). Hydrogen atoms and solvent in lattice removed for clarity. Thermal ellipsoids are drawn at 50% probability.

Table 3-1 Selected bond lengths and angles for Ir(ppz)$_2$PT$_3$Cl-*P*,(**48**).

Bond Lengths (Å)			
Ir1 – Cl1	2.4716(9)	S1 – C1	1.704(4)
Ir1 – P1	2.4075(10)	C1 – C2	1.360(6)
Ir1 – N1	2.026(3)	C2 – C3	1.405(6)
Ir1 – N3	2.037(3)	C3 – C4	1.420(5)
Ir1 – C33	2.016(4)	C4 – S1	1.727(4)
Ir1 – C42	2.057(4)	C4 – C5	1.464(5)
Torsion Angles (°)			
S1 – C4 – C5 – S2	45.3(4)	S2 – C8 – C9 – S3	136.2(14)

Single crystals of [Ir(ppz)$_2$PT$_3$-*PS*](BF$_4$) were grown from a CH_2Cl_2 – hexanes solution, and the solid-state structure is shown in Figure 3-3. Thiophene has previously

been shown to weakly coordinate to Ir(III) through its sulfur atom,[204, 218] although it more commonly coordinates via carbon.[203, 221, 222] The Ir – S bond was 2.4402 Å in length (Table 3-2), which is long, but in the range expected for a weakly coordinating atom. Other S bound thiophene rings to Ir have a similar bond length.[218, 223-226] The strong Ir – C bond in the ppz ligands facilitates and stabilizes the thiophene coordination, allowing for the CˆS or non-cyclometallating (NˆS) S bound species.[204] The sulfur of the S-bound thiophene ring adopts an sp^3 hybridization, resulting in the thiophene ring being tilted out of the equatorial plane. The tilt angle of the thiophene away from the Ir – S bond is 59.2° in the $[Ir(ppz)_2PT_3\text{-}PS](PF_6)$ complex. This tilting reorients the lone pair of electrons on the sulfur, allowing for a reduction in the unfavorable π antibonding interactions.[150, 151] The coordination of a second thiophene ring to the Ir center greatly affects the torsion angles. The S1 – C4 – C5 – S2 and the S2 – C8 – C9 – S3 torsion angles are 163.4(2)° and 167.7(2)°, respectively. The increased co-planarity of the rings indicates more π – orbital overlap. Weak π-stacking may occur between the tilted thiophene ring (containing S1) and the ppz ring (containing N4) (distance between centroids = 3.767 Å) as well as between the N1 ppz ring and the C13 phenyl ring (3.790 Å).

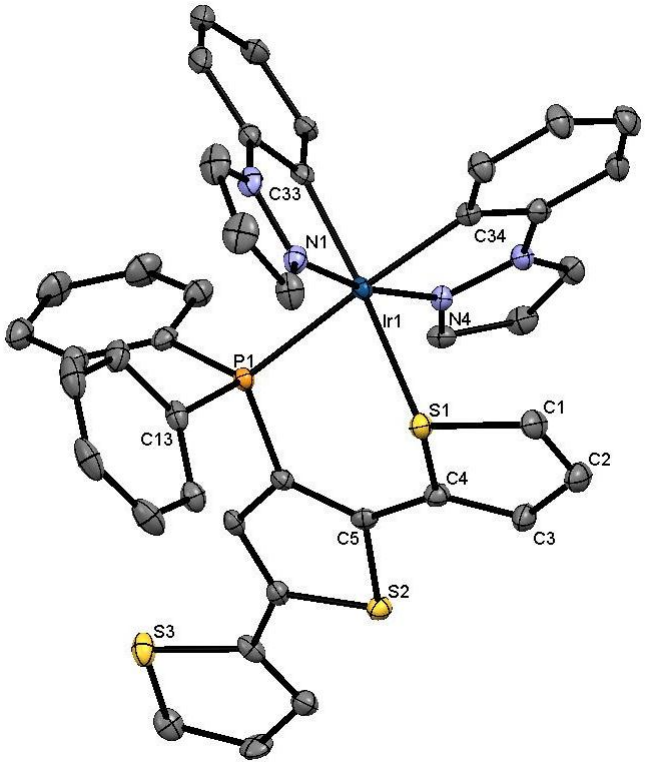

Figure 3-3 Solid-state structure of [Ir(ppz)$_2$PT$_3$-*PS*](BF$_4$), (**59**). Hydrogen atoms, counterions, and solvent in lattice removed for clarity. Thermal ellipsoids are drawn at 50% probability.

Table 3-2 Selected bond lengths and angles for [Ir(ppz)$_2$PT$_3$-*PS*](BF$_4$), (**59**).

Bond Lengths (Å)			
Ir1 – S1	2.4402(10)	S1 – C1	1.739(4)
Ir1 – P1	2.3746(10)	C1 – C2	1.338(6)
Ir1 – N1	2.028(3)	C2 – C3	1.428(6)
Ir1 – N4	2.045(3)	C3 – C4	1.369(5)
Ir1 – C33	2.023(4)	C4 – S1	1.742(4)
Ir1 – C34	2.059(4)	C4 – C5	1.445(5)
Torsion Angles (°)			
S1 – C4 – C5 – S2	163.4(2)	S2 – C8 – C9 – S3	167.7(2)

The Ir – S bond length of [Ir(ppz)$_2$PT$_3$-*PS*](BF$_4$) (2.4402(10) Å) is significantly longer than the Os – S bond (2.3543(11) Å) in the [Os(bpy)$_2$PT$_3$-*PS*](PF$_6$)$_2$ structure (**54**, Chapter 2)), as is the metal – P bond. However, the tilt angle of the thiophene ring plane away from the metal – S bond is almost identical. The torsion angle of the two bound thiophene rings is larger in the Ir complex compared to the Os complex (163.4(2)° vs 154.9(3)°). Again, the increased co-planarity of the rings results in increased π-orbital overlap of the adjacent thiophene rings.

Single crystals of Ir(ppz)$_2$PT$_3$-*PC* were grown from a MeOH solution (Figure 3-4). The Ir – C1 (carbon of the thiophene ring) bond length of 2.1318(19) Å is slightly longer, but comparable to other complexes where a thiophene ring is bonded to an Ir(III) center via a carbon.[218, 222, 223] This bond is longer than the other Ir – C bonds in the complex (to the ppz), suggesting a destabilized bonding orbital.[204] There are only a few examples known where a cyclometalated C^P ligand is coordinated to an Ir(III) center in a bidentate fashion.[227, 228,229] Ir – P bonds 2.248 to 2.336 Å in length for cyclometalated ligands have been reported. Ir – P bonds that are not in bidentate ligands have been shown to be longer, up to 2.426(2) Å in complexes such as Ir(ppy)$_2$Cl(PPh$_3$).[219] In Ir(ppz)$_2$PT$_3$-*PC*, the torsion[120] angles are 13.83° and 164.26°. The thiophene rings become more co-planar once a second ring is also bound to the metal (from Ir(ppz)$_2$PT$_3$Cl-*P* (135°) to [Ir(ppz)$_2$PT$_3$-*PS*](BF$_4$) and Ir(ppz)$_2$PT$_3$-*PC* (165°)) and the Ir – P bond gets shorter (from 2.4075(10) to 2.3203(5) Å). The tilt of the carbon bound thiophene ring away from the Ir – C bond is 5.68° in the Ir(ppz)$_2$PT$_3$-*PC* complex. Weak π-stacking is observed between the N3 ppz ring and the C13 phenyl ring (distance between centroids = 3.526 Å).

Comparing Ir(ppz)$_2$PT$_3$-*PC* to [Os(bpy)$_2$PT$_3$-*PC*](PF$_6$) (Chapter 2), there are several differences. The metal – carbon and metal – phosphorous bonds are longer in the Ir(III) complex. Additionally, the torsion angle of the two bound thiophene rings are more co-planar in the iridium complex, but the torsion angle with the unbound thiophene indicates greater co-planarity for the osmium complex. The tilt angle of the bound ring away from the metal – carbon bond is almost identical for Ir(ppz)$_2$PT$_3$-*PC* and [Os(bpy)$_2$PT$_3$-*PC*](PF$_6$).

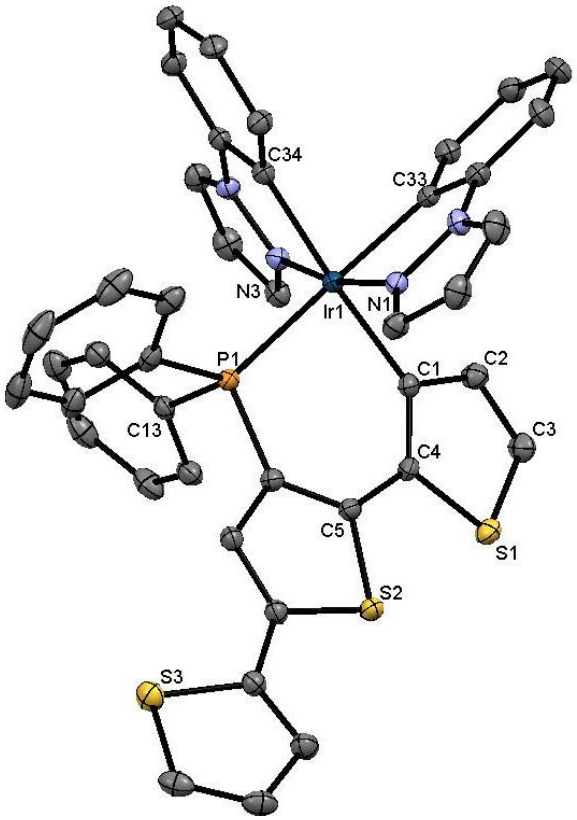

Figure 3-4 Solid-state structure of Ir(ppz)$_2$PT$_3$-*PC*, (**60**). Hydrogen atoms removed for clarity. Thermal ellipsoids drawn at 50% probability.

Table 3-3 Selected bond lengths and angles for Ir(ppz)$_2$PT$_3$-*PC*, (**60**).

Bond Lengths (Å)			
Ir1 – C1	2.1318(19)	C1 – C2	1.426(3)
Ir1 – P1	2.3203(5)	C2 – C3	1.335(3)
Ir1 – N1	2.0324(16)	C3 – S1	1.709(2)
Ir1 – N3	2.0235(16)	S1 – C4	1.7447(19)
Ir1 – C33	2.0546(19)	C4 – C1	1.387(3)
Ir1 – C34	2.0794(19)	C4 – C5	1.451(3)
Torsion Angles (°)			
S1 – C4 – C5 – S2	13.8(2)	S2 – C8 – C9 – S3	164.26(11)

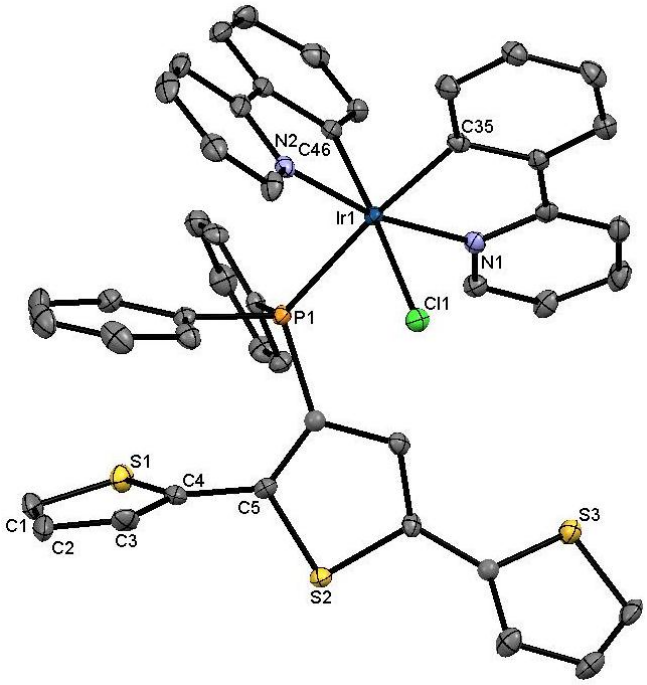

Figure 3-5 Solid-state structure of $Ir(ppy)_2PT_3Cl$-*P*, (**61**). Hydrogen atoms and solvent in lattice are removed for clarity. Thermal ellipsoids drawn at 50% probability.

For comparison, a single crystal of $Ir(ppy)_2PT_3Cl$-*P* was also obtained (Figure 3-5), grown from a CH_2Cl_2 – hexanes solution. Disorder was present in two of the thiophene rings (those not bound to the metal center, containing S1 and S3). While very similar to the analogous ppz complex, some differences in bond lengths and angles are observed. In general, most bonds are slightly longer in this complex. The Ir – Cl bond (2.4965(9)) Å) is still within the average range for Ir – Cl bonds *trans* to a carbon. The torsion angles between adjacent thiophene rings of 99.8(3)° and 139.2 (2)° (Table 3-4) indicate that one ring is almost entirely out of plane with the other and therefore there is less π-orbital overlap.

Table 3-4 Selected bond lengths and angles for $Ir(ppy)_2PT_3Cl$-*P*, (**61**).

Bond Lengths (Å)			
Ir1 – Cl1	2.4965(9)	S1 – C1	1.711(5)
Ir1 – P1	2.4218(9)	C1 – C2	1.354(9)
Ir1 – N1	2.062(3)	C2 – C3	1.403(8)
Ir1 – N2	2.050(3)	C3 – C4	1.351(7)
Ir1 – C35	2.047(3)	C4 – S1	1.730(4)
Ir1 – C46	2.007(3)	C4 – C5	1.482(4)
Torsion Angles (°)			
S1 – C4 – C5 – S2	99.8(3)	S2 – C8 – C9 – S3	139.5(2)

Section 3.3.3 – Cyclic Voltammetry

The electrochemical properties of $[Ir(ppz)_2PT_3$-*PS*$](PF_6)$, $Ir(ppz)_2PT_3$-*PC*, $[Ir(ppy)_2PT_3$-*PS*$](PF_6)$, and $Ir(ppy)_2PT_3$-*PC* were probed at room temperature using cyclic voltammetry. Each complex shows three irreversible oxidation waves (Table 3-5). Commonly for cyclometalated iridium complexes the HOMO is centered on the metal with substantial contribution from the ligand.[222] The difference in oxidation potentials between the *PS* bound and *PC* bound complexes indicates the HOMO is affected by the binding mode of the PT_3 ligand. Unfortunately, reliable reduction potentials could not be obtained for these complexes. Cyclic voltammetry experiments were not carried out on $Ir(ppz)_2PT_3Cl$-*P* and $Ir(ppy)_2PT_3Cl$-*P* due to difficulty in obtaining sufficient amounts of pure material.

The cyclic voltammograms of the $Ir(ppz)PT_3$ complexes are shown in Figure 3-6 while the analogous ppy complexes are shown in Figure 3-7. The first oxidation potential is assigned to a PT_3 based oxidation, with the others believed to be mixed metal – phenyl based and mixed metal – PT_3 based oxidations. Although, as $Ir(ppz)_3$ and $Ir(ppy)_3$ exhibit similar oxidation potentials to the first oxidation of the *PC* bound complexes,[215, 230] some contribution of the metal or metal – phenyl moiety cannot be entirely ruled out. The voltammograms of the *PS* bound complexes are similar, as are the voltammograms for

the *PC* bound complexes. The second oxidation is not as apparent in the ppz complexes as it is for the ppy complexes, suggesting the second oxidation involves the C^N ligands. Coordination of the PT_3 ligand in the *PC* binding mode results in a lowering of the oxidation potentials. This may be partly due to the more co-planar arrangement of the thiophene rings (compared to in the *PS* coordination) allowing for easier π donation, which is reflected in the oxidation potentials.[204] Additionally, in the *PC* bound complex, the ligand has a formal negative charge, compared to the *PS* bound complex where the ligand is formally neutral. The negative charge on the ligand in the *PC* bound complex is expected to lead to lower ligand-based oxidation potentials. This is also echoed in the lower energy transition observed in the absorption spectra (see below). Comparing the $[Ir(ppz)_2PT_3$-*PS*$](PF_6)$ and $[Ir(ppy)_2PT_3$-*PS*$](PF_6)$ complexes, as well as the $Ir(ppz)_2PT_3$-*PC* and $Ir(ppy)_2PT_3$-*PC* complexes it is observed that oxidations of the ppz complex occur at more positive potentials than those of the ppy complex. This may be due to the more electron-withdrawing character of the pyrazole ring compared to the pyridine ring. DFT calculations would be beneficial to support the assignment of these oxidation waves.

Table 3-5 Cyclic voltammetry data of $[Ir(ppz)_2PT_3\text{-}PS](PF_6)$, (**59**), $Ir(ppz)_2PT_3\text{-}PC$, (**60**), $[Ir(ppz)_2PT_3\text{-}PS](PF_6)$, (**62**), and $Ir(ppz)_2PT_3$-PC (**63**).[a]

Compound	E_p ±0.01 V vs. SCE
$[Ir(ppz)_2PT_3\text{-}PS](PF_6)$ (**59**)	+1.35
	+1.60
	+1.85
$Ir(ppz)_2PT_3\text{-}PC$(**60**)	+0.82
	+1.21
	+1.31
$[Ir(ppy)_2PT_3\text{-}PS](PF_6)$ (**62**)	+1.27
	+1.47
	+1.75
$Ir(ppy)_2PT_3\text{-}PC$ (**63**)	+0.71
	+1.07
	+1.29

[a]Measurements carried out in CH_3CN solution containing 0.1 M $[(n\text{-}Bu)_4N]PF_6$ supporting electrolyte.

Attempts to electropolymerize these complexes proved unsuccessful. The steric bulk of the diphenylphosphine moiety may prevent the complexes from oxidatively coupling at the terminal α-positions of the PT_3 backbone. The use of a longer oligomer could remove some of the steric bulk from the α-position of the terminal thiophenes which may allow for electrochemical polymerization.

The oxidation peak observed for $[Os(bpy)_2PT_3\text{-}PS](PF_6)_2$ (1.23 V (vs SCE), Chapter 2) is similar to that obtained for the $[Ir(ppy)_2PT_3$-PS$](PF_6)$ complex. The $[Os(bpy)_2PT_3\text{-}PC](PF_6)$ complex had 2 reversible oxidation peaks (0.28 and 0.95 V (vs SCE), Chapter 2) The higher oxidation potentials for the Ir (III) complexes may be due to a larger ionic charge (compared to Os(II)), making the metal centered oxidation more difficult.[197] The overall charge of the complexes (+2 and +1 for the Os(II) and Ir(III) *PS*

bound complexes, respectively, and +1 and for neutral *PC* bound complexes) did not have an effect on the ability of these complexes to electropolymerize.

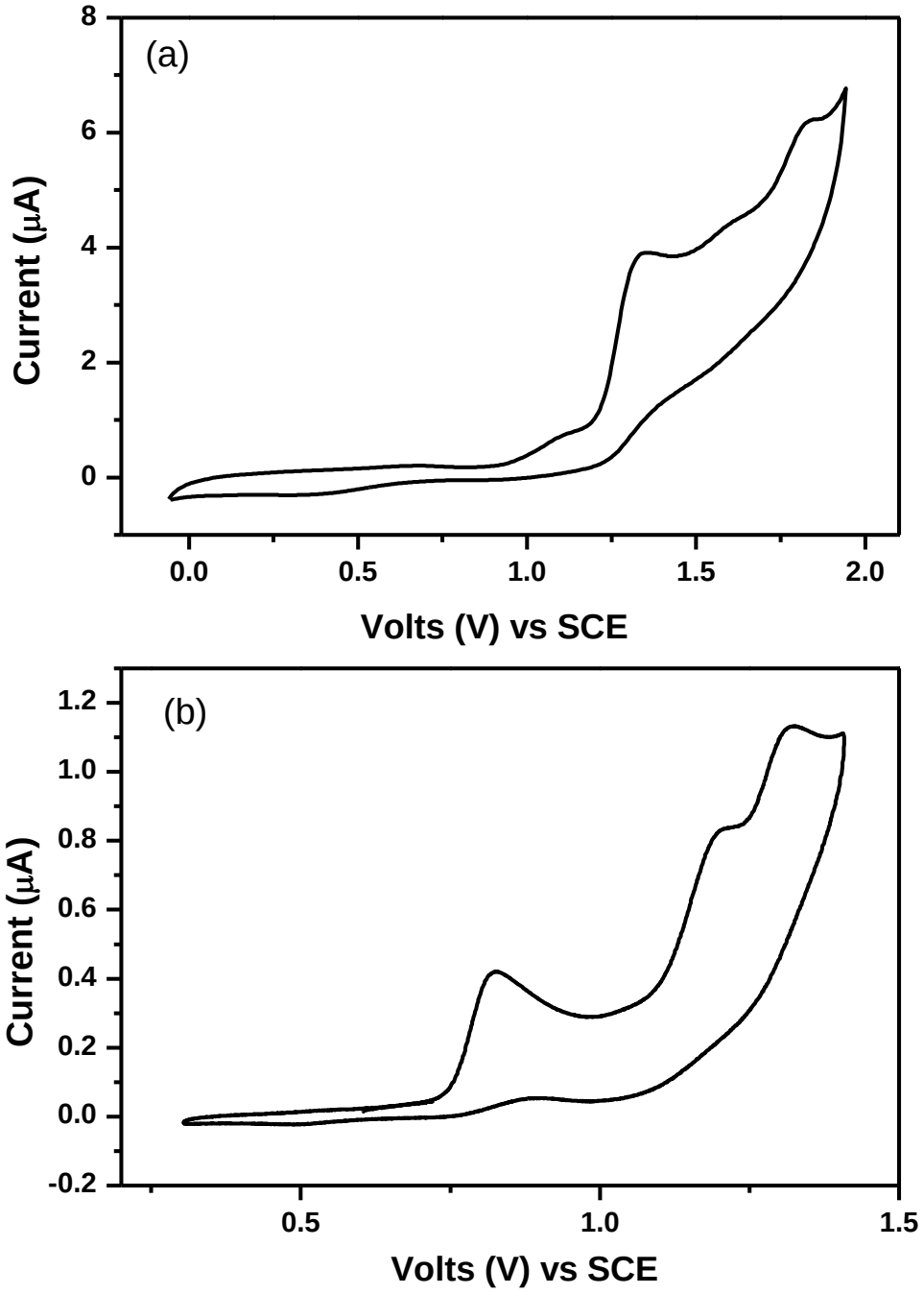

Figure 3-6 Cyclic voltammetry of (a) $[Ir(ppz)_2PT_3\text{-}PS](PF_6)$, (**59**), and (b) $Ir(ppz)_2PT_3\text{-}PC$, (**60**), on a Pt disk electrode (scan rate 100 mv/s), electrolyte = 0.1 M $[n\text{-}Bu_4N](PF_6)$, solvent = CH_3CN.

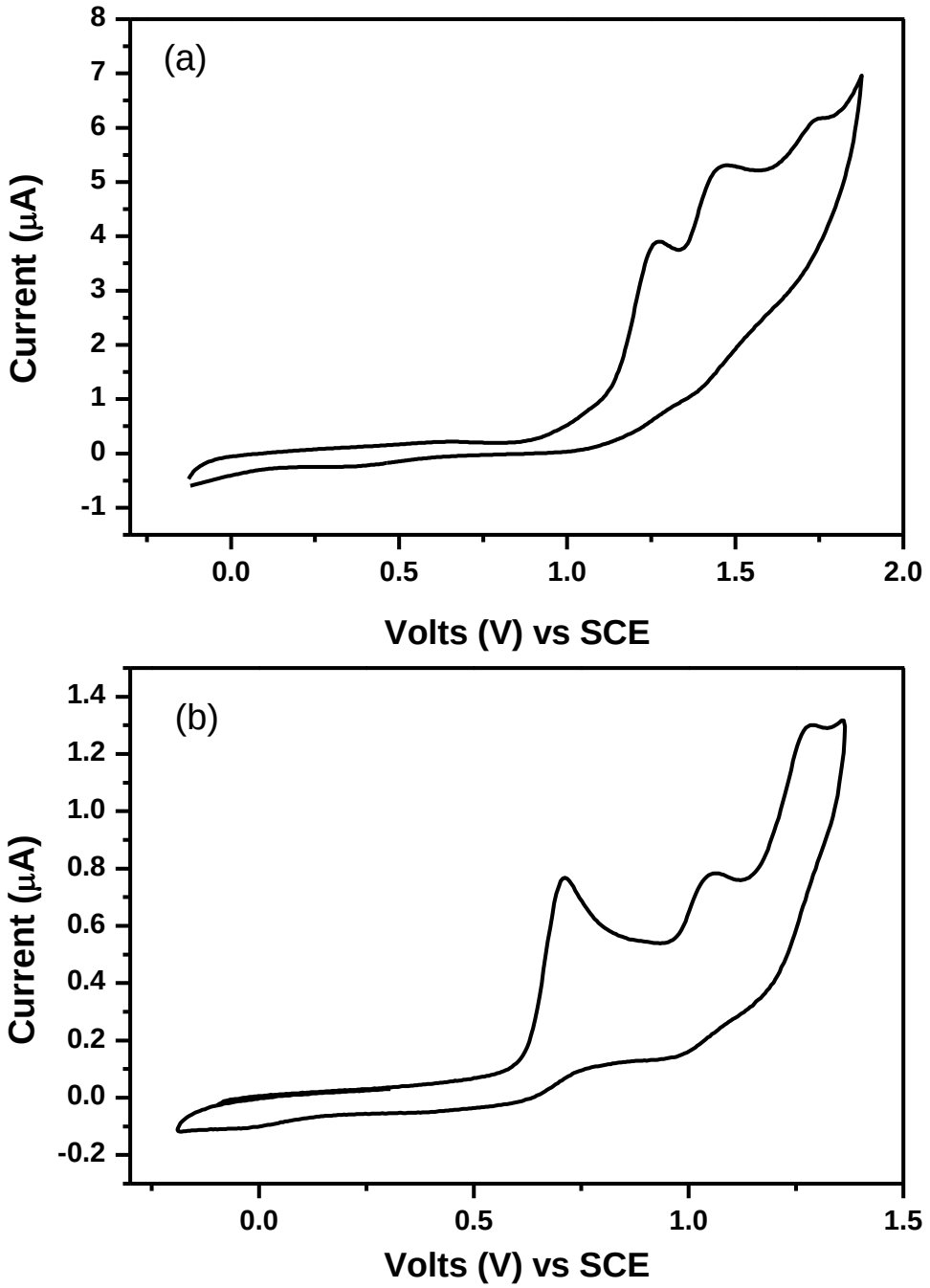

Figure 3-7 Cyclic voltammetry of (a) [Ir(ppy)$_2$PT$_3$-*PS*](PF$_6$), (**62**), and (b) Ir(ppy)$_2$PT$_3$-*PC*, (**63**), on a Pt disk electrode (scan rate 100 mv/s), electrolyte = 0.1 M [*n*-Bu$_4$N](PF$_6$), solvent = CH$_3$CN.

Section 3.3.4– Electronic Absorption Spectra

The UV-vis absorption spectra of the $Ir(ppz)_2PT_3$ complexes in CH_3CN are shown in Figure 3-8. The absorption spectra contain two major bands, one at approximately 250 nm and a lower energy band the maximum absorption of which shifts depending on binding mode; from 343 nm for $Ir(ppz)_2PT_3Cl$-*P*, to 360 nm for $[Ir(ppz)_2PT_3$-*PS*$](PF_6)$, and to 412 nm for the $Ir(ppz)_2PT_3$-*PC* complex. The tris(phenylpyrazole) Ir(III) complex, $Ir(ppz)_3$, exhibits absorption bands between 230-365 nm. In that complex, the bands above 270 nm are attributed to the $\pi \rightarrow \pi^*$ transition of the ppz ligand, while the lower energy bands are assigned as MLCT transitions.[201, 215, 231] Based on these comparisons, the band near 250 nm in the $Ir(ppz)_2PT_3$ complexes (*PS*, -*PC*, and Cl-*P* bound) is assigned as the $\pi \rightarrow \pi^*$ transition of the ppz group. The lower energy band observed between 343-412 nm is assigned as a PT_3 ligand based $\pi \rightarrow \pi^*$ transition, as this band matches that of the ligand closely. The large shift observed for the *PC* bound complex can be accounted for at least in part by the reduction in overall charge from the *PS* to *PC* bound complex (as the PT_3 ligand is formally neutral in the *PS* bound complex and monoanionic in the *PC* bound complex). In the $[Ir(ppz)_2PT_3$-*PS*$](PF_6)$ and $Ir(ppz)_2PT_3$-*PC* complexes, there is a shoulder around 310 nm possibly due to an MLCT or LLCT transition. This was not observed in the $Ir(ppz)_2PT_3Cl$-*P* species.

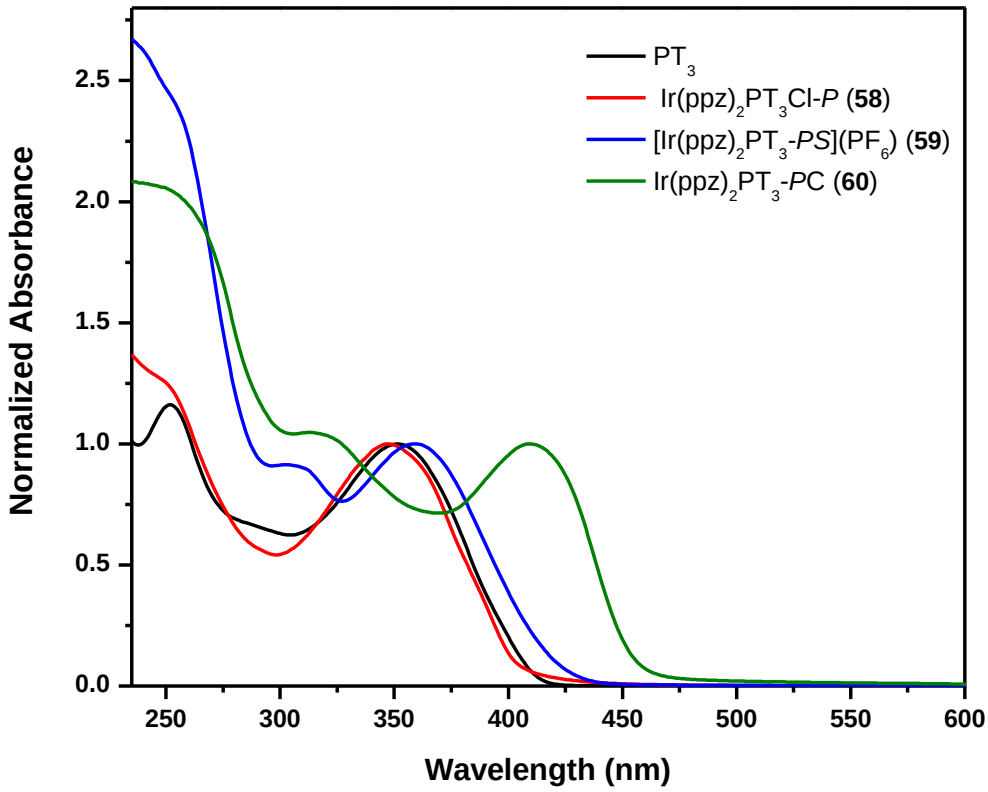

Figure 3-8 Solution absorption spectra of PT_3**,** $Ir(ppz)_2PT_3Cl$-*P*, (**58**), $[Ir(ppz)_2PT_3$-*PS*$](PF_6)$, (**59**), $Ir(ppz)_2PT_3$-*PC*, (**60**) in CH_3CN.

Tris(2-phenylpyridine)iridium, $Ir(ppy)_3$, shows intense bands between 240-350 nm assigned to the $\pi \rightarrow \pi^*$ transition of the ppy ligands. Additionally, bands between 350-450 nm have been assigned as both ^{1}MLCT and ^{3}MLCT transitions in the spectra of $Ir(ppy)_3$.[215] The spectra of the $Ir(ppy)_2PT_3Cl$-*P*, $[Ir(ppy)_2PT_3$-*PS*$](PF_6)$ and $Ir(ppy)_2PT_3$-*PC* complexes are very similar to the analogous ppz complexes. There are also two major absorption bands present, the band at approximately 260 nm is assigned as the ppy $\pi \rightarrow \pi^*$ transition, while the band occurring at lower energy is also assigned as a $\pi \rightarrow \pi^*$ transition of the PT_3 ligand. The shoulder around 310 nm is still observed in both the *PS* and *PC* bound complexes, but is not as apparent in $Ir(ppy)_2PT_3$-*PC* as it was in the analogous ppz complex. There is a shoulder around 300 nm in the $Ir(ppy)_2PT_3Cl$-*P* complex. Additionally, a lower energy shoulder at 425 nm is observed in the $Ir(ppy)_2PT_3Cl$-*P* complex which was not observed in the analgous ppz complex. This

may be a ^{3}MLCT or ^{3}LLCT transition. The Ir(ppy)$_2$PT$_3$-*PC* complex has a broader, lower energy band than the Ir(ppy)$_2$PT$_3$-*PC* complex, likely due to overlapping bands, as Ir(ppy)$_3$ exhibits lower energy absorption bands than Ir(ppz)$_3$.

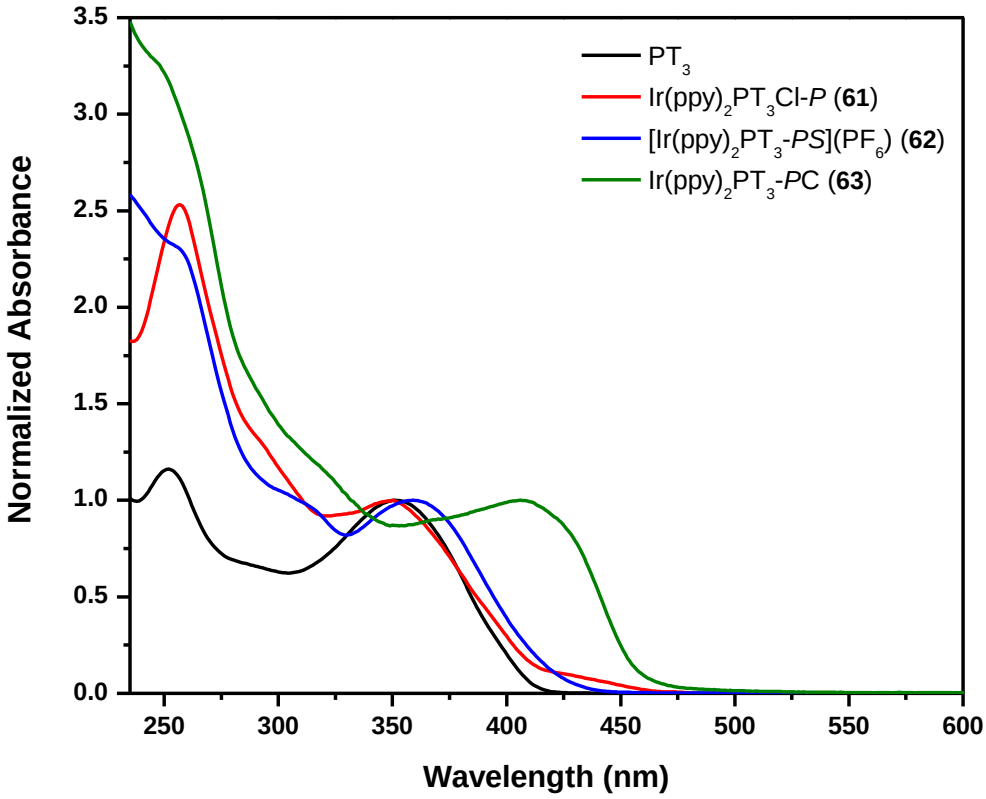

Figure 3-9 Solution absorption spectra of PT$_3$, Ir(ppy)$_2$PT$_3$Cl-*P*, (**61**), [Ir(ppy)$_2$PT$_3$-*PS*](PF$_6$), (**62**), Ir(ppy)$_2$PT$_3$-*PC*, (**63**), in CH$_3$CN.

The absorption spectra of the *PS* bound complexes are very comparable to the Ru(II) and Os(II) diimine complexes discussed in Chapter 2, with greater differences observed for the *PC* complexes. Whereas no absorption is observed above 475 nm for the Ir complexes, absorption occurs out to 650 and 800 nm for the Ru and Os *PC* species, respectively. The absence of the lower energy bands in the Ir(III) complexes may be due to the Ir center being more difficult to oxidize,[197] or a difference in the nature of the transitions observed.

Section 3.3.5 – Emission Spectra

The emission wavelength of cyclometalated Ir(III) complexes can be tuned by varying either the cyclometalating ligand and/or the XY ligand. Additionally, the electronic effects of the substituents and their position can significantly influence the photophysical properties. The effect of coordination mode of the PT_3 ligand to the cyclometalated Ir(III) centers on the emission properties was explored.

The ppz complexes showed weak emission when excited into the lowest energy absorbance band. The $Ir(ppz)_2PT_3Cl$-*P*, $[Ir(ppz)_2PT_3$-*PS*$](PF_6)$ and $Ir(ppz)_2PT_3$-*PC* complexes showed emission bands with λ_{max} at 442, 450 and 485 nm respectively (Figure 3-10). The emission lifetimes of all species are short, under 50 ns, and not sensitive to the presence of oxygen. Emission quantum yields are 0.002 and 0.003 for the $[Ir(ppz)_2PT_3$-*PS*$](PF_6)$ and $Ir(ppz)_2PT_3$-*PC* complexes respectively, while the $Ir(ppz)_2PT_3Cl$-*P* complex had a slightly higher quantum yield (0.068). PT_3 has a short-lived emission centered at 435 nm (Table 3-6), attributed to radiative decay of the singlet $\pi-\pi*$ state. *mer*-$Ir(ppz)_3$ in solution has a very weak emission at room temperature, however, at 77 K, it shows emission at 427 nm, and a lifetime on the order of tens of microseconds. *fac*-$Ir(ppz)_3$ emits at 414 nm with a similar lifetime. [215] Based on these observations, the emission band in the iridium ppz complexes is assigned to emission from a terthiophene-localized singlet state.

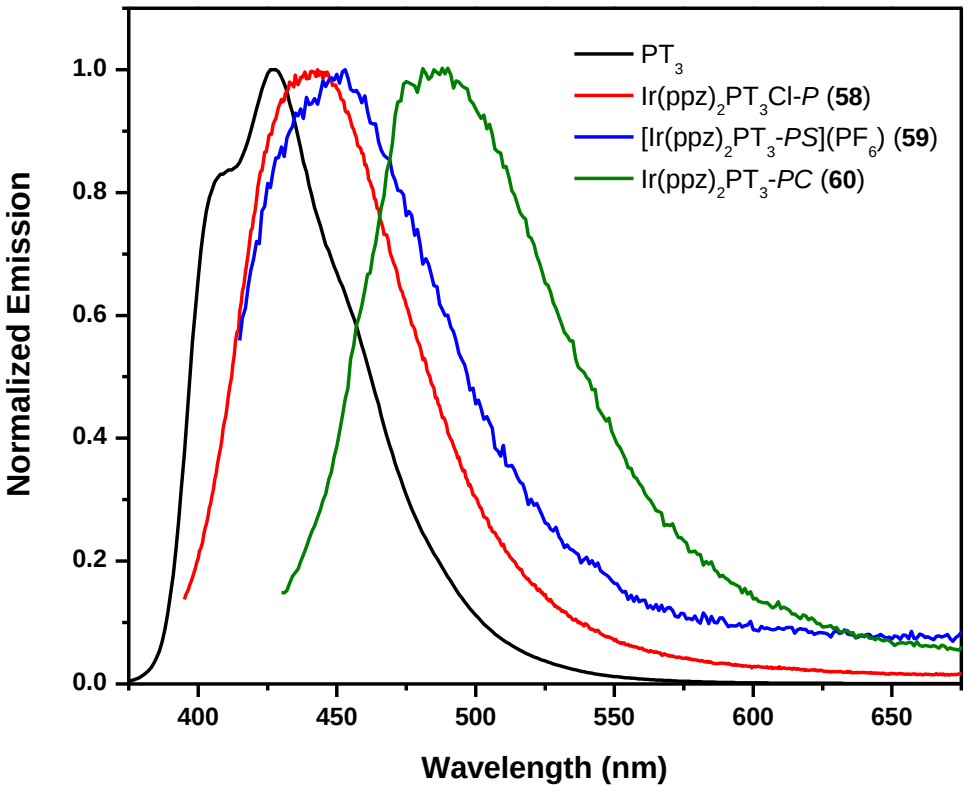

Figure 3-10 Emission spectra of PT_3, $Ir(ppz)_2PT_3Cl$-*P*, (**58**), $[Ir(ppz)_2PT_3$-*PS*$](PF_6)$, (**59**), $Ir(ppz)_2PT_3$-*PC*, (**60**), in CH_3CN.

The coordination mode of the PT_3 ligand to the Ir center resulted in changes in emission for the ppy complexes as well. $[Ir(ppy)_2PT_3$-*PS*$](PF_6)$ displays emission at 453 nm, as was observed for $[Ir(ppy)_2PT_3$-*PS*$](PF_6)$. The cyclometalated ppy *PC* bound complex has the lowest emission at 493 nm, slightly lower than the analogous ppz complex. In addition, a low energy band at 700 nm is sometimes observed. The emission quantum yields of the ppy complexes are similar to those of the ppz complexes (Table 3-6), and once again the emission lifetimes are short. This suggests that the HOMO is located on the terthiophene moiety. $Ir(ppy)_3$ shows emission at room temperature at 510 nm, while at 77 K the emission maximum shifts to 492 nm. The *mer* species has a broad emission with weak emission at room temperature, while the *fac* isomer is highly luminescent at room temperature and gives a structured emission profile.

Table 3-6 Photophysical data for cyclometalated Ir(III) - PT_3 complexes[a]

Compound	Abs λ_{max} (nm)	Em λ_{max} (nm)	QY	τ_{TA}(μs)
$Ir(ppz)_2PT_3Cl$-*P*	434	442	0.068	6.21
$Ir(ppz)_2PT_3$-*PS*	360	450	0.002	0.33
$Ir(ppz)_2PT_3$-*PC*	412	485	0.003	2.73
$Ir(ppy)_2PT_3Cl$-*P*	349	454	0.009	7.10
$Ir(ppy)_2PT_3$-*PS*	359	452	0.002	0.40
$Ir(ppy)_2PT_3$-*PC*	400	493	0.004	4.00[b]

[a]Measurements carried out in Ar sparged CH_3CN solution. [b] It was noted the lifetime of $Ir(ppy)_2PT_3$-*PC* changes with concentration.

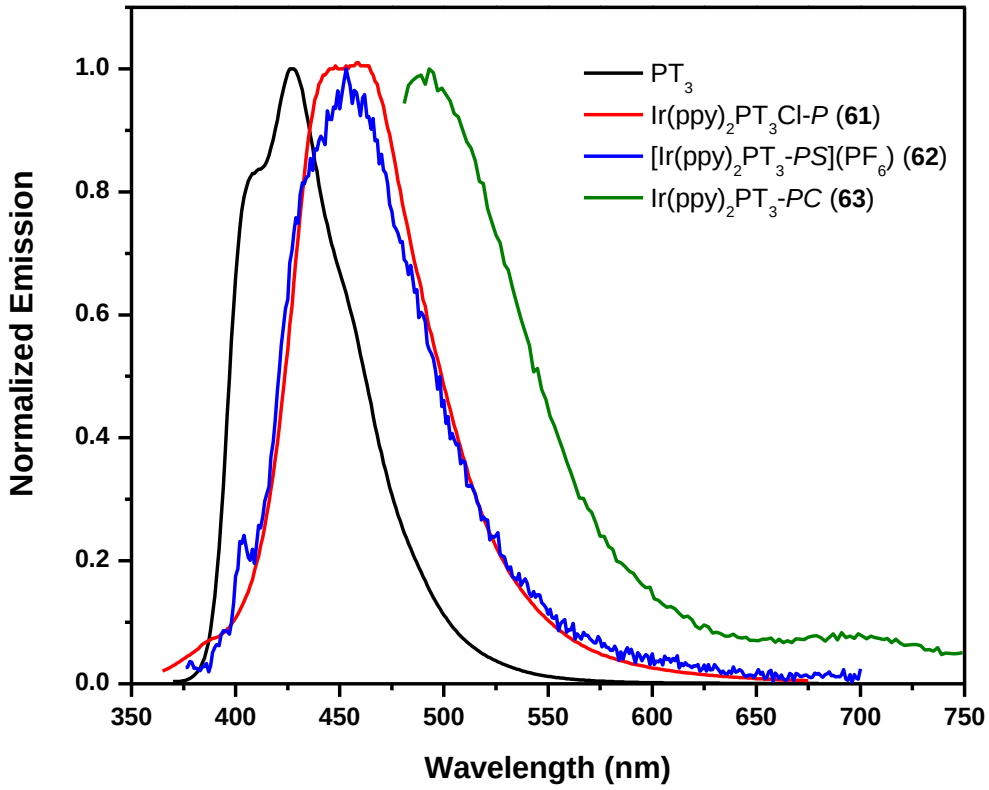

Figure 3-11 Emission spectra of PT_3, $Ir(ppy)_2PT_3Cl$-*P*, (**61**), $[Ir(ppy)_2PT_3$-*PS*$](PF_6)$, (**62**), $Ir(ppy)_2PT_3$-*PC*, (**63**), in CH_3CN.

Section 3.3.6– Transient Absorption Spectra

The nature of the excited states in these complexes was further probed using transient absorption (TA) spectroscopy. Excitation of $Ir(ppz)_2PT_3Cl$-*P* results in a broad TA band between 400-600 nm (Figure 3-12 (a)), strongly resembling the TA of T_3 (Chapter 2). This species decays monoexponentially with a lifetime of 6.2 μs in nitrogen-sparged acetonitrile (Appendix, Figure A-9), which is significantly reduced in the presence of oxygen. The TA spectrum of $Ir(ppz)_2PT_3$-*PC* is similar, (Figure 3-12 (b)) but shows a shoulder growing in at 550 nm. In argon-sparged solutions, this species has a lifetime of 2.73 μs (Appendix, Figure A-10), which decays monoexponentially. The peak and the shoulder have the same decay lifetime, suggesting they originate from the same species. $[Ir(ppz)_2PT_3$-*PS*$](PF_6)$ also shows an intense, broad TA with two bands between 400-650 nm (Figure 3-12(c)). The two bands in the TA spectra of this complex resemble the bands in the TA spectrum of PT_3 (Chapter 2), although slightly red-shifted. The TA decays monoexponentially with a lifetime of 330 ns under argon (Appendix, Figure A-11), which decreases under O_2. The dependence of the lifetime and intensity of these bands on oxygen supports the conclusion that these are all due to triplet states, and the similarity of the TA spectra to that of PT_3 suggests that a PT_3 ligand-centered triplet state (^{3}LC) is being observed.

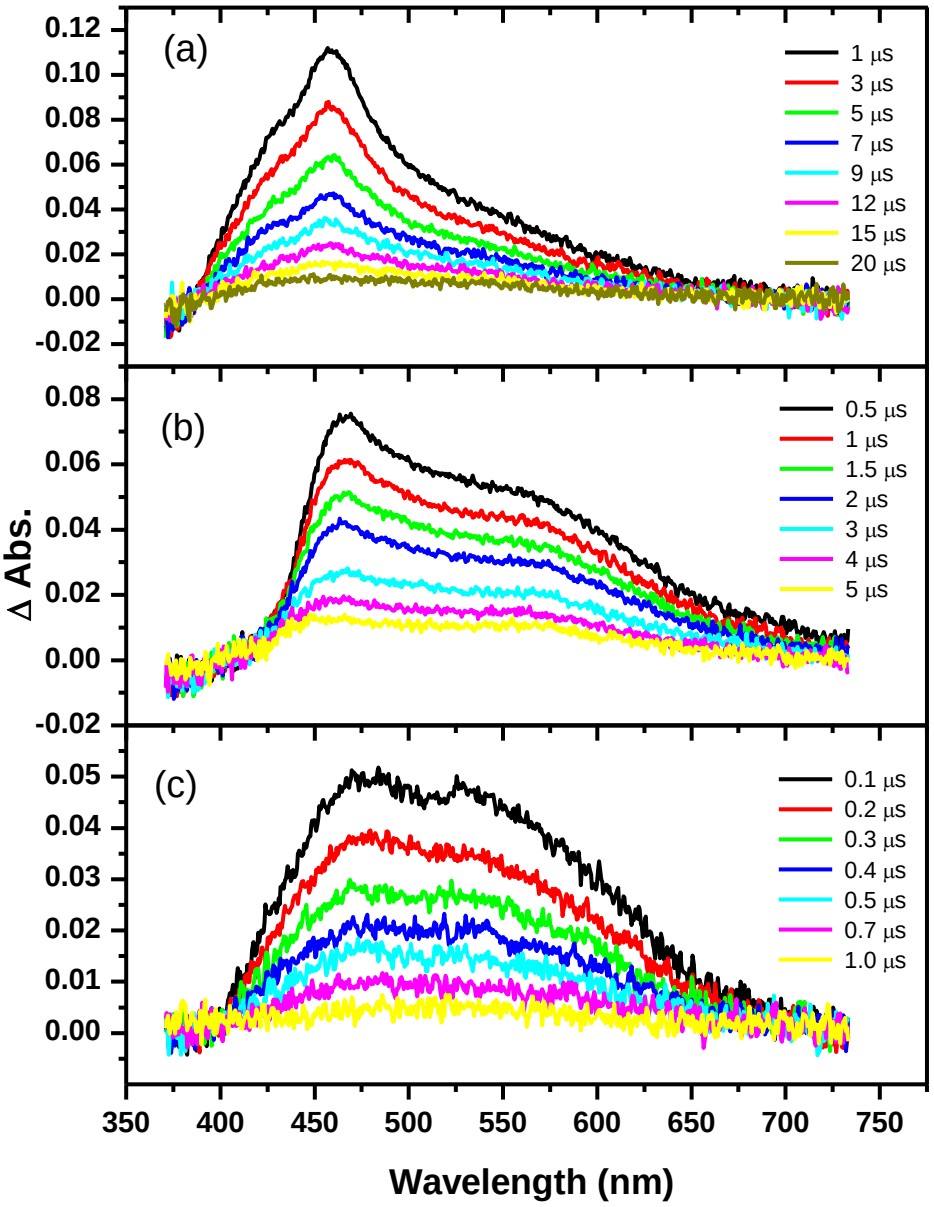

Figure 3-12 Transient absorption spectra of (a) $Ir(ppz)_2PT_3Cl$-*P*,(**58**), (b) $Ir(ppz)_2PT_3$-*PC*, (**60**), and (c) [$Ir(ppz)_2PT_3$-*PS*](PF_6), (**59**), in argon-sparged CH_3CN.

Since complexes with ppy ligands generally have a lower energy LUMO than complexes with ppz ligands, there is the possibility that using ppy as the cyclometalating ligand would result in the observation of a different excited state. However, the transient absorption spectra of the iridium ppy complexes appear similar to those of the ppz complexes, and thus, the PT_3 ligand. The lifetimes of the ppy complexes are slightly longer than those of their ppz analogues. The transient absorption of $Ir(ppy)_2PT_3Cl$-*P*

(Figure 3-13(a)) has a lifetime of 7.10 µs under argon, and this absorbance decays monoexponentially (Appendix, Figure A-12). The lifetime decreases when oxygen is present. The absorption for this complexes is broader than for $Ir(ppz)_2PT_3Cl$-*P*. The $Ir(ppy)_2PT_3$-*PC* transient spectra look similar to those for the ppz analogue. However, the peak at approximately 465 nm is not as pronounced (Figure 3-13 (b)). This also decays monoexponentially, (Appendix, Figure A-13) and the introduction of oxygen decreases the lifetime. It was noted that the excited state lifetime of $Ir(ppy)_2PT_3$-*PC* changes with concentration; the higher the concentration, the shorter the lifetime. Aggregation can affect excited state lifetimes,[232, 233] and may be causing the reduced lifetimes here. Small changes were also observed in the ground state absorption spectrum with concentration, supporting the possibility of aggregation. $[Ir(ppy)_2PT_3$-*PS*$](PF_6)$ is similar to the ppz analogue (Figure 3-13 (c)), and decays monoexponentially with a lifetime of 400 ns under argon (Appendix, Figure A-14), which decreases under O_2.

Excited state absorption spectra of $Ir(ppy)_3$ show an absorption feature at 370 nm, with a shoulder occurring around 500 nm.[234] As these features are not observed in the TA spectra for $[Ir(ppy)_2PT_3$-*PS*$](PF_6)$ and $Ir(ppy)_2PT_3$-*PC*, this supports the conclusion that the excited state observed in the TA spectra of the species do not have MLCT character, but are largely ligand-based. This is in contrast to $Os(bpy)_2PT_3$ spectra, where the *PS* species shows a ligand localized excited state, and a charge-separated excited state was observed for the *PC* complex. Presumably, the fact that a charge-separated state is not observed for these Ir complexes is a consequence of differences in the relative energy levels of these complexes, compared to the Os complexes.

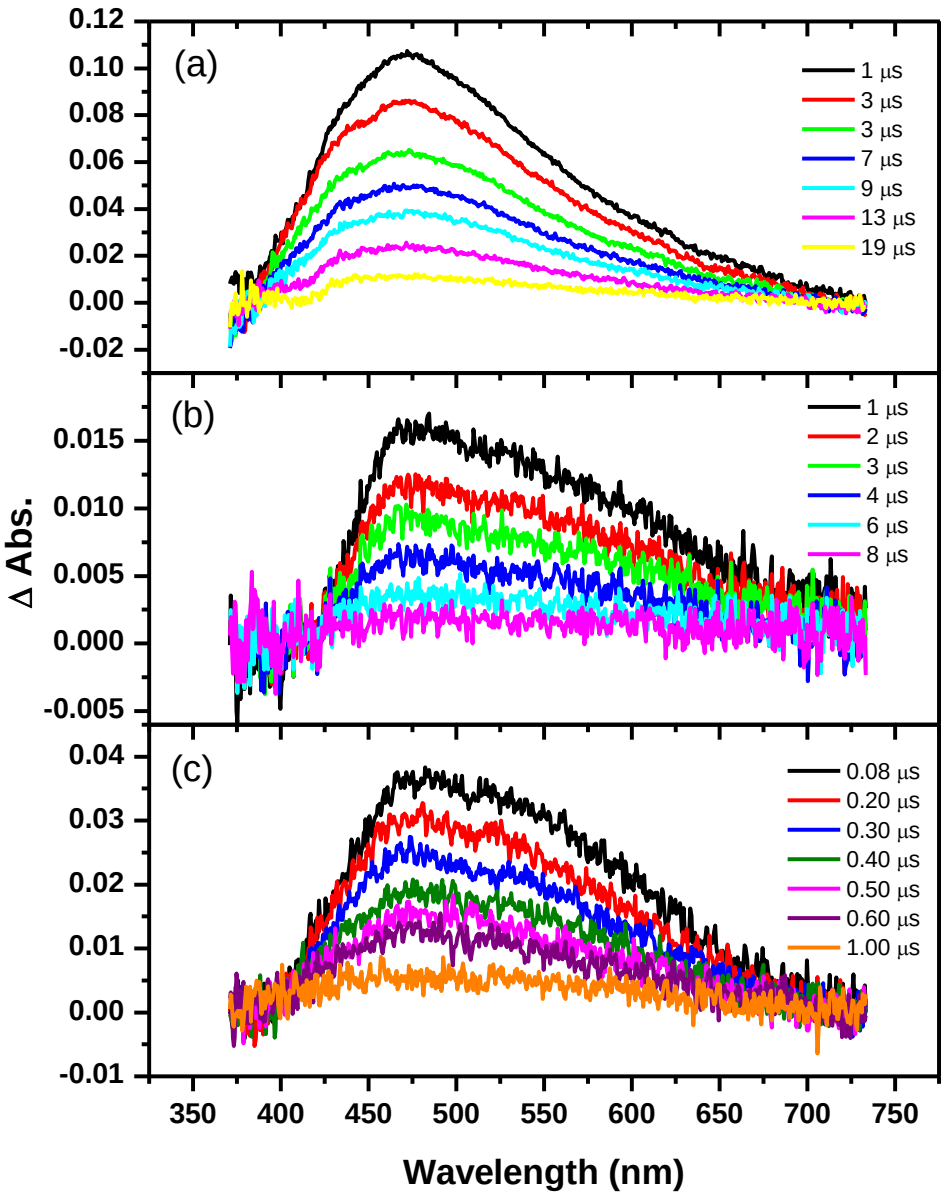

Figure 3-13 Transient absorption spectra of (a) Ir(ppy)$_2$PT$_3$Cl-*P*, (**61**), (b) Ir(ppy)$_2$PT$_3$-*PC*, (**63**), and (c) [Ir(ppy)$_2$PT$_3$-*PS*](PF$_6$), (**62**), in argon-sparged CH$_3$CN.

Section 3.4– Conclusions

Six cyclometalated iridium(III) diphenylphosphinoterthiophene complexes were synthesized: Ir(ppz)$_2$PT$_3$Cl-*P*, [Ir(ppz)$_2$PT$_3$-*PS*](PF$_6$), Ir(ppz)$_2$PT$_3$-*PC*, Ir(ppy)$_2$PT$_3$Cl-*P*, [Ir(ppy)$_2$PT$_3$-*PS*](PF$_6$), and Ir(ppz)$_2$PT$_3$-*PC*. The effect of the coordination mode to the electronic and photophysical properties was investigated. The solid-state structures indicate the torsion angles are highly dependent on binding mode. Cyclic voltammetry

was used to determine the oxidation potentials of four of these complexes. Attempts to electropolymerize the *PS* and *PC* bound complexes were unsuccessful. The absorption spectra were dominated by $\pi \rightarrow \pi^*$ transitions, and the thiophene based $\pi \rightarrow \pi^*$ transition was shifted in relation to coordination mode; the *PC* binding mode gave the lowest energy band. All of the complexes were weakly emissive, and a red shift in emission was observed from the Cl-*P* to *PS* to *PC* bound species. The emission lifetimes were very short, and assigned as PT_3 ligand-based. Transient absorption spectra show all complexes had a ligand localized excited state. However, the lifetime of the excited state varied greatly depending upon coordination: $Ir(ppz)_2PT_3$-*P* had the longest lifetime, while $Ir(ppz)_2PT_3$-*PS* had the shortest, within the series of ppz complexes investigated.

CHAPTER 4

COPPER(I) MIXED-LIGAND COMPLEXES CONTAINING A PHOSPHINO(TERTHIOPHENE) LIGAND

Section 4.1– Introduction

Recent research on the photophysical and electrochemical properties of phenanthroline and bipyridine based copper(I) complexes has demonstrated their potential application in organic light-emitting diodes (OLEDs) and light-emitting electrochemical cells (LECs),[235, 236] as well as dye sensitized solar cells (DSSCs).[237-239] The excited state lifetime of first row transition metal complexes are often short compared to their second and third row analogues, as low lying metal d-d states often allow non-radiative decay of the MLCT state. Research investigating first row transition metals as sensitizers in DSSCs has been limited, as charge injection from the dye to the semiconductor is often not achieved, leading to inefficient DSSCs. Cu(I) complexes can display longer excited state lifetimes due to their d^{10} configuration.[240] Emission from complexes with open d shells ($d^{<10}$) can be affected by thermal population of MC states from the MLCT state, leading to non-radiative decay or photochemical degradation. Closed shell d^{10} copper complexes do not exhibit non-radiative decay via this pathway, although deactivation through other pathways, such as exciplex formation, is possible.

Copper (I) complexes with substituted diimine ligands possess similar properties to $(Ru(bpy)_3)^{2+}$ salts.[241-243] Additionally, copper is more abundant than ruthenium, and has a much lower cost (approximately \$0.08/g for Cu compared to \$4.00/g for Ru).[244, 245] Cu sensitizers for photoelectrochemical cells date back to 1994.[246] Early investigations into Cu(I) sensitizers focused on *bis*-(phenanthroline) Cu(I) complexes. Substitution in the 2 and 9 positions of the phenanthroline ligands proved useful to sterically constrain the molecule, minimizing the geometry change from distorted tetrahedral to tetragonally flattened, which occurs upon excitation or oxidation (going from a formally Cu(I) to Cu(II) metal center) (Scheme 4-1).[243, 247] The geometry change can allow nucleophilic attack, leading to a five-coordinate (exciplex) species, [244, 245] which then deactivates by non-emissive deactivation pathways.

Scheme 4-1 Ref.[243]

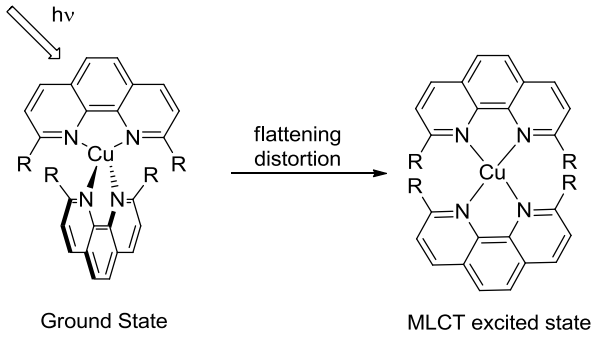

Substituted bipyridines, such as 6,6′-dimethyl-2,2′-bipyridyl-4,4′ dicarboxylic acid and corresponding methyl esters, as well as analogues with extended conjugation have been investigated (Chart 4-1, (**64**)-(**67**)).[238] These allow for attachment to TiO_2, while still sterically constraining the molecule from geometrical reorganization. The efficiency of DSSCs using these Cu(I) substituted bipyridyl complexes is lowered compared to those with Ru(II) complexes, but the cost is drastically reduced as well. Additionally, the methods used to improve Ru(II) based dyes work also with these Cu(I) complexes. Constable has since made several Cu(I) complexes using 6,6′-disubstituted 2,2′-bipyridine dicarboxylic acids (Chart 4-1 (**68**)-(**71**)).[239] Iminopyridine based complexes have also been investigated (Chart 4-1 (**72**) and (**73**)).[248] These complexes allow the Cu center to be almost tetrahedral in geometry, and allow both carboxylate groups to anchor to the TiO_2 surface. These iminopyridine complexes, however, were less efficient as sensitizers than the 6,6′-disubstituted 2,2′-bipyridine dicarboxylic acids complexes this group previously investigated.

Chart 4-1 Ref.[238, 239, 248]

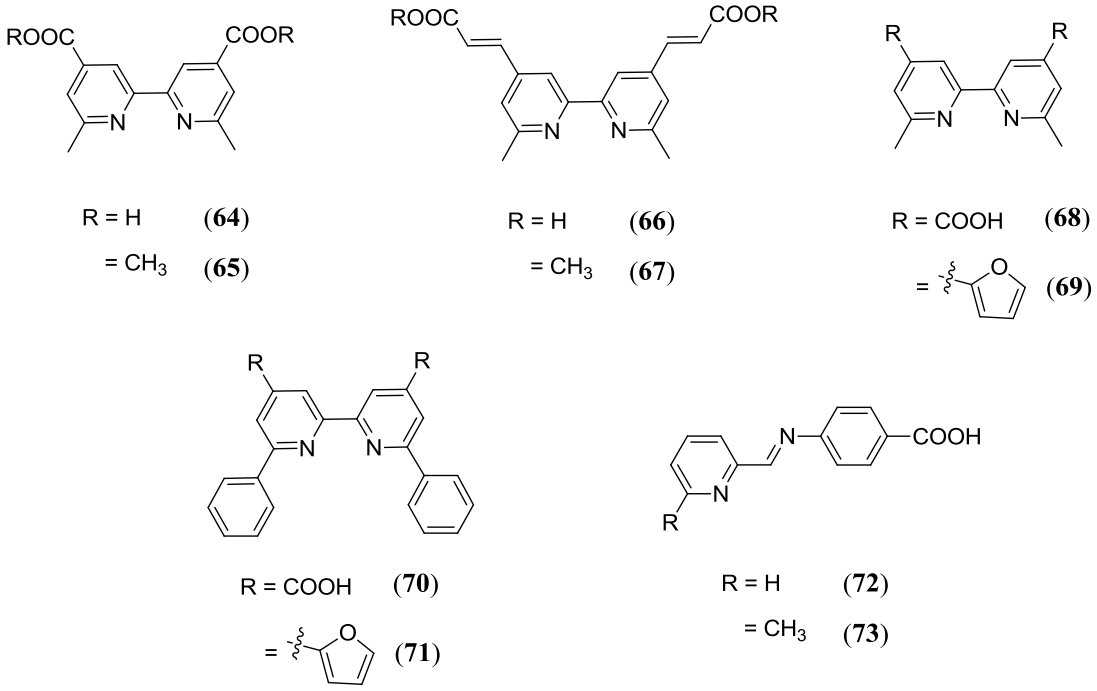

Copper complexes with mixed-ligand systems have recently gained attention, specifically, mixed-ligand complexes using diimine and phosphine ligands.[94, 240, 249-256] When considering electronic and photophysical properties, these copper complexes are more similar to Ru(II) polypyridine complexes than corresponding homoleptic Cu(I) diimine complexes. Also they possess enhanced luminescence and longer lifetimes than $Cu(diimine)_2^+$ complexes.[240] It has been observed that bidentate phosphine ligands help suppress ligand dissociation compared to monodentate phosphine ligands.[94] Robertson and coworkers[240] reported a heteroleptic Cu(I) complex containing a diimine ligand and a *bis*(2-(diphenylphosphanyl)phenyl) ether ligand, (POP), (**74**, Chart 4-2), and demonstrated its use as a sensitizer in a DSSC. The steric strain of the POP ligand can hinder distortion toward a square planar geometry upon MLCT excitation or oxidation. The photocurrents observed were lower than those reported for devices using homoleptic Cu(I) sensitizers,[238, 239, 257] believed to be due to poor absorption of the dye in the visible region. This research group is now looking to replacing the POP with a different ligand with improved absorption properties. They were successful in demonstrating that Cu(I)

sensitizers can be obtained without the need for the labour intensive 4,4′,6,6′-substituted diimine analogues.

Chart 4-2 Ref.[240]

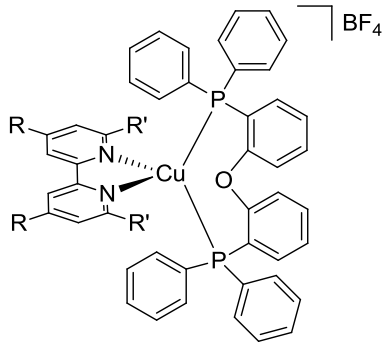

R = COOH, R' = H (**74**)

In this chapter, new mixed-ligand Cu(I) complexes using a diimine ligand and the PT_3 ligand, instead of a diphosphine ligand are described. The PT_3 ligand has a broader absorption in the visible region than the POP ligand. Poor light absorption by POP was attributed as a cause of low photocurrents. Additionally, absorption can be tuned as PT_3 is capable of binding to metal centers in various ways; via *P*, *PS* or *PC* coordination modes. Binding in a *PS* or *PC* configuration could help with complex rigidity. This, along with the bulkiness of the ligand may prevent distortion upon excitation that could lead to non-radiative decay pathways. Here, two new complexes are reported: [Cu(dmp)(MeCN)PT_3-*P*](PF_6) and [Cu(phen)PT_3-*P*](PF_6) (Chart 4-3). The absorption, transient absorption, emission, and electrochemical properties, as well as the solid-state structures of the complexes are investigated.

Chart 4-3

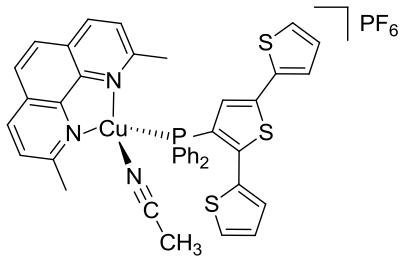

[Cu(dmp)(MeCN)PT_3-*P*](PF_6)

75

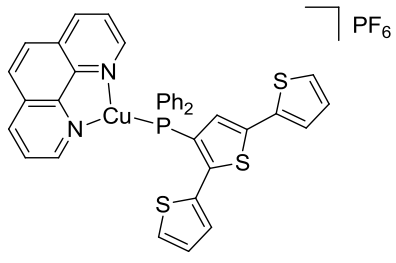

[Cu(phen)PT_3-*P*](PF_6)

76

Section 4.2 – Experimental

Section 4.2.1 – General

All reactions were performed under N_2 (99.0%) or Ar (99.997%). PT_3 was synthesized according to literature procedures.[109] All other reagents were purchased from Aldrich, Alfa Aesar or Strem and used as received. ^1H and $^{31}P\{^1H\}$ NMR spectra were collected on a Bruker AV-300 spectrometer. ^1H NMR spectra were referenced to residual solvent, and $^{31}P\{^1H\}$ NMR spectra referenced to external 85% H_3PO_4. ESI mass spectra were recorded on a Bruker Esquire-LC ion trap mass spectrometer equipped with an electrospray ion source. The solvent for the ESI-MS experiments was either methanol or dichloromethane/methanol and the concentration of the compound was ~10 μM. High resolution mass spectra (HRMS) were recorded on a Waters Micromass LCT time-of-flight mass spectrometer equipped with an electrospray ion source. CHN elemental analyses were performed using an EA1108 elemental analyzer, using calibration factors. The calibration factor was determined by analyzing a suitable certified organic standard (OAS) of a known elemental composition. All mass spectrometry and microanalysis results were obtained by the staff at the UBC Mass Spectrometry Centre. Cyclic voltammetry experiments were carried out on a Pinechem potentiostat using a Pt working electrode, Pt mesh counter electrode and a silver wire reference electrode with 0.1 M $[(n\text{-}Bu)_4N]PF_6$ supporting electrolyte which was re-crystallized 3 times from ethanol and dried under vacuum at 100 °C for 3 days. Decamethylferrocene (-0.125 V vs SCE in CH_3CN, -0.070 V vs SCE in CH_2Cl_2) was used as an internal reference to correct the measured potentials with respect to saturated calomel electrode (SCE). UV-vis spectra were obtained on a Cary 5000 spectrometer in HPLC grade solvent. Emission spectra were obtained on a PTI Quantamaster spectrometer. Transient absorption (TA) measurements and fluorescence lifetimes were carried out on a Princeton Instruments Spectra Pro 2300i Imaging Triple Grating Monochrometer/Spectrograph with a Hamamatsu Dynamic Range Streak Camera (excitation source: EKSPLA Nd:YAG laser, 35 ps pulse duration, λ = 355 nm). Solutions of the complexes in CH_3CN having an optical density of 1 at 355 nm were prepared. The UV-vis spectra were obtained before

and after each TA experiment to ensure the bulk of the sample did not change, due to degradation or another process.

Section 4.2.2 – Procedures

[Cu(dmp)(MeCN)PT_3-*P*](PF_6), (75).

[$Cu(CH_3CN)_4$](PF_6) (0.025 g) and PT_3 (0.030 g) were added to 10 mL of N_2 sparged CH_3CN. The mixture was heated to reflux, with stirring, for 12 hours. The solution was cooled to room temperature and a solution of dmp (0.013 g) in 5 mL of CH_3CN/DCM was added dropwise to the copper solution. The volume of the resulting solution was reduced, added dropwise to a solution of ammonium hexafluorophosphate (0.200 g) in H_2O (12 mL) and stirred at room temperature for 30 minutes. The precipitate, a mixture of products, was filtered and washed with copious amounts of water and diethyl ether. A small amount of powder was purified, through several washing with hexanes, ethanol and methanol, and the NMR spectrum was recorded on that sample. The remaining mixture was recrystallized by vapour diffusion of ether into a CH_3CN/CH_2Cl_2 solution, to produce yellow crystals of [Cu(dmp)(MeCN)PT_3-*P*](PF_6) (6.3 mg, 11%). ^{1}H NMR (300 MHz, CD_2Cl_2: δ 2.46 (s, 6H), 6.71 (br. s, 2H), 7.03-7.18 (m, 2H), 7.26-7.35 (m, 3H), 7.40-7.56 (m, 10H), 7.73 (d, *J*=8.5 Hz, 2H), 7.99 (s, 2H), 8.48 (d, *J* = 8.5 Hz, 2H). $^{31}P\{^1H\}$ NMR (121 MHz, CD_2Cl_2): δ 15.9 (s), -143.6 (septet, J_{PF} = 708 Hz, PF_6). m/z: $[M\text{-}PF_6]^+$ 703.1. HRMS (ESI) Calcd for $C_{38}H_{29}CuN_2PS_3$ (m/z: $[M\text{-}PF_6\text{-}MeCN]^+$): 703.0527; Found: 703.0553.

[Cu(phen)PT_3-*P*](PF_6), (76).

[$Cu(CH_3CN)_4$](PF_6) (0.050 g) and PT_3 (0.060 g) were added to 15 mL of N_2 sparged CH_3CN. The mixture was heated to reflux, with stirring, for 12 hours. The solution was cooled to room temperature and a solution of phenanthroline monohydrate (0.026 g) in 5 mL of 1:1 CH_3CN/DCM was added dropwise to the copper solution. The volume of the resulting solution was reduced, added dropwise to a solution of ammonium hexafluorophosphate (0.284 g) in H_2O (17 mL) and stirred at room temperature for 30 minutes. The precipitate was filtered and washed with copious amounts of water and

diethyl ether to yield 62 mg (56 %) of a yellow solid. ^{1}H NMR (300 MHz, CD_3CN: δ 5.87-5.99 (m, 1H), 6.36 (d, *J* = 3.4 Hz, 1H), 6.48 (d, *J* = 4.8, 1H), 6.57 (d, *J* = 2.7, 1H), 7.02 (dd, *J* = 5.3, 3.7 Hz, 1H), 7.14 (dd, *J* = 3.7, 1.1 Hz, 1H), 7.34 (dd, *J* = 5.1, 1.0 Hz, 1H), 7.51-7.59 (m, 10H), 7.85 (dd, *J* = 8.1, 4.7 Hz, 2H) 8.05 (s, 2H), 8.57 (d, *J* = 8.0 Hz, 2H), 8.79 (d, *J* = 3.4 Hz, 2H). ^{31}P{^{1}H} NMR (121 MHz, CD_2 CD_2): δ -12.7 (br. s), -143.6 (septet, J_{PF} = 708 Hz, PF_6). m/z $[M\text{-}PF_6]^+$ 675.5. HRMS (ESI) Calcd for: $C_{36}H_{25}CuN_2PS_3$ (m/z $[M\text{-}PF_6]^+$): 675.0214; Found: 675.0224. Anal. $C_{36}H_{25}CuF_6N_2P_2S_3$ requires C, 52.65; H, 3.07; N, 3.41. Found C, 52.78; H, 3.24; N, 3.28.

Section 4.2.3 – X-Ray Crystallography

Suitable crystals of [Cu(dmp)(MeCN)PT_3-*P*](PF_6) and [Cu(phen)PT_3-*P*](PF_6) were grown by vapour diffusion or from solution. The X-ray data were collected and solved by Dr. B.O. Patrick. In each case, the crystals were mounted on a glass fiber and a Bruker APEX DUO or Bruker X8 APEX II diffractometer with graphite monochromated Mo-Kα radiation was used for all measurements. Data were collected and integrated using the Bruker SAINT[113, 258] software package. Data were corrected for absorption effects using multi-scan techniques, SADABS[116] and TWINABS[259] for [Cu(dmp)(MeCN)PT_3-*P*](PF_6) and [Cu(phen)PT_3-*P*](PF_6) respectively. The data were corrected for Lorentz and polarization effects. The structures were solved by direct methods.[118] Solid-state diagrams were visualized using Mercury.[119]

[Cu(dmp)(MeCN)PT_3-*P*](PF_6), (75).

Data were collected in a series of ϕ and *ω* scans in 0.5° oscillations using 7.0 second exposures. The crystal to detector distance was 40.08 mm. The data were collected to a maximum 2θ value of 60.1°. Of the 52311 reflections that were collected, 11254 were unique (R_{int} = 0.041); equivalent reflections were merged. Data were corrected for absorption effects using the multi-scan technique (SADABS),[116] with minimum and maximum transmission coefficients of 0.859 and 0.941, respectively. Two thiophene rings (S1 – C4 and S3 – C12) are disordered by 180° rotation about a C – C bond. Restraints were employed to maintain similar geometries and thermal parameters

between the major and minor disordered fragments. All non-hydrogen atoms were refined anisotropically. All hydrogen atoms were placed in calculated positions. The final cycle of full-matrix least squares refinement[120] on F^2 was based on 11254 reflections and 555 variable parameters and converged (largest parameter shift was 0.00 times its esd).

[Cu(phen)PT_3-*P*](PF_6), (76).

Data were collected in a series of ϕ and ω scans in 0.5° oscillations using 20.0 second exposures. The crystal to detector distance was 40.15 mm. The data were collected to a maximum 2θ value of 56.2°.The material crystallizes as a three-component 'split-crystal' with components one and two related by a 4.4° rotation about the (0.08 -0.37 1.00) crystal axis, and component one and three related by a 5.0° rotation about the (1.00 -0.60 0.05) crystal axis. Data were integrated for all twin components, including both overlapped and non-overlapped reflections. In total, 89164 reflections were integrated (28124 from component one only, 28270 from component two only, 27743 from component three only, 5027 overlapped). Data were corrected for absorption effects using multi-scan the technique (TWINABS),[259] with minimum and maximum transmission coefficients of 0.733 and 0.880, respectively. The structure was solved by direct methods[118] using non-overlapped data from the major twin component. Subsequent refinements were carried out using the HKLF 5 format data set, containing data from component one and all overlaps from components two and three. The material crystalizes with disorder of one thiophene ring about the C4-C5 bond. The major disorder fragment (~78%) has the thiophene sulfur oriented away from the Cu atom, while the minor fragment had the thiophene sulfur bonded to the Cu atom. All non-hydrogen atoms were refined anisotropically. All hydrogen atoms were placed in calculated positions, but not refined. The final cycle of full-matrix least squares refinement[120] on F^2 was based on 8227 reflections and 490 variable parameters and converged (largest parameter shift was 0.00 times its esd).

Section 4.3– Results and Discussion

Section 4.3.1 – Synthesis

Typical procedure for a mixed-ligand Cu(I) complex, of type $[Cu(N\text{^}N)(P\text{^}P)](BF_4)$, involves mixing $[Cu(CH_3CN)_4](BF_4)$ with a diphosphine ligand (P^P) in DCM for two hours, followed by addition of diimine ligand (N^N) dissolved in DCM. After an additional few hours of stirring, the volume is reduced and layered with CH_3CN to give $[Cu(N\text{^}N)(P\text{^}P)](BF_4)$ in good yield.[94] (Scheme 4-2)

Scheme 4-2

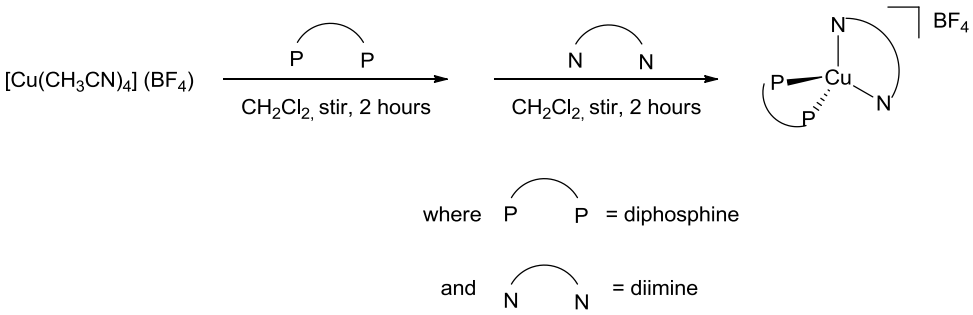

Employing a similar method here, using 2,9-dimethyl-1,10-phenanthroline (dmp) as the diimine ligand, and PT_3 instead of a P^P ligand, led to a mixture of products. Based on NMR spectroscopy and mass spectrometry analysis, it is believed the desired $[Cu(dmp)PT_3](PF_6)$ complex was formed (m/z $[M\text{-}PF_6]^+$ 703.1, $^{31}P\{^1H\}$ NMR showed a new peak that did not correspond to ligand or oxidized ligand), along with $[Cu(dmp)_2](PF_6)$ (m/z $[M\text{-}PF_6]^+$ 479.2). It has been previously reported that this homoleptic copper(I) diimine complex forms readily, even when not favored stoichiometrically.[249, 260] Li and coworkers[256] found that they could synthesize $[Cu(dmp)(P\text{^}P)](ClO_4)$ using several P^P ligands, including 1,3-*bis*(diphenylphosphino)propane (dppp), and 1,2-*bis*(diphenylphosphino)ethane (dppe), but not when using 1,2-*bis*(diphenylphosphino)benzene (bdpp). This was attributed to repulsion between the ligands, as there would be more steric crowding in a complex containing the bdpp ligand. Alternatively, failure to isolate the desired product may be

due to a kinetic effect of crystallization, as in solution it is likely there is an equilibrium between various species.[256]

Here, attempts to efficiently separate the desired product from the mixture were unsuccessful. Column chromatography yielded some pure $[Cu(dmp)_2](PF_6)$, but no evidence of the desired product. Refluxing the PT_3 ligand with the $[Cu(CH_3CN)_4](PF_6)$ before adding dmp did not help in preventing the unwanted $[Cu(dmp)_2](PF_6)$ from forming. Attempted recrystallization from DCM led to the formation of $[Cu(dmp)_2](PF_6)$, perhaps due to the stability of this complex. Eventually a small amount of material was recrystallized by vapour diffusion of ether into an DCM/CH_3CN mixture, and the solid-state molecular structure was determined to be $[Cu(dmp)(MeCN)PT_3\text{-}P](PF_6)$. The MS analysis does not show a peak for the product with coordinated MeCN. However, it is not surprising as MeCN is known to be relatively labile. It is believed that the MeCN is not coordinated in the bulk crude product, and that it binds during recrystallization with acetonitrile, as a peak that could be assigned to bound CH_3CN was not observed in the ^1H NMR spectrum of the complex before recrystallization (from the small amount that was purified via several washings). It has been reported that copper complexes with larger anions, such as PF_6^- and $V(CO)_6^-$, can yield three-coordinate trigonal planar salts.[261] Recrystallization from acetonitrile has produced four coordinate complexes, where an acetonitrile displaced the anion to bind to the copper.[261] Here, all spectroscopic investigations were carried out on the crystals of this complex, rather than the bulk material prior to recrystallization.

Changing the diimine ligand from dimethylphenanthroline to phenanthroline produced a single mixed-ligand copper(I) complex. In this case, PT_3 was heated to reflux with $[Cu(CH_3CN)_4](PF_6)$, followed by addition of phen (Scheme 4-3). No evidence of $[Cu(phen)_2](PF_6)$ was observed from mass spectrometry analysis, but a peak at m/z = 675.5 indicates the desired complex was present. This suggests steric effects may be a factor in the formation of the mixed-ligand Cu(I) containing dmp complex.

Scheme 4-3

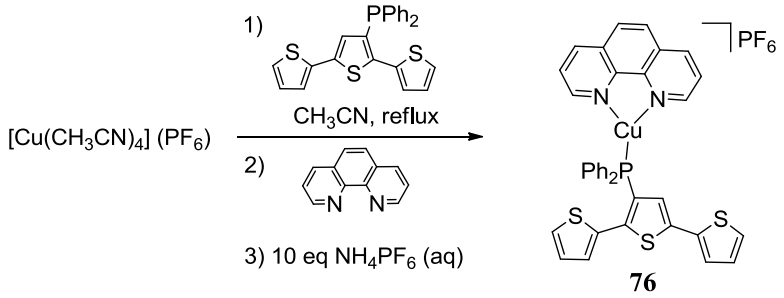

76

Section 4.3.2– Solid-State Molecular Structures

Single crystals of [Cu(dmp)(MeCN)PT_3-*P*](PF_6) were grown from vapour diffusion of diethyl ether into a CH_2Cl_2 – CH_3CN solution. The solid-state structure is shown in Figure 4-1. Disorder was present in the thiophene rings containing S1 and S3. The [Cu(dmp)(MeCN)PT_3-*P*](PF_6) complex crystalized in a distorted tetrahedral environment around the Cu center. The N1 – Cu – N2 angle of 81.29(6)° and P1 – Cu – N3 of 111.96(5)° show a substantial distortion from the expected 109.5°. This is common in these complexes, as the rigid ring system of the diimine ligand requires an acute bite angle. In other complexes were a diphosphine ligand is used, the angle varies substantially, with values between 105° and 123° observed.[250] Here, the Cu – N3 bond is the shortest Cu – N bond (Table 4-1). This bond is slightly longer than the Cu – N bond lengths in [Cu($CH_3CN)_4$](PF_6).[262] However, it is considerably longer than the Cu – N_{MeCN} bond in the three-coordinate [Cu(dmp)(MeCN)](PF_6) complex,[263] potentially due to steric effects. The Cu – N_{dmp} bonds fall with normal ranges, when compared to similar structures.[94, 249, 250] The Cu – P bond, with a length of 2.1989(5) Å, is slightly shorter than that observed for other Cu – P bonds in complexes with either bidentate diphosphine ligands or PPh_3 moieties.[94, 250, 252, 264] The S1 to S2 and S2 to S3 torsion angles of the thiophene rings are about 140° - 160° (Table 4-1), which are larger than the calculated value for terthiophene (147.6°).[220] The increased co-planarity of the rings indicates more π – orbital overlap.

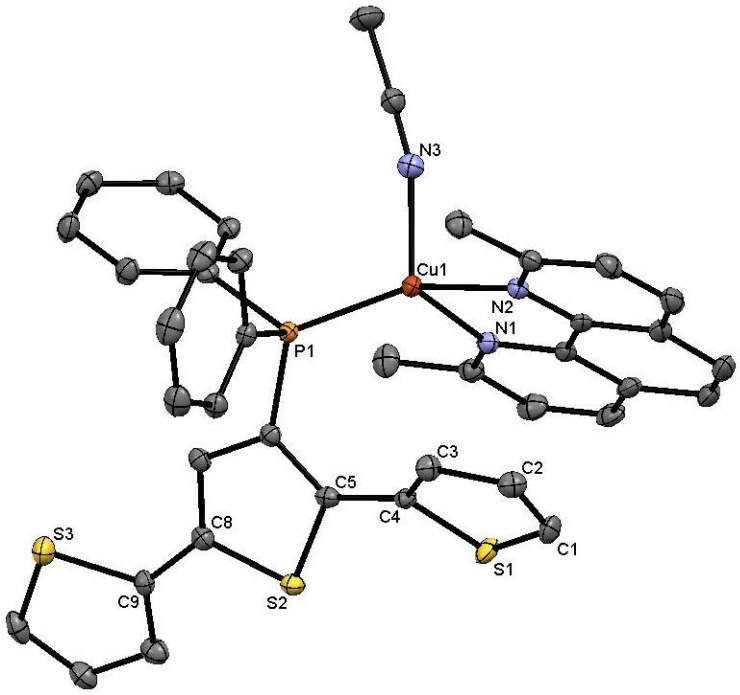

Figure 4-1 Solid-state structure of [Cu(dmp)(MeCN)PT_3-*P*](PF_6), (**75**). Hydrogen atoms and counterions were removed for clarity. Thermal ellipsoids are drawn at 50% probability.

Table 4-1 Selected bond lengths and angles for [Cu(dmp)(MeCN)PT_3-*P*](PF_6), (**75**).

Bond Lengths (Å)			
Cu1 – N1	2.0911(15)	C1 – C2	1.358(7)
Cu1 – N2	2.0634(15)	C2 – C3	1.440(13)
Cu1 – N3	2.0414(16)	C3 – C4	1.329(14)
Cu1 – P1	2.1989(5)	C4 – C5	1.455(8)
S1 – C1	1.712(7)	S1 – C4	1.753(11)
Bond Angles (°)			
N1 – Cu1 – N2	81.29(6)	P1 – Cu1 – N3	111.96(5)
N1 – Cu1 – N3	105.27(6)	P1 – Cu1 – N2	131.75(4)
N2 – Cu1 – N3	99.27(6)	P1 – Cu1 – N1	121.58(4)
Torsion Angles (°)			
S1 – C4 – C5 – S2	41.0(9)	S2 – C8 – C9 – S3	160.0(3)

Single crystals of [Cu(phen)PT_3-*P*](PF_6) were grown from a warm methanol solution, and the solid-state structure is shown in Figure 4-2. Disorder was present in the thiophene ring containing S1. Disorder in unbound thiophene rings has previously been observed with this ligand (Chapters 2 and 3), but in this case there is disorder in a bound thiophene ring. The major component is a three-coordinate Cu(I) complex, where the sulfur of the S1 thiophene ring is oriented away from the Cu center (Figure 4-2 (a)). The minor component has the S1 thiophene rotated so the sulfur is bound to the copper (Figure 4-2 (b)). As the major component is only bound through the phosphorus, it will continue to be referred to as [Cu(phen)PT_3-*P*](PF_6) throughout this Chapter. Additionally, this solid-state structure does not necessarily represent the species present in solution. The $^{31}P\{^1H\}$ NMR spectrum shows a single broad peak, along with the signals from the counter ion. Broadening of the ^{31}P NMR spectrum is caused by the quadruple ^{63}Cu and ^{65}Cu nuclei, both with I=3/2 and natural abundance of 69% and 31%, respectively.[253]

In the three-coordinate species, the Cu center is in a distorted trigonal-planar environment. The sum of the bond angles around the Cu(I) center is 349.21° (Table 4-2). The coordinated phosphorus is not in the plane with the Cu and phen ligand, instead it is above the plane by about 28°. The Cu – N bond lengths (Table 4-2) are similar to those reported for other complexes containing Cu – N_{phen} bonds.[94] The Cu – P bond, 2.1793(7) Å in length, is shorter than other Cu – P bonds in either bidentate phosphine or PPh_3 ligands,[94, 250, 252, 264] as seen for [Cu(dmp)(MeCN)PT_3-*P*](PF_6) as well. Here, the Cu – P bond is shorter than in the complex containing dmp, potentially due to steric effects due to the methyl groups in the dmp complex. The torsion angles here are about 48° and 21° for the S1 – C4 – C5 – S2 and S2 – C8 – C9 –S3 angles, respectively (Table 4-2). These values are very similar to those for [Cu(dmp)(MeCN)PT_3-*P*](PF_6).

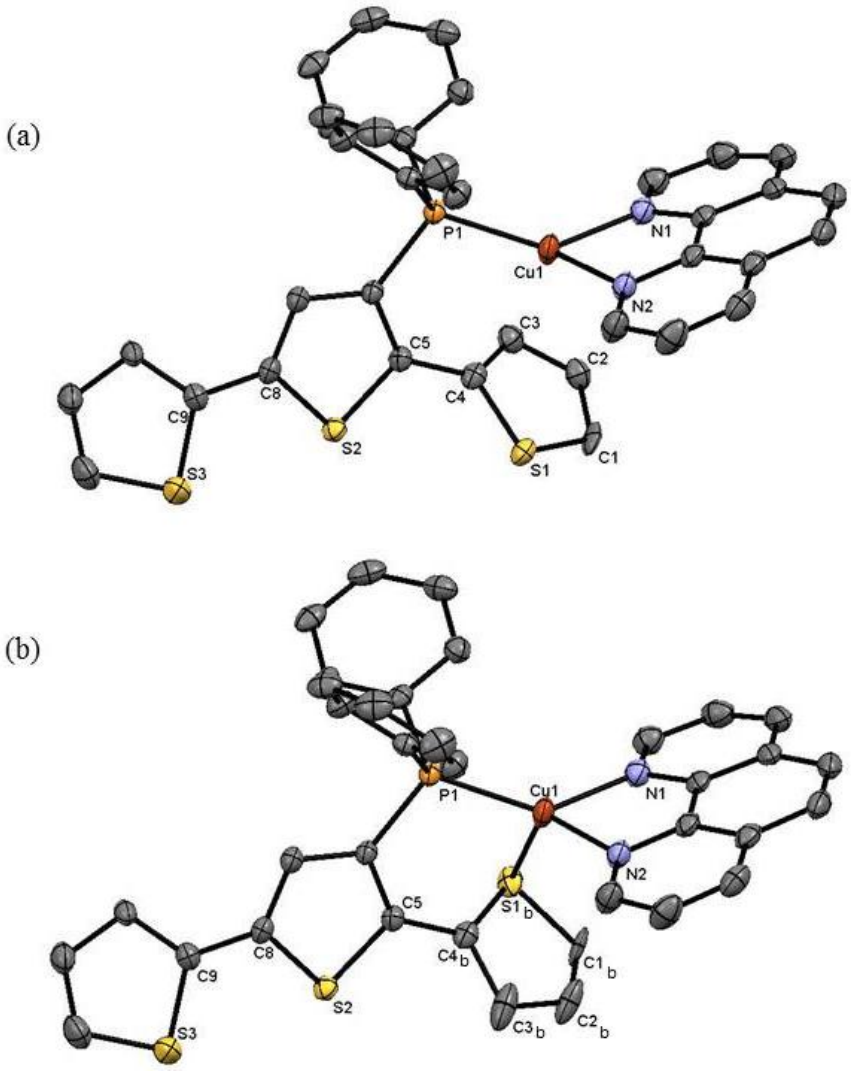

Figure 4-2 Solid-state structure of [Cu(phen)PT_3-*P*](PF_6), (**76**), showing (a) the major disorder fragment and (b) the minor fragment. Hydrogen atoms and counterions were removed for clarity. Thermal ellipsoids are drawn at 50% probability.

Table 4-2 Selected bond lengths and angles for [Cu(phen)PT_3-*P*](PF_6), (**76**).

Bond Lengths (Å)			
Cu1 – N1	2.047(2)	C1 – C2	1.393(12)
Cu1 – N2	2.036(2)	C2 – C3	1.414(14)
Cu1 – P1	2.1793(7)	C3 – C4	1.398(12)
Cu1 – S1b	2.548(16)	C4 – C5	1.461(3)
S1 – C1	1.729(9)	S1 – C4	1.706(3)
Bond Angles (°)			
N1 – Cu1 – N2	82.60(9)	P1 – Cu1 – S1b	94.0(3)
N1 – Cu1 – S1b	89.2(3)	P1 – Cu1 – N2	129.15(7)
N2 – Cu1 – S1b	121.4(3)	P1 – Cu1 – N1	137.46(7)
Torsion Angles (°)			
S1 – C4 – C5 – S2	47.7(3)	S2 – C8 – C9 – S3	21.4(3)
S1b – C4b – C5 – S2	132.5		

The minor component in the crystal structure, with the ligand bound in a *PS* mode, forms a distorted tetrahedral environment around the copper. The Cu – S bond is 2.548(16) Å, which is similar to other copper(I) – thiophene bonds,[265] although few complexes of this type have been reported. Common Cu – S distances for tetrahedral complexes (where the S is not part of a thiophene ring) are in the range of 2.27-2.5 Å,[266] though bonds up to 3.01 Å in length have been reported.[265] The bound thiophene ring is tilted out of the plane of the Cu – S bond by 85.38°, greater than what was observed for Ru(II), Os(II) and Ir(III) complexes discussed in previous Chapters. This tilting occurs to reduce unfavorable π antibonding interactions.[150, 151] The S1b – C4b – C5 – S2 torsion angle is 132.5°, which is very similar to the torsion angle in of the S1 ring in its other orientation. The binding of the thiophene ring to the copper does not appear to increase the rings' co-planarity, and therefore does not alter the amount of π – orbital overlap.

Section 4.3.3– Cyclic Voltammetry

The electrochemical properties of [Cu(phen)PT_3-*P*](PF_6) in two different solvents, CH_3CN and CH_2Cl_2, were probed at room temperature using cyclic voltammetry. The

cyclic voltamograms display some interesting differences in the different solvents. Attempted electropolymerization in both DCM and CH_3CN was unsuccessful.

In CH_3CN, four irreversible oxidation waves are observed (Table 4-3, Figure 4-3). The waves at 1.19 V and 1.74 V are quite prominent. The wave at 1.62 V appears only as a shoulder on the wave at 1.74 V. Other phosphine dimiine mixed copper(I) complexes in CH_3CN show irreversible waves between 0.50 and 1.40 Volts (vs SCE) that are assigned as Cu(I)/Cu(II) oxidation.[240] Typically, the Cu(I)/Cu(II) oxidation are the lowest potential oxidation waves observed. However, in the investigations of PT_3 complexed to ruthenium, osmium and iridium, the PT_3 based redox has been attributed as the lowest potential oxidation wave. Here, ligand-based and copper oxidation waves are both possible. Although it is difficult at present to make definitive assignments, the wave at 1.19 V may be a PT_3 based oxidation, and the wave at 1.74 V may be a Cu(I)/Cu(II) oxidation. The untethered PT_3 ligand has an oxidation at 1.30 V vs SCE, [56] and in Chapter 2, the value of the PT_3 oxidation ranged from 0.28 V to 1.48 V, dependent on metal center and coordination mode. Repeated scans show a decrease in the current and disappearance of the features. This may be caused by a non-conductive film coating the electrode, or potentially be due to decomposition from an unstable Cu(II) species being produced.

Table 4-3 Cyclic voltammetry data of [Cu(phen)PT_3-*P*](PF_6), (**76**).[a]

Solvent	$E_{1/2}$ ±0.01 V vs. SCE
CH_3CN	+1.19 [b]
	+1.62 [b]
	+1.74 [b]
	+2.03 [b]
CH_2Cl_2	+0.23
	+0.62

[a]Measurements carried out in solution containing 0.1 M [(*n*-Bu)$_4$N]PF_6 supporting electrolyte [b]Irreversible wave, E_p.

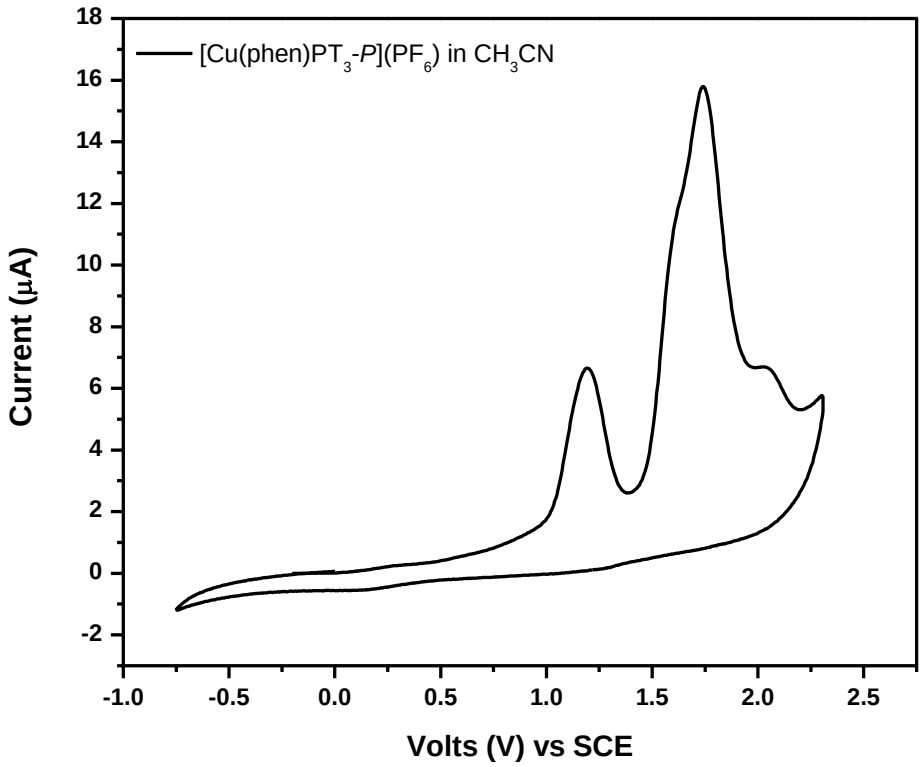

Figure 4-3 Cyclic voltammogram of [Cu(phen)PT_3-*P*](PF_6), (**76**), in CH_3CN, 0.1 M $TBAPF_6$, 100mV/s scan rate, PT disc working electrode, Pt mesh counter electrode and silver wire reference electrode.

In CH_2Cl_2, on the other hand, quasi-reversible waves are observed. The redox waves occur at 0.23 and 0.62 V vs SCE, with the lower potential wave having greater current associated with it. There may also be two reductions occurring very close together near 0.09 V, as the shape of the peak looks slightly distorted. [$Cu(phen)_2$](PF_6) has a reversible wave at 0.54 V vs SCE, attributed to the Cu(II)/Cu(I) redox couple.[267] It is possible that the wave at 0.62 V is from a Cu(I)/Cu(II) oxidation, and the wave at 0.23 V is PT_3 ligand-based. In the other complexes containing PT_3 that have been investigated, the wave occurring at the lowest potential has been assigned to a ligand-based PT_3 process. In this case, the binding mode, coordination environment and metal are all different. The [$Os(bpy)_2PT_3$-*PC*](PF_6) complex (**55**, Chapter 2) shows a reversible wave at 0.28 V, that is assigned as PT_3 based redox wave, with support of DFT calculations. This is close to the lowest redox wave observed here.

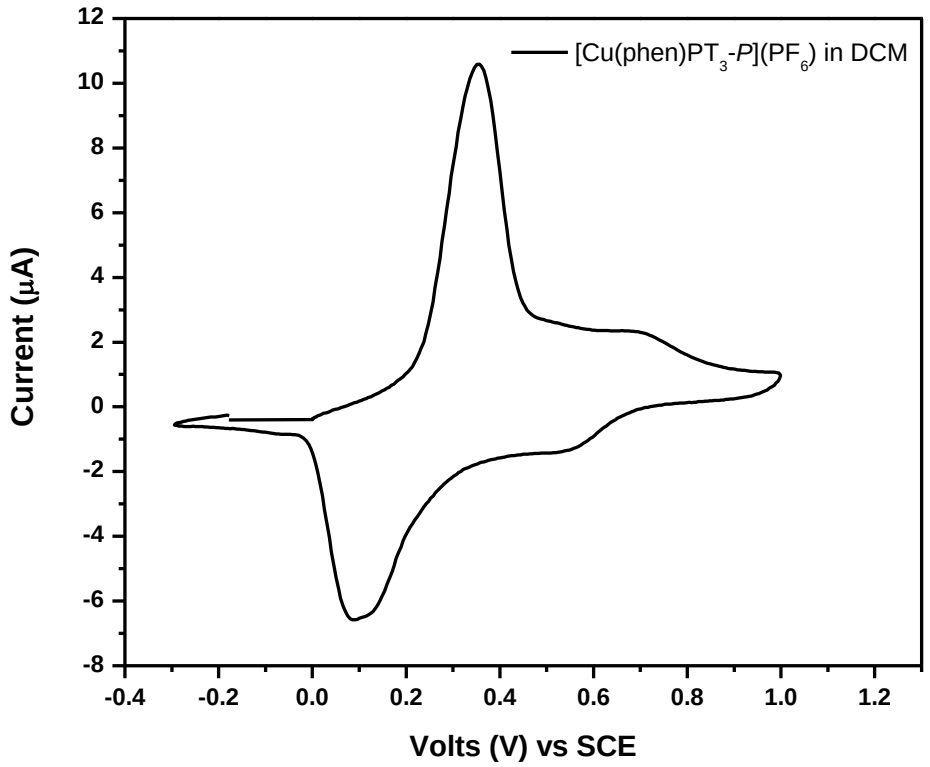

Figure 4-4 Cyclic voltammogram of [Cu(phen)PT_3-*P*](PF_6), (**76**), in CH_2Cl_2, 0.1 M $TBAPF_6$, 100mV/s scan rate, PT disc working electrode, Pt mesh counter electrode and silver wire reference electrode.

Alternatively, it is possible that the wave at 0.62 V is a decomposition product, as the current associated with that wave is much smaller than the oxidation at 0.23 V, suggesting that the waves are not both due to one electron processes.

Section 4.3.4– Electronic Absorption Spectra

The UV-vis absorption spectrum of [Cu(dmp)(MeCN)PT_3-*P*](PF_6) in CH_3CN is shown in Figure 4-5. The absorption spectrum of [Cu(dmp)(MeCN)PT_3-*P*](PF_6) contains two major bands, a band at 274 nm assigned to the $\pi \rightarrow \pi^*$ transition of the dimethylphenanthroline (dmp) group, and a lower energy band with λ_{max} = 348 nm, possibly due to a $\pi \rightarrow \pi^*$ transition of the terthienyl ligand. This absorption occurs at a similar wavelength to those of the uncomplexed PT_3 ligand and the iridium complexes (Chapter 3), that are assigned as ligand-based transitions. The UV-vis spectrum of [Cu$(dmp)_2$](PF_6) has a major band at 454 nm assigned as an metal to ligand charge transfer (MLCT) transition, and a band in the UV region assigned as a $\pi \rightarrow \pi^*$ transition

in the ligand.[267] In [Cu(dmp)(MeCN)PT_3-*P*](PF_6), there is also a weak band at 450 nm. This has been assigned as a MLCT transition. In other Cu(I) complexes, the intensity of this low energy band has been attributed to the degree of distortion the system undergoes.[268-270] It is possible the band at 450 nm is from a small amount of the homoleptic [$Cu(dmp)_2$](PF_6) complex forming in solution, but with time, the relative intensity of this band does not change. In DCM, the spectrum is similar, except the intensity of the band at 450 nm is reduced. After several days in solution, slight changes are observed; the band at 350 nm shifts to higher energy, perhaps due to ligand dissociation.

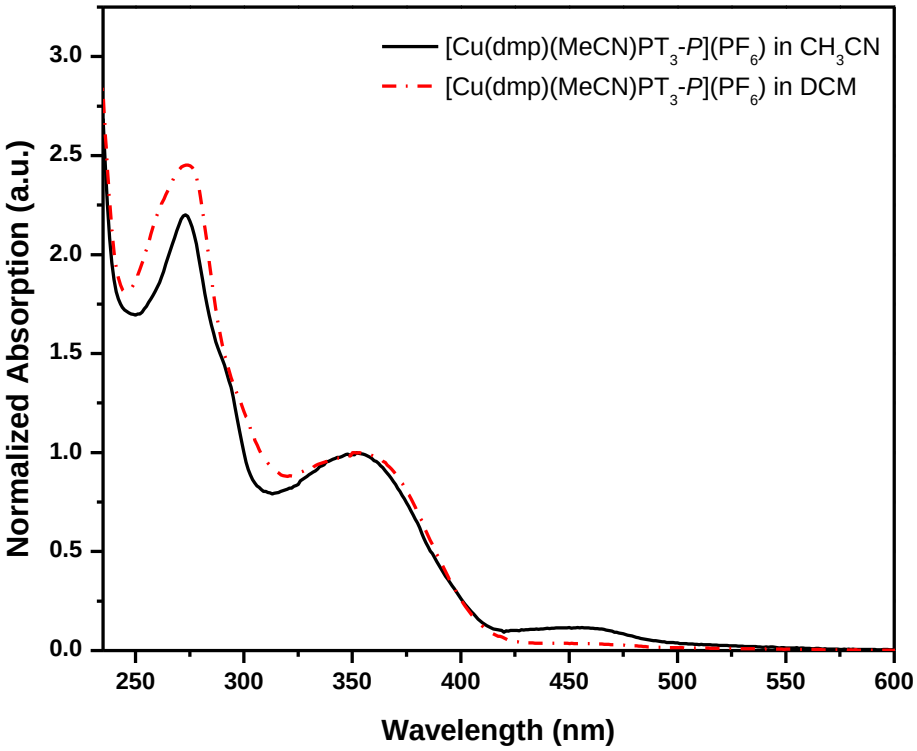

Figure 4-5 Solution absorption spectrum of [Cu(dmp)(MeCN)PT_3-*P*](PF_6), (**75**), in CH_3CN (black) and CH_2Cl_2 (red).

As with the [Cu(dmp)(MeCN)PT_3-*P*](PF_6) complex, [Cu(phen)PT_3-*P*](PF_6) exhibits two main absorption bands; one at 350 nm and the other at 265 nm. These bands are possibly due to a $\pi \rightarrow \pi^*$ transition of the PT_3 ligand, and a $\pi \rightarrow \pi^*$ transition of the phenanthroline group, respectively. In CH_3CN, a very weak shoulder at 450 nm is observed, assigned as a MLCT transition. The UV-vis spectrum of [$Cu(phen)_2$](PF_6) in

acetonitrile exhibits a main peak near 458 nm and a lower energy shoulder, both of which are assigned as MLCT states.[267, 269] Comparing the UV-vis spectra of [Cu(phen)PT_3-*P*](PF_6) to [Cu(dmp)(MeCN)PT_3-*P*](PF_6), there are only a few differences. The $\pi \rightarrow \pi^*$ transition of the diimine ligand has shifted, as a different diimine ligand is present, and the band near 450 nm is less intense. The observance of this lower energy band in the [Cu(phen)PT_3-*P*](PF_6) is further evidence that the band at 450 nm in [Cu(dmp)(MeCN)PT_3-*P*](PF_6) is not from a small amount of [Cu(dmp)$_2$](PF_6) forming, but from the complex itself as no evidence of the homoleptic copper(I) phenanthroline complex was observed. The [Cu(phen)PT_3-*P*](PF_6) spectra is reminiscent of [Cu(dmp)(MeCN)PT_3-*P*](PF_6), and it is possible that a CH_3CN group may weakly coordinate to the three-coordinate copper center in [Cu(phen)PT_3-*P*](PF_6).

In CH_2Cl_2, the $\pi \rightarrow \pi^*$ transition of the phen group appears to red shift slightly. The band near 350 nm does not shift much, and the shoulder at 450 nm vanishes.

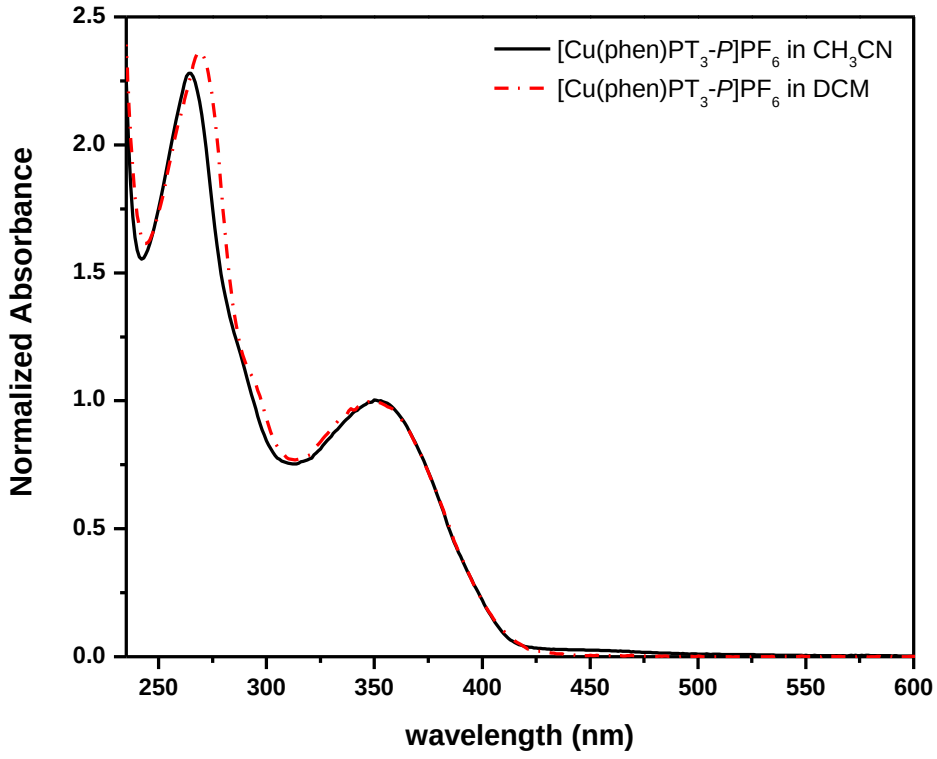

Figure 4-6 Solution absorption spectra of [Cu(phen)PT_3-*P*](PF_6), (**76**), in CH_3CN (black) and CH_2Cl_2 (red).

Section 4.3.5 – Emission Spectra

Excitation of [Cu(dmp)(MeCN)PT_3-*P*](PF_6) at 350 nm in argon-sparged CH_3CN shows weak emission centered at 441 nm, with a shoulder around 550 nm (Figure 4-7). The presence of oxygen did not have a significant effect on the emission. In CH_2Cl_2 however, the lower energy shoulder is not observed (Figure 4-7), even in argon-sparged solutions. [$Cu(dmp)_2$](PF_6) displays emission at 740 nm in DCM.[267] There is no evidence of this band when the solution is excited at 350 nm or 450 nm, even after the solution was left for several days. However, when excited at 450 nm, a very weak band is observed at about 519 nm.

Emission of [Cu(phen)PT_3-*P*](PF_6) in CH_3CN is weak. A peak at 442 nm is observed along with a shoulder at 550 nm, when excited at 350 nm (Figure 4-8). The observed emission is similar to that observed for [Cu(dmp)(MeCN)PT_3-*P*](PF_6). It is possible CH_3CN is binding weakly to the three-coordinate copper species, in which case spectroscopic similarities to [Cu(dmp)(MeCN)PT_3-*P*](PF_6) would be expected. When excited at 350 nm in a DCM solution, the emission is more intense, and the shoulder at lower energy is no longer visible (Figure 4-8). CH_3CN is considered a coordinating solvent, while DCM is considered non-coordinating. The emission spectrum of [Cu(phen)PT_3-*P*](PF_6) was also obtained in other coordinating solvents, pyridine (py) and methanol (MeOH). No evidence of the lower energy shoulder (at 550 nm) is observed in these solvents (Table 4-4). These bands are not sensitive to the presence of oxygen. No emission is observed for [$Cu(phen)_2$](PF_6).[267]

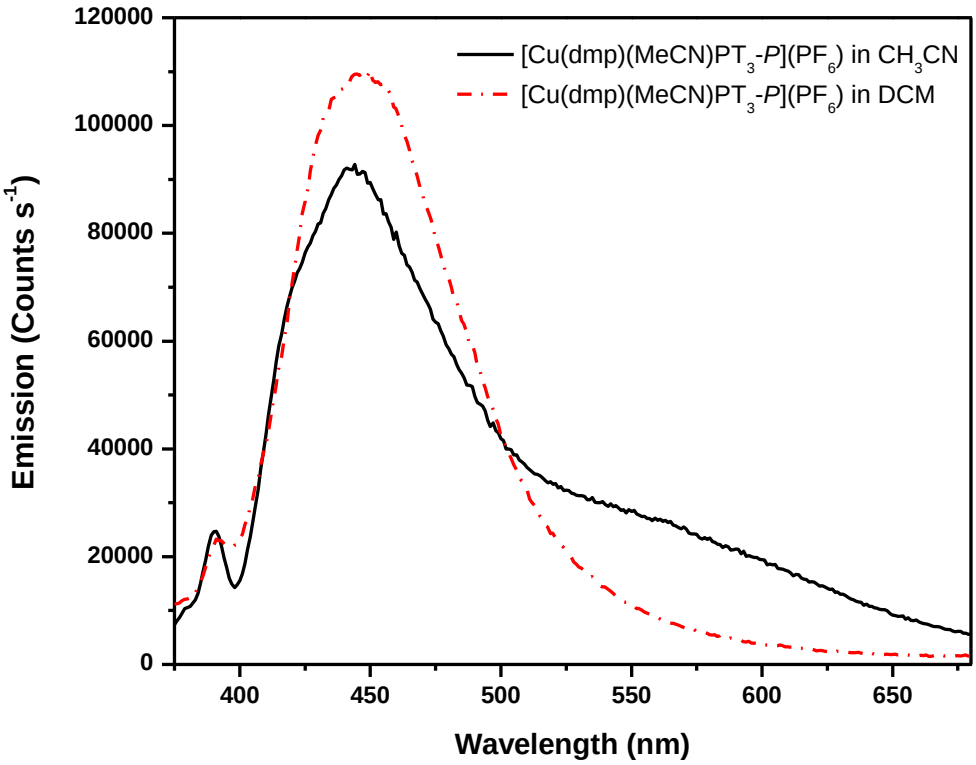

Figure 4-7 Emission spectra of [Cu(dmp)(MeCN)PT_3-*P*](PF_6), (**75**), in CH_3CN (black) and CH_2Cl_2 (red).

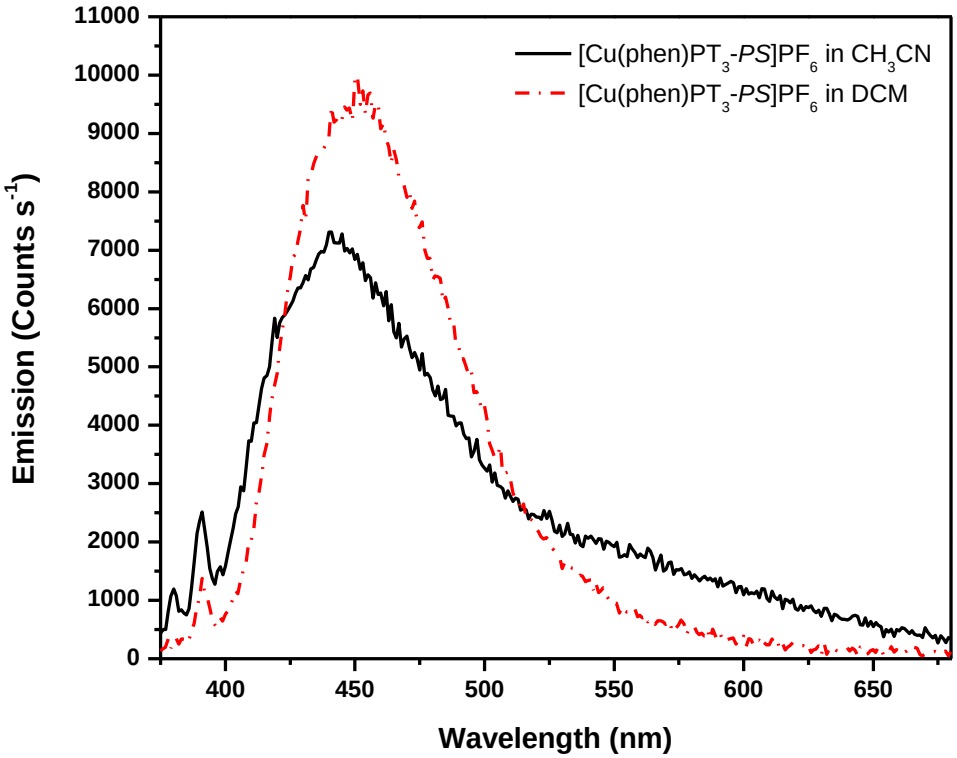

Figure 4-8 Emission spectra of [Cu(phen)PT_3-*P*](PF_6), (**76**), in CH_3CN (black) and CH_2Cl_2 (red).

Many complexes of the type [Cu(N^N)(P^P)](PF_6) exhibit emission between 560-700 nm in DCM.[94] As the emission observed for both [Cu(dmp)(MeCN)PT_3-*P*](PF_6) and [Cu(phen)PT_3-*P*](PF_6) occurs at higher energy, and is not sensitive to the presence of oxygen, it is likely a singlet ligand-based emission that is observed. Additionally, the emission lifetimes are very short (< 2 ns).

Table 4-4 Photophysical data for [Cu(dmp)(MeCN)PT_3-*P*](PF_6), (**75**), and [Cu(phen)PT_3-*P*](PF_6), (**76**), in various solvents.

Complex	Solvent	Abs λ (nm)	Em λ (nm)	Φ_{em}	τ_{TA}(μs)
75	CH_3CN	274, 293, 248, 450	441, 550 (sh)	---	8
75	CH_2Cl_2	274, 294, 351, 450	448	---	40
76	CH_3CN	267, 286, 350, 449	442, 550 (sh)	0.003	8
76	CH_2Cl_2	267, 290, 349	447	0.004	50
76	CH_3OH	268, 289, 347	430(sh), 447	---	4
76	Pyridine	348[b]	448	---	34

[a] Measurements carried out in argon-sparged solutions at room temperature [b] Solvent cut off at 330 nm.

Section 4.3.6– Transient Absorption Spectra

The transient absorption spectra of [Cu(dmp)(MeCN)PT_3-*P*](PF_6) in CH_3CN is show in Figure 4-9 (a). The TA spectra of [Cu(dmp)$_2$](PF_6) shows an absorption near 350 nm, a strong bleach centered near 450 nm and a broad absorption above 500 nm. The absorptions are attributed to reduced ligand.[267, 271, 272] In [Cu(dmp)(MeCN)PT_3-*P*](PF_6), a bleach is not observed, and the absorption band starts around 400 nm. Additionally, the shape is similar to that observed for the PT_3 ligand (Chapter 2). In this case, the complex decays monoexponentially with a lifetime of 8 μs under argon (Appendix, Figure A-15), in a CH_3CN solution. In an argon-sparged DCM solution, a new shoulder is observed around 600 nm (Figure 4-9 (b)). The excited state lifetime of the complex is enhanced, and both bands exhibit similar monoexponential decays (Table 4-4, Appendix Figures A-16 and A-17). The transient absorption spectra and decay lifetime of PT_3 are similar in CH_3CN and CH_2Cl_2 (Appendix, Figures A-18 to A-21), but exhibit longer lifetimes in argon-sparged solution than in nitrogen-sparged solution (Chapter 2).

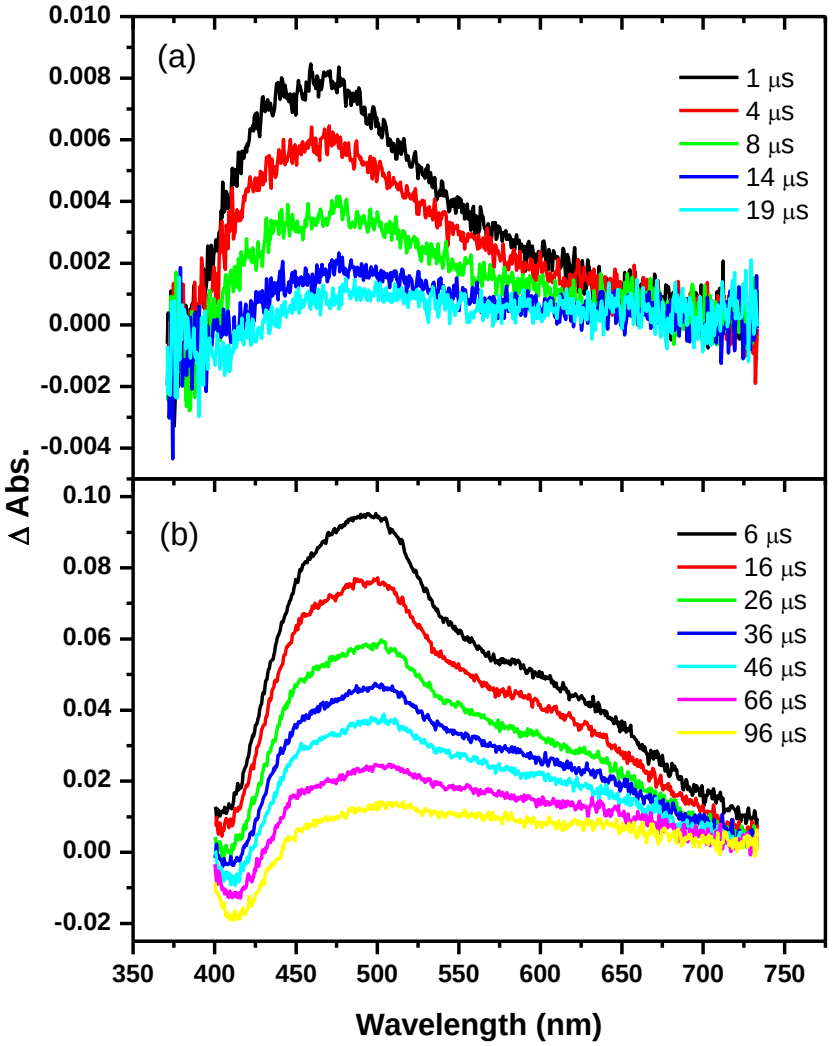

Figure 4-9 Transient absorption spectra of [Cu(dmp)(MeCN)PT_3-*P*](PF_6), (**75**), in (a) argon-sparged CH_3CN and (b) argon-sparged CH_2Cl_2.

The transient absorption spectra of [Cu(phen)PT_3-*P*](PF_6) obtained in a CH_3CN solution show a broad absorption between 400 – 600 nm (Figure 4-10 (a)), reminiscent of that seen for the previous complex, [Cu(dmp)(MeCN)PT_3-*P*](PF_6), and thus the PT_3 ligand. This complex has a lifetime of 8 μs when sparged with argon (Appendix, Figure A-22). The lifetime decreases in the presence of oxygen, suggesting a triplet state. The transient absorption spectra reported between 500 and 750 nm of [Cu(phen)$_2$](PF_6) shows a broad band with a maximum near 550 nm.[269]

When the TA spectroscopy was performed on the complex in an argon-sparged DCM solution, the bands broadened, with a new shoulder appearing which absorbs out to

700 nm (Figure 4-10 (b)). Both bands decay with the same lifetime, suggesting that each band originates from the same species. Again in this case, the lifetime (about 50 µs, Table 4-4, Appendix, Figures A-23 and A-24) is substantially longer than what was observed for the CH_3CN solution. Once again, this may be due to the acetonitrile coordinating weakly, allowing for a non-radiative decay pathway. Alternatively, the DCM stabilizies an excited state, allowing for an equilibrium between two excited states to occur.

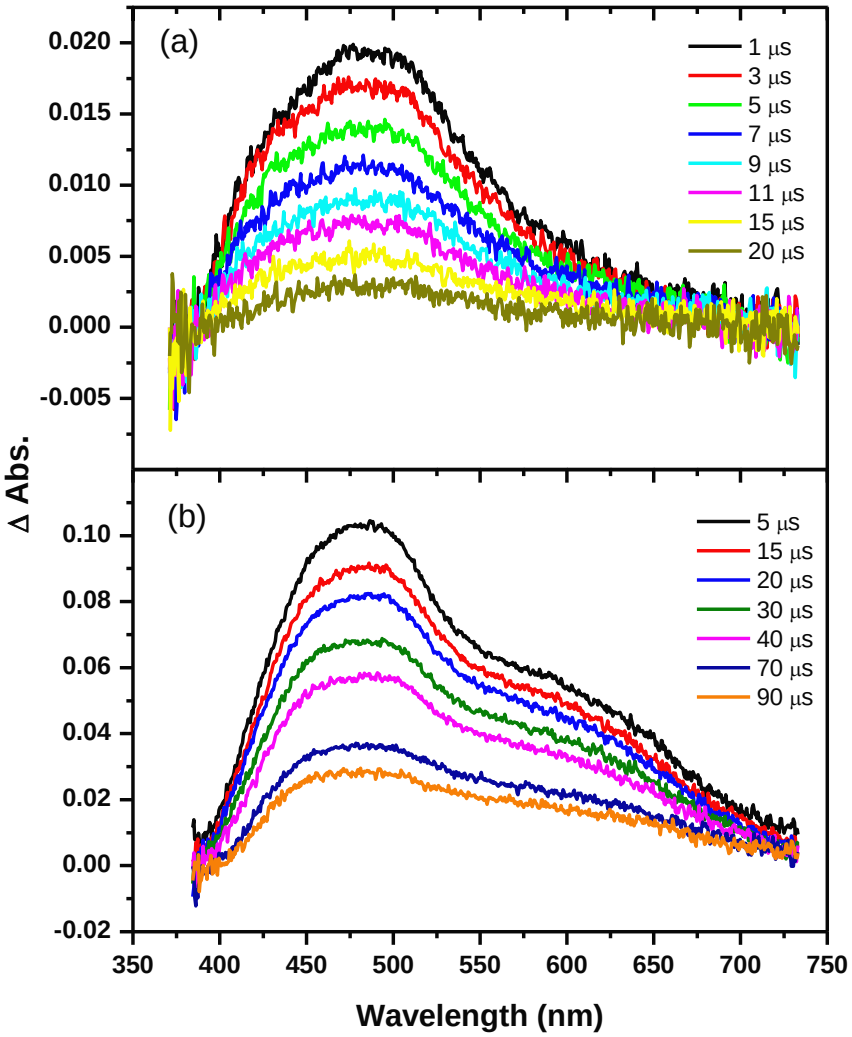

Figure 4-10 Transient absorption spectra of [Cu(phen)PT_3-*P*](PF_6), (**76**), in (a) argon-sparged CH_3CN and (b) argon-sparged CH_2Cl_2.

Previous experiments have shown that Cu(I) diimine complexes have shorter lifetimes in strongly coordinated solvents, or weak bases, compared to non-coordinating ones.[269] The authors attribute this to exciplex formation (a five coordinate species), followed by non-radiative decay. In this case, the lifetime of [Cu(phen)PT_3-*P*](PF_6) in MeOH was decreased (Table 4-4, Appendix Figures A-25 to A-26). Methanol is known to induce solvent quenching in some species.[94] This suggests that the ligands in this complex are bulky enough to suppress some exciplex formation (the complex still exhibits a relatively long lifetime), but not bulky enough to completely prevent it. In pyridine, the transient absorption resembles that of the transient in CH_3CN (Appendix Figure A-27) but the excited state lifetime is more similar to that in CH_2Cl_2 (Table 4-4, Appendix Figure A-28). The differences in the lifetimes observed for [Cu(phen)PT_3-*P*](PF_6) in CH_3OH and CH_3CN (4 and 8 μs) compared to pyridine and CH_2Cl_2 (34 and 50 μs) may be related to the dielectric constant of the solvent. Previous work has suggested a decreasing decay constant with increasing dielectric constant is indicative of polar character in the excited state.[273] In this case, there may be a charge transfer state close in energy to the triplet ligand state. In polar media, the CT state is stabilized, causing the energy to funnel from the ^{3}LC state to the CT state, which then decays very fast via a non-radiative pathway, thus shortening the observed lifetime of the triplet ligand localized state.

Section 4.4 – Conclusions

Two mixed-ligand copper(I) complexes containing the diphenylphosphino-terthiophene ligand were synthesized: [Cu(dmp)(MeCN)PT_3-*P*](PF_6) and [Cu(phen)PT_3-*P*](PF_6). The PT_3 ligand bound only through the P in [Cu(dmp)(MeCN)PT_3-*P*](PF_6), whereas the solid-state structure of [Cu(phen)PT_3-*P*](PF_6) indicated a minor component that exhibited *PS* coordination, in addition to the monodentate P bound structure. Oxidation potentials of [Cu(phen)PT_3-*P*](PF_6) were obtained using cyclic voltammetry in two different solvents, and in each case the complexes did not electropolymerize. The absorption spectra of [Cu(dmp)(MeCN)PT_3-*P*](PF_6) and [Cu(phen)PT_3-*P*](PF_6) were dominated by $\pi \rightarrow \pi^*$ transitions. All of the complexes were weakly emissive and

emission was assigned as PT_3 ligand-based. In CH_3CN, a low energy shoulder was observed in addition to the higher energy band, but the lower energy band was not observed in CH_2Cl_2. Transient absorption spectra show all complexes had a ligand localized excited state. However, the lifetime of the excited state varied greatly depending upon solvent (about 8 μs for both complexes in CH_3CN, and 40 or 50 μs in CH_2Cl_2 for [Cu(dmp)(MeCN)PT_3-*P*](PF_6) and [Cu(phen)PT_3-*P*](PF_6), respectively). The shape of the transient absorption spectra also varied with solvent; a shoulder near 600 nm was observed when the spectrum was recorded in CH_2Cl_2, but not in CH_3CN.

CHAPTER 5

CONCLUSIONS AND PERSPECTIVES

Ru(II), Os(II), Ir(III) and Cu(I) phosphine(terthiophene) complexes were synthesized and their photophysical and electrochemical properties were studied. Type I complexes containing iridium and copper metal centers were obtained when the PT_3 ligand bound to the metal via the phosphorus. Bidentate coordination of PT_3 to ruthenium, osmium and iridium resulted in the thiophene backbone being directly bound to the metal, via the sulfur or a carbon atom, to produce Type II complexes.

The coordination mode of PT_3 is central to the properties observed for these complexes. The obtained solid state structures indicate the interannular thiophene torsion angles are highly dependent on binding mode. In general, the *PC* bound complexes display increased co-planarity, which is partly reflected in the lower energy absorptions and emission bands. The complexed metal group is also important. Changing from a *bis*(bipyridine) Ru(II) group ($Ru(bpy)_2^{2+}$) to an $Os(bpy)_2^{2+}$ group leads to an increased absorption across the visible region due to enhanced spin orbit coupling. In comparison, incorporation of an $Ir(ppz)_2^{+}$ group does not result in improved absorption compared to the Ru(II) complexes. These complexes would ideally absorb out to 920 nm. Adding substituents to the bpy, ppy or ppz ligands may improve the absorption across the visible region, and beyond into the near-IR.

The cyclic voltammograms of the complexes generally show irreversible oxidation peaks. Upon *PC* coordination, the PT_3 redox potential is lowered, and in the Ru(II) and Os(II) complexes, reversible redox peaks are observed. The phosphorus bound Cu (I) phenanthroline complex displays irreversible oxidation waves in CH_3CN but shows quasi-reversible redox waves in DCM. Regardless of the binding mode of PT_3 and solvent used, these complexes do not electropolymerize.

Changes in the coordination mode are also reflected in the excited state properties. The excited state of the group 8 complexes is altered based on binding mode. For the Ru(II) and Os(II) (phosphine)terthiophene *PS* complexes, the excited state is a ligand localized triplet state, in contrast to the *PC* complexes which exhibit a charge

separated state (charge transfer from metal/PT_3 HOMO to bipyridyl LUMO). In these complexes it is feasible that charge injection could occur when the complexes are attached to a semiconductor, such as TiO_2. Unlike the group 8 metal complexes, the transient absorption spectra of all the iridium and copper complexes show a ligand localized excited state, regardless of coordination mode. These complexes would not perform well in a DSSC as charge separation does not occur in ligand localized triplet states.

It would be beneficial to probe the application of some of the complexes that have been synthesized as sensitizers in DSSCs. In order to do so, the diimine, ppy or ppz ligands would have to be substituted with carboxylate groups to allow attachment to a TiO_2 surface. This could be achieved by first synthesizing the methyl ester derivative as this is easier to characterize than the corresponding acid or carboxylate salt. If the electrochemical and photophysical properties are still favorable, then incorporation into a DSSC could be pursued. Additionally, only one ligand bearing carboxylate groups is required for attachment to TiO_2. Therefore, the use of alternative ligands in place of the second bpy/ppz/ppy group could be investigated.

Although the specific coordination mode employed doesn't result in a change in the excited state in the Ir(III) cyclometalated complexes (all triplet ligand based), the excited state lifetimes are dependent on coordination mode. The complexes in which PT_3 is coordinated in a monodentate fashion via the P atom only exhibit the longest lifetimes, presumably since in these complexes the tether is only through a single diphenyl phosphine linker (Type I vs. Type II complexes). In the copper complexes, the solvent used affects the excited state lifetimes, potentially due to exciplex formation or solvent stabilization. The incorporation of a bidentate diphosphine ligand, such as 3,3″-*bis*(diphenylphosphino)-2,2′:5′,2″-terthiophene[274] (P_2T_3, Chart 5-1) may be beneficial as binding through both phosphines may induce less strain than binding in a *PS* fashion. The extra diphenylphosphine group would add extra steric bulk, which could reduce any distortions or prevent exciplex formation.

Chart 5-1 Ref.[274]

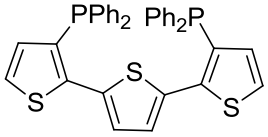

Overall, Type II complexes are found to more strongly alter the properties of the substituted terthiophene and display more π orbital overlap compared to a metal group attached only via the pendant diphenylphosphino group (Type I complex). The metal type and coordination mode of the PT_3 ligand significantly alter the photophysical properties of these complexes, as observed in the absorption, emission and transient absorption spectra of the complexes.

REFERENCES

(1) Lewis, N. S.; Nocera, D. G. *Proc. Natl. Acad. Sci. U. S. A.* **2006**, *103*, 15729-15735.

(2) Scholes, G. D.; Fleming, G. R.; Olaya-Castro, A.; van Grondelle, R. *Nat. Chem.* **2011**, *3*, 763-774.

(3) Eisenberg, R.; Nocera, D. G. *Inorg. Chem.* **2005**, *44*, 6799-6801.

(4) Fichou, D. In *Handbook of Oligo- and Polythiophenes;* Wiley-VCH: Weinheim, Germany, 1999.

(5) Wong, C. T.; Chan, W. K. *Adv. Mater.* **1999**, *11*, 455-459.

(6) Zhu, Y. B.; Millet, D. B.; Wolf, M. O.; Rettig, S. J. *Organometallics* **1999**, *18*, 1930-1938.

(7) Weinberger, D. A.; Higgins, T. B.; Mirkin, C. A.; Stern, C. L.; Liable-Sands, L. M.; Rheingold, A. L. *J. Am. Chem. Soc.* **2001**, *123*, 2503-2516.

(8) Zhu, S. S.; Swager, T. M. *Adv. Mater.* **1996**, *8*, 497-500.

(9) Higgins, T. B.; Mirkin, C. A. *Chem. Mater.* **1998**, *10*, 1589-1595.

(10) Perepichka, I. F.; Perepichka, D. F., Eds.; In *Handbook of Thiophene-Based Materials: Applications in Organic Electronic and Photonics, Volume 2: Properties and Applications;* John Wiley & Sons Ltd: United Kingdom, 2009.

(11) Chiang, C. K.; Fincher, C. R.,Jr.; Park, Y. W.; Heeger, A. J.; Shirakawa, A. H.; Louis, E. J.; Gau, S. C.; MacDiarmid, A. G. *Phys. Rev. Lett.* **1977**, *39*, 1098-1101.

(12) Shirakawa, H. *Angew. Chem. Int. Ed.* **2001**, *40*, 2575-2580.

(13) Heeger, A. J. *Angew. Chem. Int. Ed.* **2001**, *40*, 2591-2611.

(14) MacDiarmid, A. G. *Angew. Chem. Int. Ed.* **2001**, *40*, 2581-2590.

(15) Hall, N. *Chem. Commun.* **2003**, 1-4.

(16) "The Nobel Prize in Chemistry 2000". *http://www.nobelprize.org/nobel_prizes/chemistry/laureates/2000/* (accessed Feb. 27, 2012).

(17) Skotheim, T. A.; Elsenbaumer, R. L.; Reynolds, J. R., Eds.; In *Handbook of Conducting Polymers;* Marcel Dekker, Inc.: New York, 1998; Vol. 2nd Edition, Revised and Expanded.

(18) Elsenbaumer, R. L.; Jen, K. Y.; Oboodi, R. *Synth. Met.* **1986**, *15*, 169-174.

(19) Jen, K. Y.; Miller, G. G.; Elsenbaumer, R. L. *J. Chem. Soc. , Chem. Commun.* **1986**, 1346-1347.

(20) McCullough, R. D.; Tristram-Nagle, S.; Williams, S. P.; Lowe, R. D.; Jayaraman, M. *J. Am. Chem. Soc.* **1993**, *115*, 4910-4911.

(21) McCullough, R. D.; Lowe, R. D.; Jayaraman, M.; Anderson, D. L. *J. Org. Chem.* **1993**, *58*, 904-912.

(22) Krische, B.; Zagorska, M. *Synth. Met.* **1989**, *28*, C263-C268.

(23) Andersson, M. R.; Selse, D.; Berggren, M.; Järvinen, H.; Hjertberg, T.; Inganäs, O.; Wennerström, O.; Österholm, J. E. *Macromolecules* **1994**, *27*, 6503-6506.

(24) Yamamoto, T.; Sanechika, K.; Yamamoto, A. *J. Polym. Sci., Part C: Polym. Lett.* **1980**, *18*, 9-12.

(25) Kumada, M. *Pure Appl. Chem.* **1980**, *52*, 669-679.

(26) Lin, J. W. P.; Dudek, L. P. *J. Polym. Sci., Part A: Polym. Chem.* **1980**, *18*, 2869-2873.

(27) McCullough, R. D.; Lowe, R. D. *J. Chem. Soc., Chem. Commun.* **1992**, 70-72.

(28) McCullough, R. D.; Williams, S. P.; Tristram-Nagle, S.; Jayaraman, M.; Ewbank, P. C.; Miller, L. *Synth. Met.* **1995**, *69*, 279-282.

(29) Chen, T. A.; Wu, X. M.; Rieke, R. D. *J. Am. Chem. Soc.* **1995**, *117*, 233-244.

(30) Wolf, M. O. *Adv. Mater.* **2001**, *13*, 545-553.

(31) Stott, T. L.; Wolf, M. O. *Coord. Chem. Rev.* **2003**, *246*, 89-101.

(32) Moorlag, C.; Sih, B. C.; Stott, T. L.; Wolf, M. O. *J. Mater. Chem.* **2005**, *15*, 2433-2436.

(33) Perepichka, I. F.; Perepichka, D. F., Eds.; In *Handbook of Thiophene-Based Materials: Applications in Organic Electronic and Photonics, Volume 1: Synthesis and Theory;* John Wiley & sons Ltd: United Kingdom, 2009.

(34) Abd-El-Aziz, A. S.; Manners, I., Eds.; In *Frontiers in Transition Metal-Containing Polymers;* John Wiley & Sons, Inc.: Hoboken, New Jersey, 2007.

(35) Higgins, S. J.; Jones, C. L.; Francis, S. M. *Synth. Met.* **1999**, *98*, 211-214.

(36) Tan, L.; Curtis, M. D.; Francis, A. H. *Macromolecules* **2002**, *35*, 4628-4635.

(37) Byrne, P. D.; Mueller, P.; Swager, T. M. *Langmuir* **2006**, *22*, 10596-10604.

(38) Weinberger, D. A.; Higgins, T. B.; Mirkin, C. A.; Liable-Sands, L. M.; Rheingold, A. L. *Angew. Chem. Int. Ed.* **1999**, *38*, 2565-2568.

(39) Trouillet, L.; De Nicola, A.; Guillerez, S. *Chem. Mater.* **2000**, *12*, 1611-1621.

(40) Walters, K. A.; Trouillet, L.; Guillerez, S.; Schanze, K. S. *Inorg. Chem.* **2000**, *39*, 5496-5509.

(41) Araki, K.; Endo, H.; Masuda, G.; Ogawa, T. *Chem. Eur. J.* **2004**, *10*, 3331-3340.

(42) Zhu, S. S.; Kingsborough, R. P.; Swager, T. M. *J. Mater. Chem.* **1999**, *9*, 2123-2131.

(43) Nazeeruddin, M. K.; Kay, A.; Rodicio, I.; Humphrybaker, R.; Muller, E.; Liska, P.; Vlachopoulos, N.; Grätzel, M. *J. Am. Chem. Soc.* **1993**, *115*, 6382-6390.

(44) Chen, C. Y.; Wu, S. J.; Wu, C. G.; Chen, J. G.; Ho, K. C. *Angew. Chem. Int. Ed.* **2006**, *45*, 5822-5825.

(45) Majewski, M. B.; de Tacconi, N. R.; MacDonnell, F. M.; Wolf, M. O. *Inorg. Chem.* **2011**, *50*, 9939-9941.

(46) Hjelm, J.; Handel, R. W.; Hagfeldt, A.; Constable, E. C.; Housecroft, C. E.; Forster, R. J. *Inorg. Chem.* **2005**, *44*, 1073-1081.

(47) Zhu, X. J.; Holliday, B. J. *Macromol. Rapid Commun.* **2010**, *31*, 904-909.

(48) Lee, J. C.; Tomita, I.; Endo, T. *Macromolecules* **1998**, *31*, 5916-5919.

(49) Kang, B. S.; Kim, D. H.; Jung, T. S.; Jang, E. K.; Pak, Y.; Shin, S. C.; Park, D. S.; Shim, Y. B. *Synth. Met.* **1999**, *105*, 9-12.

(50) Jung, T. S.; Kim, J. H.; Jang, E. K.; Kim, D. H.; Shim, Y. B.; Park, B.; Shin, S. C. *J. Organomet. Chem.* **2000**, *599*, 232-237.

(51) Kingsborough, R. P.; Swager, T. M. *Chem. Mater.* **2000**, *12*, 872-874.

(52) Powell, A. B.; Bielawski, C. W.; Cowley, A. H. *J. Am. Chem. Soc.* **2010**, *132*, 10184-10194.

(53) Kean, C. L.; Miller, D. O.; Pickup, P. G. *J. Mater. Chem.* **2002**, *12*, 2949-2956.

(54) Pozo-Gonzalo, C.; Berridge, R.; Skabara, P. J.; Cerrada, E.; Laguna, M.; Coles, S. J.; Hursthouse, M. B. *Chem. Commun.* **2002**, 2408-2409.

(55) Chang, X.; Kim, M. Y.; Kim, Y. J.; Huh, H. S.; Lee, S. W. *Dalton Trans.* **2007**, 792-801.

(56) Clot, O.; Wolf, M. O.; Patrick, B. O. *J. Am. Chem. Soc.* **2001**, *123*, 9963-9973.

(57) Mucci, A.; Parenti, F.; Pigani, L.; Seeber, R.; Zanardi, C.; Pilo, M. I.; Spano, N.; Manassero, M. *J. Mater. Chem.* **2003**, *13*, 1287-1292.

(58) Zhang, F.; Goetz, G.; Winkler, H. D. F.; Schalley, C. A.; Bäuerle, P. *Angew. Chem. Int. Ed.* **2009**, *48*, 6632-6635.

(59) Zhang, F.; Bäuerle, P. *J. Am. Chem. Soc.* **2007**, *129*, 3090-3091.

(60) Milum, K. M.; Kim, Y. N.; Holliday, B. J. *Chem. Mater.* **2010**, *22*, 2414-2416.

(61) Chawdhury, N.; Kohler, A.; Friend, R. H.; Wong, W. Y.; Lewis, J.; Younus, M.; Raithby, P. R.; Corcoran, T. C.; Al-Mandhary, M. R. A.; Khan, M. S. *J. Chem. Phys.* **1999**, *110*, 4963-4970.

(62) Lewis, J.; Long, N. J.; Raithby, P. R.; Shields, G. P.; Wong, W. Y.; Younus, M. *J. Chem. Soc., Dalton Trans.* **1997**, 4283-4288.

(63) Sauvage, J. P.; Kern, J. M.; Bidan, G.; Divisia-Blohorn, B.; Vidal, P. L. *New J. Chem.* **2002**, *26*, 1287-1290.

(64) Vidal, P. L.; Billon, M.; Divisia-Blohorn, B.; Bidan, G.; Kern, J. M.; Sauvage, J. P. *Chem. Commun.* **1998**, 629-630.

(65) Vidal, P. L.; Divisia-Blohorn, B.; Bidan, G.; Kern, J. M.; Sauvage, J. P.; Hazemann, J. L. *Inorg. Chem.* **1999**, *38*, 4203-4210.

(66) Bäuerle, P.; Ammann, M.; Wilde, M.; Goetz, G.; Mena-Osteritz, E.; Rang, A.; Schalley, C. A. *Angew. Chem. Int. Ed.* **2007**, *46*, 363-368.

(67) Reddinger, J. L.; Reynolds, J. R. *Chem. Mater.* **1998**, *10*, 1236-1243.

(68) Kingsborough, R. P.; Swager, T. M. *J. Am. Chem. Soc.* **1999**, *121*, 8825-8834.

(69) Clot, O.; Akahori, Y.; Moorlag, C.; Leznoff, D. B.; Wolf, M. O.; Batchelor, R. J.; Patrick, B. O.; Ishii, M. *Inorg. Chem.* **2003**, *42*, 2704-2713.

(70) Stott, T. L.; Wolf, M. O.; Patrick, B. O. *Inorg. Chem.* **2005**, *44*, 620-627.

(71) Kuchison, A. M.; Wolf, M. O.; Patrick, B. O. *Inorg. Chem.* **2010**, *49*, 8802-8812.

(72) Sebastian, M.; Hissler, M.; Fave, C.; Rault-Berthelot, J.; Odin, C.; Reau, R. *Angew. Chem. Int. Ed.* **2006**, *45*, 6152-6155.

(73) Hobbs, M. G.; Baumgartner, T. *Eur. J. Inorg. Chem.* **2007**, 3611-3628.

(74) Li, G.; Bhosale, S.; Tao, S.; Guo, R.; Bhosale, S.; Li, F.; Zhang, Y.; Wang, T.; Fuhrhop, J. H. *Polymer* **2005**, *46*, 5299-5307.

(75) Shimidzu, T.; Segawa, H.; Wu, F. P.; Nakayama, N. *J. Photochem. Photobiol., A* **1995**, *92*, 121-127.

(76) Collins, G. E.; Campbell, W. M.; Officer, D. L.; Burrell, A. K. *Org. Biomol. Chem.* **2005**, *3*, 2075-2084.

(77) Lind, S. J.; Gordon, K. C.; Gambhir, S.; Officer, D. L. *Phys. Chem. Chem. Phys.* **2009**, *11*, 5598-5607.

(78) Segawa, H.; Wu, F. P.; Nakayama, N.; Maruyama, H.; Sagisaka, S.; Higuchi, N.; Fujitsuka, M.; Shimidzu, T. *Synth. Met.* **1995**, *71*, 2151-2154.

(79) O'Regan, B.; Grätzel, M. *Nature* **1991**, *353*, 737-740.

(80) Nazeeruddin, M. K.; Péchy, P.; Renouard, T.; Zakeeruddin, S. M.; Humphry-Baker, R.; Comte, P.; Liska, P.; Cevey, L.; Costa, E.; Shklover, V.; Spiccia, L.; Deacon, G. B.; Bignozzi, C. A.; Grätzel, M. *J. Am. Chem. Soc.* **2001**, *123*, 1613-1624.

(81) Nazeeruddin, M. K.; De Angelis, F.; Fantacci, S.; Selloni, A.; Viscardi, G.; Liska, P.; Ito, S.; Bessho, T.; Grätzel, M. *J. Am. Chem. Soc.* **2005**, *127*, 16835-16847.

(82) Chen, C. Y.; Wang, M.; Li, J. Y.; Pootrakulchote, N.; Alibabaei, L.; Ngoc-Le, C. H.; Decoppet, J. D.; Tsai, J. H.; Grätzel, C.; Wu, C. G.; Zakeeruddin, S. M.; Grätzel, M. *ACS Nano* **2009**, *3*, 3103-3109.

(83) Zeng, W.; Cao, Y.; Bai, Y.; Wang, Y.; Shi, Y.; Zhang, M.; Wang, F.; Pan, C.; Wang, P. *Chem. Mater.* **2010**, *22*, 1915-1925.

(84) Grätzel, M. *J. Photochem. Photobiol., C* **2003**, *4*, 145-153.

(85) Chou, C. C.; Wu, K. L.; Chi, Y.; Hu, W. P.; Yu, S. J.; Lee, G. H.; Lin, C. L.; Chou, P. T. *Angew. Chem. Int. Ed.* **2011**, *50*, 2054-2058.

(86) Bessho, T.; Yoneda, E.; Yum, J.; Guglielmi, M.; Tavernelli, I.; Imai, H.; Rothlisberger, U.; Nazeeruddin, M. K.; Grätzel, M. *J. Am. Chem. Soc.* **2009**, *131*, 5930-5934.

(87) Bomben, P. G.; Robson, K. C. D.; Sedach, P. A.; Berlinguette, C. P. *Inorg. Chem.* **2009**, *48*, 9631-9643.

(88) Wadman, S. H.; Kroon, J. M.; Bakker, K.; Lutz, M.; Spek, A. L.; van Klink, G. P. M.; van Koten, G. *Chem. Commun.* **2007**, 1907-1909.

(89) Yella, A.; Lee, H. W.; Tsao, H. N.; Yi, C.; Chandiran, A. K.; Nazeeruddin, M. K.; Diau, E. W. G.; Yeh, C. Y.; Zakeeruddin, S. M.; Grätzel, M. *Science* **2011**, *334*, 629-634.

(90) Hagfeldt, A.; Boschloo, G.; Sun, L.; Kloo, L.; Pettersson, H. *Chem. Rev.* **2010**, *110*, 6595-6663.

(91) Grätzel, M. *Acc. Chem. Res.* **2009**, *42*, 1788-1798.

(92) Polo, A. S.; Itokazu, M. K.; Iha, N. Y. M. *Coord. Chem. Rev.* **2004**, *248*, 1343-1361.

(93) Mayo, E. I.; Kilsa, K.; Tirrell, T.; Djurovich, P. I.; Tamayo, A.; Thompson, M. E.; Lewis, N. S.; Gray, H. B. *Photochem. Photobiol. Sci.* **2006**, *5*, 871-873.

(94) Cuttell, D.; Kuang, S. M.; Fanwick, P. E.; McMillin, D. R.; Walton, R. A. *J. Am. Chem. Soc.* **2002**, *124*, 6-7.

(95) Kalyanasundaram, K. In *Photochemistry of Polypyridine and Porphyrin Complexes;* Academic Press: London, 1992.

(96) Anderson, P. A.; Keene, F. R.; Meyer, T. J.; Moss, J. A.; Strouse, G. F.; Treadway, J. A. *J. Chem. Soc., Dalton Trans.* **2002**, 3820-3831.

(97) Liang, Y.; Feng, D.; Guo, J.; Szarko, J. M.; Ray, C.; Chen, L. X.; Yu, L. *Macromolecules* **2009**, *42*, 1091-1098.

(98) Howard, I. A.; Laquai, F.; Keivanidis, P. E.; Friend, R. H.; Greenham, N. C. *J. Phys. Chem. C* **2009**, *113*, 21225-21232.

(99) Clarke, T. M.; Durrant, J. R. *Chem. Rev.* **2010**, *110*, 6736-6767.

(100) Walters, K. A.; Ley, K. D.; Cavalaheiro, C. S. P.; Miller, S. E.; Gosztola, D.; Wasielewski, M. R.; Bussandri, A. P.; van Willigen, H.; Schanze, K. S. *J. Am. Chem. Soc.* **2001**, *123*, 8329-8342.

(101) Meyer, T. J. *Pure Appl. Chem.* **1986**, *58*, 1193-1206.

(102) Moorlag, C.; Clot, O.; Wolf, M. O.; Patrick, B. O. *Chem. Commun.* **2002**, 3028-3029.

(103) Moorlag, C.; Wolf, M. O.; Bohne, C.; Patrick, B. O. *J. Am. Chem. Soc.* **2005**, *127*, 6382-6393.

(104) Moorlag, C.; Sarkar, B.; Sanrame, C. N.; Baeuerle, P.; Kaim, W.; Wolf, M. O. *Inorg. Chem.* **2006**, *45*, 7044-7046.

(105) Kober, E. M.; Meyer, T. J. *Inorg. Chem.* **1982**, *21*, 3967-3977.

(106) Balazs, G. C.; del Guerzo, A.; Schmehl, R. H. *Photochem. Photobiol. Sci.* **2005**, *4*, 89-94.

(107) Carlson, B.; Phelan, G. D.; Kaminsky, W.; Dalton, L.; Jiang, X. Z.; Liu, S.; Jen, A. K. Y. *J. Am. Chem. Soc.* **2002**, *124*, 14162-14172.

(108) Nakabayashi, Y.; Nakamura, K.; Kawachi, M.; Motoyama, T.; Yamauchi, O. *J. Biol. Inorg. Chem.* **2003**, *8*, 45-52.

(109) Clot, O.; Wolf, M. O.; Yap, G. P. A.; Patrick, B. O. *J. Chem. Soc., Dalton Trans.* **2000**, 2729-2737.

(110) Sullivan, B. P.; Salmon, D. J.; Meyer, T. J. *Inorg. Chem.* **1978**, *17*, 3334-3341.

(111) Aranzaes, J. R.; Daniel, M. C.; Astruc, D. *Can. J. Chem.* **2006**, *84*, 288-299.

(112) *SAINT*, Version 7.46A. **1997-2007**.

(113) *SAINT*, Version 7.60A. **1997-2009**.

(114) *SAINT*, Version 7.03A. **1997-2003**.

(115) *SADABS*, Bruker Nonius area detector scaling and absorption correction, 2007/4. **2007**.

(116) *SADABS*, Bruker Nonius area detector scaling and absorption correction, 2008/1. **2008**.

(117) *SADABS*, Bruker Nonius area detector scaling and absoption correction, V2.10. **2003**.

(118) Altomare, A.; Burla, M. C.; Camalli, M.; Cascarano, G. L.; Giacovazzo, C.; Guagliardi, A.; Moliterni, A. G. G.; Polidori, G.; Spagna, R. *J. Appl. Crystallogr.* **1999**, *32*, 115-119.

(119) Bruno, I. J.; Cole, J. C.; Edgington, P. R.; Kessler, M.; Macrae, C. F.; McCabe, P.; Pearson, J.; Taylor, R. *Acta Crystallogr., Sect. B: Struct. Sci.* **2002**, *58*, 389-397.

(120) Least Squares function minimized: $\Sigma w(F_o^2 - F_c^2)^2$.

(121) Guerra, C. F.; Snijders, J. G.; te Velde, G.; Baerends, E. J. *Theor. Chem. Acc.* **1998**, *99*, 391-403.

(122) Guerra, C. F.; Visser, O.; Snijders, J. G.; te Velde, G.; Baerends, E. J. In *Methods and Techniques for Computational Chemistry;* Clementi, E., Corongiu, G., Eds.; STEF: Cagliari, Italy, 1995, pp 305-395.

(123) Baerends, E. J.; Ellis, D. E.; Ros, P. *Chem. Phys.* **1973**, *2*, 41-51.

(124) Boerrigter, P. M.; Velde, G. T.; Baerends, E. J. *Int. J. Quantum Chem.* **1988**, *33*, 87-113.

(125) Velde, G. T.; Baerends, E. J. *J. Comput. Phys.* **1992**, *99*, 84-98.

(126) Snijders, J. G.; Baerends, E. J.; Vernooijs, P. *At. Data Nucl. Data Tables* **1981**, *26*, 483-509.

(127) Krijn, J.; Baerends, E. J. *Fit Functions in the HFS Method*; Internal Report (in Dutch), Vrije Universiteit, Amsterdam, The Netherlands, 1984.

(128) Slater, J. C. In *Quantum Theory of Molecules and Solids;* McGraw-Hill: New York, 1974; Vol. 4.

(129) Vosko, S. H.; Wilk, L.; Nusair, M. *Can. J. Phys.* **1980**, *58*, 1200-1211.

(130) Becke, A. D. *J. Chem. Phys.* **1986**, *84*, 4524-4529.

(131) Becke, A. D. *Phys. Rev. A.* **1988**, *38*, 3098-3100.

(132) Perdew, J. P. *Phys. Rev. B: Condens. Matter* **1986**, *33*, 8822-8824.

(133) Perdew, J. P. *Phys. Rev. B: Condens. Matter* **1986**, *34*, 7406-7406.

(134) Fan, L. Y.; Ziegler, T. *J. Chem. Phys.* **1991**, *94*, 6057-6063.

(135) Schipper, P. R. T.; Gritsenko, O. V.; van Gisbergen, S. J. A.; Baerends, E. J. *J. Chem. Phys.* **2000**, *112*, 1344-1352.

(136) Chang, C.; Pelissier, M.; Durand, P. *Phys. Scripta* **1986**, *34*, 394-404.

(137) van Lenthe, E.; Baerends, E. J.; Snijders, J. G. *J. Chem. Phys.* **1993**, *99*, 4597-4610.

(138) van Lenthe, E.; van Leeuwen, R.; Baerends, E. J.; Snijders, J. G. *Int. J. Quantum Chem.* **1996**, *57*, 281-293.

(139) Glendening, E. D.; Badenhoop, J. K.; Reed, A. E.; Carpenter, J. E.; Bohmann, J. K.; Morales, C. M.; Weinhold, F. *NBO*, 5.0.; Theoretical Chemistry Institute, University of Wisconsin: Madison, WI. 2001. http://www.chem.wisc.edu/~nbo5.

(140) Guerra, C. F.; Handgraaf, J. W.; Baerends, E. J.; Bickelhaupt, F. M. *J. Comput. Chem.* **2004**, *25*, 189-210.

(141) Hirshfeld, F. L. *Theor. Chim. Acta* **1977**, *44*, 129-138.

(142) Parr, R. G.; Ayers, P. W.; Nalewajski, R. F. *J. Phys. Chem. A* **2005**, *109*, 3957-3959.

(143) Bultinck, P.; Van Alsenoy, C.; Ayers, P. W.; Carbo-Dorca, R. *J. Chem. Phys.* **2007**, *126*, 144111 (1-9).

(144) Mandado, M.; Van Alsenoy, C.; Mosquera, R. *J. Phys. Chem. A* **2004**, *108*, 7050-7055.

(145) Rodriguez, J. I.; Bader, R. F. W.; Ayers, P. W.; Michel, C.; Gotz, A. W.; Bo, C. *Chem. Phys. Lett.* **2009**, *472*, 149-152.

(146) Rodriguez, J. I.; Koester, A. M.; Ayers, P. W.; Santos-Valle, A.; Vela, A.; Merino, G. *J. Comput. Chem.* **2009**, *30*, 1082-1092.

(147) Michalak, A.; DeKock, R. L.; Ziegler, T. *J. Phys. Chem. A* **2008**, *112*, 7256-7263.

(148) Kober, E. M.; Caspar, J. V.; Sullivan, B. P.; Meyer, T. J. *Inorg. Chem.* **1988**, *27*, 4587-4598.

(149) Breu, J.; Stoll, A. J. *Acta Crystallogr., Sect. C: Cryst. Struct. Commun.* **1996**, *52*, 1174-1177.

(150) Harris, S. *Polyhedron* **1997**, *16*, 3219-3233.

(151) Palmer, M.; Carter, K.; Harris, S. *Organometallics* **1997**, *16*, 2448-2459.

(152) Constable, E. C.; Raithby, P. R.; Smit, D. N. *Polyhedron* **1989**, *8*, 367-369.

(153) Nagle, J. K. *J. Am. Chem. Soc.* **1990**, *112*, 4741-4747.

(154) Bratsch, S. G. *J. Chem. Educ.* **1984**, *61*, 588-589.

(155) Arounaguiri, S.; Easwaramoorthy, D.; Ashokkumar, A.; Dattagupta, A.; Maiya, B. G. *Proc. Indian Acad. Sci. -Chem. Sci.* **2000**, *112*, 1-17.

(156) Zhou, M.; Robertson, G. P.; Roovers, J. *Inorg. Chem.* **2005**, *44*, 8317-8325.

(157) Sardarian, A.; Coe, B. J.; Douglas, K. T. *Transition Met. Chem.* **2003**, *28*, 905-907.

(158) Shaw, G. B.; Styers-Barnett, D. J.; Gannon, E. Z.; Granger, J. C.; Papanikolas, J. M. *J. Phys. Chem. A* **2004**, *108*, 4998-5006.

(159) Huisman, C. L.; Huijser, A.; Donker, H.; Schoonman, J.; Goossens, A. *Macromolecules* **2004**, *37*, 5557-5564.

(160) Crutchley, R. J.; Lever, A. B. P. *Inorg. Chem.* **1982**, *21*, 2276-2282.

(161) Garner, R. N.; Joyce, L. E.; Turro, C. *Inorg. Chem.* **2011**, *50*, 4384-4391.

(162) Beeston, R. F.; Larson, S. L.; Fitzgerald, M. C. *Inorg. Chem.* **1989**, *28*, 4187-4189.

(163) A weak short-lived shoulder at ~ 500-525 nm is also observed in the emission spectra of the complexes.

(164) Siebert, R.; Winter, A.; Dietzek, B.; Schubert, U. S.; Popp, J. *Macromol. Rapid Commun.* **2010**, *31*, 883-888.

(165) Wilson, G. J.; Launikonis, A.; Sasse, W. H. F.; Mau, A. W. H. *J. Phys. Chem. A* **1997**, *101*, 4860-4866.

(166) Song, L. Q.; Feng, J.; Wang, X. S.; Yu, J. H.; Hou, Y. J.; Xie, P. H.; Zhang, B. W.; Xiang, J. F.; Ai, X. C.; Zhang, J. P. *Inorg. Chem.* **2003**, *42*, 3393-3395.

(167) Tyson, D. S.; Luman, C. R.; Zhou, X. L.; Castellano, F. N. *Inorg. Chem.* **2001**, *40*, 4063-4071.

(168) Lee, S.; Luman, C. R.; Castellano, F. N.; Lin, W. B. *Chem. Commun.* **2003**, 2124-2125.

(169) Strouse, G. F.; Schoonover, J. R.; Duesing, R.; Boyde, S.; Jones, W. E.; Meyer, T. J. *Inorg. Chem.* **1995**, *34*, 473-487.

(170) Fabian, R. H.; Klassen, D. M.; Sonntag, R. W. *Inorg. Chem.* **1980**, *19*, 1977-1982.

(171) Sun, Y.; Liu, Y.; Turro, C. *J. Am. Chem. Soc.* **2010**, *132*, 5594-5595.

(172) Tyson, D. S.; Castellano, F. N. *J. Phys. Chem. A* **1999**, *103*, 10955-10960.

(173) Simon, J. A.; Curry, S. L.; Schmehl, R. H.; Schatz, T. R.; Piotrowiak, P.; Jin, X. Q.; Thummel, R. P. *J. Am. Chem. Soc.* **1997**, *119*, 11012-11022.

(174) Evans, C. H.; Scaiano, J. C. *J. Am. Chem. Soc.* **1990**, *112*, 2694-2701.

(175) Emmi, S. S.; D'Angelantonio, M.; Beggiato, G.; Poggi, G.; Geri, A.; Pietropaolo, D.; Zotti, G. *Radiat. Phys. Chem.* **1999**, *54*, 263-270.

(176) Moorlag, C. Ph.D. Thesis, University of British Columbia, Vancouver, British Columbia, Canada, 2006.

(177) Aly, S. M.; Ho, C. L.; Fortin, D.; Wong, W. Y.; Abd-El-Aziz, A. S.; Harvey, P. D. *Chem. Eur. J.* **2008**, *14*, 8341-8352.

(178) Haga, M.; Ale, M. M.; Koseki, S.; Yoshimura, A.; Nozaki, K.; Ohno, T. *Inorg. Chim. Acta* **1994**, *226*, 17-24.

(179) Aly, S. M.; Ho, C. L.; Wong, W. Y.; Fortin, D.; Harvey, P. D. *Macromolecules* **2009**, *42*, 6902-6916.

(180) Zhang, L. P.; Chen, B.; Wu, L. Z.; Tung, C. H.; Cao, H.; Tanimoto, Y. *Chem. Eur. J.* **2003**, *9*, 2763-2769.

(181) Danilov, E. O.; Pomestchenko, I. E.; Kinayyigit, S.; Gentili, P. L.; Hissler, M.; Ziessel, R.; Castellano, F. N. *J. Phys. Chem. A* **2005**, *109*, 2465-2471.

(182) Wallin, S.; Davidsson, J.; Modin, J.; Hammarstrom, L. *J. Phys. Chem. A* **2005**, *109*, 4697-4704.

(183) Maubert, B.; McClenaghan, N. D.; Indelli, M. T.; Campagna, S. *J. Phys. Chem. A* **2003**, *107*, 447-455.

(184) Turro, N. J. In *Modern Molecular Photochemistry;* The Benjamin/Cummings Publishing Co., Inc.: Menlo Park, California, 1978.

(185) Lamansky, S.; Djurovich, P.; Murphy, D.; Abdel-Razzaq, F.; Kwong, R.; Tsyba, I.; Bortz, M.; Mui, B.; Bau, R.; Thompson, M. E. *Inorg. Chem.* **2001**, *40*, 1704-1711.

(186) Lamansky, S.; Djurovich, P.; Murphy, D.; Abdel-Razzaq, F.; Lee, H. E.; Adachi, C.; Burrows, P. E.; Forrest, S. R.; Thompson, M. E. *J. Am. Chem. Soc.* **2001**, *123*, 4304-4312.

(187) Baranoff, E.; Bolink, H. J.; De Angelis, F.; Fantacci, S.; Di Censo, D.; Djellab, K.; Grätzel, M.; Nazeeruddin, M. K. *Dalton Trans.* **2010**, *39*, 8914-8918.

(188) Baldo, M. A.; Thompson, M. E.; Forrest, S. R. *Nature* **2000**, *403*, 750-753.

(189) Adachi, C.; Kwong, R. C.; Djurovich, P.; Adamovich, V.; Baldo, M. A.; Thompson, M. E.; Forrest, S. R. *Appl. Phys. Lett.* **2001**, *79*, 2082-2084.

(190) Slinker, J. D.; Gorodetsky, A. A.; Lowry, M. S.; Wang, J. J.; Parker, S.; Rohl, R.; Bernhard, S.; Malliaras, G. G. *J. Am. Chem. Soc.* **2004**, *126*, 2763-2767.

(191) Goldsmith, J. I.; Hudson, W. R.; Lowry, M. S.; Anderson, T. H.; Bernhard, S. *J. Am. Chem. Soc.* **2005**, *127*, 7502-7510.

(192) DeRosa, M. C.; Hodgson, D. J.; Enright, G. D.; Dawson, B.; Evans, C. E. B.; Crutchley, R. J. *J. Am. Chem. Soc.* **2004**, *126*, 7619-7626.

(193) Amao, Y.; Ishikawa, Y.; Okura, I. *Anal. Chim. Acta* **2001**, *445*, 177-182.

(194) Zhang, K. Y.; Lo, K. K. W. *Inorg. Chem.* **2009**, *48*, 6011-6025.

(195) Lo, K. K. W.; Hui, W. K.; Chung, C. K.; Tsang, K. H. K.; Ng, D. C. M.; Zhu, N. Y.; Cheung, K. K. *Coord. Chem. Rev.* **2005**, *249*, 1434-1450.

(196) Tamayo, A. B.; Garon, S.; Sajoto, T.; Djurovich, P. I.; Tsyba, I. M.; Bau, R.; Thompson, M. E. *Inorg. Chem.* **2005**, *44*, 8723-8732.

(197) Flamigni, L.; Collin, J. P.; Sauvage, J. P. *Acc. Chem. Res.* **2008**, *41*, 857-871.

(198) Wong, W. Y. *J. Organomet. Chem.* **2009**, *694*, 2644-2647.

(199) Nozaki, K. *J. Chin. Chem. Soc.* **2006**, *53*, 101-112.

(200) Sajoto, T.; Djurovich, P. I.; Tamayo, A.; Yousufuddin, M.; Bau, R.; Thompson, M. E.; Holmes, R. J.; Forrest, S. R. *Inorg. Chem.* **2005**, *44*, 7992-8003.

(201) Fei, T.; Gu, X.; Zhang, M.; Wang, C.; Hanif, M.; Zhang, H.; Ma, Y. *Synth. Met.* **2009**, *159*, 113-118.

(202) Tsuboyama, A.; Iwawaki, H.; Furugori, M.; Mukaide, T.; Kamatani, J.; Igawa, S.; Moriyama, T.; Miura, S.; Takiguchi, T.; Okada, S.; Hoshino, M.; Ueno, K. *J. Am. Chem. Soc.* **2003**, *125*, 12971-12979.

(203) Kozhevnikov, D. N.; Kozhevnikov, V. N.; Shafikov, M. Z.; Prokhorov, A. M.; Bruce, D. W.; Williams, J. A. G. *Inorg. Chem.* **2011**, *50*, 3804-3815.

(204) Ren, X.; Giesen, D. J.; Rajeswaran, M.; Madaras, M. *Organometallics* **2009**, *28*, 6079-6089.

(205) Huo, S. Q.; Deaton, J. C.; Rajeswaran, M.; Lenhart, W. C. *Inorg. Chem.* **2006**, *45*, 3155-3157.

(206) Deaton, J. C.; Young, R. H.; Lenhard, J. R.; Rajeswaran, M.; Huo, S. *Inorg. Chem.* **2010**, *49*, 9151-9161.

(207) Baranoff, E.; Fantacci, S.; De Angelis, F.; Zhang, X.; Scopelliti, R.; Grätzel, M.; Nazeeruddin, M. K. *Inorg. Chem.* **2011**, *50*, 451-462.

(208) Davies, D. L.; Lowe, M. P.; Ryder, K. S.; Singh, K.; Singh, S. *Dalton Trans.* **2011**, *40*, 1028-1030.

(209) Sprouse, S.; King, K. A.; Spellane, P. J.; Watts, R. J. *J. Am. Chem. Soc.* **1984**, *106*, 6647-6653.

(210) Flack, H. D. *Acta Crystallogr., Sect. A: Found. Crystallogr.* **1983**, *39*, 876-881.

(211) Bernardinelli, G.; Flack, H. D. *Acta Crystallogr., Sect. A: Found. Crystallogr.* **1985**, *41*, 500-511.

(212) Dedeian, K.; Djurovich, P. I.; Garces, F. O.; Carlson, G.; Watts, R. J. *Inorg. Chem.* **1991**, *30*, 1685-1687.

(213) Nonoyama, M. *Bull. Chem. Soc. Jpn.* **1974**, *47*, 767-768.

(214) Colombo, M. G.; Brunold, T. C.; Riedener, T.; Gudel, H. U.; Fortsch, M.; Burgi, H. B. *Inorg. Chem.* **1994**, *33*, 545-550.

(215) Tamayo, A. B.; Alleyne, B. D.; Djurovich, P. I.; Lamansky, S.; Tsyba, I.; Ho, N. N.; Bau, R.; Thompson, M. E. *J. Am. Chem. Soc.* **2003**, *125*, 7377-7387.

(216) Edkins, R. M.; Wriglesworth, A.; Fucke, K.; Bettington, S. L.; Beeby, A. *Dalton Trans.* **2011**, *40*, 9672-9678.

(217) Wu, L. L.; Sun, I. W.; Yang, C. H. *Polyhedron* **2007**, *26*, 2679-2685.

(218) McGee, K. A.; Mann, K. R. *Inorg. Chem.* **2007**, *46*, 7800-7809.

(219) Wang, Y.; Teng, F.; Tang, A.; Wang, Y.; Xu, X. *Acta Crystallogr., Sect. E: Struct. Rep. Online* **2005**, *61*, M778-M780.

(220) DiCesare, N.; Belletete, M.; Marrano, C.; Leclerc, M.; Durocher, G. *J. Phys. Chem. A* **1998**, *102*, 5142-5149.

(221) You, Y.; Han, Y.; Lee, Y.; Park, S. Y.; Nam, W.; Lippard, S. J. *J. Am. Chem. Soc.* **2011**, *133*, 11488-11491.

(222) Bandini, M.; Bianchi, M.; Valenti, G.; Piccinelli, F.; Paolucci, F.; Monari, M.; Umani-Ronchi, A.; Marcaccio, M. *Inorg. Chem.* **2010**, *49*, 1439-1448.

(223) Paneque, M.; Poveda, M. L.; Salazar, V.; Taboada, S.; Carmona, E.; Gutierrez-Puebla, E.; Monge, A.; Ruiz, C. *Organometallics* **1999**, *18*, 139-149.

(224) Paneque, M.; Poveda, M. L.; Carmona, E.; Salazar, V. *Dalton Trans.* **2005**, 1422-1427.

(225) Sanchez-Delgado, R. A.; Herrera, V.; Bianchini, C.; Masi, D.; Mealli, C. *Inorg. Chem.* **1993**, *32*, 3766-3770.

(226) Rao, K. M.; Day, C. L.; Jacobson, R. A.; Angelici, R. J. *Inorg. Chem.* **1991**, *30*, 5046-5049.

(227) Lin, C. H.; Chi, Y.; Chung, M. W.; Chen, Y. J.; Wang, K. W.; Lee, G. H.; Chou, P. T.; Hung, W. Y.; Chiu, H. C. *Dalton Trans.* **2011**, *40*, 1132-1143.

(228) Hung, J. Y.; Chi, Y.; Pai, I. H.; Yu, Y. C.; Lee, G. H.; Chou, P. T.; Wong, K. T.; Chen, C. C.; Wu, C. C. *Dalton Trans.* **2009**, 6472-6475.

(229) Chang, Y. Y.; Hung, J. Y.; Chi, Y.; Chyn, J. P.; Chung, M. W.; Lin, C. L.; Chou, P. T.; Lee, G. H.; Chang, C. H.; Lin, W. C. *Inorg. Chem.* **2011**, *50*, 5075-5084.

(230) Connelly, N. G.; Geiger, W. E. *Chem. Rev.* **1996**, *96*, 877-910.

(231) Nam, E. J.; Kim, J. H.; Kim, B. O.; Kim, S. M.; Park, N. G.; Kim, Y. S.; Kim, Y. K.; Ha, Y. *Bull. Chem. Soc. Jpn.* **2004**, *77*, 751-755.

(232) Guldi, D. M.; Prato, M. *Acc. Chem. Res.* **2000**, *33*, 695-703.

(233) Howe, L.; Zhang, J. Z. *J. Phys. Chem. A* **1997**, *101*, 3207-3213.

(234) Ichimura, K.; Kobayashi, T.; King, K. A.; Watts, R. J. *J. Phys. Chem.* **1987**, *91*, 6104-6106.

(235) Barbieri, A.; Accorsi, G.; Armaroli, N. *Chem. Commun.* **2008**, 2185-2193.

(236) Armaroli, N.; Accorsi, G.; Holler, M.; Moudam, O.; Nierengarten, J. F.; Zhou, Z.; Wegh, R. T.; Welter, R. *Adv. Mater.* **2006**, *18*, 1313-1316.

(237) Sakaki, S.; Kuroki, T.; Hamada, T. *J. Chem. Soc., Dalton Trans.* **2002**, 840-842.

(238) Bessho, T.; Constable, E. C.; Grätzel, M.; Redondo, A. H.; Housecroft, C. E.; Kylberg, W.; Nazeeruddin, M. K.; Neuburger, M.; Schaffner, S. *Chem. Commun.* **2008**, 3717-3719.

(239) Constable, E. C.; Redondo, A. H.; Housecroft, C. E.; Neuburger, M.; Schaffner, S. *Dalton Trans.* **2009**, 6634-6644.

(240) Linfoot, C. L.; Richardson, P.; Hewat, T. E.; Moudam, O.; Forde, M. M.; Collins, A.; White, F.; Robertson, N. *Dalton Trans.* **2010**, *39*, 8945-8956.

(241) McMillin, D. R.; Buckner, M. T.; Ahn, B. T. *Inorg. Chem.* **1977**, *16*, 943-945.

(242) McMillin, D. R.; McNett, K. M. *Chem. Rev.* **1998**, *98*, 1201-1219.

(243) Armaroli, N. *Chem. Soc. Rev.* **2001**, *30*, 113-124.

(244) Metal Prices and News. *www.metalprices.com/freesite* (accessed April 16, 2012).

(245) Ruthenium Prices and Ruthenium Price Charts - InvestmentMine. *www.infomine.com/investment/metal-prices/ruthenium/* (accessed April 16, 2012).

(246) Alonso-Vante, N.; Nierengarten, J. F.; Sauvage, J. P. *J. Chem. Soc., Dalton Trans.* **1994**, 1649-1654.

(247) Miller, M. T.; Gantzel, P. K.; Karpishin, T. B. *Inorg. Chem.* **1998**, *37*, 2285-2290.

(248) Bozic-Weber, B.; Constable, E. C.; Housecroft, C. E.; Neuburger, M.; Price, J. R. *Dalton Trans.* **2010**, *39*, 3585-3594.

(249) Kuang, S. M.; Cuttell, D. G.; McMillin, D. R.; Fanwick, P. E.; Walton, R. A. *Inorg. Chem.* **2002**, *41*, 3313-3322.

(250) Saito, K.; Arai, T.; Takahashi, N.; Tsukuda, T.; Tsubomura, T. *Dalton Trans.* **2006**, 4444-4448.

(251) Listorti, A.; Accorsi, G.; Rio, Y.; Armaroli, N.; Moudam, O.; Gégout, A.; Delavaux-Nicot, B.; Holler, M.; Nierengarten, J. *Inorg. Chem.* **2008**, *47*, 6254-6261.

(252) Costa, R. D.; Tordera, D.; Orti, E.; Bolink, H. J.; Schoenle, J.; Graber, S.; Housecroft, C. E.; Constable, E. C.; Zampese, J. A. *J. Mater. Chem.* **2011**, *21*, 16108-16118.

(253) Hsu, C.; Lin, C.; Chung, M.; Chi, Y.; Lee, G.; Chou, P.; Chang, C.; Chen, P. *J. Am. Chem. Soc.* **2011**, *133*, 12085-12099.

(254) Czerwieniec, R.; Yu, J.; Yersin, H. *Inorg. Chem.* **2011**, *50*, 8293-8301.

(255) Chen, J. L.; Cao, X. F.; Gu, W.; Wen, H. R.; Shi, L. X.; Rong, G.; Luo, P. *Inorg. Chem. Commun.* **2011**, *14*, 1894-1897.

(256) Li, X. L.; Ai, Y. B.; Yang, B.; Chen, J.; Tan, M.; Xin, X. L.; Shi, Y. H. *Polyhedron* **2012**, *35*, 47-54.

(257) Bozic-Weber, B.; Constable, E. C.; Housecroft, C. E.; Kopecky, P.; Neuburger, M.; Zampese, J. A. *Dalton Trans.* **2011**, *40*, 12584-12594.

(258) *SAINT*. Version 7.68A. **1997-2010**.

(259) Sheldrick, G. M. *Acta Crystallogr., Sect. A: Found. Crystallogr.* **2008**, *64*, 112-122.

(260) King, G.; Gembicky, M.; Coppens, P. *Acta Crystallogr., Sect. C: Cryst. Struct. Commun.* **2005**, *61*, M329-M332.

(261) Hanna, J. V.; Boyd, S. E.; Healy, P. C.; Bowmaker, G. A.; Skelton, B. W.; White, A. H. *Dalton Trans.* **2005**, 2547-2556.

(262) Black, J. R.; Levason, W.; Webster, M. *Acta Crystallogr., Sect. C: Cryst. Struct. Commun.* **1995**, *51*, 623-625.

(263) Munakata, M.; Maekawa, M.; Kitagawa, S.; Matsuyama, S.; Masuda, H. *Inorg. Chem.* **1989**, *28*, 4300-4302.

(264) Hashimoto, M.; Igawa, S.; Yashima, M.; Kawata, I.; Hoshino, M.; Osawa, M. *J. Am. Chem. Soc.* **2011**, *133*, 10348-10351.

(265) Hanton, L. R.; Richardson, C.; Robinson, W. T.; Turnbull, J. M. *Chem. Commun.* **2000**, 2465-2466.

(266) Stålhandske, C. M. V.; Stålhandske, C. I.; Persson, I.; Sandström, M.; Jalilehvand, F. *Inorg. Chem.* **2001**, *40*, 6684-6693.

(267) Ruthkosky, M.; Castellano, F. N.; Meyer, G. J. *Inorg. Chem.* **1996**, *35*, 6406-6412.

(268) Siddique, Z. A.; Yamamoto, Y.; Ohno, T.; Nozaki, K. *Inorg. Chem.* **2003**, *42*, 6366-6378.

(269) Lockard, J. V.; Kabehie, S.; Zink, J. I.; Smolentsev, G.; Soldatov, A.; Chen, L. X. *J. Phys. Chem. B* **2010**, *114*, 14521-14527.

(270) Ichinaga, A. K.; Kirchhoff, J. R.; McMillin, D. R.; Dietrich-Buchecker, C. O.; Marnot, P. A.; Sauvage, J. P. *Inorg. Chem.* **1987**, *26*, 4290-4292.

(271) Turro, C.; Chung, Y.; Leventis, N.; Kuchenmeister, M.; Wagner, P.; Leroi, G. *Inorg. Chem.* **1996**, *35*, 5104-&.

(272) Kato, T.; Shida, T. *J. Am. Chem. Soc.* **1979**, *101*, 6869-6876.

(273) Wu, S. H.; Ling, J. W.; Lai, S. H.; Huang, M. J.; Cheng, C. H.; Chen, I. C. *J. Phys. Chem. A* **2010**, *114*, 10339-10344.

(274) Kuchison, A. M.; Wolf, M. O.; Patrick, B. O. *Dalton Trans.* **2011**, *40*, 6912-6921.

APPENDIX

Table A-1 Selected crystallographic data for $[Ru(phen)_2PT_3\text{-}PS](PF_6)_2$, **(52)**, $[Os(bpy)_2PT_3\text{-}PS](PF_6)_2$ **(54)**, and $[Os(bpy)_2PT_3\text{-}PC](PF_6)$ **(55)**.

	$[Ru(phen)_2PT_3\text{-}PS](PF_6)_2$	$[Os(bpy)_2PT_3\text{-}PS](PF_6)_2$	$[Os(bpy)_2PT_3PC](PF_6)$
Formula	$C_{51}H_{39}N_4OF_{12}P_3S_3Ru$	$C_{46}H_{37}N_4S_3OsP_3F_{12}Cl_4$	$C_{44}H_{32}N_4PS_3OsPF_6$
Crystal Colour, Habit	yellow, tablet	red, plate	brown, blade
Dimensions / mm	0.05 × 0.14 × 0.17	0.05 × 0.30 × 0.50	0.03 × 0.20 × 0.45
Temperature / K	173 (1)	173 (1)	173 (1)
Crystal System	Triclinic	monoclinic	monoclinic
Space Group	*P* -1 (#2)	*P* $2_1/c$ (#14)	*C 2/c* (#15)
a / Å	10.7574(4)	11.1984(8)	39.8697(9)
b / Å	11.9596(5)	20.8114(16)	9.4270
c / Å	21.2088(9)	21.9881(17)	28.1007
α /deg	104.616(1)	90.0	90
β /deg	103..562(1)	91.752(4)	130.946
γ /deg	94.916(1)	90.0	90
V / $Å^3$	2536.1(2)	5122.0(7)	7977.5(3)
Z	2	4	8
ρ_{calc} / g cm^{-1}	1.626	1.809	1.797
μ (Mo kα)	6.16 cm^{-1}	29.98 mm^{-1}	35.03 mm^{-1}
R1[a] (I>2.00σ(I))	0.039	0.037	0.030
wR2[a] (I>2.00σ(I))	0.090	0.088	0.061
Goodness of fit	1.01	1.07	1.01

[a]Function minimized. $\Sigma w(F_o^2\text{-}F_c^2)^2$, $R1 = \Sigma \, ||Fo| - |Fc|| \, / \, \Sigma \, |Fo|$, $wR2 = [\Sigma \, (w \, (Fo^2 - Fc^2)^2 \,) / \, \Sigma \, w(Fo^2)^2]^{1/2}$

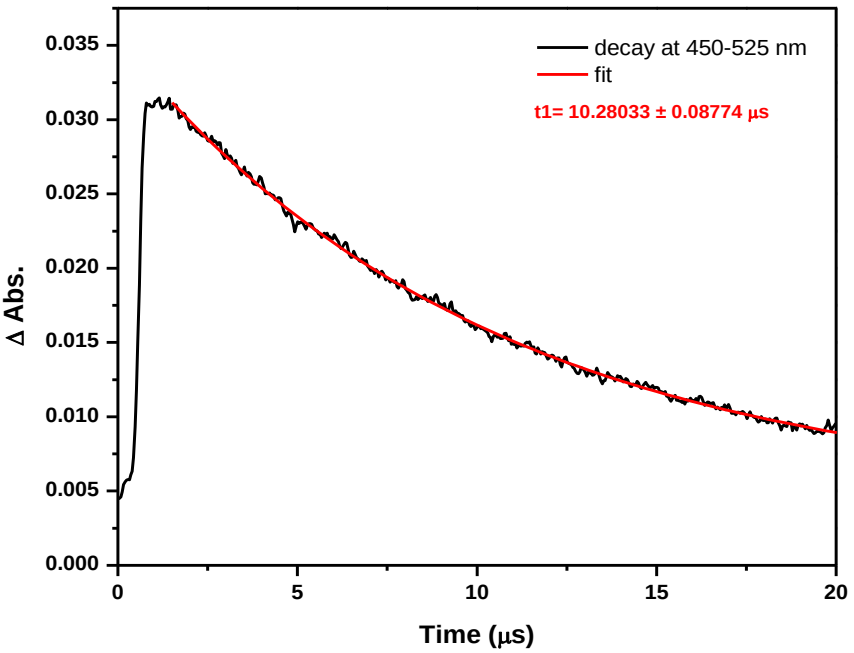

Figure A-1 Decay of transient signal averaged over the 450 - 525 nm wavelength region for PT_3 (black) upon excitation at 355 nm in N_2 sparged CH_3CN, and the monoexponential fit (red).

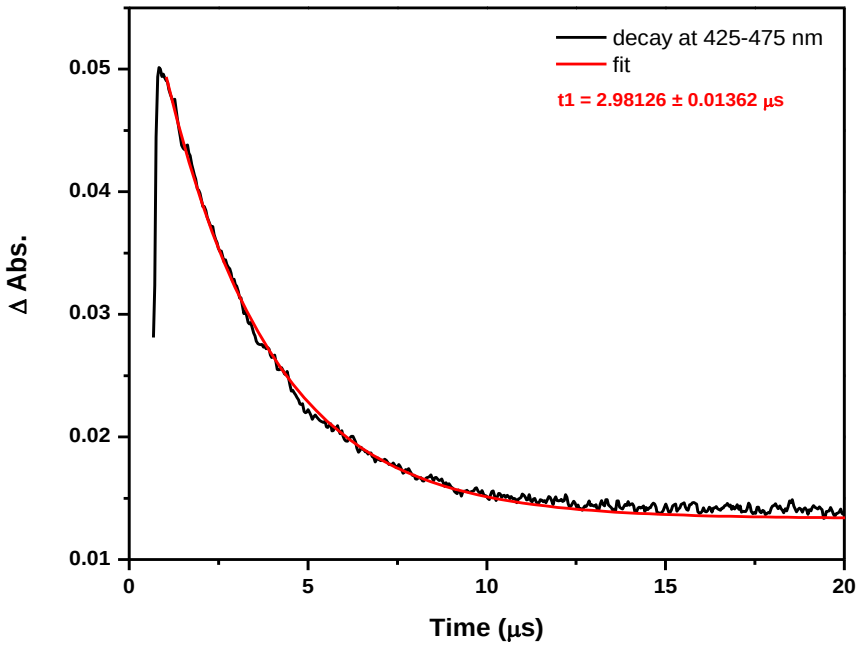

Figure A-2 Decay of transient signal averaged over the 425 - 475 nm wavelength region for T_3 (black) upon excitation at 355 nm in N_2 sparged CH_3CN, and the monoexponential fit (red).

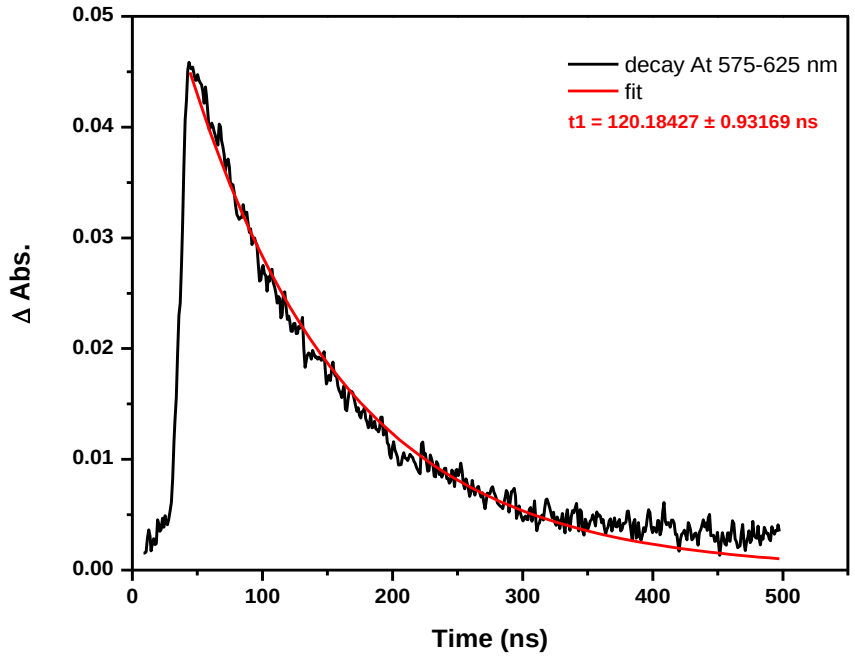

Figure A-3 Decay of transient signal averaged over the 575 - 625 nm wavelength region for [Ru(bpy)$_2$PT$_3$-*PS*](PF$_6$)$_2$, (**48**), (black) upon excitation at 355 nm in N$_2$ sparged CH$_3$CN, and the monoexponential fit (red).

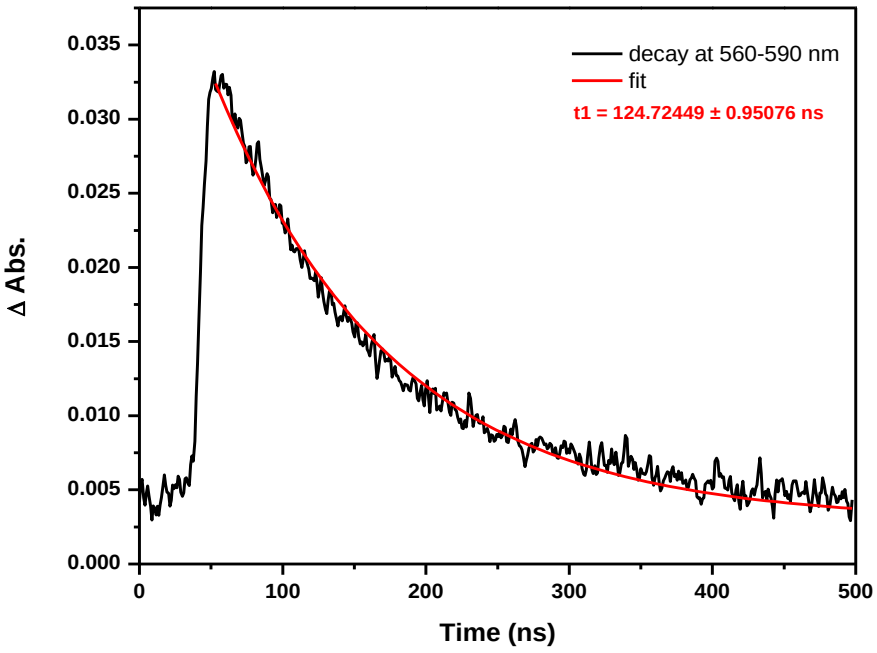

Figure A-4 Decay of transient signal averaged over the 560 - 590 nm wavelength region for [Ru(phen)$_2$PT$_3$-*PS*](PF$_6$)$_2$, (**52**), (black) upon excitation at 355 nm in N$_2$ sparged CH$_3$CN, and the monoexponential fit (red).

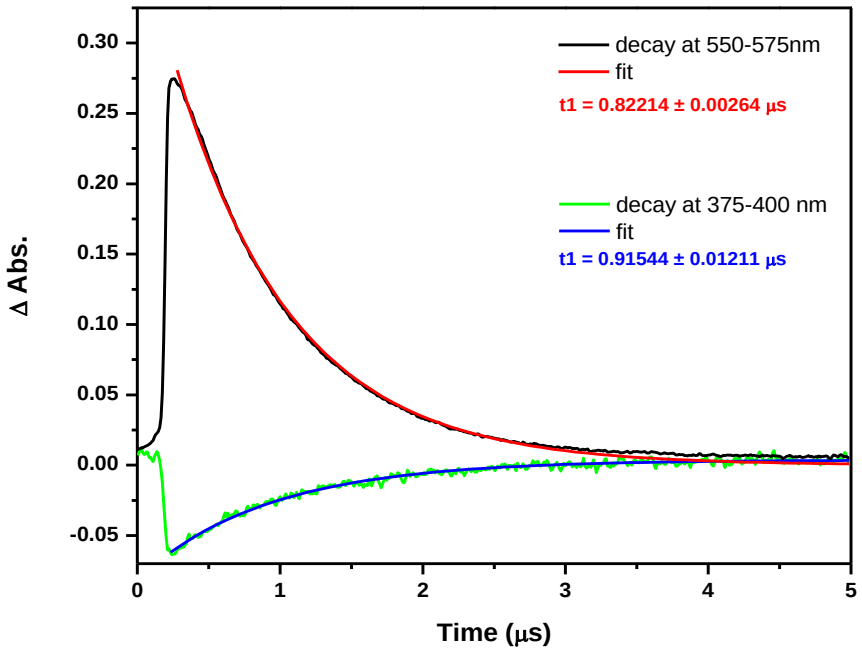

Figure A-5 Decay of transient signal averaged over the 550 - 575 nm (black) and 375-400 nm (green) wavelength regions for [Os(bpy)$_2$PT$_3$-*PS*](PF$_6$)$_2$, (**54**), upon excitation at 355 nm in N_2 sparged CH_3CN, and the monoexponential fits (red and blue, respectively).

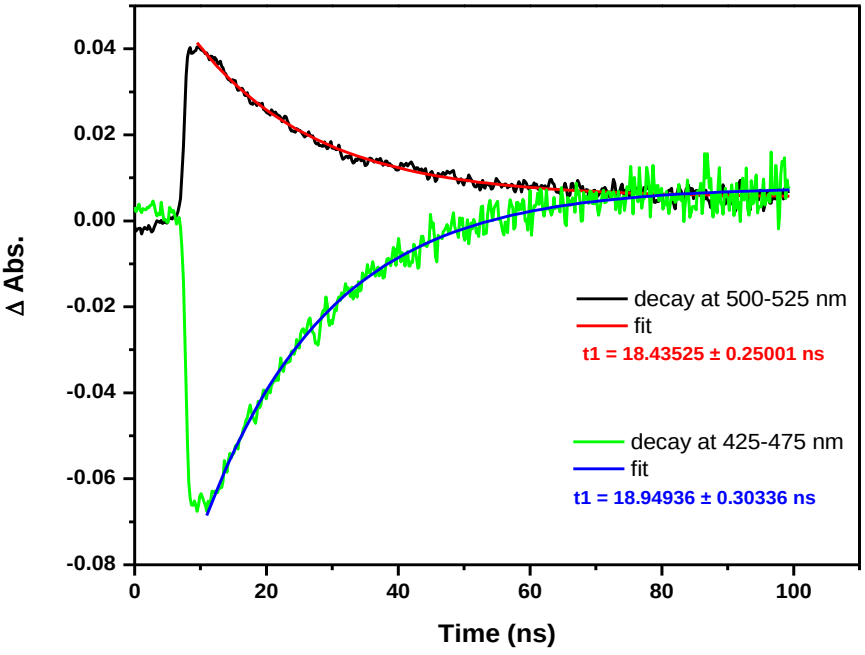

Figure A-6 Decay of transient signal averaged over the 500 - 525 nm (black) and 425-475 nm (green) wavelength regions for [Ru(bpy)$_2$PT$_3$-*PC*](PF$_6$), (**49**), upon excitation at 355 nm in N_2 sparged CH_3CN, and the monoexponential fits (red and blue, respectively).

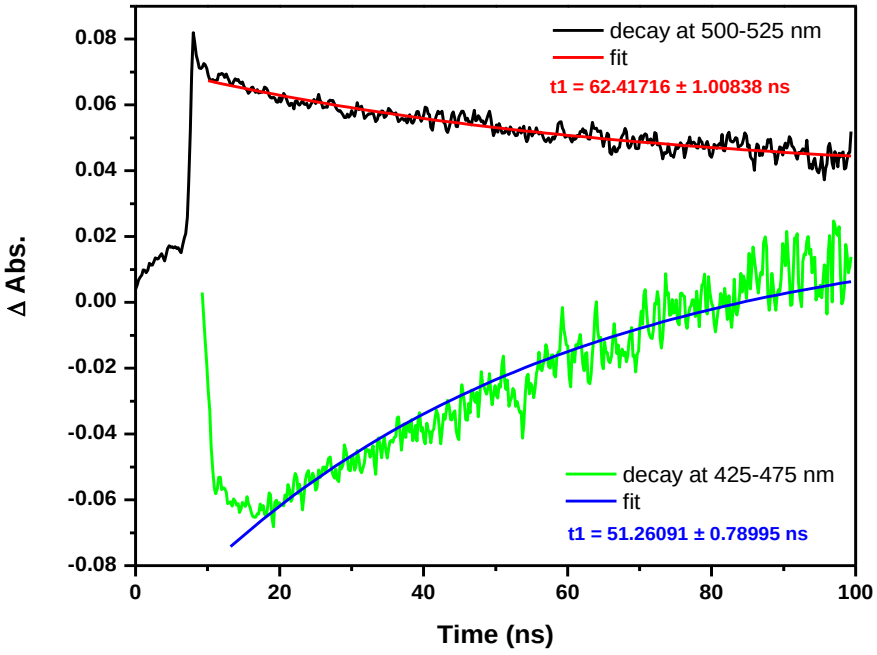

Figure A-7 Decay of transient signal averaged over the 500 - 525 nm (black) and 425-475 nm (green) wavelength regions for [Ru(phen)$_2$PT$_3$-*PC*](PF$_6$), (**53**), upon excitation at 355 nm in N_2 sparged CH_3CN, and the monoexponential fits (red and blue, respectively).

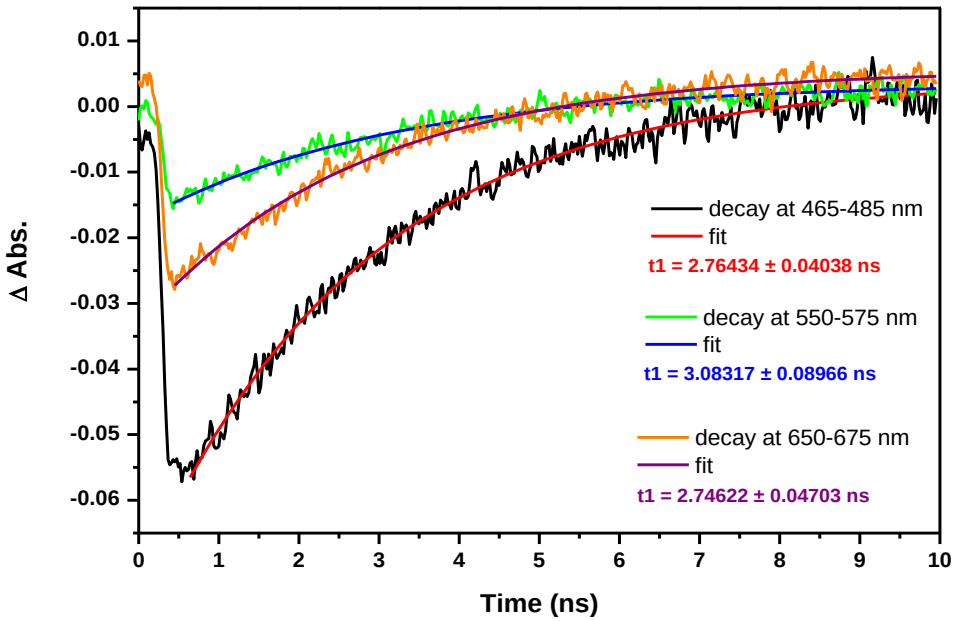

Figure A-8 Decay of transient signal averaged over the 465-485 nm (black), 550 - 575 nm (green) and 650-675 nm (orange) wavelength regions for [Os(bpy)$_2$PT$_3$-*PC*](PF$_6$), (**55**), upon excitation at 355 nm in N_2 sparged CH_3CN, and the monoexponential fits (red, blue, and purple, respectively).

Table A-2 Selected crystallographic data for $Ir(ppz)_2PT_3Cl$-*P*, (**58**), $[Ir(ppz)_2PT_3$-*PS*$](BF_4)$, (**59**), and $Ir(ppz)_2PT_3$-*PC*, (**60**).

	$Ir(ppz)_2PT_3Cl$-*P*	$[Ir(ppz)_2PT_3$-*PS*$](BF_4)$	$Ir(ppz)_2PT_3$-*PC*
Formula	$C_{43}H_{33}N_4PS_3IrCl_3$	$C_{44}H_{35}BN_4F_4PS_3IrCl_4$	$C_{42}H_{30}IrN_4PS_3$
Crystal Colour, Habit	yellow, irregular	yellow, blade	brown, prism
Dimensions / mm	0.10 × 0.10 × 0.15	0.02 × 0.10 × 0.35	0.20 × 0.28 × 0.29
Temperature / K	90 (1)	90(1)	100(1)
Crystal System	Triclinic	orthorhombic	monoclinic
Space Group	*P* -1 (#2)	*P* $2_12_12_1$ (#19)	*P* $2_1/n$ (#14)
a / Å	9.8502(11)	9.1409(8)	9.9313(3)
b / Å	13.0136(14)	20.640(2)	17.0695(4)
c / Å	16.0601(17)	24.406(2)	20.9214(5)
α /deg	78.905(6)	90	90
β /deg	76.782(7)	90	91.624(1)
γ /deg	89.430(7)	90	90
V / $Å^3$	1965.4(4)	4604.7(7)	3545.2(2)
Z	2	4	4
ρ_{calc} / g cm^{-1}	1.743	1.684	1.705
μ (Mo kα) /cm^{-1}	38.40	33.56	40.26
R1[a] (I>2.00σ(I))	0.032	0.031	0.020
*w*R2[a] (I>2.00σ(I))	0.077	0.071	0.042
Goodness of fit	1.06	1.04	1.03

[a]Function minimized. $\Sigma w(F_o^2-F_c^2)^2$, $R1 = \Sigma ||F_o| - |F_c|| / \Sigma |F_o|$, $wR2 = [\Sigma (w (F_o^2 - F_c^2)^2)/ \Sigma w(F_o^2)^2]^{1/2}$

Table A-3 Selected crystallographic data for $Ir(ppy)_2PT_3Cl$-*P*, (**61**).

	$Ir(ppy)_2PT_3Cl$-*P*
Formula	$C_{47}H_{35}N_2PS_3IrCl_3$
Crystal Colour, Habit	yellow, irregular
Dimensions / mm	0.04 × 0.06 × 0.16
Temperature / K	90 (1)
Crystal System	Monoclinic
Space Group	*P n* (#7)
a / Å	11.420(1)
b / Å	11.204(1)
c / Å	16.843(1)
α /deg	90º
β /deg	106.532(2)
γ /deg	90º
V / $Å^3$	2065.8(3)
Z	2
ρ_{calc} / g cm^{-1}	1.694
μ (Mo kα) /cm^{-1}	36.54
R1[a] (I>2.00σ(I))	0.036
*w*R2[a] (I>2.00σ(I))	0.052
Goodness of fit	0.874

[a]Function minimized. $\Sigma w(F_o^2-F_c^2)^2$, $R1 = \Sigma ||F_o| - |F_c|| / \Sigma |F_o|$, $wR2 = [\Sigma (w (F_o^2 - F_c^2)^2)/ \Sigma w(F_o^2)^2]^{1/2}$

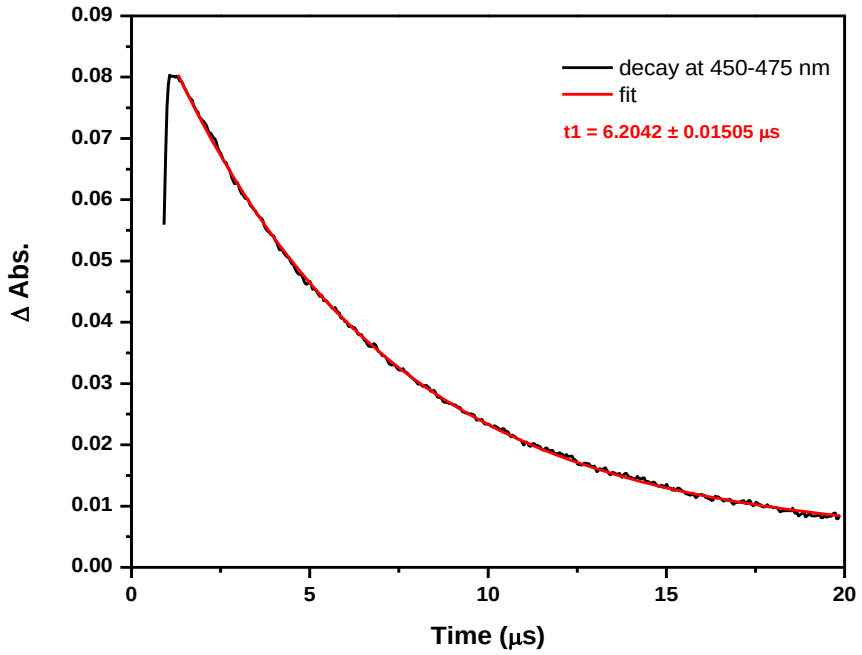

Figure A-9 Decay of the transient signal averaged over the 450 - 475 nm wavelength region for Ir(ppz)$_2$PT$_3$Cl-*P*, (**58**), (black) upon excitation at 355 nm in argon-sparged CH_3CN, and the monoexponential fit (red).

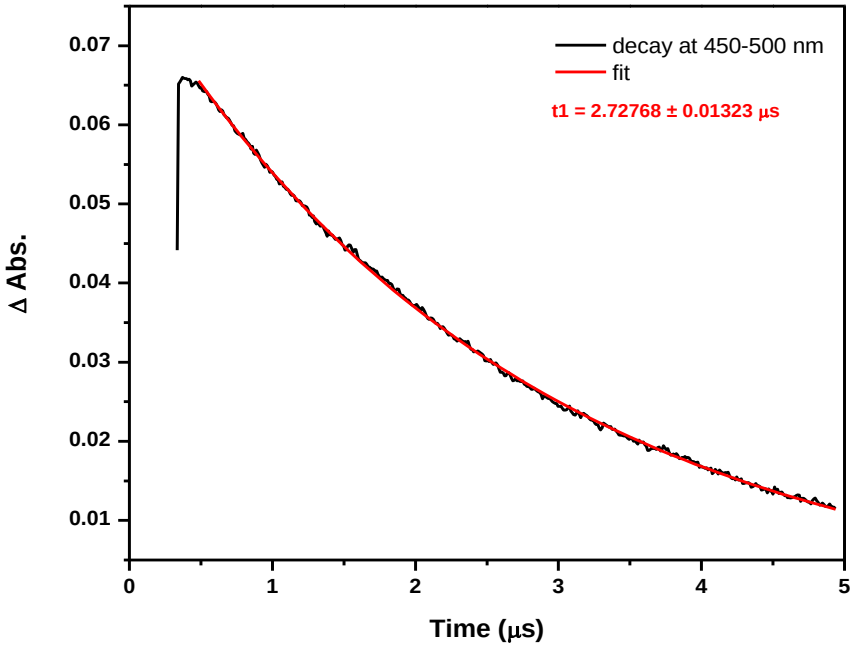

Figure A-10 Decay of the transient signal averaged over the 450 -500 nm wavelength region for Ir(ppz)$_2$PT$_3$-*PC*, (**60**), (black) upon excitation at 355 nm in argon-sparged CH_3CN, and the monoexponential fit (red).

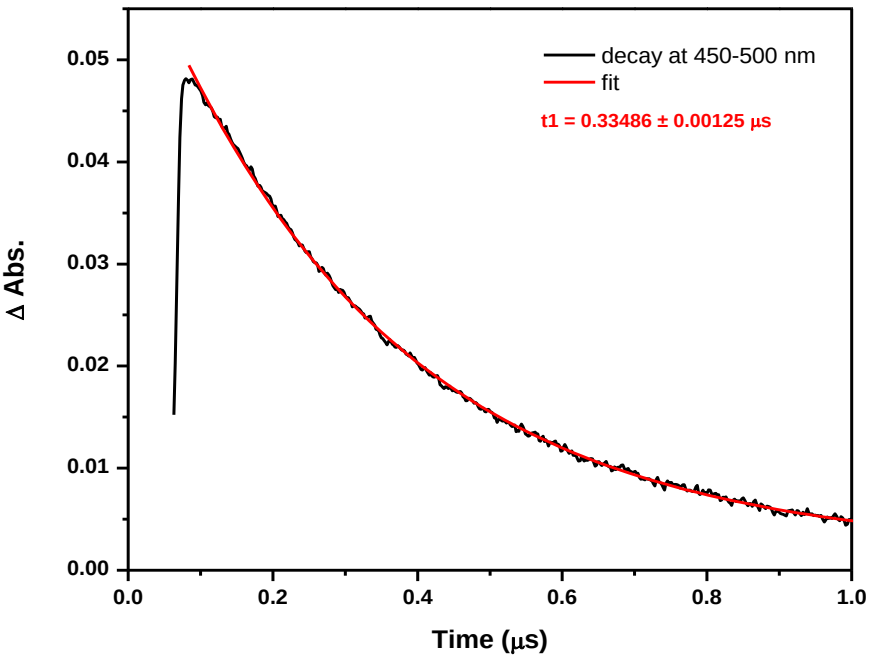

Figure A-11 Decay of the transient signal averaged over the 450 -500 nm wavelength region for [Ir(ppz)$_2$PT$_3$-*PS*](PF$_6$), (**59**), (black) upon excitation at 355 nm in argon-sparged CH_3CN, and the monoexponential fit (red).

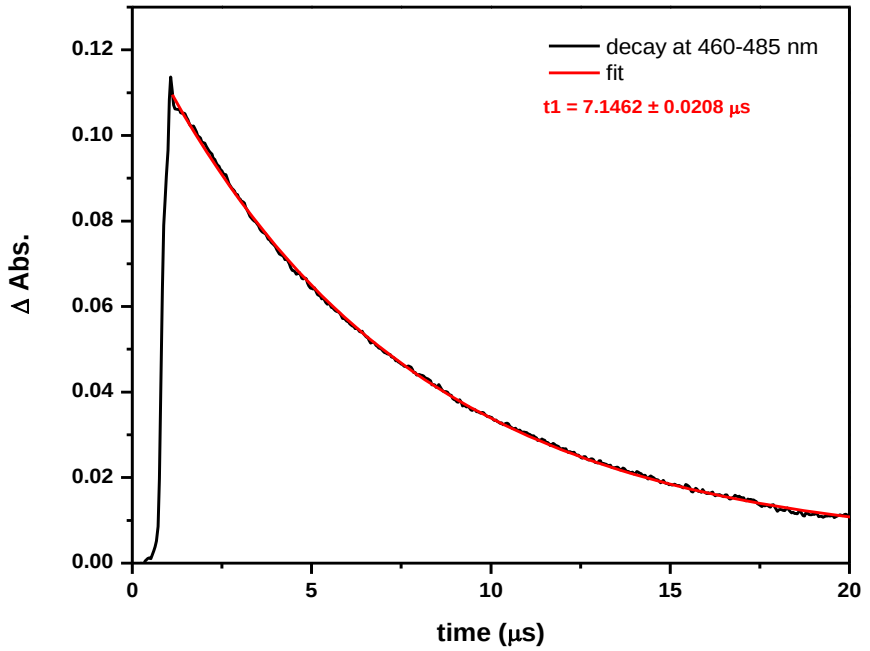

Figure A-12 Decay of the transient signal averaged over the 460 -485 nm wavelength region for Ir(ppy)$_2$PT$_3$Cl-*P*, (**61**), (black) upon excitation at 355 nm in argon-sparged CH_3CN, and the monoexponential fit (red).

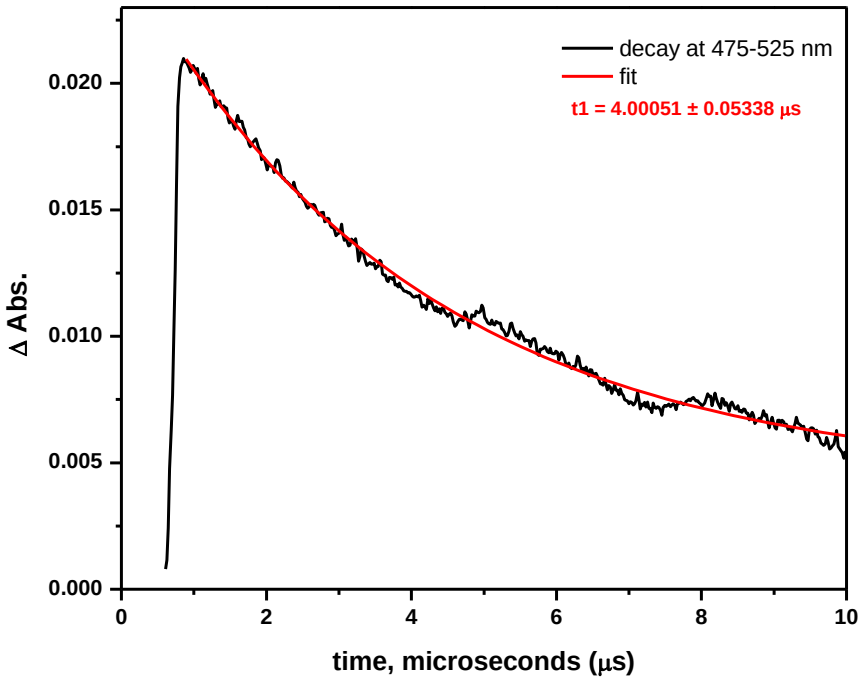

Figure A-13 Decay of the transient signal averaged over the 475 -525 nm wavelength region for $Ir(ppy)_2PT_3$-*PC*, (**63**), (black) upon excitation at 355 nm in argon-sparged CH_3CN, and the monoexponential fit (red).

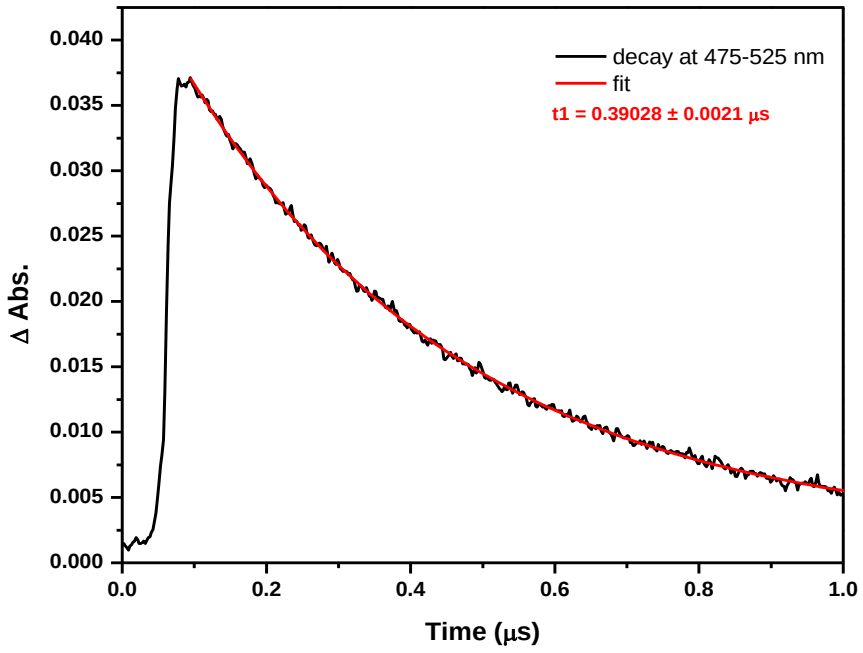

Figure A-14 Decay of the transient signal averaged over the 475-525 nm wavelength region for $[Ir(ppz)_2PT_3$-*PS*$](PF_6)$, (**62**), (black) upon excitation at 355 nm in argon-sparged CH_3CN, and the monoexponential fit (red).

Table A-4 Selected crystallographic data for [Cu(dmp)(MeCN)PT_3-*P*](PF_6), (**75**), and [Cu(phen)PT_3-*P*](PF_6), (**76**).

	[Cu(dmp)(MeCN)PT_3-*P*](PF_6)	[Cu(phen)PT_3-*P*](PF_6)
Formula	$C_{40}H_{32}N_3P_2F_6\ S_3Cu$	$C_{36}H_{25}N_2F_6P_2S_3Cu$
Crystal Colour, Habit	yellow, rod	yellow, irregular
Dimensions / mm	0.07 × 0.12 × 0.30	0.13 × 0.22 × 0.25
Temperature / K	90 (1)	100 (1)
Crystal System	monoclinic	triclinic
Space Group	*P* $2_{1/c}$ (#14)	*P* -1 (#2)
a / Å	11.5178 (9)	12.137(1)
b / Å	9.1509(7)	12.343(1)
c / Å	36.983(3)	13.457(1)
α /deg	90	74.841(5)
β /deg	98.276(1)	80.130(5)
γ /deg	90	61.167(4)
V / $Å^3$	3857.4(5)	1702.0(3)
Z	4	2
ρ_{calc} / g cm^{-1}	1.533	1.602
μ (Mo kα)	8.76 cm^{-1}	9.84 cm^{-1}
R1[a] (I>2.00σ(I))	0.039	0.045
*w*R2[a] (I>2.00σ(I))	0.078	0.103
Goodness of fit	1.06	1.04

[a]Function minimized. $\Sigma w(F_o^2-F_c^2)^2$, $R1 = \Sigma ||F_o| - |F_c|| / \Sigma |F_o|$, $wR2 = [\Sigma (w (F_o^2 - F_c^2)^2)/ \Sigma w(F_o^2)^2]^{1/2}$

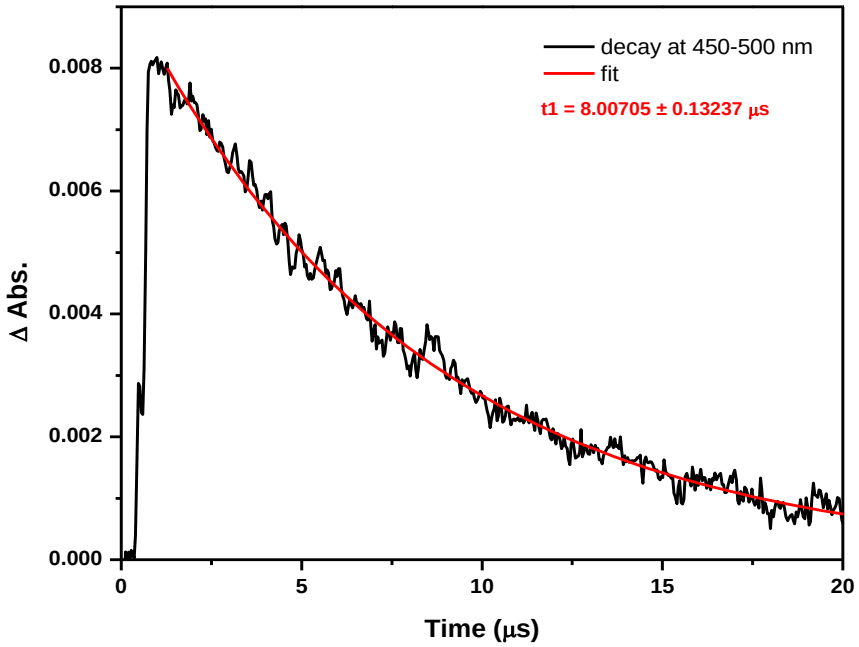

Figure A-15 Decay of the transient signal averaged over the 450-500 nm wavelength region for [Cu(dmp)(MeCN)PT$_3$-*P*](PF$_6$), (**75**), (black) upon excitation at 355 nm in argon-sparged CH_3CN, and the monoexponential fit (red).

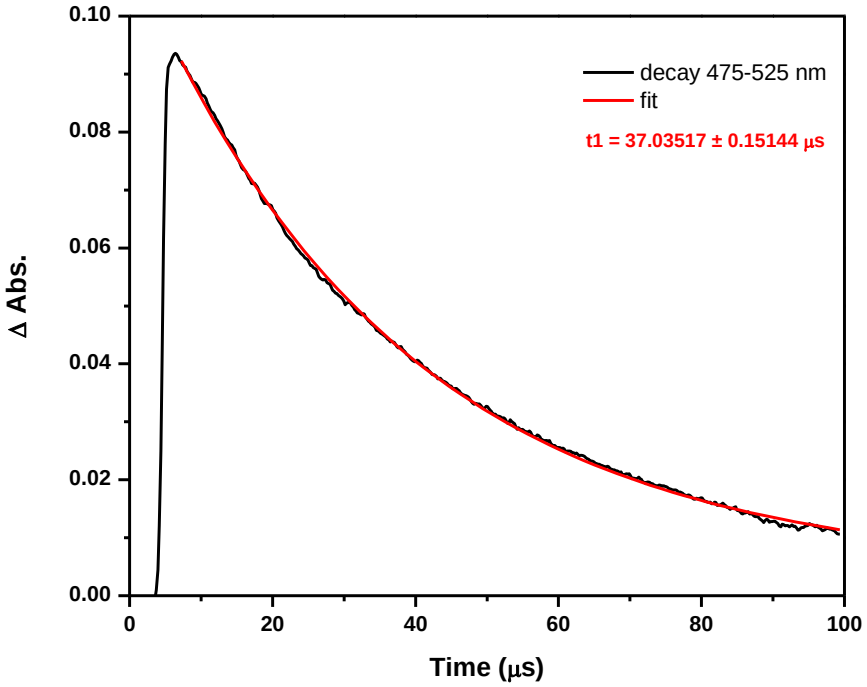

Figure A-16 Decay of the transient signal averaged over the 475-525 nm wavelength region for [Cu(dmp)(MeCN)PT$_3$-*P*](PF$_6$), (**75**), (black) upon excitation at 355 nm in argon-sparged CH_2Cl_2, and the monoexponential fit (red).

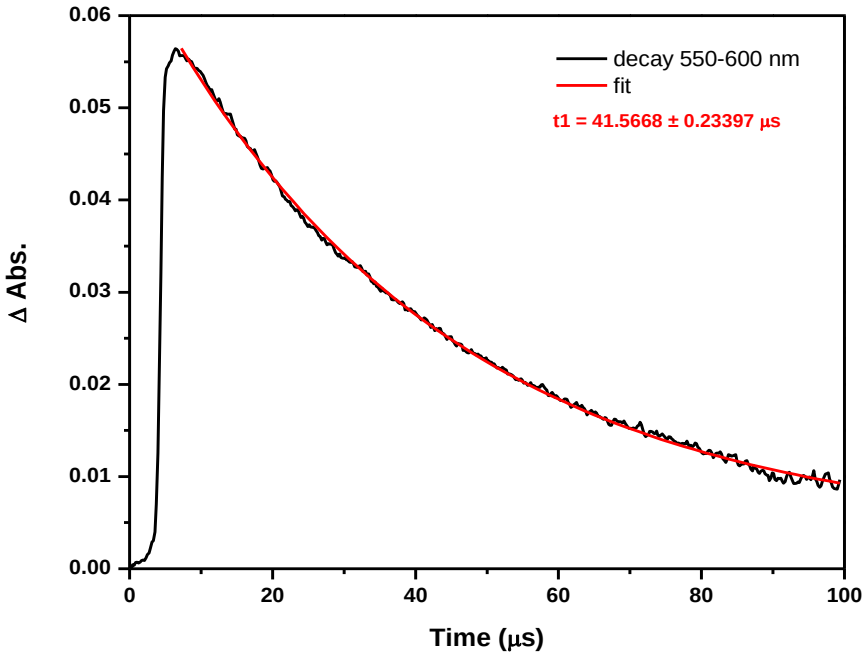

Figure A-17 Decay of the transient signal averaged over the 550-600 nm wavelength region for [Cu(dmp)(MeCN)PT_3-*P*](PF_6), (**75**), (black) upon excitation at 355 nm in argon-sparged CH_2Cl_2, and the monoexponential fit (red).

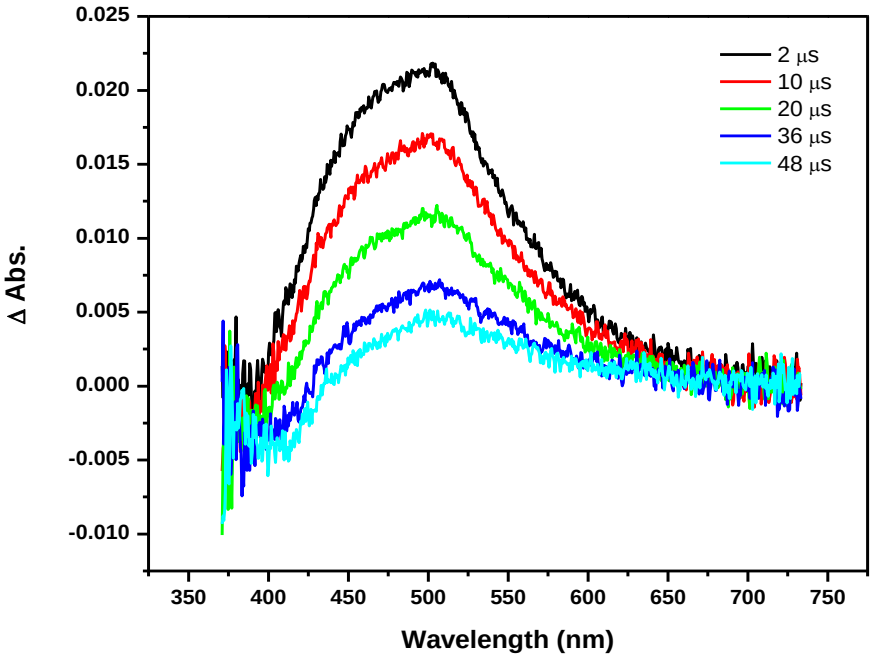

Figure A-18 Transient absorption spectra of PT_3 in argon-sparged CH_3CN.

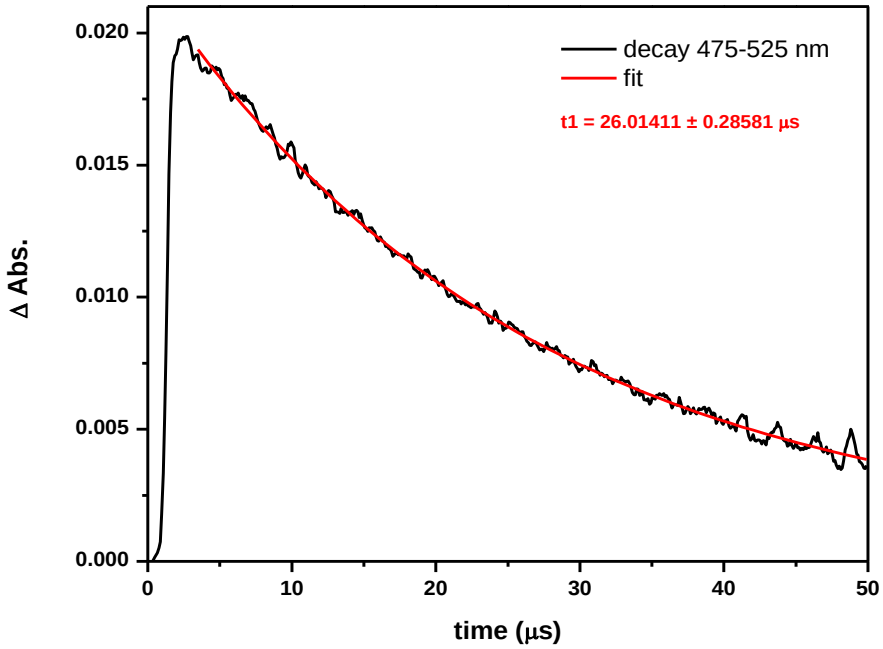

Figure A-19 Decay of the transient signal averaged over the 475-525 nm wavelength region for PT_3 (black) upon excitation at 355 nm in argon-sparged CH_3CN, and the monoexponential fit (red).

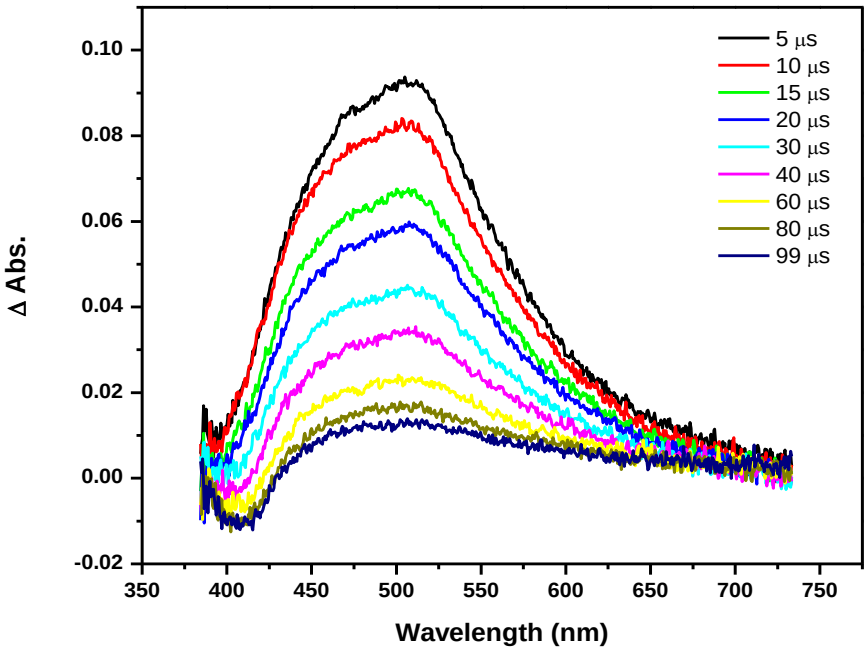

Figure A-20 Transient absorption spectra of PT_3 in argon-sparged CH_2Cl_2.

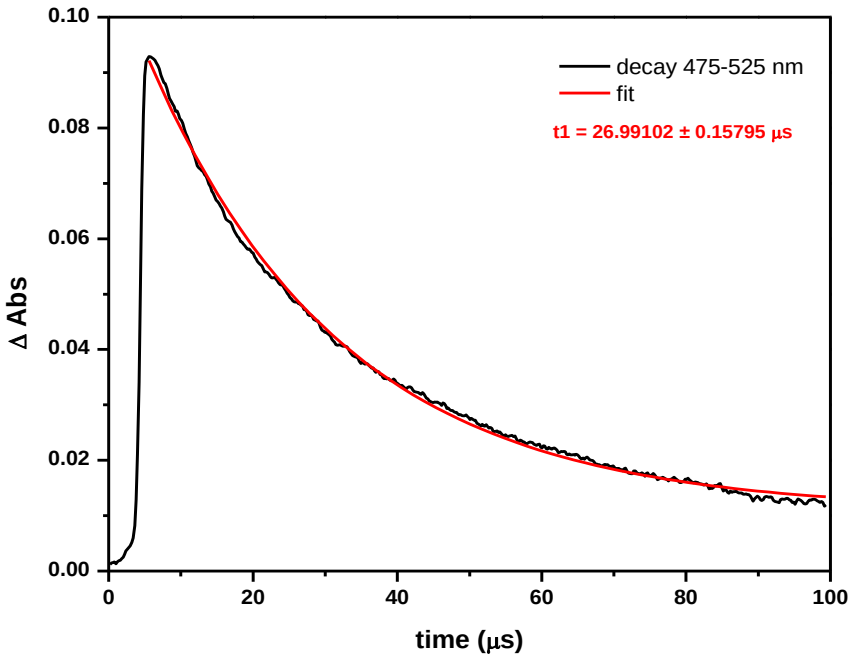

Figure A-21 Decay of the transient signal averaged over the 475-525 nm wavelength region for PT_3 (black) upon excitation at 355 nm in argon-sparged CH_2Cl_2, and the monoexponential fit (red).

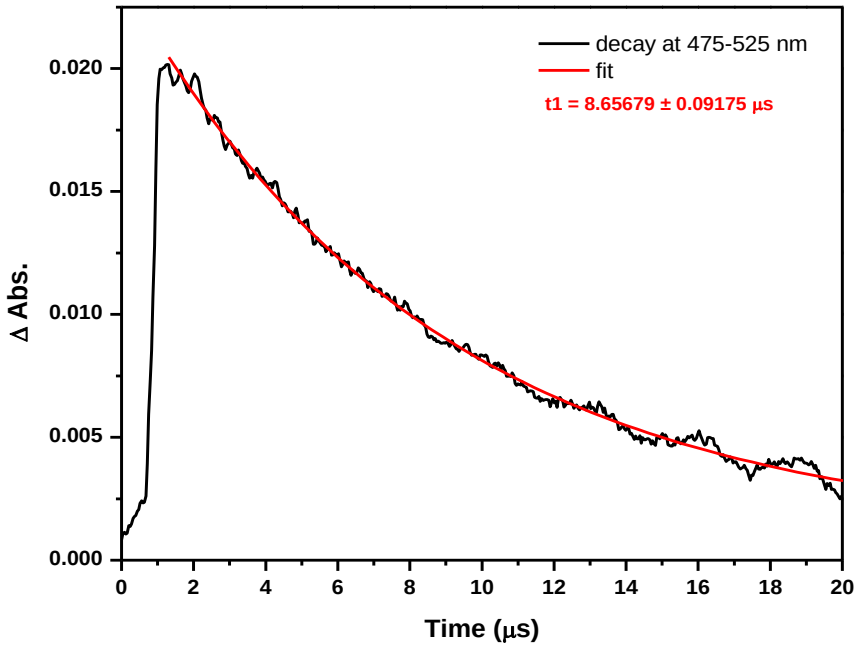

Figure A-22 Decay of the transient signal averaged over the 450-500 nm wavelength region for [Cu(phen)PT_3-*P*](PF_6), (**76**), (black) upon excitation at 355 nm in argon-sparged CH_3CN, and the monoexponential fit (red).

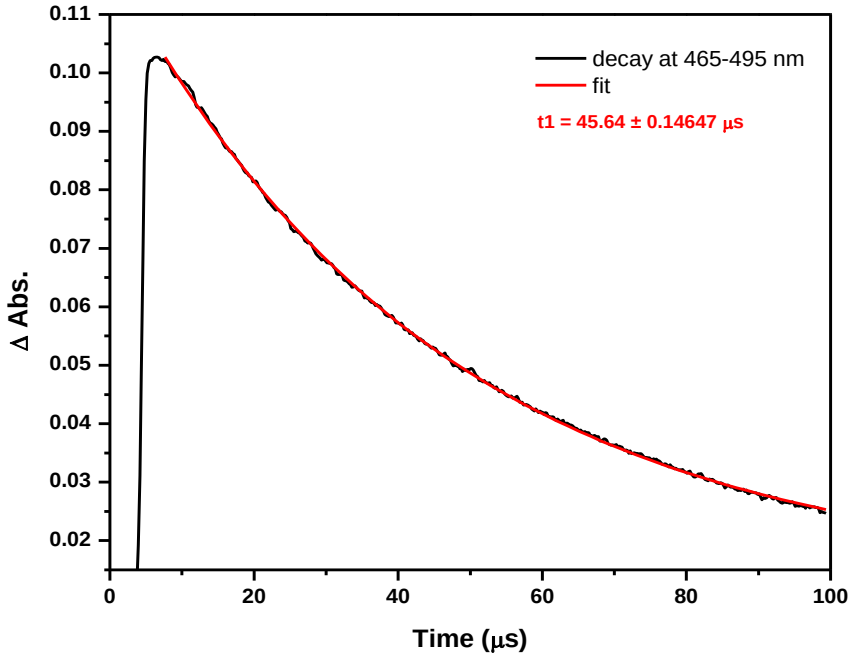

Figure A-23 Decay of the transient signal averaged over the 450-500 nm wavelength region for [Cu(phen)PT_3-*P*](PF_6), (**76**), (black) upon excitation at 355 nm in argon-sparged CH_2Cl_2, and the monoexponential fit (red).

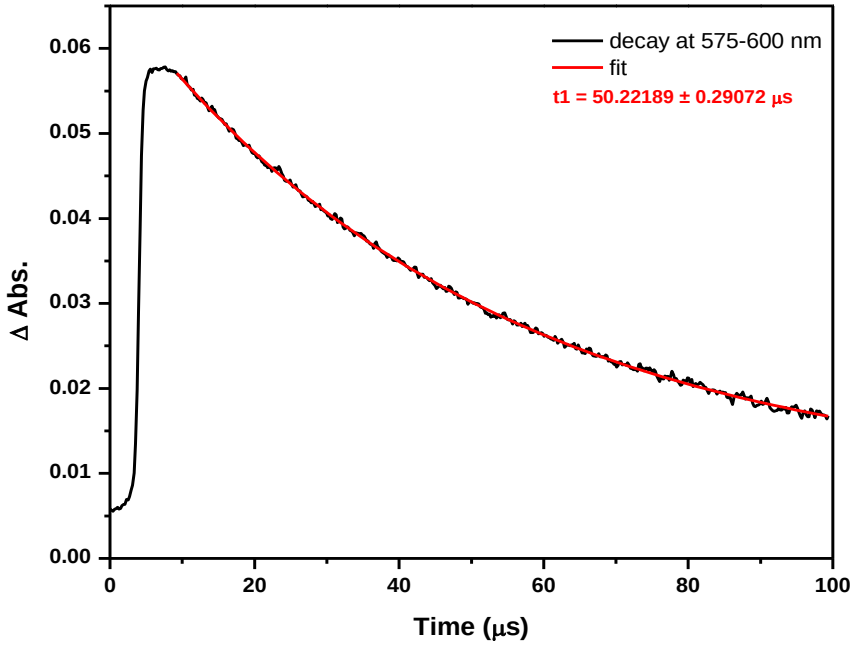

Figure A-24 Decay of the transient signal averaged over the 575-600 nm wavelength region for [Cu(phen)PT_3-*P*](PF_6), (**76**), (black) upon excitation at 355 nm in argon-sparged CH_2Cl_2, and the monoexponential fit (red).

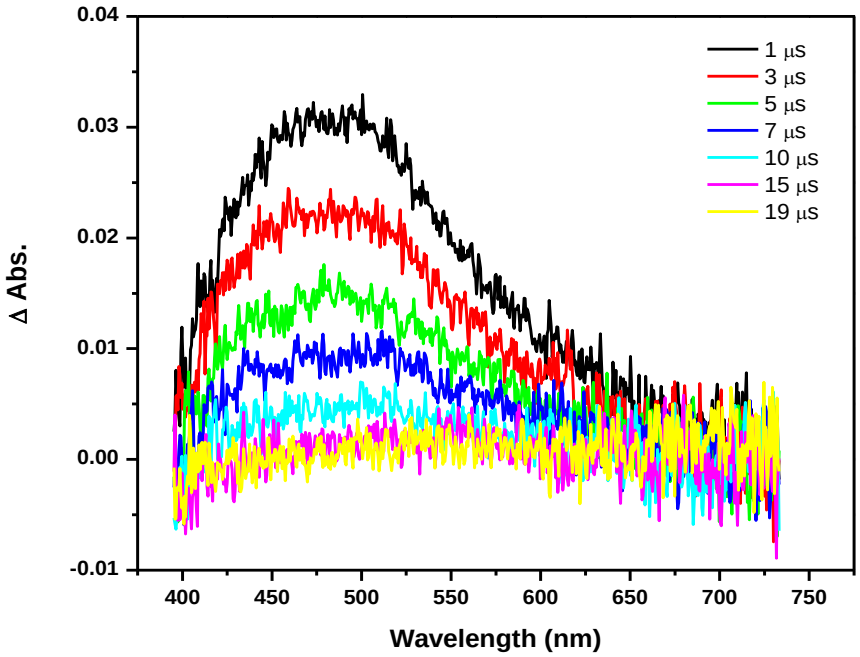

Figure A-25 Transient absorption spectra of [Cu(phen)PT_3-*P*](PF_6), (**76**), in argon-sparged CH_3OH.

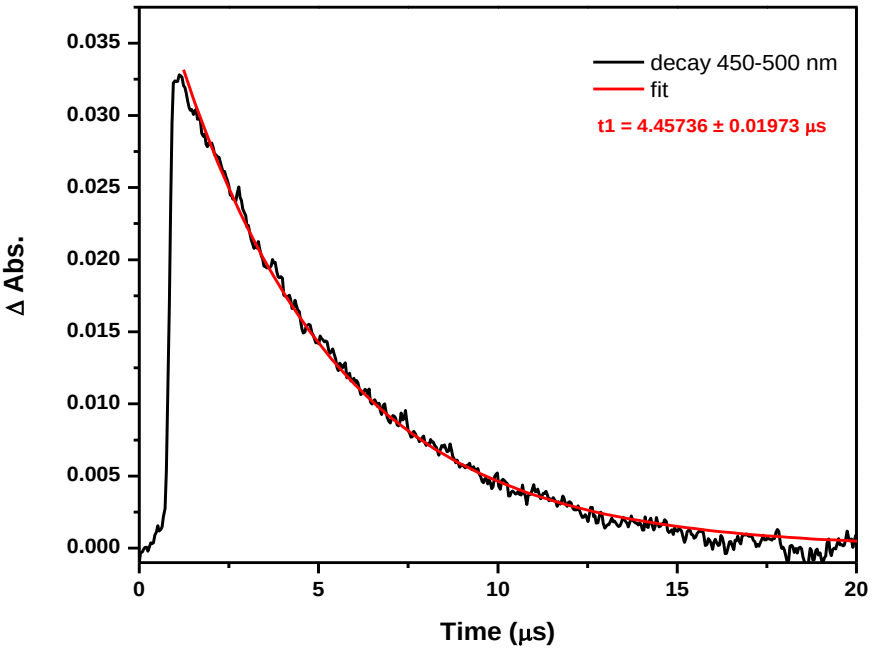

Figure A-26 Decay of the transient signal averaged over the 450-500 nm wavelength region for [Cu(phen)PT_3-*P*](PF_6), (**76**), (black) upon excitation at 355 nm in argon-sparged CH_3OH, and the monoexponential fit (red).

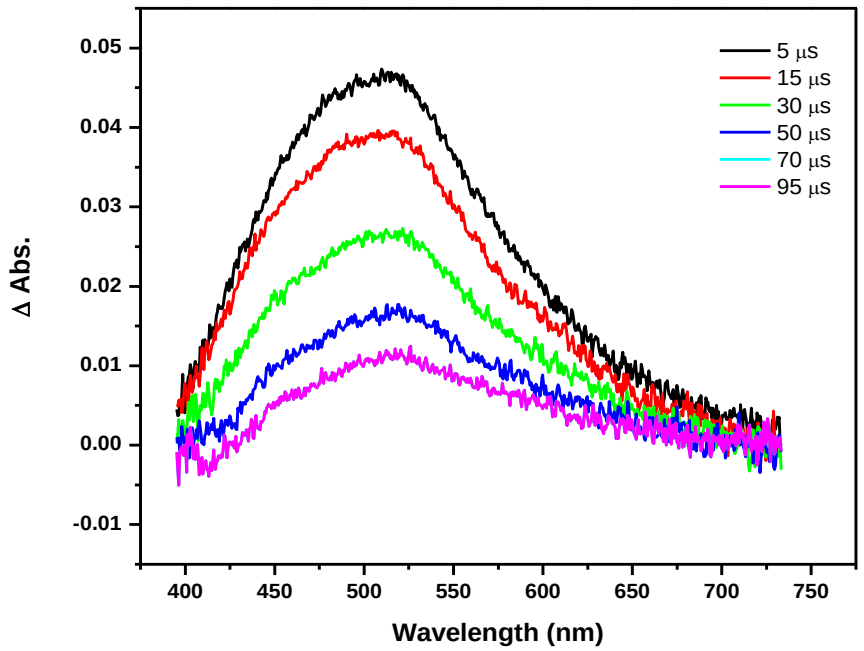

Figure A-27 Transient absorption spectra of [Cu(phen)PT_3-*P*](PF_6), (**76**), in argon-sparged pyridine.

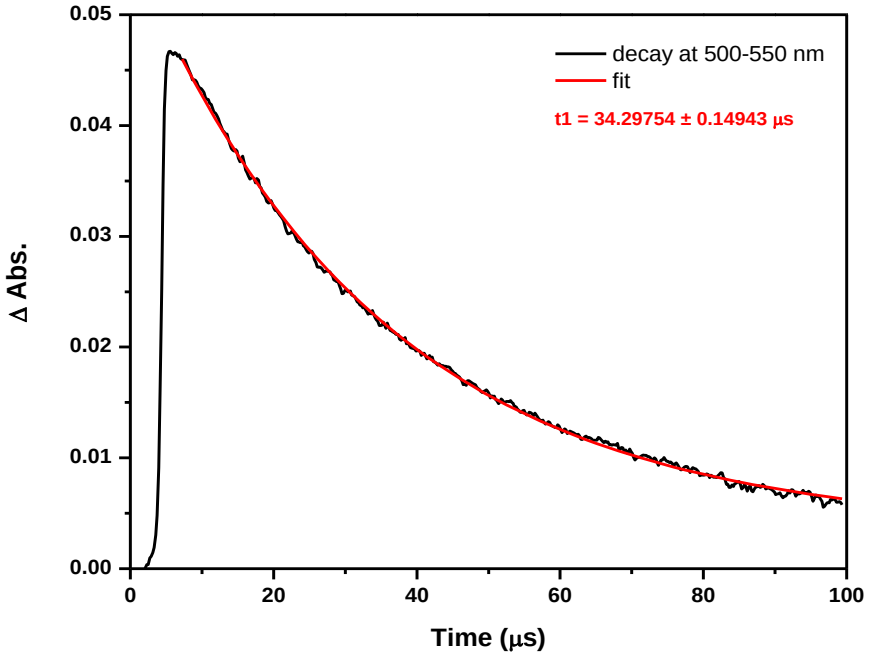

Figure A-28 Decay of the transient signal averaged over the 450-500 nm wavelength region for [Cu(phen)PT_3-*P*](PF_6), (**76**), (black) upon excitation at 355 nm in argon-sparged pyridine, and the monoexponential fit (red).